THE UNIVERSITY OF HULL

Efficiency enhancement and degradation processes in Cu_xS/CdS thin film solar cells

being a thesis submitted for the degree of

Doctor of Philosophy

in the University of Hull

by

Mohamed Al-Achkar BSc (Aleppo University, Syria)

August 1990

To my parents

my wife

and my children

(Julian and Laura)

Abstract

An investigation has been made into the structure and properties of polycrystalline Cu_xS-CdS solar cells in order to develop an improved understanding of some of the processes which lead to unsatisfactory reproducibility and long term stability of the characteristics of these devices. The cells studied during this project were fabricated using vacuum evaporation for production of the CdS base layer and the well known chemical exchange process in a CuCl solution for formation of the Cu_xS layer. In view of the non-uniform thickness of the Cu_xS layer and non-planar structure of the Cu_xS-CdS interface, it was found to be necessary to employ a variety of different characterisation techniques to monitor changes in the structure and properties of the devices. These techniques included I/V, C-V, spectral response and sheet resistance measurements, electrochemical analysis, cathodoluminescence spectroscopy and Rutherford backscattering.

Detailed consideration was given to the influence of the conditions of formation on the properties of each cell component, in order to establish procedures necessary for the production of reproducible structures. Particular attention was paid to the rate of growth of the Cu_xS layer and a theoretical analysis was developed to account for the time dependence of the growth in mean thickness of the Cu_xS layer in terms of the contributions associated with growth at the surface of the CdS layer and in the CdS grain boundary regions. The grain boundary contribution was found to be very sensitive to the CdS grain structure and to the previous treatment given to the CdS layer. Pre-annealing in air at 200°C enhanced the grain boundary penetration

while the effect of ion implantation (with either Cu or Zn ions) was found to depend on the initial structure and the implantation conditions, but substantial improvements in the photovoltaic conversion efficiency were shown to be possible as a result of such treatment.

The rate of degradation of cells exposed to air was also found to be dependent on the previous history of the cell. An increased concentration of Cd in the Cu_xS film (due to diffusion from the CdS layer) appeared to reduce the rate of degradation while use of the standard stabilizing treatment (deposition of Cu overlayer followed by annealing in air) was shown to reduce interfacial diffusion as well as protecting the front surface of the Cu_xS layer against oxidation.

Acknowledgements

I would like to thank Aleppo University for a research scholarship and my family in Syria for additional financial support during the course of my studies in Hull. Also I wish to thank Professor F.J. Bryant for making available the research facilities of the Physics Department and I would like to express my sincere gratitude to my supervisor Dr C.G. Scott for his continuous guidance and encouragement. Many thanks are also due to Mr J. Reed for his help with the cathodoluminescence measurements, Mr D. Wright for his assistance with the annealing procedures, Mr T. Sinclair for his scanning electron microscopy work, Mrs V. Hewer for her invaluable general technical assistance and Mrs F. Hanson for typing the thesis.

Finally, I wish to thank all my Arabic and English friends for their encouragement and support and especially my patient wife Anita for doing everything possible to ensure that I could devote all my time to this research project.

CONTENTS

Page

Chapter One — Introduction

1.1 Energy sources and energy conversion 1

1.2 Photovoltaic power generation 2

1.3 Thin film Cu_xS-CdS cells 6

Chapter Two — Theoretical Consideration

2.1 The photovoltaic effect 9

2.2 The p-n junction photovoltaic converter 9

2.2.a The ideal case 9

2.2.b The practical case 16

2.3 The metal-semiconductor junction (Schottky diode) 17

2.4 The p-n heterojunction 19

2.5 The space charge region and capacitance-voltage studies for solar cells 24

2.6 Diffusion processes in polycrystalline films 30

Chapter Three — The structure and characteristics of Cu_xS-CdS cells

3.1 Historical background 33

3.2 The CdS layer 35

3.2.1 General properties 35

3.2.2 Structure of vacuum evaporated CdS films 37

3.2.3 Electrical characteristics of vacuum evaporated CdS films 39

3.3 The copper sulphide layer 42

3.3.1 Structure and composition of copper sulphide 42

3.3.2 Electrical and optical properties 43

3.3.3 Film formation processes 45

Page

3.4 Properties of Cu_2S-CdS solar cells 47

3.4.1 Influence of cell structure 47

3.4.2 Cell characteristics and junction models 48

3.4.3 Degradation and cell stability 52

Chapter Four . Experimental systems and procedures

4.1 Fabrication of CdS films 59

4.1.1 The vacuum evaporator system 59

4.1.2 Substrate preparation 60

4.1.3 The CdS film deposition process 61

4.2 Electrical characterisation of CdS layers 63

4.3 Formation of copper sulphide layers 64

4.4 Characterisation of copper sulphide layers 66

4.4.1 Sheet resistance measurements 66

4.4.2 Electrochemical analysis for determination of thickness and stoichiometry 66

4.5 Formation of front contacts 68

4.6 Optional cell fabrication and post-fabrication processes 69

4.6.1 Annealing in different atmospheres 69

4.6.2 Ion implantation 69

4.7 Characterisation of Cu_xS-CdS solar cells 71

4.7.1 The current-voltage characteristics 71

4.7.2 Scanning electron microscopy 72

4.7.3 Photovoltaic spectral response measurements 72

4.7.4 The cathodoluminescence system 73

4.7.5 Rutherford backscattering technique 74

Page

Chapter Five Results

5.1 Structure and properties of the CdS layer 76

5.1.1 Substrate preparation 76

5.1.2 Effect of different CdS source materials 78

5.1.3 The effect of film deposition conditions 82

5.1.4 CdS surface topography and effects of etching 84

5.1.5 Effect of ion implantation 88

5.2 Formation and properties of the copper sulphide layer 90

5.2.1 Production of Cu_xS layers 90

5.2.2 Growth of Cu_xS on annealed CdS substrates 97

5.2.3 Copper sulphide stoichiometry 103

5.2.4 Luminescence characteristics 109

5.3 Characteristics of complete Cu_xS/CdS cells 120

5.3.1 I-V characteristics 120

5.3.2 Photosensitivity spectral response 125

5.3.3 Effect of annealing 128

5.3.4 Effect of ion implantation 136

5.4 Stability of Cu_xS/CdS cells 143

5.4.1 Variation ofcell characteristics with time 143

5.4.2 Processes associated with Cu_xS/CdS interface 146

5.4.3 Processes influencing the Cu_xS layer 155

(i) Electrochemical analysis 156

(ii) Sheet resistance and measurements 158

(iii) Luminescence 162

(iv) Rutherford backscattering 165

5.4.4 Stabilization of cell structure and characteristics 169

Page

Chapter Six Summary and conclusions

6.1	The CdS base layer	175
6.2	The Cu_xS absorber layer	176
6.3	Characteristics of Cu_xS-CdS cells	179
6.4	Stability of Cu_xS-CdS cells	181
6.5	Concluding remarks	183

References

CHAPTER ONE

INTRODUCTION

1.1 Energy sources and energy conversion

During the last two decades, questions concerning trends in energy requirements have been treated with increasing seriousness in both developed and underdeveloped countries around the world. It is now recognised that certain forms of energy (the fossil fuels) on which we have come to rely are limited resources and that great care must be taken to ensure that these resources do not become too depleted before suitable alternatives are made available. While nuclear energy is already well established in some countries, there is widespread concern about the safety of this type of technology, especially in relation to long term storage of radioactive waste products. As a result, there is a growing reluctance to become dependent upon nuclear energy for our future energy needs. In the search for alternative energy sources, particular consideration is now being given to the use of the effectively non-depletable energy which we receive from the sun, either directly, as solar radiation, or indirectly, via the wind, ocean waves and river flows, as a result of a variety of natural energy conversion processes. Of course, it is the sun's energy which is also responsible for the generation of our present capital energy resources, in the form of the fossil fuels, as a result of chemical energy conversion processes in living organisms many millions of years ago.

There is no doubt that the natural energy flows which are driven by the sun represent a vast resource, sufficient both to replace the fossil fuels and to meet the expected future increased demand for

energy, but severe difficulties arise in the conversion of this energy to a suitable form at reasonable cost.

Since his appearance on earth, man has tried, with relative success, to master the forces of nature for his own benefit. Our primitive ancestors first attempted energy conversion, when they tried to replace or amplify the limited forces of their muscles by the use of such primitive weapons and tools as stones and animal bones. Later, the discovery of fire and the wheel were real revolutions in energy conversion, and, consequently, in the way of life of mankind. The continuing search for new sources of energy eventually led to the discovery of electricity, in the eighteenth century, causing a further dramatic impact on all aspects of life. Electrical energy has been demonstrated to be the most convenient form of energy to which all other forms of energy may be converted. It is easy to transport, easy to control, and easy to transform into any form of work desired by the consumer. At the present time, the conversion of primary energy (mainly fossil fuels) into electrical energy involves a series of intermediate transformations, (e.g. to thermal energy and mechanical energy) which lead to limitations in efficiency, reliability and compactness. With increasing interest in the utilization of solar energy, it is clearly preferable to convert the solar radiation directly into electricity. This can be achieved by making use of semiconductor devices which exhibit the photovoltaic effect.

1.2 Photovoltaic power generation

Any device which converts electromagnetic radiation directly into electricity is called a photovoltaic generator. The photovoltaic effect was discovered in 1839 when Becquerel (1) noted that a

difference of potential was developed when light was shone onto an electrode immersed in an electrolytic solution. Four decades later, work on solid materials led to the observation of the same effect by Adams and Day (2) in selenium. Later studies showed that the photovoltaic effect could arise in other solids for example in copper oxide (3). Although the origin of the photovoltaic effect was not understood at this time, its usefulness soon became clear and selenium photovoltaic cells were employed for many years in photographic exposure meters. Eventually, it was realized that the behaviour of these cells depended upon the existence of an energy barrier and, following the development of semiconductor theory, a more complete understanding of the effects which occur in photovoltaic devices gradually emerged. As a result of this improved understanding, together with rapid improvements in semiconductor materials technology during the last three decades, many different types of photovoltaic devices have now been investigated and steadily increasing energy conversion efficiencies have been reported. For example, since the first reference to Si solar cells in 1954 (4), their efficiency has increased from 6% (suitable only for use in certain low energy systems, such as digital watches and toys) to more than 15% in systems which can provide the major power source for spacecraft and communications satellites.

The light weight and compactness of semiconductor solar cells has made them ideally suited for use in power systems for earth satellites and other space vehicles and there is no doubt that these space applications have been the main driving force behind most of the developments in solar cell technology over these last three decades. With continued expansion in space related activities, this stimulus is

expected to be maintained into the forseeable future. However, in the course of these developments for space applications, emphasis has been placed on the operational reliability of the cells rather than on cost. For terrestial applications, particularly for large scale systems, the cost will be an important factor and much research is now being directed towards the development of new materials and cell fabriction technologies capable of providing large area, high efficiency, low cost cell arrays. In fact, silicon solar cells are still the most commonly used devices for both terrestial and space applications. Each time alternative cell types or other power sources have seemed ready to compete, new advances providing increased efficiency, reduced weight or lower costs for Si cells have maintained their overall superiority. The already proven reliability of Si cell technology in space application has provided a solid foundation for the deployment of Si cell arrays in terrestial, remote locations. Reliability has been maintained by developing new mounting and packaging techniques to protect the devices, allowing exploitation of the inherent stability that solid-state devices possess.

The development of relatively small, photovoltaic power systems in small villages around the world can provide great benefits for the local communities and it is in such applications that current photovoltaic technology seems to be best suited as a terrestial power source. To compete with modern conventional power installations vast areas of ground would need to be covered with huge numbers of photovoltaic modules, each consisting of many, interconnected individual single crystal Si cells. Although some relatively large systems (in excess of 1 MW) have been constructed using these types

of module (5), the high cell fabrication and module assembly costs make them uneconomic for such purposes. Alternative approaches for high power requirements include the use of concentrator systems and thin film systems.

By making use of concentrators, a large solar radiation flux can be collected without the need for a correspondingly large area of high cost semiconductor material. The photovoltaic cells in such systems are placed at the focus of the concentrator (lens or reflector) which can be fabricated from much cheaper material. As the photovoltaic cells can be small area devices, it may be economically viable to use materials which are even more expensive than Si if these are capable of yielding higher conversion efficiences (as in the case of GaAs). The use of simple single homojunction devices limit the efficiency to a maximum achievable value of 28% (6), but further improvements can be achieved making use of multijunction devices which appear to be capable of realizing efficiencies up to 35% (7) (8). The multijunction solar cell consists of two or more single-junction cells stacked in optical series with the highest band gap structure located at the illuminated surface and the lowest band gap junction at the back. Each cell in the stack absorbs and converts energy in only a restricted wavelength band of the incident solar spectrum but the resultant effect is that a higher fraction of the total incident spectrum contributes to the electrical output of the cell (compared with a single-junction cell). In order to illustrate the relative complexity of these multijunction systems, figure 1.1 shows a schematic cross section of a monolithic, and the alternative mechanically stacked, AlGaAs-Si tandem solar cell system suggested by Gale and coworkers (9).

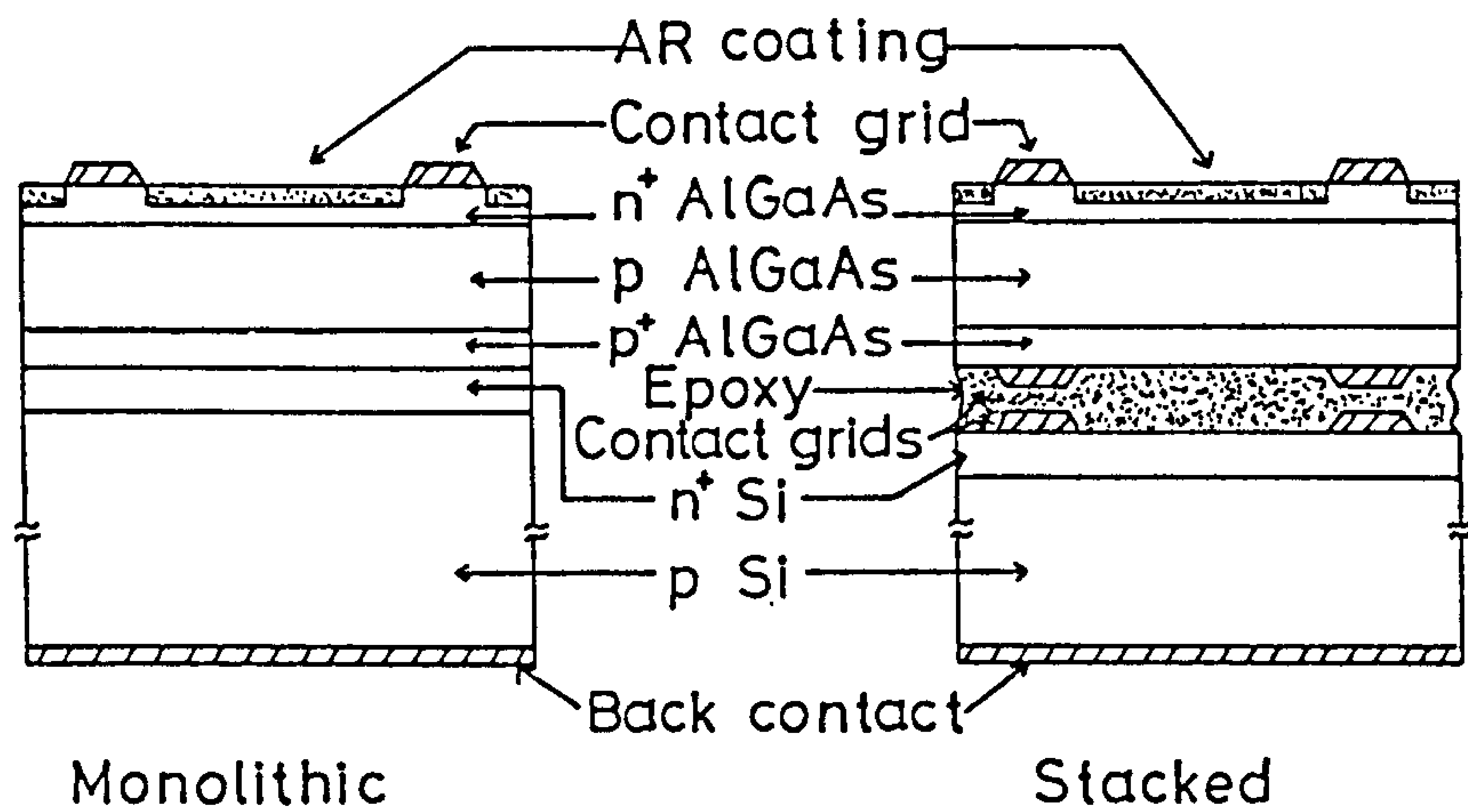

Fig.(1.1) Schematic cross sections of AlGaAs-Si tandem solar cells using the monolithic and hybrid approaches. Ref. (9).

There are two main problems associated with concentrator systems. The first is related to the heat generated as a result of concentrating the solar radiation. If this heat is not removed efficiently then the temperature of the cell will increase causing a reduction in photovoltaic conversion efficiency and, possibly, some permanent damage to the device. The second problem involves the need for tracking to ensure that the sun light remains focussed on the solar cells. Although both these problems can be satisfactorily overcome, it should be noted that they involve additional cost.

The thin film approach avoids both these problems by making the device area equal to the collector area but cheapness is maintained by using thin, polycrystalline or amorphous layers instead of single crystal materials. There are many different materials (e.g. Cu_2S, CdTe, CdS, $CuInSe_2$, Zn_3P_3, GaAs and amorphous silicon) which have been used in photovoltaic devices and several of these have exhibited respectable efficiencies as shown in table (1.1) although the efficiency of these thin film devices is clearly less than single junction silicon solar cells. In addition to the reduced efficiency, the characteristics of thin film devices are generally less reproducible and less stable than single crystal cells. However, an improved understanding of the associated problems is gradually being developed.

1.3 Thin film Cu_2S-CdS cells

Like several of the other compound semiconductor solar cell systems listed in table 1.1, the research history of Cu_2S-CdS cells has been marked by periods of intense interest and rapid improvements in reported cell performance. The interest in Cu_2S-CdS

Table (1-1) Representative efficiency of some thin-film solar cells.

Cell	Best efficiency reported (%)	Ref.
Amorphous Si	12	10
$GaAsP^+/n$ homojunction	8.1	11
$CdS/CuInSe_2$	10.4	12
$Zn_xCd_{1-x}S/CuInSe_2$	12.5	13
Cu_2S/CdS	9.15	14
$Zn_xCd_{1-x}S/Cu_2S$	10.2	15
CdS/CdTe	12.8	16
$CdS/CuInS_2$	3.25	17
CdS/InP	5.7	18
Mg/Zn_3P_2	4.3	19

polycrystalline devices was particularly strong after it was demonstrated at an early stage that the cells could be fabricated using techniques which could be relatively easily scaled up for commercial production. Unfortunately, the early attempts at large scale production were not successful and it seems that these devices now carry a reputation for poor reproducibility and poor operational stability. In spite of more recent improvements in production line techniques which were found to yield significant improvements in performance (20), commercial interest in Cu_2S has declined while alternative materials primarily $CuInSe_2$ and CdTe are now being investigated more intensively (21). The lack of confidence particularly in the stability of Cu_2S/CdS cells is due partly to the absence of a full understanding of the degradation processes which can occur. It is for this reason that, during the study described in this thesis, an attempt was made to develop an improved understanding of these processes. Of course the problem is made more complicated in polycrystalline systems by the complex geometry of the component layers and interfaces. As the cells have properties which are critically dependent on every component part of the device, a very high degree of control is required at every stage of cell construction in order to achieve suitably reproducible results. As a result of this, the early stages of this study were concerned with developing reliable cell fabrication procedures. Details of these procedures and of the various characterisation techniques employed during the investigation are given in chapter 4 of this thesis following a review of the basic semiconductor theory relating to solar cells (chapter 2) and an account of established characteristics of Cu_2S/CdS cells

(chapter 3). Details of the results obtained during the project are given in chapter 5 and the conclusions are presented in chapter 6.

CHAPTER TWO

THEORETICAL CONSIDERATIONS

2.1 The photovoltaic effect

The photovoltaic effect arises when electron-hole pairs are generated by the absorption of photons having energy E greater than the band gap of the absorbing material. ($E = h\nu$, where h is Planck's constant, and ν is the frequency of the incident radiation). If the electron-hole pairs are separated by a built-in electric field due to an internal potential barrier (e.g. at a metal-semiconductor or semiconductor-semiconductor junction) a photogenerated current and voltage is produced.

2.2 The p-n junction photovoltaic converter

2.2.a The ideal case

When a p-type region lies adjacent to an n-type region of the same material, in such a way as not to destroy the crystalline integrity of the material we have a p-n homojunction. At this junction there is a built-in electric field, under thermal equilibrium conditions, due to the transfer of some holes from the p to the n region and of some electrons from the n to the p-region, leaving uncompensated donor and acceptor ions on either side of the junction. The associated potential difference across the junction is known as the diffusion voltage and is shown as V_{np} in figure 2.1. The direction of the junction field is such as to assist the transport of minority carriers and oppose the transport of majority carriers across

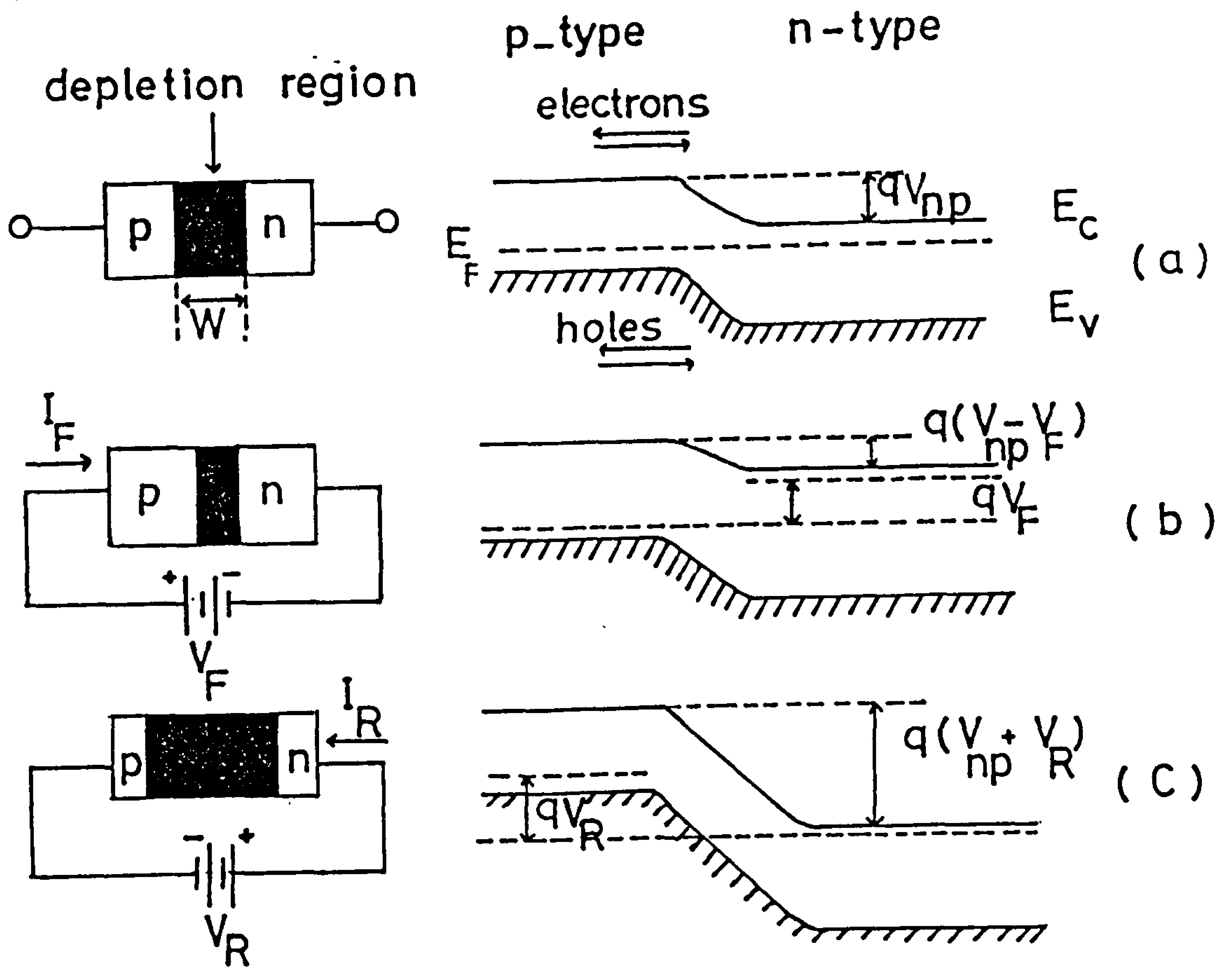

Fig.(2.1) Schematic representaions of depletion layer width and energy band diagram for a p-n junction under various biasing conditions (a) Thermal-equilibrium (b) Under forward bias (c) Under reverse bias.

the junction, but under thermal equilibrium conditions there are equal electron and hole currents in both directions, as shown figure 2.1(a), and the net current flow across the junction is zero. The opposing contribution to the electron and hole currents are referred to as the 'drift' and 'diffusion' components. The hole current consists of (a) minority holes from the n-region drifting into the p-region under the influence of the electric field E at the junction and (b) majority holes from the p-region diffusing under the hole concentration gradient into the n-region. Similarly the electron current consists of minority carriers drifting from the p-region, and majority carriers diffusing from the n-region. Therefore the situation under thermal equilibrium conditions is represented by the equation:

$$J_{p,n} = J_{p,n}\,(\text{drift}) + J_{p,n}\,(\text{diffusion}) = 0$$

or: $$J_p = qpu_pE - q\,D_p\,\frac{dp}{dx} = 0 \qquad (2.2.1)$$

$$J_n = qn\,u_n\,E + q\,D_n\,\frac{dn}{dx} = 0 \qquad (2.2.2)$$

where J_p, J_n are the hole and electron current densities, E is the electric field at the junction, u_p,u_n are the hole and the electron mobilities, D_p,D_n are the diffusion coefficients for holes and electrons, q is the electron charge, and p,n are the concentrations for holes and electrons respectively. In order to determine the electric field and potential variations at the p-n junction, the space charge distribution in this region must be known. The simplest case to consider is that of an abrupt junction between uniformly doped regions of a semiconductor, as might be approximately achieved by

shallow diffusion doping or low-energy ion implantation. In such an abrupt junction the charge densities on each side of the depletion layer are as shown in figure 2.2 where x = o at the junction between the p- and n- regions. (This interface is assumed to form a plane lying perpendicular to the X-axis.) There is a uniform density of uncompensated ionized donor atoms N_d extending a distance w_n into the n-region and a similarly uniform distribution of uncompensated ionized acceptor atoms of density N_a extending a distance $- w_p$ into the p-region. (Here it is assumed that the depletion region between $-w_p$ and $+w_p$ is very wide in comparison with the transition regions at the edges of the depletion layer where the donor/acceptor ion space charge is partially compensated by free carriers). For this case, the relationship between the space charge and the electrostatic potential ψ can be expressed by Poisson's equation in the form:

$$\frac{d^2\psi}{dx^2} \equiv - \frac{dE}{dx} = - \frac{q}{\varepsilon} \left(N_d - N_a + P - n\right) \qquad (2.2.3)$$

where, ε is the permittivity of the material. The free carrier concentrations, n and p, within the depletion region are considered to be negligible so that for the p-region of the depletion layer ($-w_p < x < \emptyset$) equation (2.2.3) can be written as:

$$\frac{dE}{dx} = - \frac{qNa}{\varepsilon} \qquad (2.2.4)$$

while in the n-region of the depletion layer ($o < x < w_n$) it becomes:

$$\frac{dE}{dx} = - \frac{q\ N_d}{\varepsilon} \qquad (2.2.5)$$

Integrating equations (2.2.4) and (2.2.5) and employing the boundary

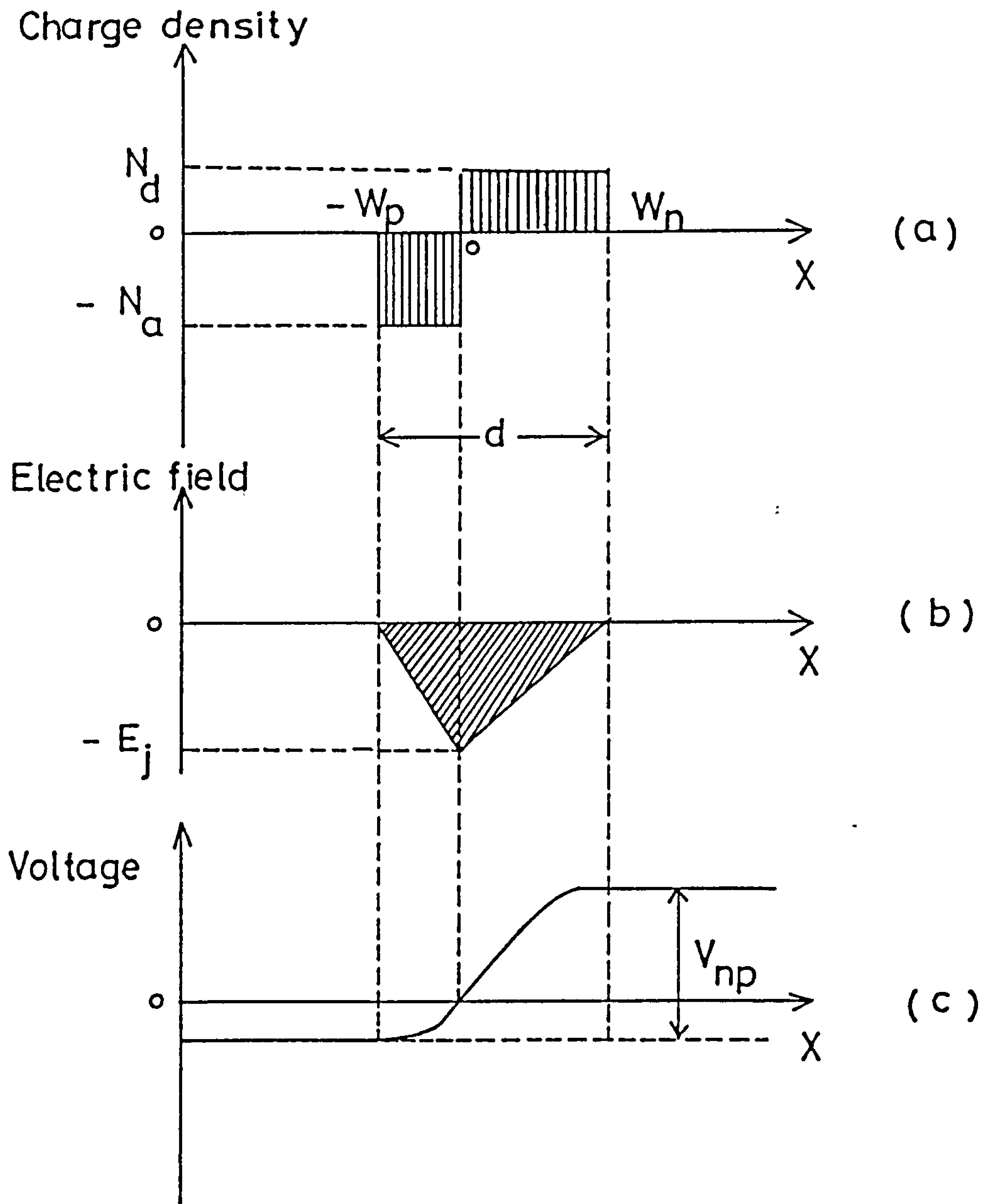

Fig.(2.2) Depletion layer at an abrupt junction (a) charge density distribution (b) electric field (c) voltage distribution.

conditions, $E_p = 0$ when $x = -w_p$ and $E_n = 0$ when $x = w_n$, yields the relationships:

$$E_p = -\frac{qN_a}{\varepsilon}(x + W_p), \qquad (-w_p<x<0) \qquad (2.2.8)$$

$$E_n = \frac{qN_d}{\varepsilon}(x - W_n), \qquad (0<x<w_n) \qquad (2.2.9)$$

Since x is negative in the p-region and positive in the n region, the magnitude of the field in each region increases as x approaches zero, and when $x = 0$

$$E_p = E_n = E_j = -\frac{qN_aW_p}{\varepsilon} = -\frac{qN_dW_n}{\varepsilon} \qquad (2.2.10)$$

E_j is thus the maximum field existing in the depletion layer and also from equation (2.2.10) we find:

$$N_a w_p = N_d w_n \qquad (2.2.11)$$

which expresses the fact that the total negative charge on one side of the junction is equal to the total positive charge on the other side, and also that the depletion layer penetrates a shorter distance into the more heavily doped region. The electric potential as a function of the position within the depletion layer may be found by integrating equations (2.2.8) and (2.2.9), since $\Psi = -\int E dx$. The result has the form shown in figure 2.2.C By using the appropriate boundary conditions, the total potential difference across the junction (the built-in voltage) can be expressed in terms of the contribution from each side, thus:

$$V_p = -\int_{-w_p}^{0} E dx = -\frac{qN_a}{2\varepsilon} w_p^2 \qquad (2.2.12)$$

on the p side and on the n side:

$$V_n = -\int_0^{w_n} E dx = \frac{qN_d}{2\varepsilon} w_n^2 \qquad (2.2.13)$$

The total junction potential is then given by:

$$V_{np} = V_n + \left| V_p \right| = \frac{q}{2\varepsilon} (N_a w_p^2 + N_d w_n^2) \qquad (2.2.14)$$

Making use of equation (2.2.11), it can then be shown that the total width of the depletion region is given by:

$$w = w_n + w_p = \left(\frac{2\varepsilon V_0}{q} \cdot \frac{(N_a + N_d)}{N_a N_d} \right)^{1/2} \qquad (2.2.15)$$

and the electric field at the junction becomes:

$$E_j = \left[\frac{2qV_{np}}{\varepsilon} \cdot \left(\frac{N_a . N_d}{N_a + N_d} \right) \right]^{1/2} \qquad (2.2.16)$$

If we apply a positive voltage V_F to the p side with respect to the n side, the p-n junction becomes forward-biased, as shown in figure 2.1(b). The total electrostatic potential across the junction decreases by V_F ; that is, it is replaced with $(V_{np} - V_F)$. Thus forward bias reduces the depletion layer width and the junction electric field. If we apply a positive voltage V_R to the n side with respect to the p-side, the p-n junction becomes reverse-biased and the total electrostatic potential across the junction increases by V_R ; that is, it is replaced by $(V_{np} + V_R)$ as shown in figure 2.1(c). Here, the reverse bias increases both the depletion layer width and the electric field strength at the junction. Upon illumination, the semiconductor absorbs photons with energies greater than E_g generating electron-hole pairs which are separated by the electric field at the junction. The photogenerated minority carriers

which diffuse to the junction will cross over into the regions where they are the majority carriers. The resulting current through an external circuit with load resistance R , causes a potential difference V_L between the electrodes which makes the junction forward biased. This bias results in a diode current which opposes the light-generated current I_L . The total current I flowing through R is therefore given by $I = I_L - I_D$, where I_D is the diode current which would flow in the dark under the same bias conditions. For the ideal case in which charge transport across the junction is assumed to be controlled by diffusion, this current can be expressed as

$$I_D = I_S \exp\left[\left(\frac{qV}{KT} \right) - 1 \right] \qquad (2.2.17)$$

where q is the electronic charge, k is Boltzmann's constant, T is the absolute temperature and I_S is the reverse saturation current given by:

$$J_S = \frac{I_s}{A} = qN_cN_v \left[\frac{1}{N_a}\sqrt{\frac{D_n}{\tau_n}} + \frac{1}{N_d}\sqrt{\frac{D_p}{\tau_p}} \right] \exp\left[\frac{-E_g}{KT}\right] \qquad (2.2.18)$$

where A is the device area, τ_n and τ_p are the lifetime of electrons and holes respectively, N_c is the effective density of states in the conduction band and N_v is the density of states in the valence band. It follows that the I - V characteristics of an ideal p-n homojunction solar cell, represented by the equivalent circuit shown in figure 2.3(a) can be described by the equation:

$$I = I_L - I_S \left[\exp\left(\frac{qV}{KT} \right) - 1 \right] \qquad (2.2.19)$$

A plot of equation (2.2.19) is shown in figure 2.3(b).

By putting I =0 in equation (2.2.19) the open circuit voltage V_{oc} can be expressed as:

$$V_{oc} = \frac{KT}{q} \ln\left[\frac{I_L}{I_S} + 1 \right] \approx \frac{KT}{q} \ln\frac{I_L}{I_S} \qquad (2.2.20)$$

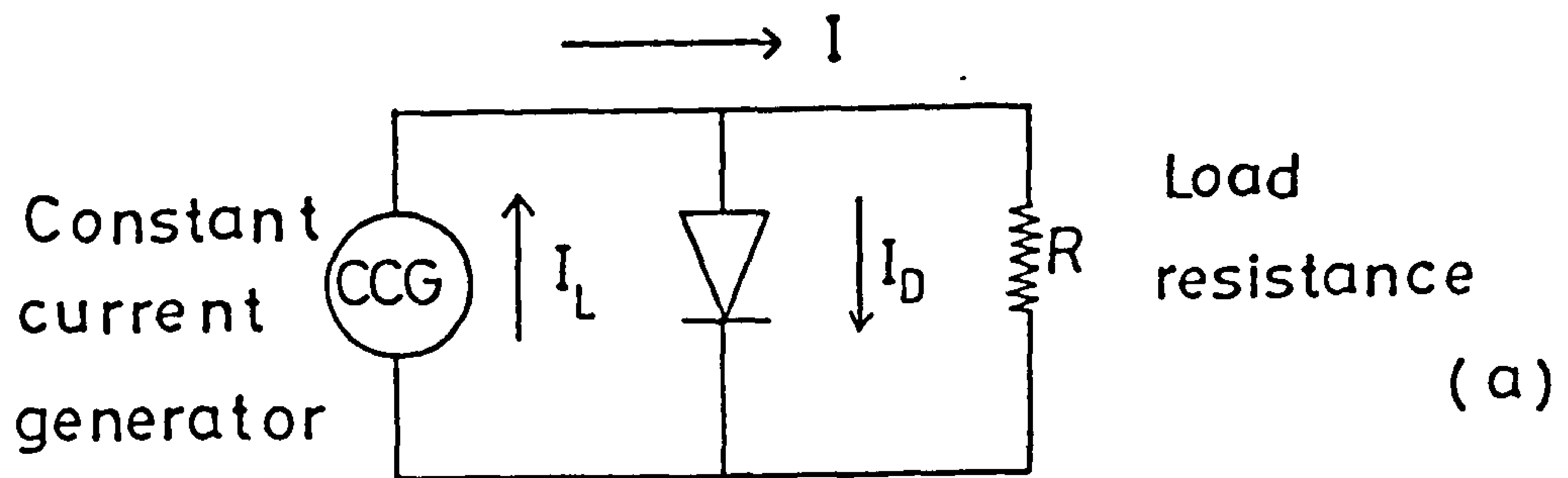

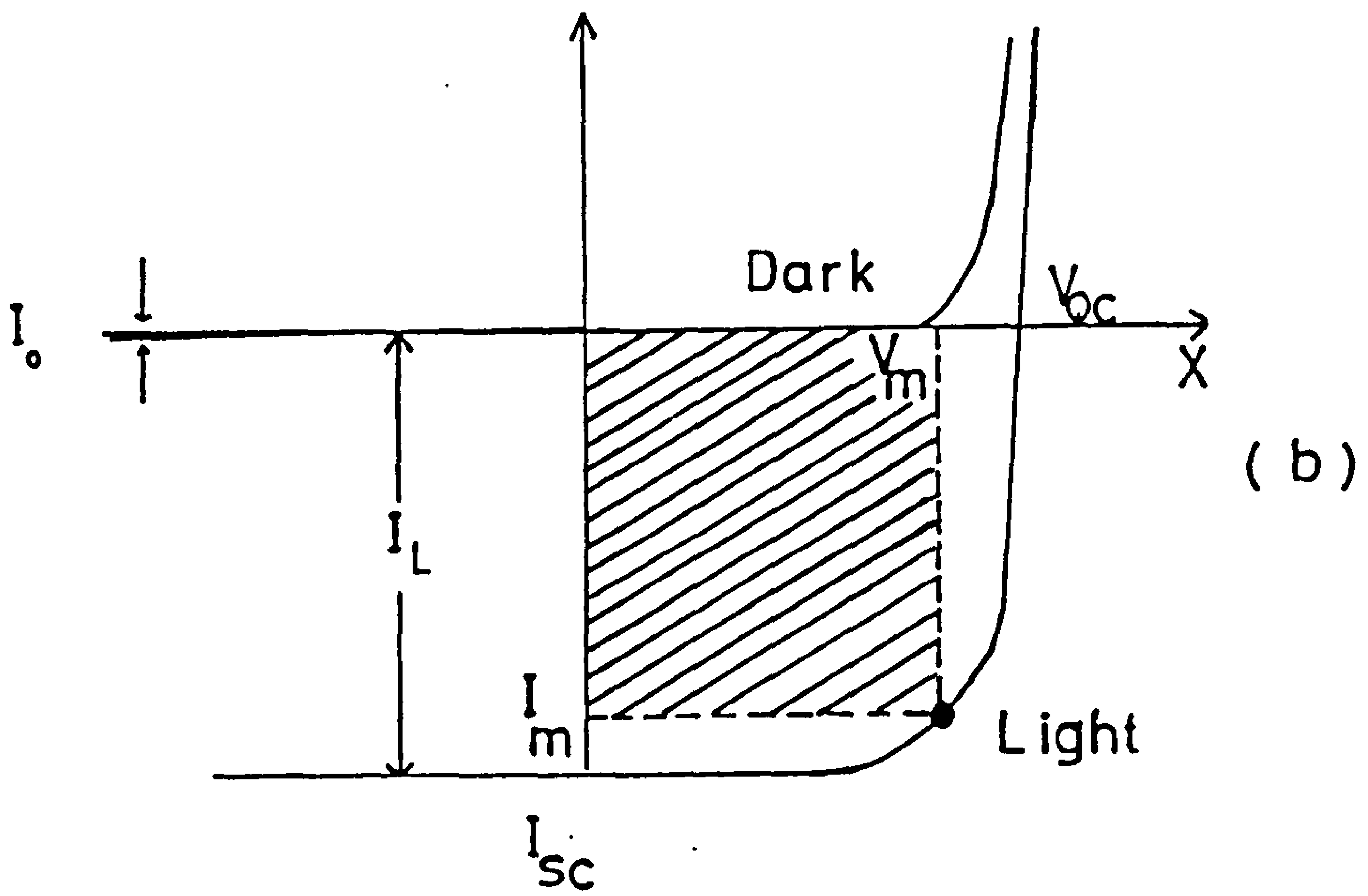

Fig.(2.3) (a) Equivalent circuit for an ideal p-n junction solar cell (b) I-V characteristics for an ideal p-n junction.

and by putting V =o in equation (2.2.19), the short-circuit current I_{SC} is given by : $I_{SC} = I_L$.

The maximum efficiency η of a solar cell is defined as:

$$\eta = \frac{P_m}{P_o} = \frac{V_{oc} \cdot I_{SC} \cdot FF}{P_o} \quad (2.2.21)$$

where P_o is the incident power of the solar radiation, P_m is the maximum electrical power output from the cell, and FF is the fill factor defined by reference to figure 2.3(b) as:

$$FF = \frac{I_m \cdot V_m}{I_{SC} \cdot V_{oc}} \quad (2.2.22)$$

where I_m and V_m are the current and the voltage corresponding to the maximum power P_m.

Selection of the best materials for photovoltaic cells can be made by calculating the maximum efficiency which can be achieved. As the maximum photogenerated current is determined by the numbers of incident photons with energy greater than the band gap of the material, it is clear, that the maximum short-circuit current must increase as the band gap of the material reduces. However, as equations (2.2.18) and (2.2.20) show that the open circuit voltage falls as the band gap is reduced, there is clearly an optimum band gap for maximum overall efficiency as has been shown by Prince (22) and Loferski (23), making various assumptions concerning the cell parameters and spectral distribution of the incident radiation. A typical result is shown in figure 2.4. Although these calculations neglect reflection, transmission and recombination losses they clearly help to identify those materials with potential for high efficiency

and the band gaps of some relevant materials are shown in this figure.

2.2.b. The practical case

A real solar cell differs from an ideal one in having finite values of series resistance R_s and shunt resistance R_{sh}, and there may be several transport mechanisms involving carrier generation, recombination and tunnelling processes as well as diffusion. For example, under forward bias, the existence of recombination centres close to the centre of the band gap can be shown to yield a recombination current of density $q \frac{Wn_i}{2\tau_r} \exp \frac{qV}{2kT}$, where τ_r is the effective recombination lifetime, and n_i is the interface carrier concentration. At low bias voltages, this contribution to the forward bias current may be large in comparison with the diffusion current contribution so that the current-voltage relationship has the form $J \propto e^{\frac{qV}{2kT}}$ instead of $J \propto e^{\frac{qV}{kT}}$ as expected from equation (2.2.17) (for $V \gg kT/q$). At higher bias voltages, the diffusion current may become the dominant contribution. In general, the exponential factor in the current voltage relationship is usually written as $e^{\frac{qV}{nkT}}$ where n is known as the diode ideality factor. Clearly $n = 1$ for the ideal case [equation (2.2.17)] and $n = 2$ when recombination is the dominant current mechanism but it can take a value between 1 and 2 when the two contributions are of similar magnitude. The series resistance R_s in a practical cell consists of the resistance of the neutral regions in the top and base layers as well as the top and the bottom contacts, while the shunt resistance arises from various leakage paths (e.g. at the cell edges and grain boundaries). An increase in R_s reduces I_{sc} but does not affect V_{oc}, while reducing R_{sh}

affects the open-circuit voltage, as is clear from the equivalent circuit for a practical p-n junction shown in figure 2.5. Taking account of the various factors referred to above, the J-V relationship for a practical p-n junction under illumination can be expressed as:

$$J = \sum_i J_{si} \left[\exp \left(\frac{q(V-JR_s)}{n_i kT} \right) - 1 \right] + \frac{V-JR_s}{R_{sh}} - J_L \qquad (2.2.23)$$

where J_L is the light generated current density, J_{si} is the saturation current density for the ith current contribution, and n_i is the corresponding diode ideality factor.

2.3 The metal-semiconductor junction (Schottky diode)

When a metal is joined to an n-type semiconductor, and they have different work functions ϕ_m and ϕ_s for metal and semiconductor respectively a Schottky barrier is formed provided $\phi_m > \phi_s$. Initially, when the junction is made, electrons flow from the semiconductor to the metal until the Fermi levels on each side of the junction coincide. The metal thereby acquires a negative surface charge, while a positive space charge develops on the semiconductor side due to uncompensated donor atoms distributed throughout this material to a distance w from the junction as shown in figure 2.6. After contact, electrons can diffuse from semiconductor to metal if they have sufficient thermal energy to overcome the contact potential barrier $q V_{ms} = \phi_m - \phi_s$. This would result in an increase in the height of the barrier, but there is an equal and opposite flow of electrons from the metal to the semiconductor to maintain equilibrium. The actual transport mechanisms which determine the J/V characteristics of metal-semiconductor junctions have been studied

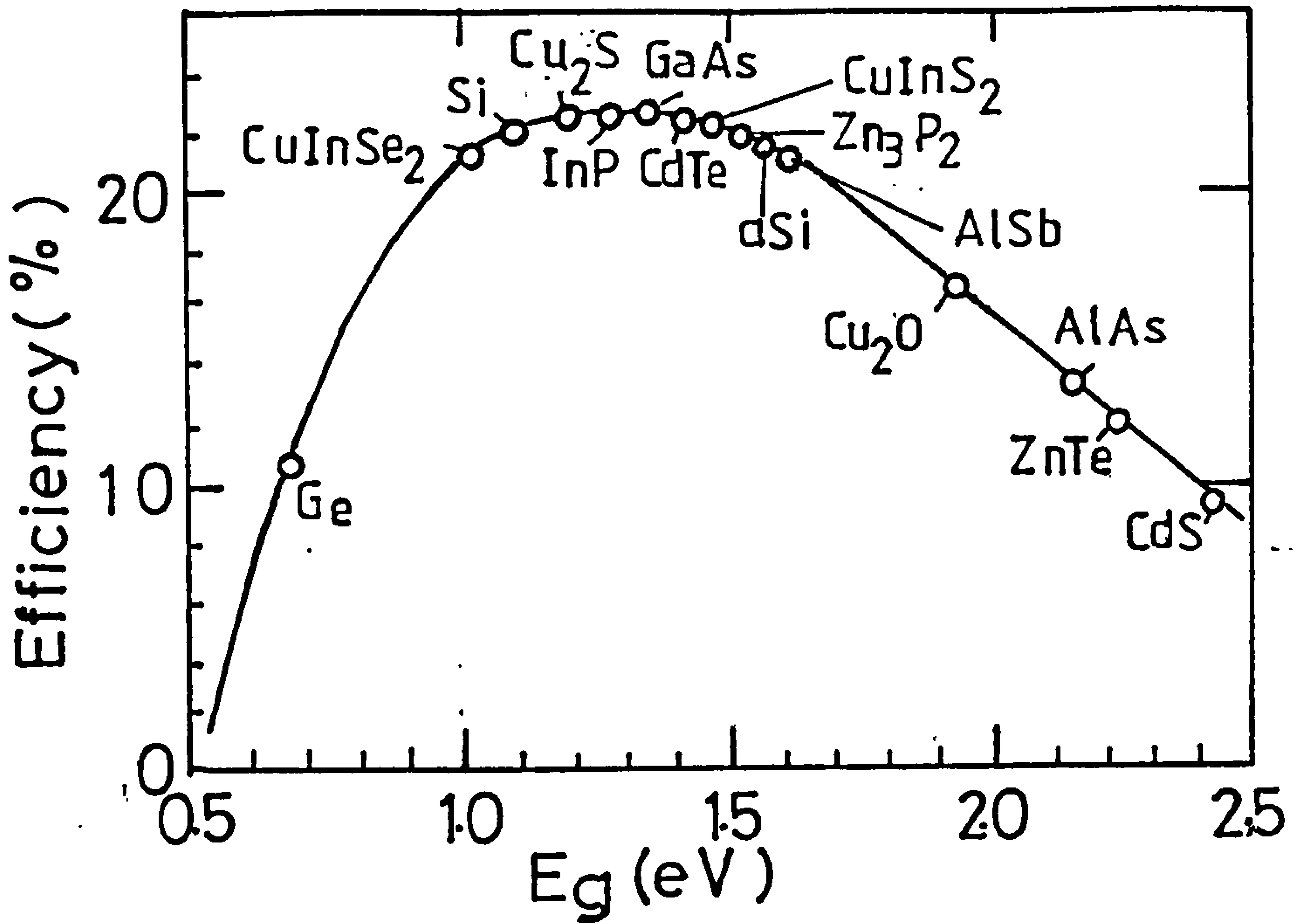

Fig.(2.4) Maximum conversion efficiency against energy band-gap for several semiconductor materials.

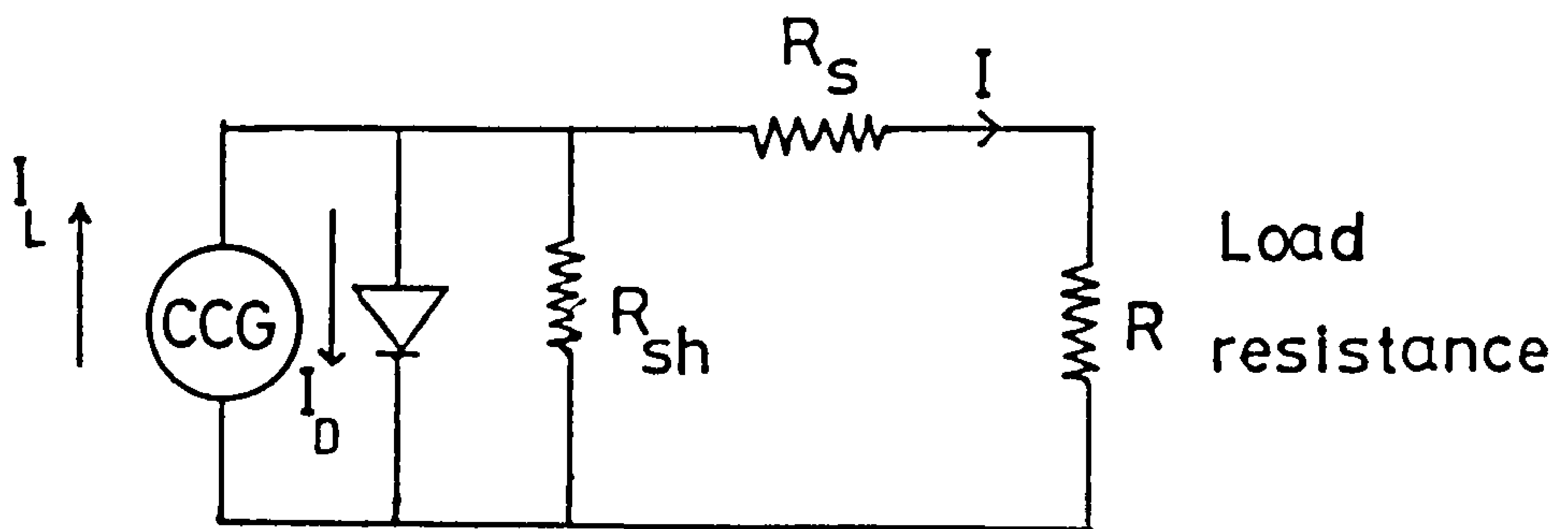

Fig.(2.5) Equivalent circuit for practical p-n junction.

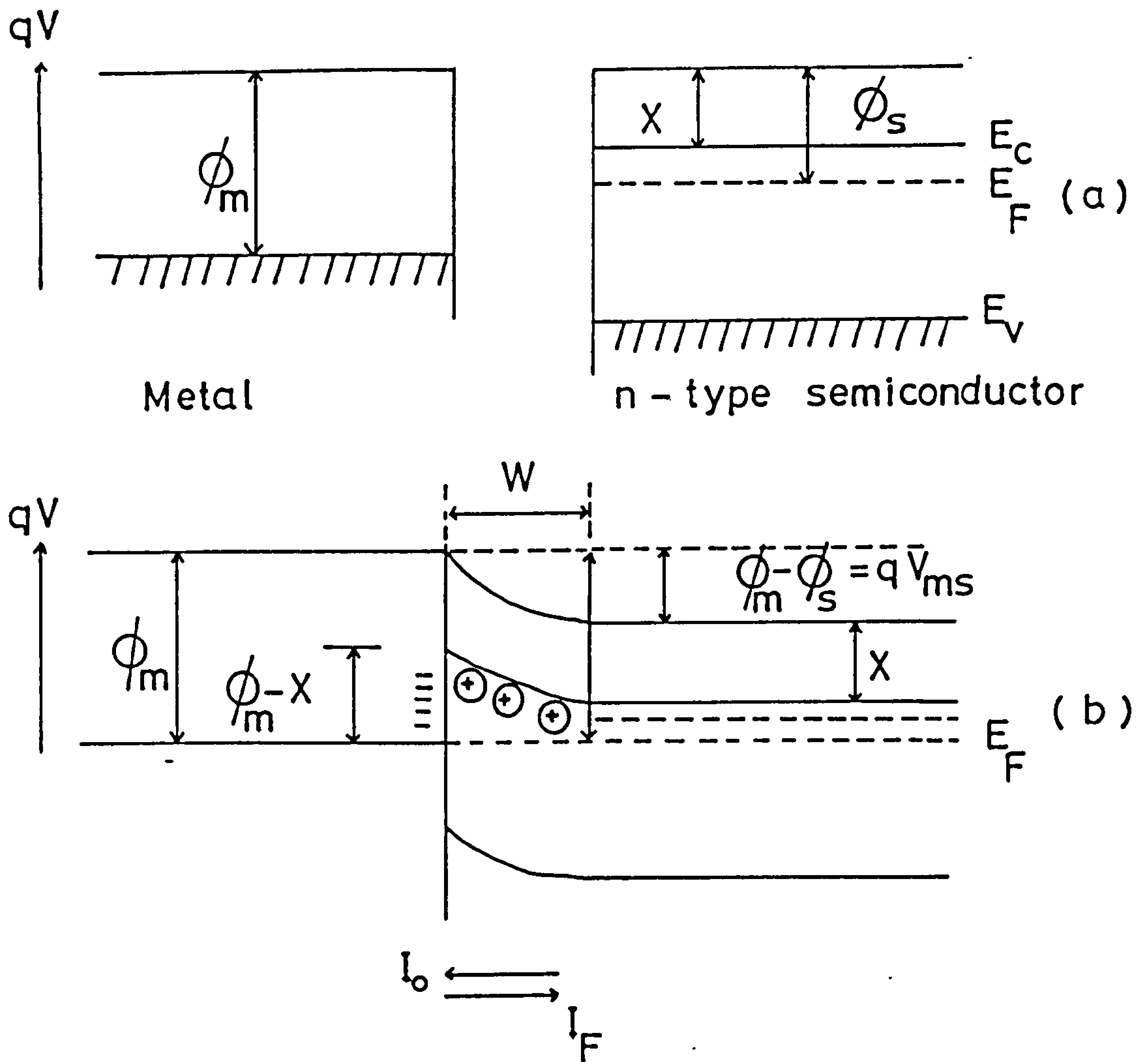

Fig.(2.6) Contact between a metal and an n-type semiconductor, $\phi_m > \phi_s$. (a) Energy diagram before contact (b) Energy diagram after contact.

theoretically by Wagner et al (24), Card et al (25) and Rhoderick et al (26). The most important transport processes are thermionic emission of electrons over the top of the barrier, carrier recombination in the depletion region, and quantum-mechanical tunnelling through the barrier. If the dominant mechanism is that of emission over the barrier, the J-V relationship will be given by:

$$J = A^* T^2 \exp\left(\frac{-q\phi_b}{KT}\right)\left[\exp\left(\frac{qV}{KT}\right) - 1\right] \qquad (2.3.1)$$

where A^* is the effective Richardson constant, and ϕ_b is the barrier height. This assumes that the electron mean free path is longer than the depletion layer width. If this is not the case, then current transport through the junction region is limited by diffusion and it can be shown in this case that (27):

$$J = qN_c\mu_e E_{max} \exp\left(\frac{-q\phi_b}{KT}\right)\left[\exp\left(\frac{qV}{KT}\right) - 1\right] \qquad (2.3.2)$$

where E_{max} is the maximum electric field within the barrier, and μ_e is the mobility of the electrons. It is clear that this diffusion model predicts J-V characteristics which, unlike the thermionic model, are dependent on material properties such as carrier mobility, and doping concentration within the depletion layer. Also equation (2.3.2) shows that J_s is proportional to E_{max} and is therefore dependent on V. However, as the doping concentration increases, the depletion layer width reduces and the simple thermionic process then dominates. As in the case of the p-n junction, it is usually found that the experimental forward characteristics follow a relationship of the form:

$$J = J_o \exp\left[\left(\frac{qV}{nKT}\right) - 1\right] \qquad (2.3.3)$$

where the diode quality factor takes values greater than 1 due to recombination in the depletion region and tunnelling through the barrier.

Additional deviations from the simple (ideal) theory arise due to the presence of interfacial layers which can have beneficial effects on the properties of Schottky barrier solar cells. For example, with a thin insulating layer between the metal and semiconductor, the current crossing the junction is reduced in accordance with the tunnelling probability through this layer. The reverse saturation current from equation (2.3.1) can then be expressed as (28):

$$J_s = A^* T^2 \exp\left[\frac{-q\phi_b}{KT}\right] \exp(-a\sigma) \qquad (2.3.4)$$

where a is a constant and σ is the thickness of the insulating layer. Using equation (2.2.20) it can then be seen that the open-circuit voltage is given by:

$$V_{oc} = \phi_b + \frac{Ka\sigma}{q} + \frac{KT}{q} \ln\left[\frac{J_L}{A^*T^2}\right] \qquad (2.3.5)$$

It is clear that the presence of the insulating layer makes the value of V_{oc} larger than that of a simple Schottky barrier solar cell, and that it increases as the insulating layer thickness is increased. However, beyond an optimum thickness (~20Å in metal - SiO_2 - Si diodes) the overall efficiency reduces as a result of the diminished short circuit current.

2.4 The p-n Heterojunction

A heterojunction is produced by the connection of two dissimilar semiconductors. A junction which is formed between two different

semiconductors of the same type of conductivity is called an isotype heterojunction, and when the conductivity types are different an anisotype heterojunction is formed. The properties of heterojunctions have been reviewed by Hill et al (29), Parish and Cosey (30), Fonash et al (31), and more recently by Fahrenbruc and Bube (32). The first theoretical model to explain the electronic properties of such junctions was proposed by Anderson (33). Figure 2.7 shows the energy-band diagram of a heterojunction as suggested by Anderson. The case shown is for a junction formed from two semiconductors, having different band gaps E_{g_p} and E_{g_n} (where $E_{g_p} < E_{g_n}$) and different work functions ϕ_p, ϕ_n and electron affinities χ_p, χ_n. As in the case of the p-n homojunction and metal-semiconductor junction the establishment of thermal equilibrium conditions, with a uniform Fermi level throughout the system, requires the formation of a space-charge region adjacent to the interface. This consists of an uncompensated positive space charge of ionized donors in the n-layer of width w_n, and an uncompensated negative space-charge of ionized acceptors in the p-layer of width w_p. The total band bending associated with the space charge region is determined by the difference between the work functions of the two semiconductors ($q V_{n.p} = \phi_p - \phi_n$) while the relationship between w_p and w_n depends on the doping densities in the respective material. Assuming that diffusion is the dominant transport process and that the hole current is negligible (due to a large barrier for holes) the current voltage characteristics for the heterojunction shown in figure 2.7 can be expressed in the form: (27)

$$J = q \left(\frac{D_n}{\tau_n} \right)^{1/2} \cdot \left(\frac{n_i^2}{N_a} \right) \left[\exp \left(\frac{qV}{KT} \right) - 1 \right] \qquad (2.4.1)$$

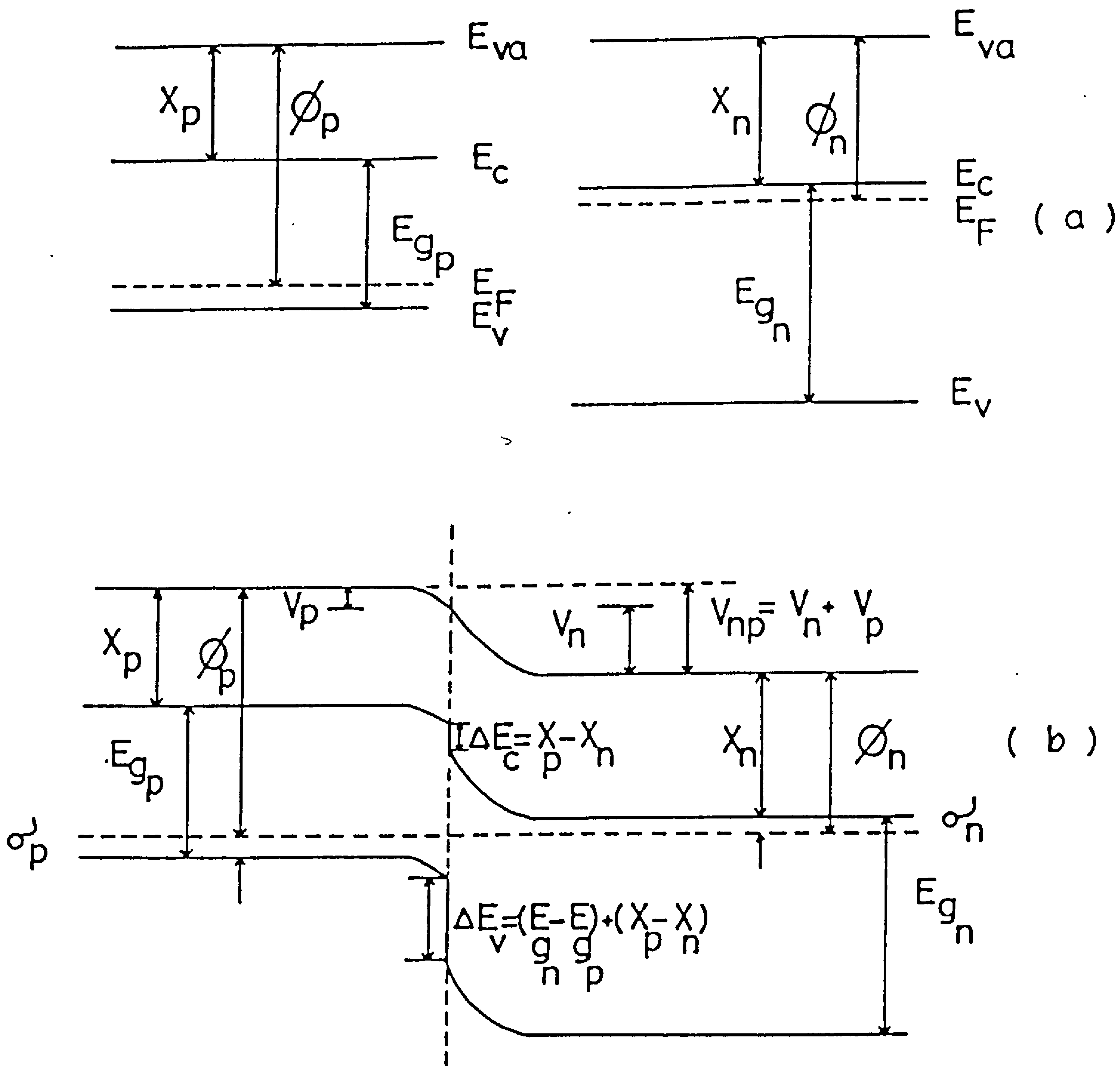

Fig.(2.7) Energy band diagram for a heterojunction according to Anderson (33), (a) Before contact (b) After contact.

where n_i is the intrinsic carrier concentration in the p-region and V is the applied bias, equal to $V'_p + V'_n$ where V'_p and V'_n are the components of V dropped across the space-charge region, on either side of the junction.

Anderson's model assumes that there are no interface states present, so that the band-edge discontinuities depend only on the electron affinities and the band gaps of the two materials. In this case $\Delta E_c = \chi_p - \chi_n$, and $\Delta E_v = \chi_n - \chi_p + E_{g_n} - E_{g_p}$. Figure 2.7(b) shows that ΔE_c is negative and as this increases in magnitude the equilibrium junction potential V_{np} is reduced. This has the effect of reducing the open-circuit voltage V_{oc} which can be generated. When $\Delta E_c > 0$ there will be a conduction band spike which prevents the photo-generated carriers on the p-side of the junction being transported across to the n-side. While it provides a basis for understanding heterojunction properties, Anderson's model has failed to explain satisfactorily the observed C-V and J-V characteristics as a function of temperature due to neglecting the role of interface states through which recombination and tunnelling can occur. In the case of the Cu_2S-CdS heterojunction the Cu_2S p-type semiconductor is assumed to have a very high doping concentration ($\sim 10^{19}$ cm^{-3}), so that, the band bending at the junction occurs almost exclusively in the CdS region. The possible current transport processes in Cu_2S/CdS heterojunction are illustrated in figure 2.8. Paths 1 and 5 represent diffusion of electrons and holes as discussed above. Path 2 relates to recombination at the band edge of the CdS through interface states, and paths 3 and 4 represent electron and hole tunnelling currents. In

practice it is believed that path 3 dominates in cells as they are initially prepared due to the narrow CdS space charge width, but after heat treatment of the cell which results in a broadening of the CdS space charge region, recombination via paths 2 and 4 are then dominant. Assuming that the current flow is limited by interfacial recombination (characterised by a recombination velocity S_I) Rothwarf has shown (34) that the J/V relationship can be written as:

$$J = \frac{V}{R_{sh}A_1} + q\frac{A_j}{A_1} N_{c2} S_I \exp\left(\frac{-\phi_p}{KT}\right)\left[\exp\left(\frac{q(V-JR_sA_1)}{nKT}\right) -1\right] -j_L \quad (2.4.2)$$

where the interface recombination velocity S_I is related to the misfit dislocation density at the interface between the Cu_2S and the CdS layer, A_j and A_1 are respectively the actual junction area and the effective planar area of the cell, and J_L is the light generated current which flows through the cell electrodes to the external load. In front wall cells it is assumed that most of the light generated current originates from photon absorption in the Cu_xS layer. However, J_L is less than the total minority current generated in the Cu_xS layer, J_{L_0} due to losses at the interface. By reference to figure 2.9, current conservation at the junction gives the relation: J_{Lo} = J_R + J_L where J_R is the current which returns to the Cu_2S via interface states, J_R can be expressed as $q.S_I.n_I$ where n_I is the electron concentration just inside the CdS at the junction. By expressing J_L in the form $J_L = q\, n_I \mu E$ where E is the electric field strength in the CdS at the interface, and μ is the electron mobility, it can be shown that (34)

$$J_{sc} \approx J_L = J_{Lo}\left[\frac{\mu E}{S_I+\mu E}\right] \quad (2.4.3)$$

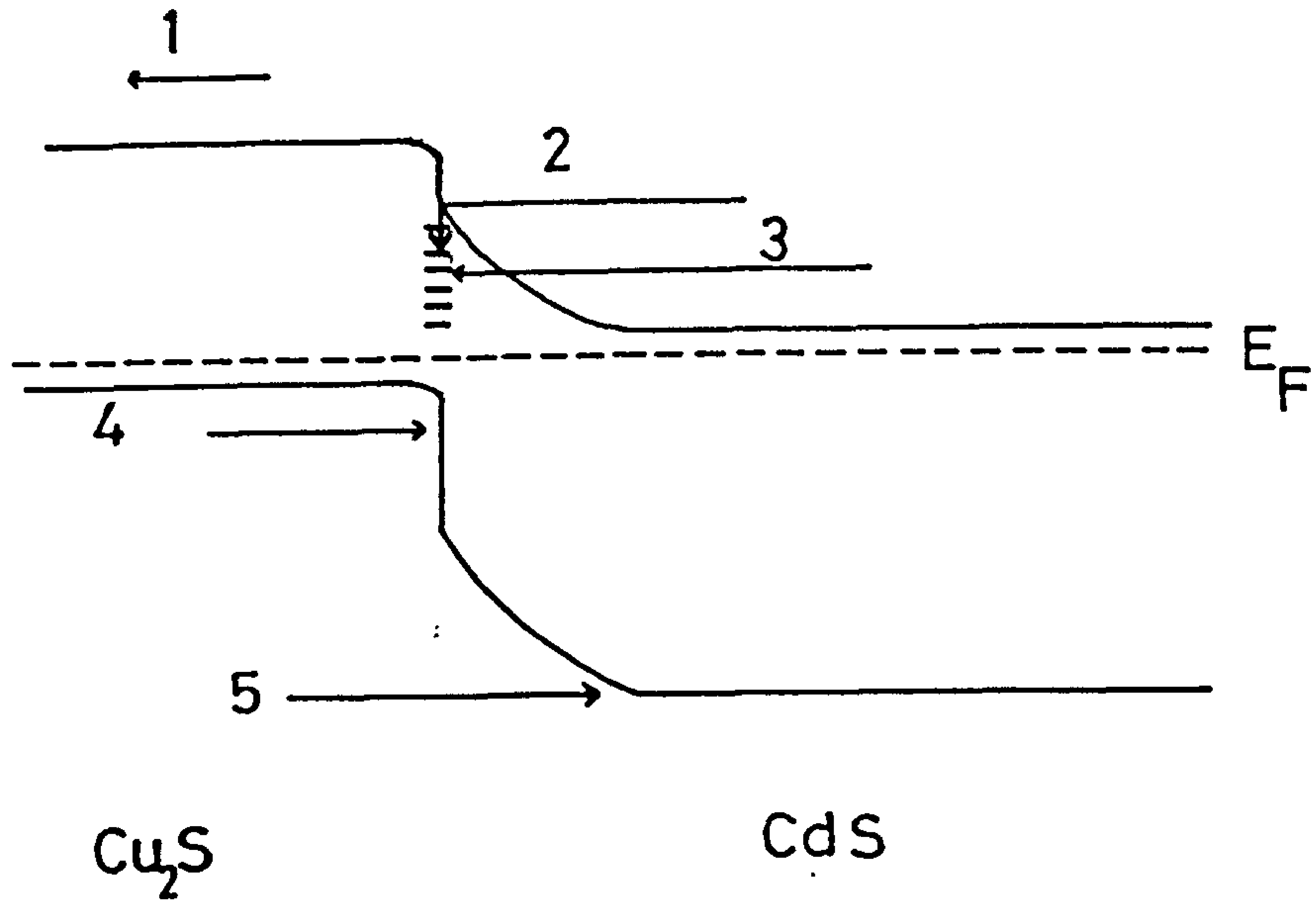

Fig.(2.8) Energy band diagram for Cu_2S/CdS illustrating various dark current paths.

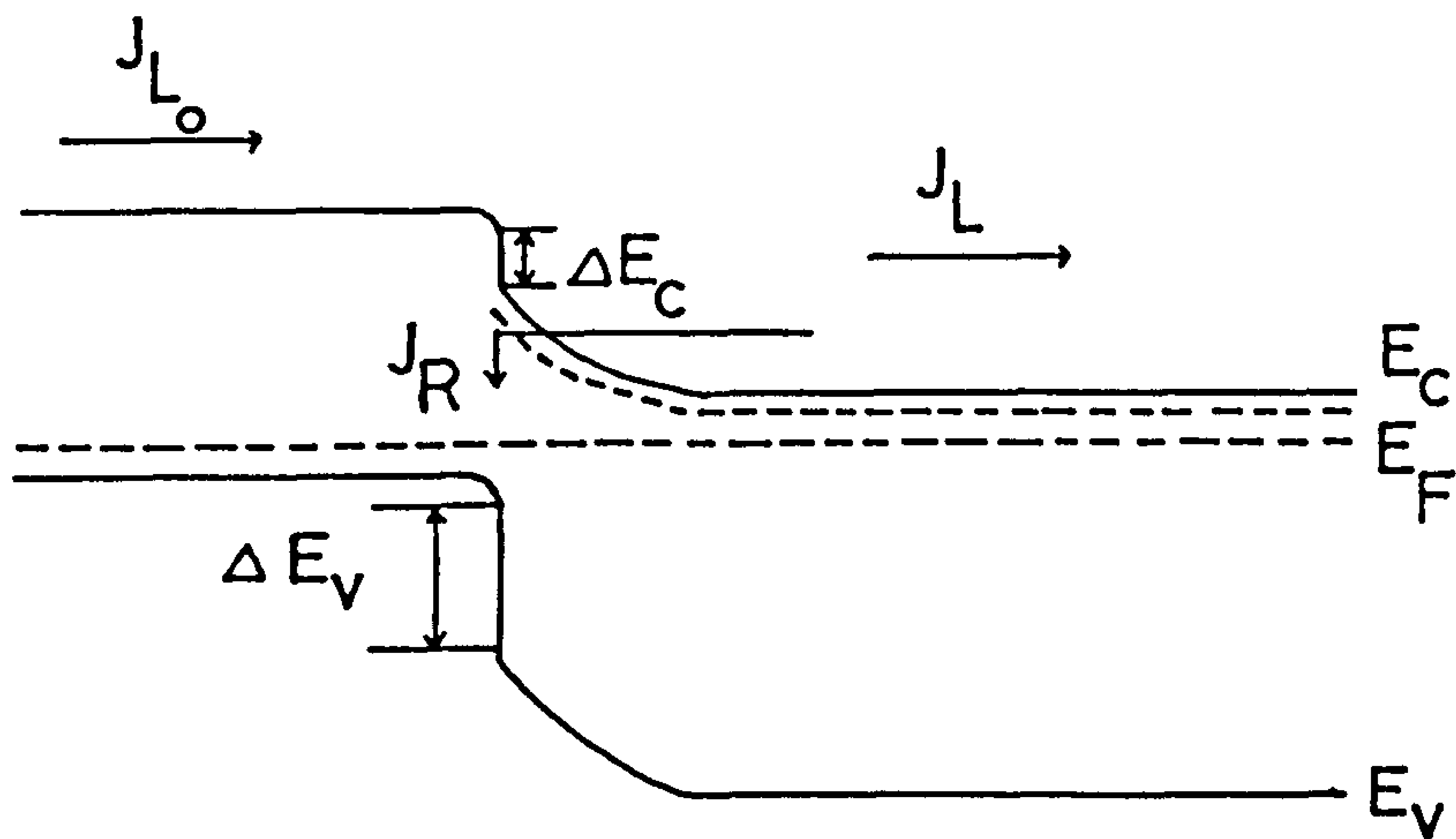

Fig.(2.9) Energy band diagram for Cu_2S/CdS solar cell, illustrating the light generated current densities.

The factor in the square bracket is known as the interface collection factor, ICF. Clearly the electric field in the CdS space charge region is a very important parameter in determining the short-circuit current which can be achieved under particular illumination conditions. As is clear from equations (2.2.10) and (2.2.16) the electric field can be written as:

$$E = \frac{qN_d w}{\varepsilon} = \left(\frac{2qVN_d}{\varepsilon}\right)^{1/2} \qquad (2.4.4)$$

assuming that $N_a >> N_d$. Thus the electric field E is dependent on the net positive charge density in the space charge-region. Therefore by increasing the shallow donor density N_d, and reducing of the width of the space-charge region w the value of E is increased. If there are deep levels in the band gap of the CdS, light reaching the CdS may cause these deep levels to be ionized, thereby, increasing the positive space charge density and subsequently the electric field. Therefore, an increase in J_L can result from light reaching the CdS layer due to an increase in ICF. The open-circuit voltage V_{oc} can be defined by setting J = o in relation (2.4.2) as:

$$q\,V_{oc} = (E_{g_p} - \Delta E_c) + KT\left[\ln J_{sc} - \ln q\,N_{c2}\,S_I - \ln \frac{A_j}{A_1}\right] \qquad (2.4.5)$$

where shunt conductance has been neglected and ϕ_b replaced by (E_{g_p} - ΔE_c), assuming that there is negligible band bending on the Cu_xS side of the junction. A plot of q V_{oc} versus T gives q $V_{oc} = E_{g_p} - \Delta E_c$ at the T = o intercept. It is clear that V_{oc} can be increased by decreasing ΔE_c. This can only be done by changing one of the components of the cell to achieve a better match between their electron affinities as has been found (9) in (CdS-ZnS)/Cu_2S solar

cells in which $V_{oc} \approx 1$ volt was obtained (35). Unfortunately, it is found that the resistivity of CdZnS increases as the Zn concentration increases so that improvements in operation efficiency are not obtained for Zn/Cd concentration ratios of greater than about 0.2. In fact, Hall et al (15), working on dipped $Cu_2S/Cd_{1-x}Zn_xS$ cells found that the optimum composition was in the range ($0.1 < X < 0.2$). With x = 0.16 they obtained an open circuit voltage of 0.6 V and efficiency of 10.2 % which compares well with the conventional Cu_2S/CdS devices which have produced a best efficiency 9.15% as reported by Bragagnolo et al (14). It must also be noted that V_{oc} is dependent on the process of cell fabrication which has an influence on the junction area A_J between the Cu_2S and CdS layers. The area A_J can be several times larger than the normal area $A_\perp$ of the cell due to formation of Cu_2S in the CdS grain boundaries. Equation (2.4.5) shows that this clearly decreases the open-circuit voltage according to the relation:

$$\Delta V_{oc} = \left(\frac{KT}{q} \right) \ln \left(\frac{A_J}{A_\perp} \right) \quad (2.4.6)$$

2.5 The space charge region and capacitance-voltage studies for solar cells

As indicated in the previous sections, the characteristics of any semiconductor junction device are determined by the structure of the potential barrier at the interface. It follows that, in order to understand the properties of junction devices, it is necessary to obtain detailed information about the junction barrier and the associated space charge distribution.

One technique which has been widely used to obtain such information involves the measurement of the junction capacitance as a function of externally applied bias voltage. The variation of

capacitance with bias voltage can provide information on the space charge density variation in the vicinity of the junction, the width of the depletion region and equilibrium potential difference across the junction.

As has been previously mentioned (section 2.4), in order to produce good diode characteristics in Cu_2S-CdS solar cells, it is necessary to perform a post-fabrication heat treatment which causes copper ions to diffuse from the Cu_2S layer into the CdS substrate to form a semi-insulating (i) layer of copper-compensated CdS (36). The energy band diagram for the configuration is shown in figure 2.10.

Clearly there is a non-homogeneous space charge region in such a system and care is needed in the interpretation of the associated capacitance-voltage (C-V) characteristics. In order to demonstrate the effects of a variety of different space charge distributions, it will be convenient to consider an idealised model in which the space charge region is divided into a number of sections lying parallel to the interface. Such a model was first employed by Hall and Singh[37] for analysing Cu_2S-CdS junctions. As shown in figure 2.11, they considered the space charge layer to be divided into three regions (all within the n-type CdS) including:

(a) a high space charge density layer from $x = 0$ to $x = d_1$

(b) a lower charge density in a partially compensated region from $x = d_1$ to $x = d_2$, and

(c) a further high density region from $x = d_2$ to w associated with the high conductivity bulk CdS.

For this system, the electrostatic potential ψ is subject to the following boundary conditions:

University Library Hull

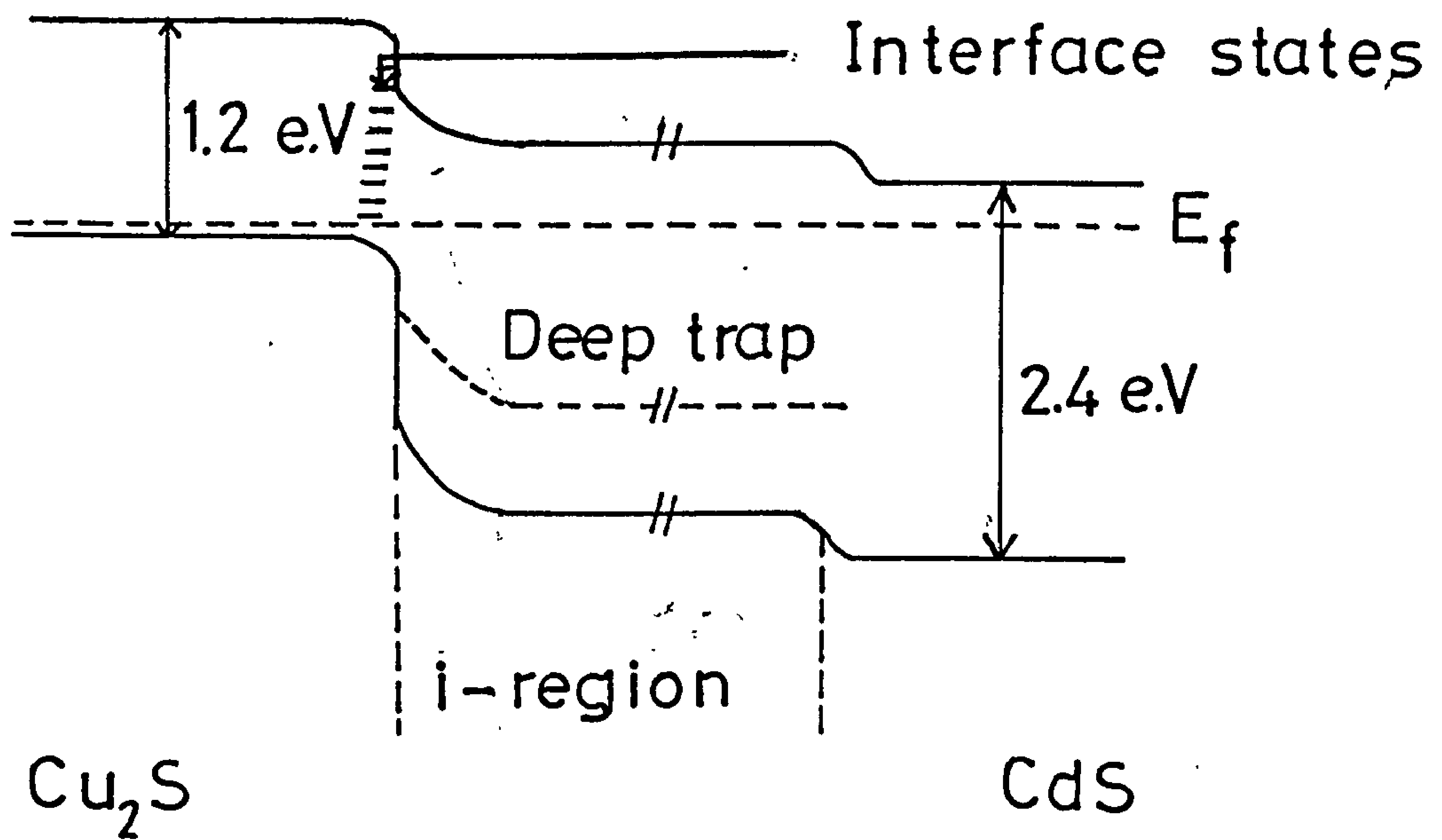

Fig.(2.10) Energy band diagram for a Cu_2S/i-CdS/CdS structure.

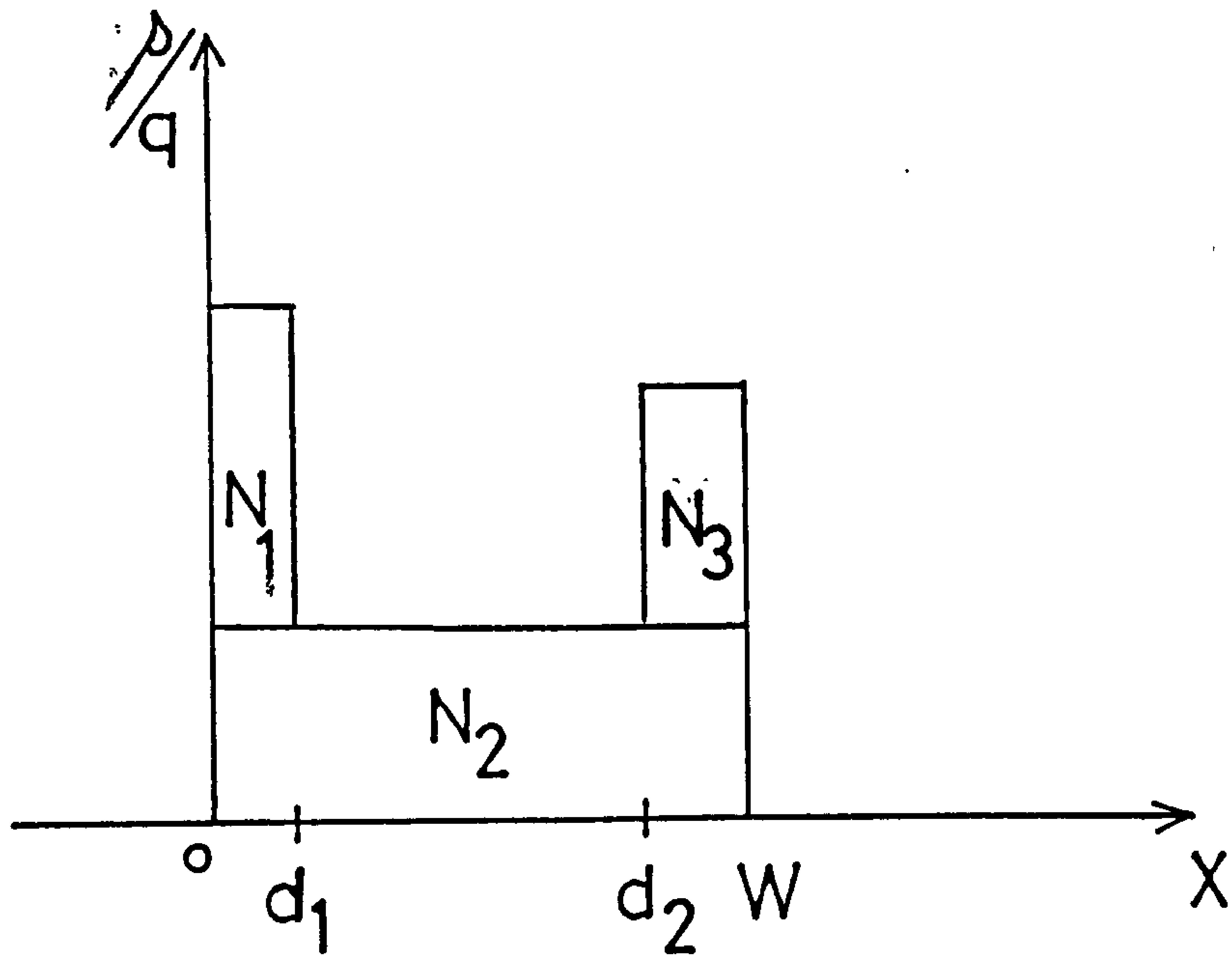

Fig.(2.11) The charge density profile within the CdS layer of a Cu_2S/CdS cell. (Hall and Singh model (37)).

$$\frac{d\psi}{dx} = 0 \quad \text{at } x = w$$

$$\psi = 0 \quad \text{at } x = 0 \qquad (2.5.1)$$

$$\psi = V_D + V \quad \text{at } x = w$$

where V_D is the diffusion voltage and V is the applied voltage. The space-charge density distribution may be represented by the expressions:

$$\rho = q \left[\frac{N_1}{1+ \exp[a(x-d_1)]} + N_2 + N_3 \left(1- \frac{1}{1+ \exp[b(x-d_2)]}\right) \right] \qquad (2.5.2)$$

for $0 \leq x \leq w$, and
$\rho = 0$ for $x > w$

where the space charge density in the high space-charge density surface region is $q(N_1 + N_2)$, the space-charge density in the compensated layer is qN_2, and the space-charge density for the bulk, CdS region is $q(N_2 + N_3)$. The parameters a and b are required to describe the spatial variation of charge within the transition layers between one space-charge region and the next. It follows that Poisson's equation may be written in one-dimensional form as:

$$\frac{d^2\psi}{dx^2} = -\frac{q}{\varepsilon} \left[\frac{N_1}{1+ \exp[a(x-d_1)]} + N_2 + N_3 \left(1- \frac{1}{1+ \exp[b(x-d_2)]}\right)\right] \qquad (2.5.3)$$

and this can be integrated to give ψ as a function of x by making use of the boundary conditions expressed in equation (2.5.1) together with the requirement that no discontinuities in ψ should exist at the boundary between the three regions. Then for the case where $a = b = \infty$ (abrupt changes in charge density) the expressions for the potential

in each of the three regions are:

$$\psi_{x \leq d_1} = -\left(\frac{q}{\varepsilon}\right)\left[(N_1+N_2)\frac{1}{2}\ x^2 - (N_2+N_3)\ w\ x - (N_1d_1-N_3d_2)x\right] \quad (2.5.4)$$

$$\psi_{d_1 \leq x \leq d_2} = -\left(\frac{q}{\varepsilon}\right)\left[N_2\frac{1}{2}x^2 - N_1\frac{1}{2}d_1^2 - (N_2+N_3)\ w\ x + N_3d_2\ x\right] \quad (2.5.5)$$

$$\psi_{x \geq d_2} = -\left(\frac{q}{\varepsilon}\right)\left[(N_2+N_3)\frac{1}{2}\ x^2 - (N_2+N_3)\ w\ x + \frac{1}{2}N_2d_1^2-\frac{1}{2}N_1d_1^2\right] \quad (2.5.6)$$

It follows from eq. (2.5.1) and (2.5.6) that the space-charge width w can be written as:

$$w = \left(\frac{2\varepsilon(V+V_D)}{q(N_2+N_3)} + \frac{N_3d_2^2}{N_2+N_3} - \frac{N_1d_1^2}{N_2+N_3}\right)^{\frac{1}{2}} \quad (2.5.7)$$

The junction capacitance C is related to the total space charge Q by

$$C = \frac{dQ}{dV} \qquad \text{where}$$

$$Q = qA\left[N_1d_1+N_2\ w+N_3(w-d_2)\right] \quad (2.5.8)$$

$$= qA\left[N_1d_1-N_3d_2+(N_2+N_3)\ w\right] \quad (2.5.9)$$

and A is the area of the junction.

If we assume that d_1, d_2, N_1, N_2 and N_3 are not functions of voltage V, then:

$$\frac{dQ}{dV} = qA(N_2+N_3)\frac{dw}{dV} \quad (2.5.10)$$

Using equations (2.5.7) and (2.5.10) it is seen that the capacitance-voltage relationship can be written as:

$$\left(\frac{1}{C}\right)^2 = \left(\frac{2}{A^2\varepsilon q(N_2+N_3)}\right) V + \left(\frac{2}{A^2\varepsilon q(N_2+N_3)}\right)\left[V_D + \frac{q}{2\varepsilon}(N_3 d_2^2 - N_1 d_1^2)\right] \qquad (2.5.11)$$

and it is clear from equations (2.5.7) and (2.5.11) that $C = \frac{\varepsilon A}{W}$ as for a simple single region space charge distribution. Three cases can usefully be considered in the case of Cu_2S-CdS solar cells.

Case I. When $N_1 = N_3 = 0$ then equations (2.5.7) and (2.5.11) can be written as follows:

$$W = \left[\frac{2\varepsilon(V+V_D)}{qN_2}\right]^{\frac{1}{2}} \qquad (2.5.12)$$

$$\text{and } \left(\frac{1}{C}\right)^2 = \left(\frac{2}{A^2\varepsilon qN_2}\right)(V+V_D) \qquad (2.5.13)$$

This situation applies to the simplest form of p-n junction or ideal metal-semiconductor device. According to equation (2.5.13) a graph of C^{-2} against the reverse bias voltage V allows N_2 to be detemined from the slope and the diffusion voltage V_D to be obtained from the intercept on the voltage axis.

Case II. When we have a conductive interface layer for which $N_1 > N_2$ and $N_3 = 0$, equations (2.5.7) and eq. (2.5.11) become:

$$W = \left(\frac{2\varepsilon(V+V_D)}{qN_2} - \frac{N_1}{N_2} d_1^2\right)^{\frac{1}{2}} \qquad (2.5.14)$$

$$\text{and } \left(\frac{1}{C}\right)^2 = \left(\frac{2}{A^2\varepsilon qN_2}\right) V + \left(\frac{2}{A^2\varepsilon qN_2}\right)\left(V_D - \frac{q}{2\varepsilon} N_1 d_1^2\right) \qquad (2.5.15)$$

In this case, the extrapolated intercept on the voltage axis for a plot of C^{-2} vs V is no longer equal to the diffusion voltage V_D, but rather $V_D - \frac{q}{\varepsilon} N_1 d_1^2$, while the slope of the plot still determines

N_2. As the thickness of the conducting surface layer is increased the space-charge layer thickness decreases and an effective barrier-reduction effect can occur as a result of electron tunnelling.

Case III. This case relates to a situation where an insulating region lies adjacent to the interface, as is expected to arise when copper diffuses from the Cu_2S layer into the CdS. In this case $N_3 > N_2$ and $N_1 = \emptyset$ so that equation (2.5.7) and equation (2.5.11) become:

$$w = \left[\left(\frac{2\varepsilon(V+V_D)}{q(N_2+N_3)} \right) + \frac{N_3 d_2^2}{N_2+N_3} \right]^{\frac{1}{2}} \qquad (2.5.16)$$

$$\left(\frac{1}{C}\right)^2 = \frac{2}{A^2 \varepsilon q(N_2+N_3)} V + \frac{2}{A^2 \varepsilon q(N_2+N_3)} \left(V_D + \frac{q}{2\varepsilon} N_3 d_2^2\right) \qquad (2.5.17)$$

and a plot of C^{-2} against V allows $(N_2 + N_3)$ to be determined from the slope. The voltage-axis intercept then occurs at

$$V^* = V_D + \left(\frac{q}{2\varepsilon}\right) N_3 d_2^2 \qquad (2.5.18)$$

As d_2 increases, the second term becomes dominant in relation (2.5.18) and the intercept can be written as:

$$V_D^* = \frac{q}{2\varepsilon} \cdot N_3 d_2{}^2 \qquad (2.5.19)$$

so that the insulating region width d_2 can be obtained. Again, as d_2 increases, the second term in equation (2.5.16) becomes dominant, so that the depletion layer thickness (which is given by C^{-1}) becomes directly proportional to d_2. As d_2 is governed by a diffusion process (discussed in the next section), it is clearly possible to use measurement of the capacitance as a function of diffusion time to estimate a value for the diffusion coefficient of the species which produces the semi-insulating layers, as shown by Sullivan[38].

2.6 Diffusion Processes in Polycrystalline Films

As has been previously mentioned, the fabrication of Cu_2S-CdS solar cells usually involves an annealing stage during which the compositionsof the layers on each side of the Cu_2S-CdS junction are modified as a result of interfacial diffusion. Although this diffusion process leads to the desired increase in the efficiency of the cells, further diffusion effects apparently contribute to degradation of the cell efficiency causing an undesired reduction in the operational lifetime of these devices. Clearly it is necessary to understand the diffusion mechanisms involved in both the efficiency enhancement and efficiency degradation processes if any attempt is to be made to control them.

In fact diffusion is one of the most important processes employed in the semiconductor industry, and a great deal of research has been carried out to provide information about the diffusion processes which can occur in a semiconductor.

The mathematical basis of the subject was provided by Fick[39]. Fick's first law states that the rate of transfer of diffusing particles through unit area is proportional to the magnitude of the concentration gradient measured normal to the area. Thus if the X axis is chosen as the direction of a concentration gradient, the flux of atoms in the X direction is given by:

$$J_x = - D \frac{dc(x,t)}{dx} \qquad (2.6.1)$$

where C(x,t) is the concentration of atoms, which depends on both time and distance, and D is the diffusion coefficient. The negative sign in the relation (2.6.1) indicates that the diffusion takes place down the concentration gradient, from high to low values of C. Using

equation (2.6.1) together with a continuity condition, Fick's second law is obtained (again assuming one dimensional flow) in the form:

$$\frac{dc(x,t)}{dt} = D \frac{d^2c(x,t)}{dx^2} \qquad (2.6.2)$$

The concentration profile of a diffusing species can be found by using equation (2.6.2) subject to the appropriate boundary conditions determined by the experimental conditions. For example for a limited supply of diffusant at the surface of a plane slab of semiconductor (at $x = o$), the concentration at a depth x should be given by [39]

$$c(x,t) = c_o \exp\left[- \frac{x^2}{4Dt} \right] \qquad (2.6.3)$$

where C_o is dependent on the initial surface concentration of the impurity, and on the time of diffusion t.

In Cu_2S-CdS solar cells the diffusion of copper from the Cu_2S layer into the CdS layer occurs during cell annealing. However since the CdS is in the form of a polycrystalline layer with the constituent crystallites lying perpendicular to the substrate, diffusion can occur both into the grains and via the grain boundaries. For bulk diffusion into the grains, equation (2.6.3) becomes:

$$c_g(x,t) = c_o \exp\left(- \frac{x^2}{4D_g t} \right) \qquad (2.6.4)$$

where D_g is the diffusion coefficient in the grain. Levine et al[40] and Le Claire[41] have analysed the grain boundary diffusion process in terms of an idealized structure in which the grain boundary is assumed to be an isotropic slab of material of width σ normal to the top surface of an otherwise homogeneous section of semiconductor as in

figure 2.12(a). Diffusion within the grain boundary is characterised by a diffusion coefficient D_{gb} where it is expected that $D_{gb} \gg D_g$ so that the grain boundary constant concentration contours follow a form of the type shown in figure 2.12(b). Making use of the boundary conditions $C_g = C_{gb}$ and $D_g \frac{d\,C_g}{\partial x} = D_{gb} \frac{dC_{gb}}{\partial x}$ at the grain-grain boundary interface, where C_g is the concentration in the grain (outside the slab) and C_{gb} is the concentration in the grain boundary (within the slab), solution of Fick's diffusion equations can be shown to yield the relation

$$D_{gb}\,\sigma = \left(\frac{\partial(\ell n\bar{c})}{\partial(y^{6/5})}\right)^{-\frac{5}{3}} \left(\frac{4D_g}{t}\right)^{\frac{1}{2}} \left[\frac{\partial(\ell n\,\bar{c}_{gb})}{\partial[(\eta B^{-\frac{1}{2}})]^{\frac{6}{5}}}\right]^{\frac{5}{3}} \qquad (2.6.5)$$

where η and B are dimensionless parameters defined as:

$$\eta = \frac{y}{(D_g t)^{\frac{1}{2}}} \quad , \quad B = \frac{D_{gb}}{D_g} \cdot \frac{(\frac{1}{2}\sigma)}{(D_g t)^{\frac{1}{2}}}$$

and $\bar{C}$ is the average concentration as a function of depth as determined by standard profiling techniques. For $B \gg 1$ the last term of equation (2.6.5) is found to be independent of time, temperature and concentration for the diffusion process and is equal to 0.78[41]. Thus, it follows from equation (2.6.5) that by measuring the concentration-depth profile and plotting the result as ln $\bar{C}$ against $Y^{6/5}$, D_{gb} can be obtained (42).

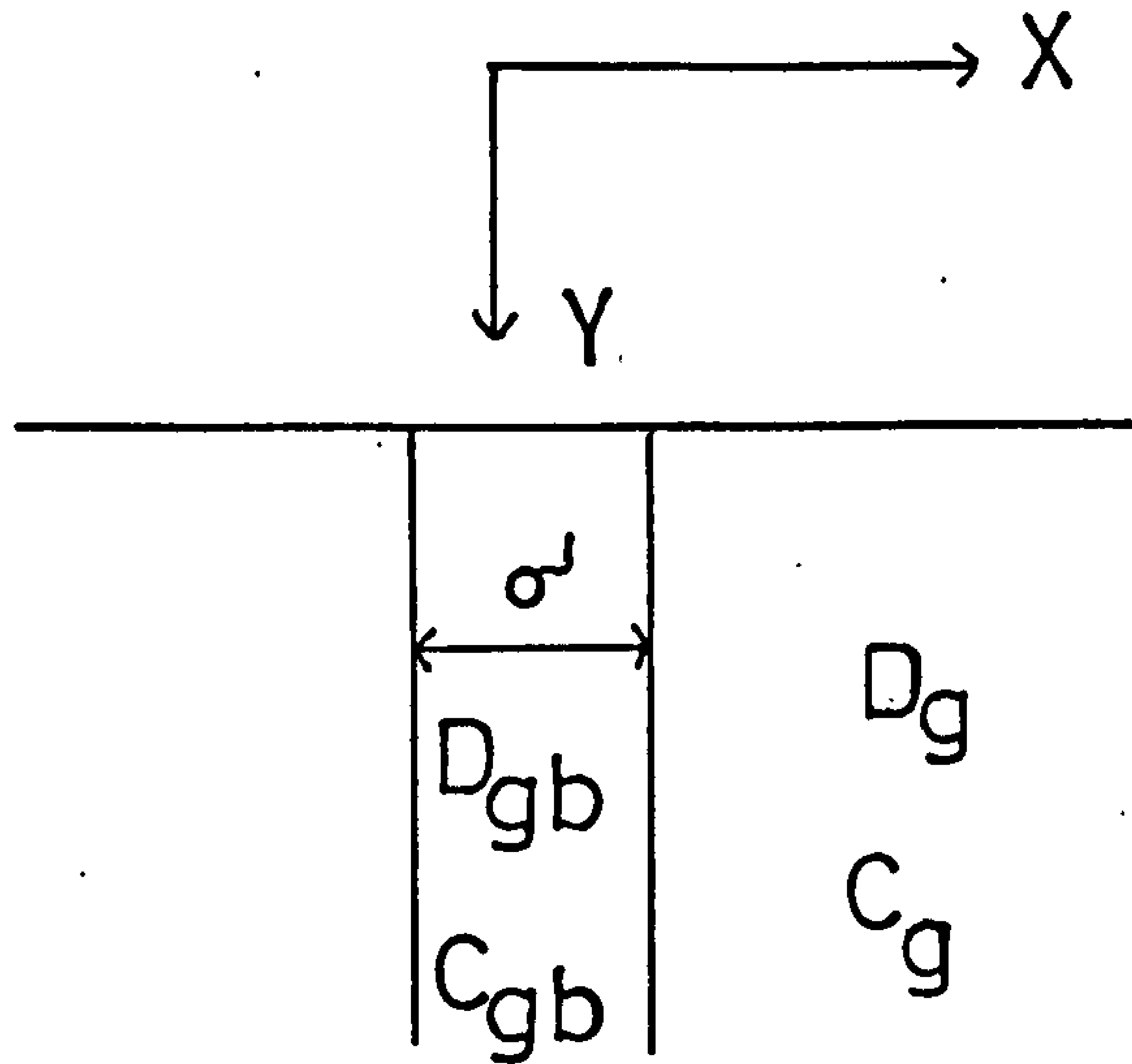

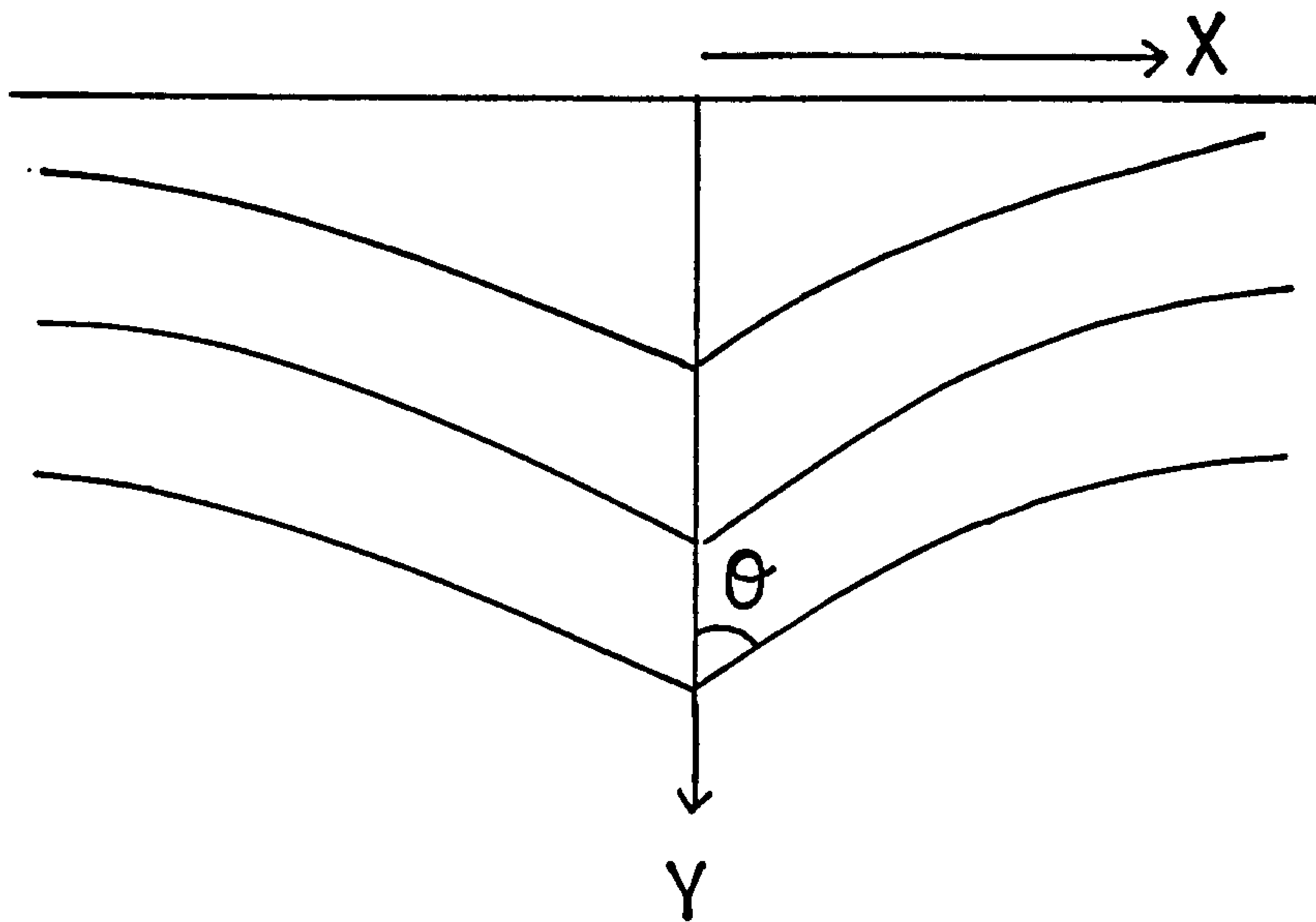

Fig.(2.12) (a) Model used for grain boundary diffusion analysis.
(b) Typical grain boundary concentration contours,

CHAPTER THREE

THE STRUCTURE AND CHARACTERISTICS OF Cu_xS/CdS SOLAR CELLS

3.1 Historical Background

The earliest reports of work on polycrystalline CdS films for use in photovoltaic cells were those of Nadjakov and coworkers in 1954 (43) and Carlson et al in 1956 (44). Since that time much technological progress has been accomplished in thin film deposition techniques paving the way for the development of thin film cells, not only based on CdS but also on a variety of other materials. However, while work on thin film solar cell systems has steadily progressed, valuable contributions to this progress have come from studies of single crystals. Indeed special interest in photovoltaic processes involving CdS can be said to have developed from work by Reynolds and coworkers (45) who demonstrated the production of voltages at illuminated copper, silver, and gold contacts on CdS single crystals. This was followed up by Williams and Bube (46) who studied the behaviour of several electroplated metal contacts to CdS crystals and found that copper gave the largest photovoltaic response. At that time it was assumed that a simple metal-semiconductor junction was involved but it is probable that an interfacial layer of Cu_xS had been produced as suggested by Cusano (47) and Keating (48). In fact, there was a good deal of controversy concerning the origin of the photovoltaic effect in Cu-CdS devices and it was several years before the role of Cu_xS was finally confirmed, as discussed more fully in section 3.4.

With growing interest in solar cells for use in space, the development of light weight, large area photovoltaic devices was given particular importance and Cu/CdS cells were showing great promise. After Moss (49) made some Cu-CdS thin film cells with efficiency ~ 1% in 1960 steady improvements in the performance of these devices were reported. Middleton et al (50) used thicker CdS films and increased the efficiency up to 3.5%. By 1967, with the work of Hill and Kermidas (51), Selle et al (52) and Potter and Schalla (53), the importance of the Cu_xS layer, as the main photon absorber in the system, was firmly established and with greater care being taken over the formation of this layer, efficiencies of up to 7% were being reported by a group at the Clevite Corporation (54,55,56) where pilot mass production lines were being developed. During subsequent years there were a number of improvements in the design and construction of Cu_xS/CdS thin film solar cells (notably at the Institute of Energy Conversion (IEC), University of Delaware). These improvements included evaporation of CdS onto Zinc coated copper substrates and the design of a highly transmitting (~ 96%) gold grid top contact together with an antireflection coating. These modifications resulted in steady increases in the efficiency until 1980 when Bragagnolo and coworkers (14) achieved an efficiency of 9.15% which is the best value so far reported for Cu_xS-CdS cells. Although most of the experimental work which has contributed to these developments has involved the use of small area laboratory test samples, the cell fabrication process has been scaled up for commercial production by a number of companies. While the results have been encouraging, the commercial exploitation has not been entirely satisfactory due mainly to doubts concerning the

stability of the devices. Most recently, a pilot production line was established at the Nukem company in Germany (57,58) using techniques developed at the University of Stuttgart, which had produced cells with efficiencies up to 8% and proven stability over periods of several years (59,60). The Nukem modules, consisting of 10 cells of 10x10 cm^2, achieved overall efficiency up to 6% and although some modules showed no degradation after 6 months operation, some others suffered from increased series resistance due to problems associated with the front grid contact (61). This project like all the previous commercial production has now been discontinued but, in a recent review of the prospects for commercial development of Cu_2S-CdS cells, Hill and Meakin (62) have expressed the view that these cells may yet prove to be capable of successful commercial production, either as single junction devices or as part of a multijunction system. This project was undertaken in order to make a contribution towards the improved understanding of the cell behaviour which will be necessary if the improvements in efficiency and stability required for commercial success are to be achieved.

3.2 The CdS layer

3.2.1 General properties

CdS is one of the II-VI group of semiconducting compounds, many of which have technological importance. During the past four decades, CdS has received considerable attention because of its use in a variety of electronic, photoconducting and photovoltaic devices. Cadmium sulphide has a direct band gap of about 2.4 eV at room temperature. It is a n-type semiconductor without intentional doping as a result of sulphur vacancies which can be induced by the

incorporation of excess Cd during film or crystal growth. The CdS compound crystallizes with either the zinc blende or the wurtzite structure. The zinc blende structure can be considered to be formed from two interpenetrating cubic close packed lattices with lattice parameter a = 5.832 Å. Each cation has four nearest anionic neighbours at a distance of $a\sqrt{3/4}$ at the corners of a regular tetrahedron. The wurtzite structure is composed of two interpenetrating close packed hexagonal lattices displaced with respect to each other by a distance 3c/8 along the hexagonal c axis. It is usually the wurtzite phase which predominates in CdS thin films although the zinc blende form can be found in films produced at low temperatures (63,64,65).

As the base layer in a variety of heterojunction solar cells which have been demonstrated to provide good conversion efficiencies (such as Cu_2S/CdS (14), $CuInSe_2$/CdS (66,67,21), InP/CdS (68,69), CdTe/CdS (70,71,72) the CdS film plays only a minor role in the light absorption process, but it has a significant effect on the overall performance of the device through its influence on junction transport processes and the series resistance R_s. In polycrystalline films the existence of grain boundaries results in a large number of defects which can play an important role in determining device characteristics. Clearly, in order to build an understanding of the electronic properties of these polycrystalline devices, it has been necessary to pay a great deal of attention to the cell fabrication process in order to ensure that reproducible characteristics were achieved.

Many different techniques have been used for the formation of CdS layers, including sputtering (73,74,75), chemical spray deposition

(76,77,78), sintering (79), electrophoresis (80,81) and vacuum vapour deposition (82,14,83). It is the latter process which has been used in production of Cu_xS/CdS cells with the highest reported efficiency (14) and this same method has been employed during the course of this project. In Cu_xS/CdS cells, the key roles of the CdS film are (i) to provide a base structure for the topotaxial formation of the Cu_xS absorber layer and (ii) to act as the collector for electrons which are generated as a result of absorption of photons within the Cu_xS layer. It follows that the structural properties and electrical properties of the CdS films are of special concern and these are discussed in the next two sections for the case of evaporated layers.

3.2.2. Structure of vacuum evaporated CdS films

Although CdS films can be produced from the vapour phase using separate Cd and S sources, it is usual to employ a single source of the compound in powder or tablet form. CdS evaporates congruently, but the structure and stoichiometry of the resultant films are very dependent on the experimental conditions. It is generally observed that films of CdS produced by evaporation onto neutral substrates at temperatures in excess of ~ 150°C have a polycrystalline structure with columnar, hexagonal grains tending to lie parallel to each other, with the C-axis of the grains at right angles to the plane of the substrate. The spread of grain orientations relative to the substrate is very dependent on the deposition conditions and the film thickness. At one extreme, for very thin films (~ a few Angstroms thick) the grains tend to be almost randomly distributed but for films greater than 20 μm thick (as used in most solar cells) the C-axis is very clearly aligned to the substrate normal, the alignment becoming more

precise as the deposition rate falls (84) and the substrate temperatures increases (85,86). This behaviour is assumed to result from the existence of a preferred growth direction for the crystallites (the C-axis direction). In this case, during the early stages of growth, the crystallites which happen to lie with the C-axis nearly perpendicular to the substrate will grow more rapidly than those with other orientations so that the film becomes more highly orientated as the thickness increases. Grain size is also very dependent on the film deposition conditions and film thickness. While grain widths of a few μm are typical for 20 μm thick layers, it has been shown (87) that there is a significant increase in grain width with increased substrate temperature and lowered deposition rate. From the earlier remarks concerning the film growth process it is not surprising to find from SEM micrographs (62) that the grain width diminishes as the distance from the substrate diminishes.

Having prepared films with the required thickness and properties, an etching treatment has been found to be one of the most important steps in the formation of high output frontwall Cu_2S-CdS solar cells. The etching is usually carried out just prior to formation of the Cu_2S layer, using strong HCl acid solution. The etching has two directly observable effects (88,89); it textures the film surface which becomes covered with a variety of pyramid shaped structures, and it forms deep etch pits, which appear to be associated with non-uniformities in the CdS film structure. The degree of surface texturing of the CdS films has been found to vary directly with time, temperature and acid concentration, but the degree of pitting seems to be more strongly affected by the time of etch than by the temperature and acid

concentration (88). The effect of texturing is to reduce the light reflection losses and hence to increase the photon absorption leading to a higher cell current. It has been suggested that etching opens the grain boundaries in the CdS film thus encouraging deeper penetration of the Cu_2S layer during the subsequent barrier formation (90). Deep grain boundary protrusions and deep etch pits have generally been considered to be harmful since they lower the internal shunt resistance of the cell and can cause short circuits. However, Shirland (91) has suggested that the etch pits might be helpful to cell output by providing a channel for the Cu_2S layer to form laterally in the grain boundaries intersecting the walls of the deep etch pits. Also, he could not detect any opening of grain boundaries that could be attributed to the HCl etch but Norian and Edington (92) have reported that etching does produce crevices at the grain boundary sites.

3.2.3 Electrical characteristics of vacuum evaporated CdS films

As noted above, the role of the CdS is to act as a base or window layer, rather than as a minority carrier generator layer, so that the presence of defects and impurities, which might assist minority carrier recombination, are not so serious here as in the photon absorber layer. Although the presence of such defects might be expected to have an important effect on the charge transport processes at the Cu_xS-CdS interface (as discussed in chapter 2) it has been shown that relatively good cell efficiencies can be achieved using CdS films containing significant concentrations of impurities (93). However, in order to avoid series resistance losses, it is essential for the electrical resistance of the base layer to be low.

For polycrystalline films the presence of grain boundaries with associated potential barriers (94) tends to increase the resistance of these layers but this effect is more serious for current flow in the direction parallel to the substrate than for the direction perpendicular to the film, the direction in which the columnar grains are arranged. Fortunately, this is the direction of current flow through the CdS film in conventional front-wall Cu_xS-CdS cells so that a low series resistance is assured provided the free carrier (electron) concentration is sufficiently large ($\sim 10^{17}$ cm^{-3}) (34) and the grain size is not too small ($\gtrsim 1$ μm) (93).

The free carrier concentration in the CdS film can be controlled by doping or by adjustments in the film deposition process which have an influence on the stoichiometry. The vapour deposition process involves first the dissociation of the CdS source molecules and their subsequent recombination on the substrate surface. However, as the sulphur vapour pressure is higher than the cadmium vapour pressure, the resultant films tend to have an excess of cadmium, the excess increasing as the substrate temperature is lowered (95). Thus the stoichiometry and associated carrier concentrations can be altered significantly by changes in the deposition parameters, as demonstrated in a recent study by Bryant and coworkers (96) who achieved a variation of carrier concentration over the range 10^{15}-10^{18} cm^{-3} in 20-30 μm thick films using deposition rates between 0.3 and 1.0 μm/min and substrate temperatures between 205°C and 295°C.

The electrical properties of vacuum-evaporated CdS thin films have been studied by a number of workers (97,98,99). However, in view of the influence of the growth conditions on the grain structure, as discussed in the last section, it is not surprising that conflicting

reports can be found concerning the deposition parameters necessary to produce high conductivity CdS films. For example, while it is usually found that the conductivity increases with increasing deposition rate (96), Wilson and Woods (84) have reported the opposite influence but it should be noted that their films were less than 5 μm thick and would therefore be composed of smaller and more randomly orientated grains than those in the thicker films (> 20 μm) generally employed in the fabrication of Cu_xS-CdS cells, as mentioned in the previous section. Thus, the average resistivity of the films would be expected to reduce as the film thickness is increased, as observed by Shallcross (100) and Gorski (101). A similar result was obtained by Berger et al (102) for the case of CdSe films. They explained this in terms of an increase in the free carrier mobility as the crystallites become larger in the thicker films while Vergunas (103) suggested that the resistivity of his CdS films decreased with thickness because of the increasingly parallel alignment of the fibre axes for the crystallites within these films.

The use of doping to reduce the resistivity of CdS films has been widely investigated, with In being the most common element employed. Such investigations indicate that the required reduction in film resistivity is frequently accompanied by other less beneficial effects. In one investigation, Shirland et al (104) evaporated a series of films onto glass substrates from CdS charges which contained various concentrations of indium up to 1 mole %. In addition to reducing the resistivity, the dopant also caused a change in the optical transmission of the films which varied linearly with the doping level upto 0.1 mole %. However, early CdS cells made at the

Clevite Corporation (105,106) were In-doped and gave reasonable efficiencies, as long as the CdS layer thickness was over 5 μm. Doping with Zn was found to improve the ohmic contact with the substrate, but in spite of this there was a resultant reduction in the efficiency. Similarly doping with CuCl was found to lower the efficiency due to a reduction in the open-circuit voltage. On the other hand, doping with CuCl and $CdCl_2$ (107) has been found to decrease the series resistance and to improve the overall photovoltaic response of the cells. Attempts have also been made to tailor the characteristics of the CdS film so that it has the required properties in different regions of the layer. For example, Hill (29) found that a CdS charge composed of pure CdS in the bottom half of the ampoule and CdS + 0.01% $CdCl_2$ in the top half of the ampoule, gave rise to a CdS thin film in which the resistivity was low at the back surface, leading to an improved contact with the molybdenum substrate, and higher towards the outer surface where the junction to the Cu_xS layer is formed. The conversion efficiencies of cells made with these layers were higher than those made with uniformly doped CdS layers.

3.3 The copper sulphide layer

3.3.1 Structure and composition of copper sulphide

The phase diagram for the Cu-S system is relatively complex as can be seen in figure 3.1. The details have been reviewed by a number of authors (33,108,109,99). For good photovoltaic behaviour in solar cells, it is the copper-rich chalcocite (x=2) phase which is of primary importance but, as can be seen in figure 3.1 there are several other stable phases with a variety of temperature dependent crystal structures. At room temperature, the possible phases include

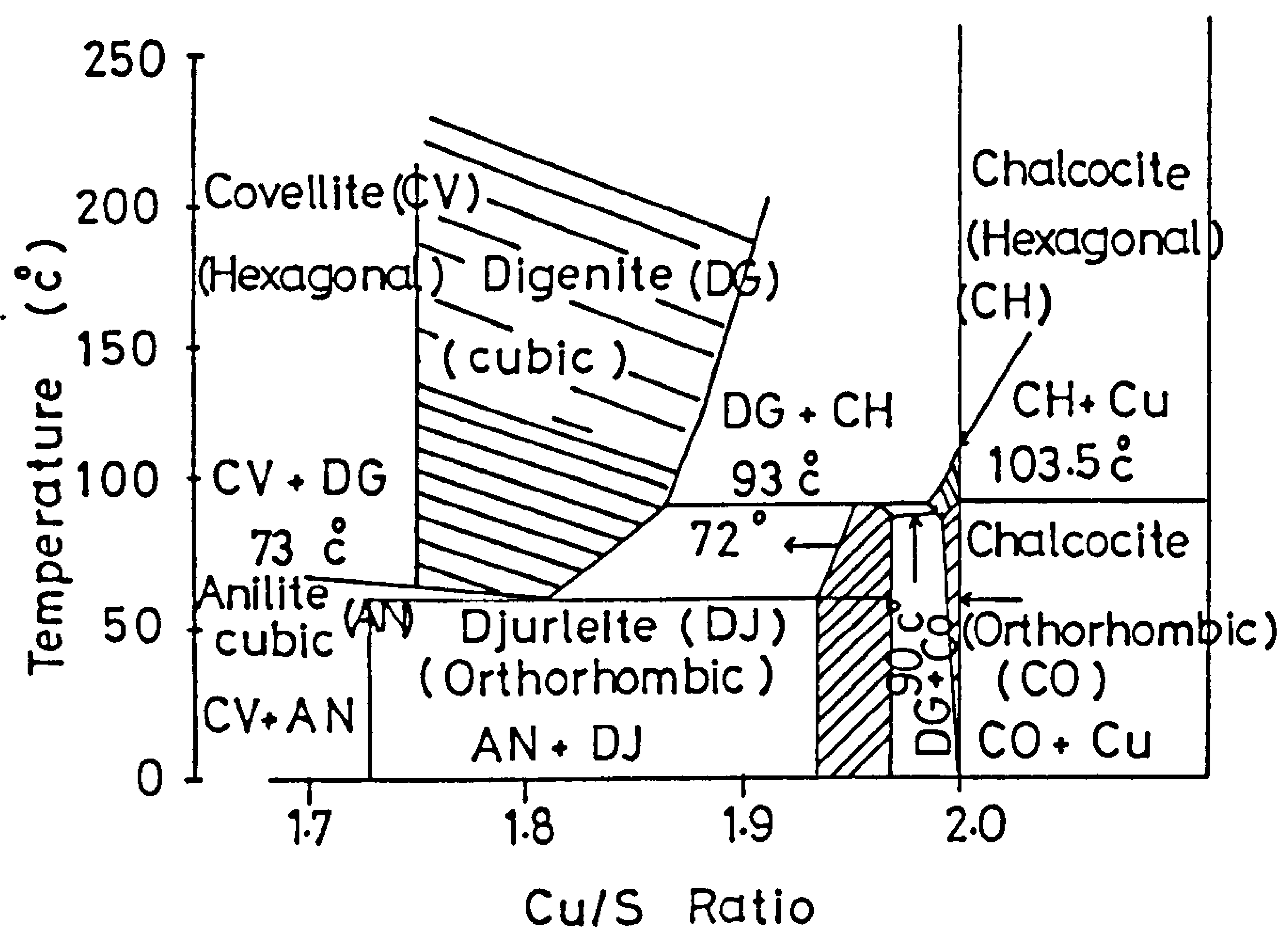

Fig.(3.1) Phase diagram of the Cu-S system. Ref. (83).

djurleite (x = 1.93-1.96), digenite (x~1.8), anilite (x = 1.75) and covellite (x = 1) and for samples with composition ratio x outside the limit of existence of one of these phases, a mixture of phases is generated. The structure and composition of both bulk and thin film samples of the material have been studied using a variety of techniques. Mathieu et al (110) made use of electrochemical analysis and this technique was further developed by Vedel (111). Loferski et al (112) studied the composition of Cu_xS layers by x-ray and cathodoluminescence measurements while Mulder et al (113) used microchemical analysis and atomic absorption spectroscopy methods. In samples of Cu_xS produced by topotaxial growth on CdS, Cd ions are replaced by Cu ions leaving the sulphur sub-lattice relatively unchanged (109,114,115). While this S sub-lattice remains as a rigid, ordered structure the Cu sub-lattice is considerably more disordered as the Cu ions are relatively mobile and can position themselves in a variety of equivalent sites. The properties of Cu_xS are found to be very sensitive to small changes in composition and, as might be expected, the composition of Cu_xS in thin film form is highly dependent on the method of fabrication and the ambient conditions. These features are discussed in the following sections.

3.3.2 Electrical and optical properties

Cuprous sulphide has been shown (116,117) to be a degenerate p-type semiconductor with the carrier concentration being dependent on the stoichiometry. As the stoichiometry changes from that of Cu_2S towards a sulphur-rich composition there are corresponding changes in the apparent electrical parameters of the material which effectively becomes a mixture of phases as indicated in the phase diagram of

figure 3.1. The associated increase in density of the copper vacancies in the system leads to an increase in the free hole concentration and, thereby, to an increase in conductivity, as the Cu vacancies act as shallow acceptor centres. Such variations in conductivity have been reported by a number of authors including Palz et al (118) and Burton and Windawi (119). At room temperature, the conductivity of Cu_2S is typically $\sim 10^2$ (ohm cm)$^{-1}$ but this increases by more than 2 orders of magnitude for $Cu_{1.8}S$. Other parameters which are of particular significance for layers used in solar cells are the minority carrier diffusion length and the photon absorption coefficient. Measurements of the minority carrier diffusion length have been made by several different groups (120,121,113,122,123,124). The results range from 1.7 µm to 0.1 µm (124) or less (120,121,113). As in the case of the conductivity measurements, this wide variation in the results can be attributed to differences in the stoichiometry of the materials studied by the various groups. Indeed, the work reported by Mulder (120) has demonstrated that the diffusion length for chalcocite is significantly greater than that for djurleite.

Variations in the observed properties due to differences in material structure and composition have proved to be particularly troublesome in relation to measurements of the optical absorption coefficient of Cu_xS layers and its dependence on wavelength. While the absorption coefficient for chalcocite is generally found to be higher than for any of the copper defficient phases at any wavelength (125), there have been considerable inconsistencies in the data obtained in different laboratories. Some examples of measurements, which have been reported for Cu_2S (126,127,128,113,129) are shown in figure 3.2. While these results include significant variations in

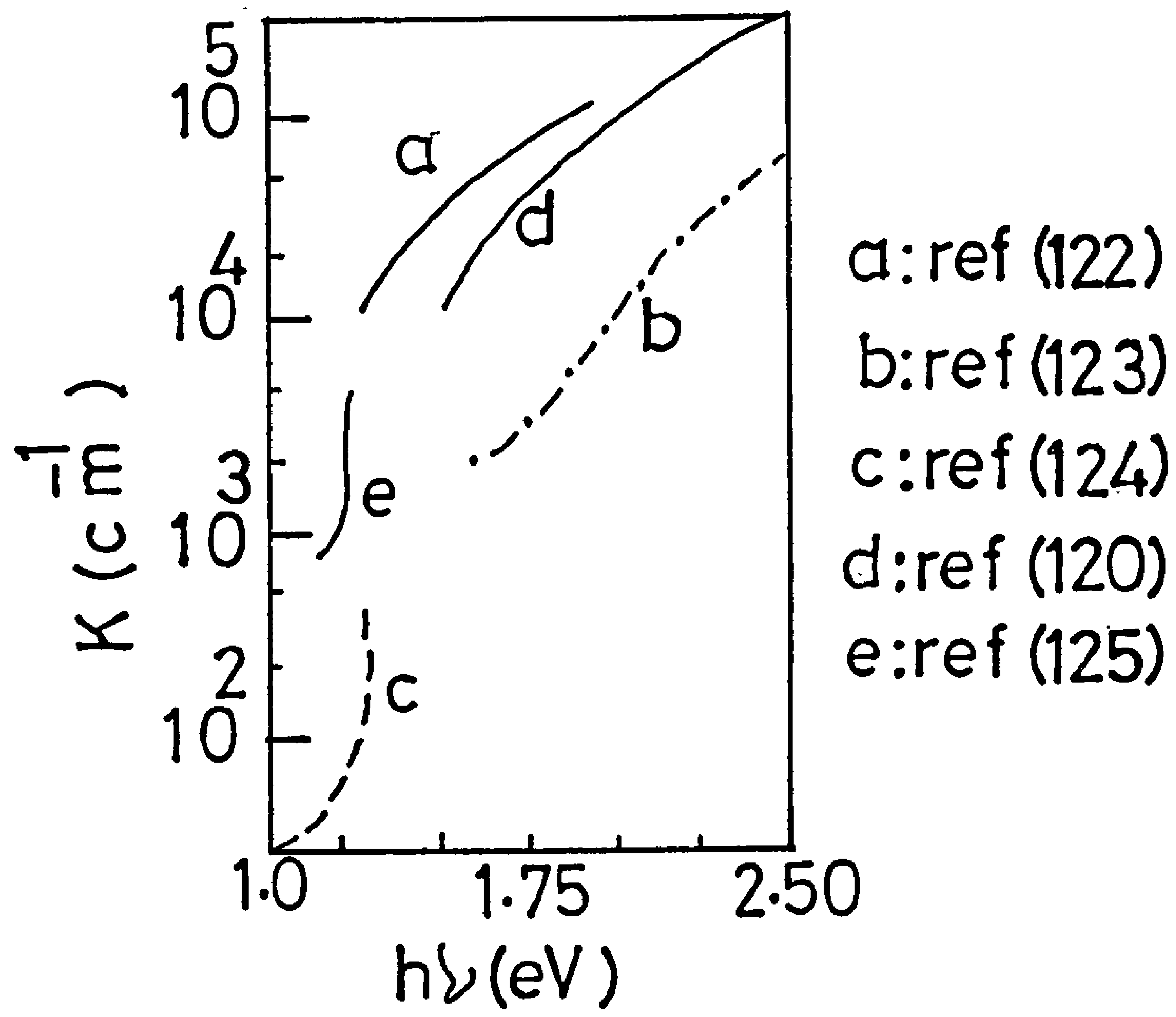

Fig.(3.2) Optical absorption curves of Cu_2S after different authors.

magnitude of the absorption coefficient, the spectral dependence appears to indicate a clear absorption edge at ~ 1.2 eV and a further rise at 1.7-2.5 eV. The spectral dependence of the absorption coefficient can be used to determine the nature of the band gap (direct or indirect) involved in the absorption process. Such an analysis for Cu_xS data from several different laboratories (113,128,130,131,132) leads to the conclusion that there is an indirect band gap of ~ 1.2 eV and a direct band gap of ~ 1.8 eV, although the absorption coefficient in the region of 1.2 eV seems to be higher than might be expected for indirect transitions. There is still much uncertainty concerning these assignments as more recent studies by Eser and Cambridge (133) have suggested that there might be an indirect band gap of 1.1 eV together with a direct gap of 1.28 eV and supportive evidence for the existence of a low energy direct gap has come from cathodoluminescence studies (134,135). These studies show that chalcocite produces a luminescence peak at 0.96 μm (1.28 eV) and from the shape and half-width of this peak, a direct transition has been inferred. Additional studies of the relationship between the absorption coefficient and sheet resistance by Rothwarf and Windawi (136) have indicated that the best fit between experimental results and theoretical calculation is achieved by making the assumption that Cu_2S acts as a direct band gap semiconductor.

3.3.3 Film formation processes

During the course of the various investigations into the properties of Cu_xS, particularly for use in solar cells, many techniques have been used for fabricating the Cu_xS films. These include the solid state reaction process involving an evaporated CuCl

layer (137,138,115,139,140), direct Cu_xS evaporation (141), electrodeposition (146), spray pyrolysis (142), and the most commonly employed wet dipping process (144,143,145,146), which is the method used in this investigation. As described more fully in section (4.3), the wet-dip (or Clevite) method involves an exchange of Cu ions for Cd ions in the lattice of CdS. This is achieved by immersing the CdS into a hot concentrated CuCl solution. Salkalachen et al (147) found the pH of the CuCl solution plays an active role in controlling the Cu_xS growth processes. With a pH of 4.6 the thickness was observed to increase with time parabolically while in solutions of lower pH (about 3.4) a faster linear growth mechanism was dominant. Other factors which influence the Cu_xS layer growth process are the grain size and morphology of the CdS parent surface and the relative concentrations of cadmium and sulphur atoms at this surface (148).

During the chemical exchange process, the Cu_xS layer tends to grow preferentially at the grain boundaries of CdS (92,150,149) forming deep intrusions into the CdS film so that the resultant Cu_xS layer has a very non-uniform thickness. However, in cells exhibiting good conversion efficiencies, average Cu_xS thicknesses in the range 0.1-0.4 μm have been reported (14,34,151,152). The non-uniform thickness is thought to be accompanied by non-uniform composition. This has been studied by Vedel et al (153) who used electrochemical analysis to determine the change in composition as the growth of the Cu_xS layer proceeds. He proposed that, during the initial stages of the Cu_xS film growth, non-stoichiometric copper sulphide forms at the interface between the CdS and the $CuCl_2$ solution arriving through channels which were assumed to exist in the cuprous sulphide due to

the difference in molar volume between CdS and copper sulphide. This Cu_xS was believed to be subsequently transformed into Cu_2S, producing a two layer film structure as represented schematically in figure 3.3. The observed stoichiometry ratio for the layer as a whole is therefore a mean value $\bar{x}$ for the two regions of width l' and l". Assuming that l' remains constant during the growth it follows that the value of $\bar{x}$ moves closer to 2 as l" increases with increased growth time.

3.4 Properties of Cu_2S-CdS solar cells

3.4.1 Influence of cell structure

As has been mentioned previously, Cu_2S/CdS cells can be fabricated using either single crystal or polycrystalline CdS, with the Cu_2S layer being formed using one of several different techniques (see section 3.3). These different fabrication processes result in Cu_2S-CdS junctions with very different geometric shapes and different crystallographic structures. It follows that the electrical and photovoltaic properties of the resultant cells are dependent upon the details of the fabrication process and, indeed, upon any post-fabrication treatment. Although a number of basic characteristics might be expected to be common to all cell types, it is clear that any detailed consideration of cell behaviour must take account of fabrication conditions and the resultant structure of the cells involved.

As has been previously noted, the Cu_2S-CdS cells with the highest reported efficiencies have been those formed using the Clevite technique and, as described in section (4.3), this technique results in cells with a highly non-planar interface due to the deep penetration of Cu_2S at the CdS grain boundaries. The experimental

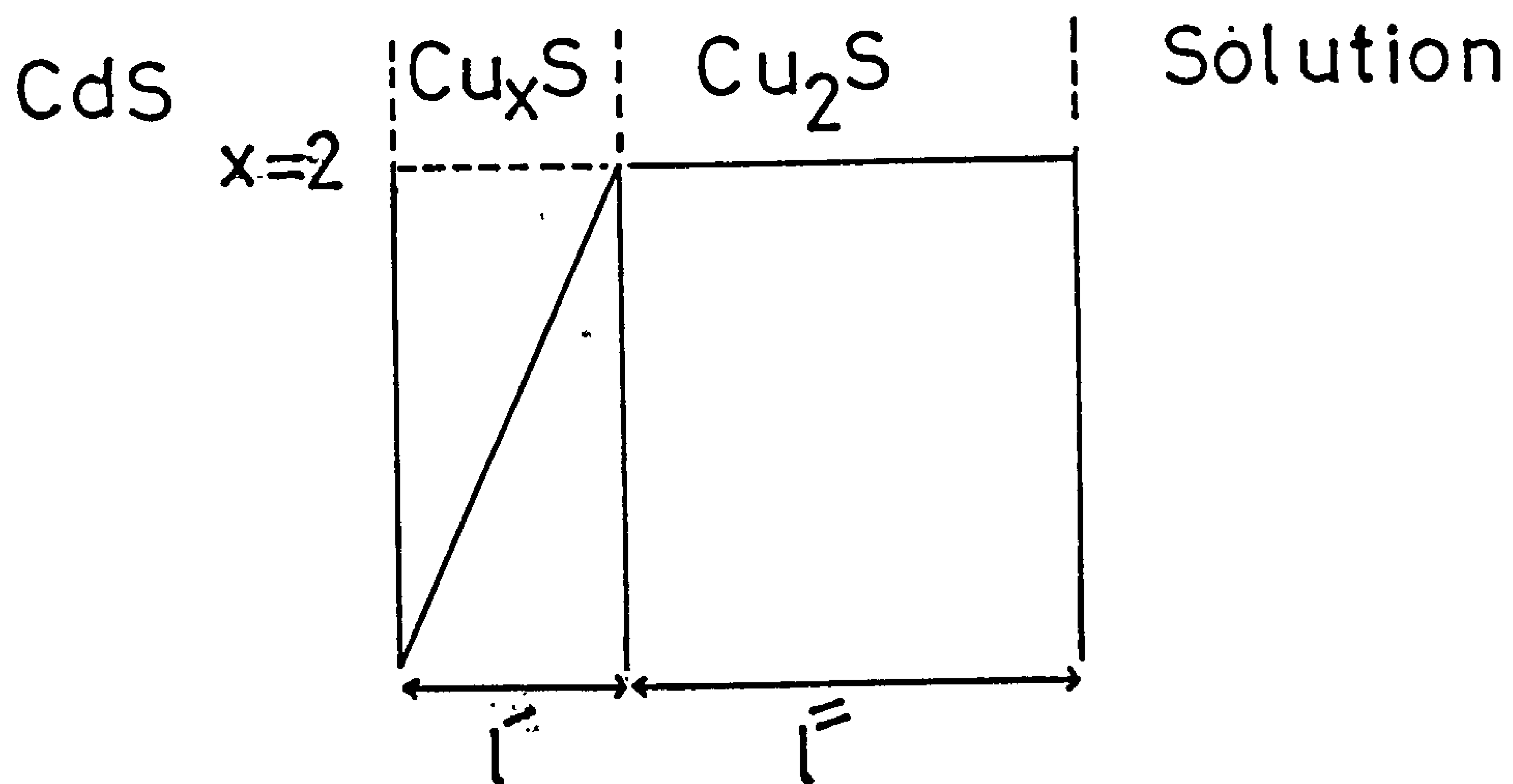

Fig.(3.3) Model for the formation of a Cu_2S layer.

work reported in chapter 5 is primarily concerned with cells having this structure and in sections 3.4.2 and 3.4.3 the background literature concerning the operation and stability of this type of device is reviewed.

3.4.2 Cell characteristics and junction models

Due to the possibility of short circuits arising as a result of the rapid penetration of Cu_2S along grain boundaries when using the Clevite cell fabrication process, a relatively thick CdS base layer is required but in order to ensure that this does not lead to an associated high series resistance for the cell, the conductivity of the CdS layer must be high and carrier concentrations in excess of 10^{17} cm^{-3} are considered to be necessary. As a consequence of this, the depletion layer at the interface with a freshly formed Cu_2S layer is usually sufficiently narrow to allow tunneling mechanisms to play a dominant role in the junction conduction process so that, prior to any post-fabrication heat treatment, the junction is only weakly rectifying. The effect of any subsequent heat-treatment is to widen the depletion region on the CdS side of the junction due to the formation of a more insulating CdS region close to the interface as a result of the diffusion of Cu from the Cu_2S layer. The diffused copper forms acceptor centres which compensate the shallow donor states in the CdS layer, thereby leading to a reduced space charge density in this region (see section 2.5). The correspondingly wider depletion layer reduces the tunneling probability leading to much more rectifying I/V characteristics.

Attempts to explain all the observed electrical and photovoltaic properties of these cells has resulted in a number of different energy

band models being proposed. Each of these models has been supported by a considerable amount of experimental data which has been the subject of several reviews (99,29,108,154). As mentioned in section 3.1 the early results obtained by Williams and Bube (46) were explained in terms of a metal-semiconductor barrier (figure 3.4), while Grimmeiss and Memming (155) assumed that the barrier was associated with a p-n junction within the CdS layer (figure 3.5). This was assumed to be due to a layer of p-type CdS being formed close to the surface as a result of a high concentration of diffused copper. The idea of a Cu_2S layer being formed at the CdS surface was first proposed by Cusano (47). This was supported by Keating (48) and soon adopted by several other groups including the Clevite group who eventually developed the model shown in figure 3.6. In this model, it was assumed that light was absorbed almost entirely within the thin (~ 0.3 μm thick) p-type Cu_2S layer (with band gap energy ~ 1.2 eV) and that the resultant photogenerated electrons diffused to the p-n junction where the conduction band discontinuity favoured transfer of the electrons to the CdS side to provide the photogenerated current. In an earlier model from Potter and Schalla (156) shown in figure 3.7, it was assumed that the electrons were photoexcited directly into the CdS conduction band from the Cu_2S valence band over a barrier of ~ 0.85 eV, while Balkanski and Chone (157) focussed attention on the Cu_2S-CdS interface states and suggested that the observed long wavelength photoresponse was associated with photoexcitation of electrons from a quasi-continuous distribution of such interface states.

It should be noted that according to the model proposed by Potter and Schalla (156) the Cu_2S is highly degenerate and the Fermi level

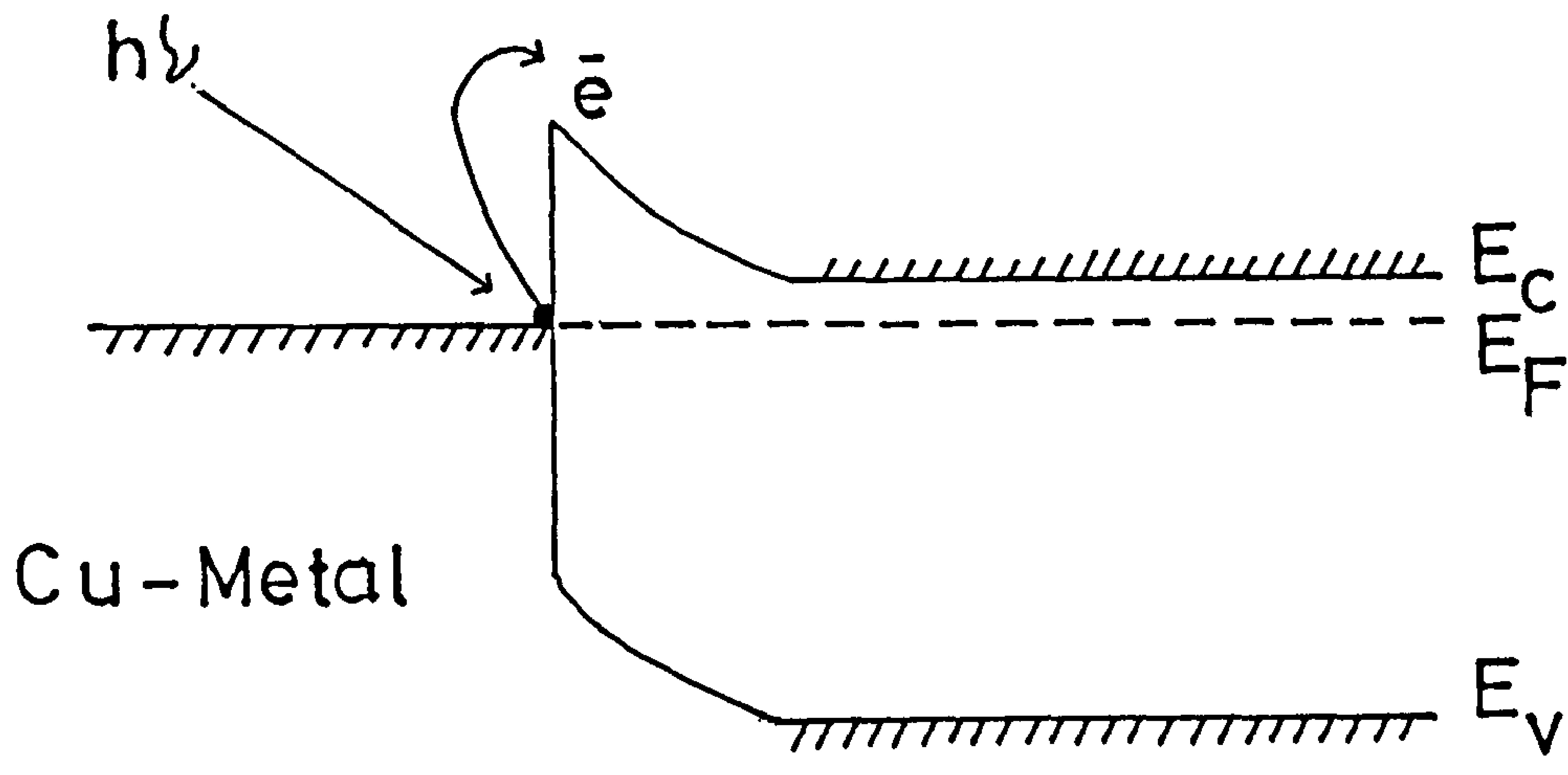

Fig.(3.4) Energy band diagram according to Williams and Bube (46).

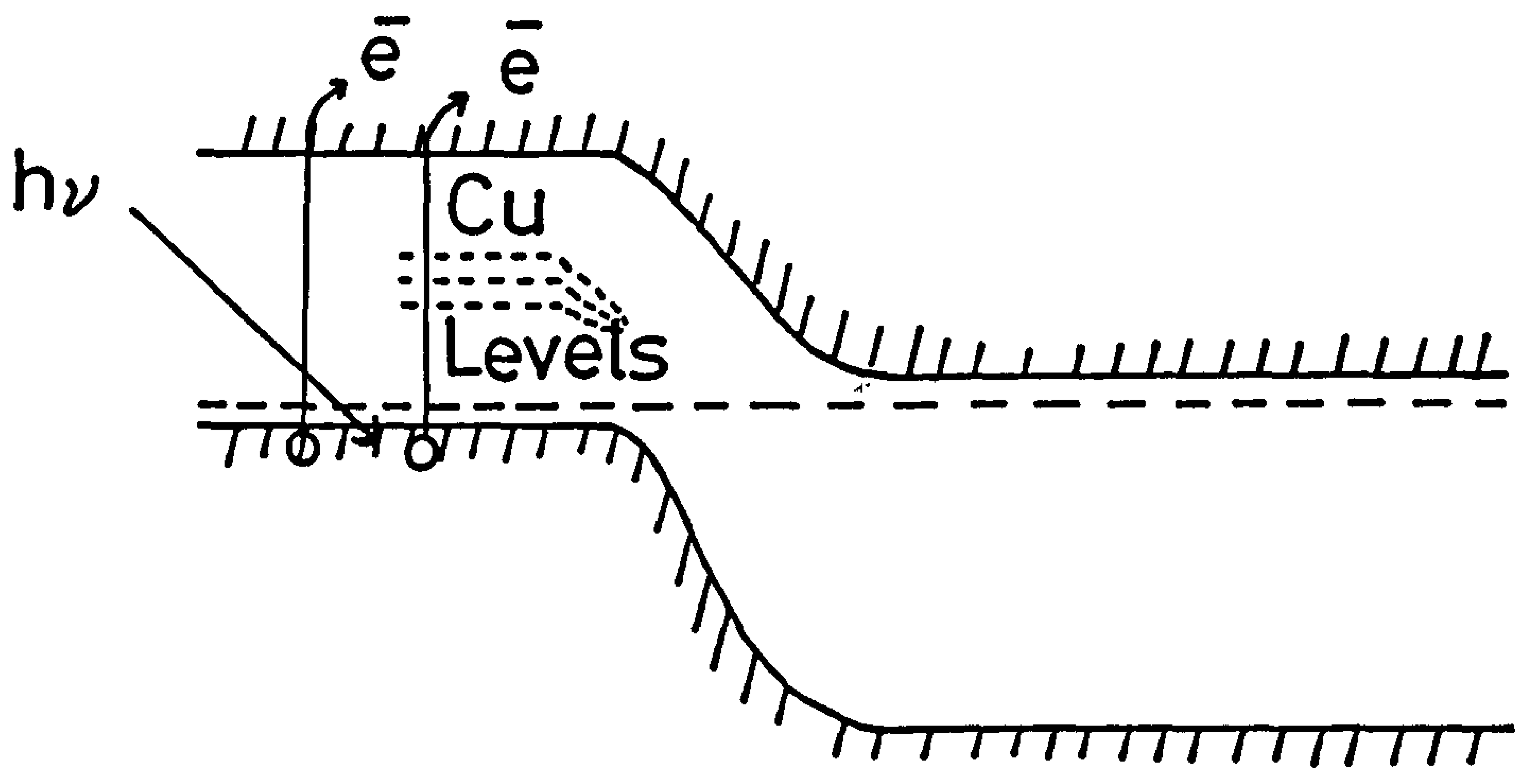

Fig.(3.5) Energy band diagram according to Grimmeiss and Memming (155).

Fig.(3.6) Energy band diagram for the Shiozawa (Clevite) model (36).

Fig.(3.7) Energy band diagram according to Potter (156).

lies within the valence band so that the Cu_2S is essentially playing the role of a metal from which photoemission occurs into the CdS layer in agreement with the earlier theory of Williams and Bube (46). However, most experimental observations can be explained using variants of the Clevite model, an important feature of which relates to the effect of light on the semi-insulating layer of CdS adjacent to the interface. As mentioned earlier, this layer is due to the presence of copper acceptor centres which are introduced by diffusion during the course of post-fabrication heat-treatment. In view of the different cell fabrication and annealing conditions which have been employed at different times and at different laboratories, it is not surprising that there have been some disagreements concerning the extent of this insulating layer and the importance of its role. Likewise, a number of other details of the model have been the subject of debate including the size and polarity of the conduction band edge discontinuity. In contrast to the Clevite model, an early model proposed by workers at Stanford (158,159) and Stuttgart (160) included a conduction band spike at the Cu_2S-CdS interface, as shown in figure 3.8. According to this model, photogenerated electrons in the Cu_2S layer reach the CdS layer by tunneling through the spike. As the probability for tunneling is dependent on the width of this spike the photogenerated current would be controlled by the space charge density in the photoconductive semi-insulating CdS region. With the cell in the dark, the ionized donor states in this region are compensated by the occupied Cu acceptor centres so that the space charge density is low and the space charge layer width is correspondingly large. However, under illumination, the effect of hole trapping by the

acceptor states is to cause the space charge width to be reduced (as shown in figure 3.8) and the probability for electron tunneling through the conduction band spike to be increased.

The idea of a conduction band spike was also proposed by Te Velde (161) and Deb (162) who argued that the observed changes in I/V characteristics due to different annealing treatment could be explained in terms of variations in the conduction band edge discontinuity. A spike was assumed to exist after annealing in air as a result of oxygen penetrating the Cu_2S layer to form electron traps at the Cu_2S-CdS interface. Te Velde concluded that the best efficiency is obtained by adjusting the discontinuity to zero.

Taking account of results obtained by the many research groups engaged in work on Cu_2S-CdS cells, the currently accepted model which can be used to account for the majority of observed cell characteristics is that shown in figure 3.9. The basic features of the model have been discussed by Rothwarf (34) and by Riben and Feucht (163) and can be summarised as follows:

(i) The Fermi energy lies close to the top of the valence band in the Cu_2S layer where the carrier concentration is determined by the density of copper vacancies;

(ii) the carrier concentration deep inside the CdS layer is in excess of 10^{17} cm^{-3} but is significantly less at the interface (due to copper diffusion) so that the equilibrium junction diffusion voltage in optimised cells lies almost exclusively in the CdS layer;

(iii) due to the 4% lattice mismatch between the Cu_2S and CdS, there is a large density of interface states ($\sim 10^{13}$ cm^{-2});

(iv) the electron affinity of CdS exceeds that of Cu_2S yielding a conduction band discontinuity of ~ 0.2 eV.

Fig.(3.8) Energy band diagram for the Stanford model (158,159).

Fig.(3.9) Energy band diagram proposed by the Delaware group (34,145).

According to this model, it is assumed that the photocurrent is produced mainly as a result of photon absorption within the Cu_2S layer but photoexcitation and carrier trapping processes within the CdS depletion region have a significant influence on space charge distribution, as explained earlier, and thereby influence the charge conduction processes. Under forward bias in the dark the dominant transport process involves thermionic emission of electrons over the CdS barrier and recombination through interface states. Under illumination, the rate at which photogenerated minority carriers in the Cu_2S layer reach the CdS collector is dependent on the electric field E at the interface, as described in section (2.4) where the interface collection factor is given as $\mu E/S_I + \mu E$. E is clearly dependent on the distribution and density of donors and acceptors in the CdS layer as well as on the intensity and wavelength of light reaching the space charge region. The I/V characteristics at room temperature for cells which had been given some post-fabrication heat treatment have been found (34) to fit the relationship (2.4.2) in section 2.4. By setting the current density in relation (2.4.2) to zero, the open-circuit voltage is shown, in relation (2.4.5) to be dependent on the process of cell fabrication as this has an influence on the junction area between the Cu_2S and CdS layers. The formation of Cu_2S layer deeply along the grain boundaries increases the junction area and reduces V_{OC} according to relation (2.4.6).

3.4.3 Degradation and cell stability

Degradation has long been recognised as a major problem for Cu_xS/CdS solar cells (29,164). Of course, any changes in the properties of any component part of a cell during operation can

contribute to a reduction in its efficiency but in front wall cells the properties of the very thin Cu_2S layer are particularly sensitive to chemical reactions at the free surface as well as to interdiffusion processes at the interface with the CdS film. The rate of copper diffusion from Cu_xS layer into the CdS layer has been shown to be reduced by doping. Palz et al (118, 35) produced cells with improved stability by doping the CdS layer with In while investigations by Konstantinova and Kanev (165) indicated that Bi doping could be successful. Alternatively the interfacial diffusion process can be inhibited by adjusting the stoichiometry of the near surface region of the CdS layer. This has been done by Bryant and coworkers (166) who controlled the deposition parameters during CdS film growth in order to provide a thin layer (~ 1 μm) of high resistivity CdS in the vicinity of the junction. A substantial improvement in cell stability was achieved but the process is very difficult to control and account needs to be taken of the amount of CdS removed during etching of the CdS layer prior to dipping. Loss of copper from the Cu_2S by this diffusion mechanism or by any accompanying oxidation at the free surface during cell operation has the deleterious effect of reducing the Cu/S atomic ratio which leads to both a reduction in the photon absorption coefficient and a decrease in the minority carrier diffusion length (167) and, thereby, to a fall in the light-generated current (34). An additional degradation process which can occur at defect sites within a cell is that of electrochemical decomposition of the Cu_xS layer. This can lead to the formation of metallic copper nodules or filaments which can short circuit the cell (168,169,170,171). Mathieu and coworkers (172) carried out a fundamental study of this process which has a threshold voltage

between 0.35 and 0.4 V. Of course, it is clear, from the models of the Cu_2S/CdS system presented in the previous section, that under ideal conditions the voltage drop across the Cu_2S layer should be very small, as the major portion of the cell voltage should be confined to the CdS layer. However, as has been previously noted, the cell does not have a simple planar structure and at certain sites (e.g. cracks and other growth defects within the CdS layer) the Cu_2S formation process is such that the resultant Cu_xS is subjected to a substantial photovoltage. Making use of a laser scanning technique it has been possible to reveal the location of defects responsible for electrolytic decomposition (173) and, by means of a high power laser pulse, these defects have been removed by vaporisation, leaving a cell which was subsequently resistant to this type of degradation process.

Processes involving chemical interaction between the Cu_2S layer and the ambient atmosphere have been a major subject for discussion throughout the history of development of Cu_2S/CdS solar cells. While the efficiency of these cells has been shown to be improved by heating in gases such as carbon monoxide (174), hydrogen (15,175), argon (14), detrimental effects are observed in cells exposed to oxidising gases such as chlorine, bromine, iodine and oxygen (118). It is well known that unprotected cells degrade rapidly when exposed to air and that the effect is accelerated by the presence of moisture (167). This was originally assumed to be due to the formation of a surface layer of copper oxide with a consequent reduction in the x value of the underlying Cu_xS. The process could be reversed by annealing in a reducing atmosphere (167, 176) but it is clear that contact with the air needs to be avoided to achieve stable operation. However, simple

hermetic sealing has not proved to be successful (177) and this has prompted more detailed studies of the degradation processes which occur at the Cu_xS surface. As a result of these studies involving the use of a variety of modern analytical techniques, it is apparent that the simple oxidation mechanism referred to above is incorrect. Instead of copper oxide being formed, current evidence indicates that a compound of cadmium is formed, as first suggested by Florio and coworkers (178) who used atomic absorption spectroscopy (AAS) to analyse the composition of an acid soluble surface oxide on air-degraded cells. Their result indicated that the source of cadmium must be the underlying CdS layer and further evidence for a flow of Cd from the CdS layer to the Cu_xS surface has been provided by Bryant et al (166) using Auger profiling and Uppal et al (179,180) using XPS techniques. The overall reaction, as suggested by Florio (178) can be expressed as:

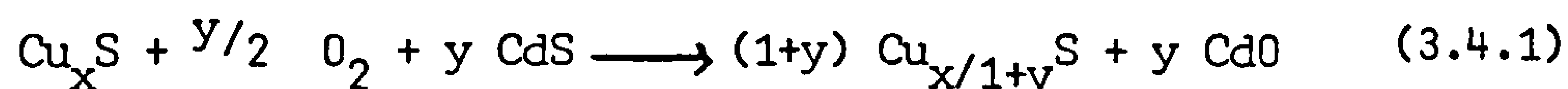

$$Cu_xS + {}^{y}/_{2}\ O_2 + y\ CdS \longrightarrow (1+y)\ Cu_{x/1+y}S + y\ CdO \qquad (3.4.1)$$

The associated change in the stoichiometry of the Cu_xS layer has been measured using the electrochemical technique developed by Castel and Vedel (181) and several different studies (60, 182) have confirmed that x is close to 2 in high efficiency cells and x decreases as the efficiency degrades, upon exposure to air. Until recently, it was assumed that the reduced x factor was due to an increased concentration of Cu^{+2} ions as compared with the concentration of Cu^{+} ions in the Cu_xS layer (118). However, recent XPS studies by Partain and coworkers (183) have shown that Cu^{+2} ions can be detected only after a very long exposure to hot moist air and they are then present only in a thin surface layer. No Cu^{+2} ions could be detected within

the bulk of the Cu_xS layer even after treatments which would have reduced the x value to below 1.9. This result is consistent with that obtained by Bhide et al (184) and suggests that the non-stoichiometric defects associated with x values less than 2 are accommodated by a variable valence state for S rather than for Cu as proposed by Folimer and Jellinek (185). Evidence has also been presented (179, 180,183) to indicate that exposure to air can produce a new surface reaction product containing sulphur in the 6+ valence state. This is believed to be due to the formation of copper or cadmium sulphate. The production of $CdSO_4$ has been shown to be strongly favoured thermodynamically (183) and this accordingly provides an explanation for the appearance of both Cd and S^{+6} ions at the Cu_xS surface.

Consideration of other possible surface reactions has provided information concerning the mechanism involved in possible cell stabilisation treatments. One such treatment is that developed by Bogus and Mattes (186) in which a layer of Cu(~100 Å thick) is deposited onto the cell surface and subsequently heated in air at 180°C. It has been shown that this treatment should result in a layer of CuO being formed and, as a reaction between this oxide and CdS is not favoured thermodynamically, the outward diffusion of Cd from the CdS layer to the cell surface should not occur. This is consistent with the observations of Bryant et al (166) who compared Auger profiles for different cells which had been heated in air at 200° for 90 minutes. While an unprotected cell showed signs of significant displacement of Cd to the cell surface, no such outward diffusion was observed for a cell coated with 100 Å of Cu. The protective CuO film can alternatively be generated by exposing the Cu_xS layer to a

hydrogen plasma to produce a Cu rich surface layer before heating in air (187).

It must be emphasised that a CuO layer provides effective protection only in a dry environment. The XPS studies mentioned earlier (183) show that surface Cu^{+2} ions are present when cells are exposed to moist air due to the formation of CuO by removal of Cu from the Cu_xS layer with a consequent reduction in the x value. This is consistent with the common observation that cells exposed to moist air degrade rather rapidly to very low performance levels (167). It is clear therefore that a CuO layer only stabilizes air exposed Cu_xS/CdS devices kept in a dry atmosphere so that these cells need to be hermetically sealed as well as having the CuO protective layer. As mentioned earlier, the use of hermetic sealing alone has been shown to be unsatisfactory (177). It appears that Cr_2O_3 should be even more stable than CuO as a protective layer (183) and it is claimed (188) that this is more effective in absorbing ultraviolet radiation which can also degrade the cell. For cells using both a hermetic seal and a CuO or Cr_2O_3 protective layer, operational life times of up to 10 years have been estimated (189) and this is consistent with the Stuttgart group's (190, 137) report of stable operation during 3 years rooftop trials for their copper-oxide protected cells sealed between two sheets of glass. An alternative technique has been suggested by Donaghey et al (191) for stabilizing Cu_xS/CdS solar cells by using a Cu-containing alloy in contact with the Cu_xS layer in order to force its x value to remain at the desired magnitude. By varying the Cu content in the alloy (for example Cu/Au), Donaghey has determined the copper concentration required to maintain the x value between 1.9996 and 1.999 in the Cu_xS layer. (His calculations were based on the

electrochemical data of Mathieu et al (172)). This technique would be appropriate for back wall cells but it is not yet clear whether the process of controlling the x value of the Cu_xS layer is sufficient to keep a Cu_xS/CdS device at a high performance level (167). In addition, it may be necessary to maintain the Cu_xS in the desired monochlinic form of chalcocite, as opposed to the tetragonal or cubic forms, and recent transmission electron microscopy studies of Sands et al (192, 193) have indicated that the monoclinic structure is only formed exclusively on the S face of CdS when this surface is tilted at an angle greater than 60° to the basal plane due to careful etching in HCl. However, the role played by the morphology of the CdS surface has never been carefully studied and it has been suggested (183) that this could be important in relation to problems of reproducibility.

CHAPTER FOUR

EXPERIMENTAL SYSTEMS AND PROCEDURES

4.1 Fabrication of CdS films

4.1.1 The vacuum evaporator system

The vapour deposition process was carried out in a conventional vacuum evaporation unit with a 12" working chamber pumped by a 3" oil diffusion pump. With a liquid nitrogen trap above the pump, pressures in the region of 10^{-6} torr could be achieved. The zinc-coated copper sheets onto which the CdS was to be deposited were covered with a mask and clamped onto a stainless steel block which was positioned so that the surface to be coated was lying perpendicular to the source as in figure 4.1. A heating coil was built into the substrate holder and the temperature of this assembly was measured using a chromel-alumel thermocouple. CdS powder was placed into a quartz crucible with quartz wool blocking the top of the crucible to avoid spattering of the powder during evaporation. The quartz crucible was in the form of a double-walled cylinder and this was heated by a molybdenum foil element wrapped around a quartz former within the inner cylinder, as shown in figure 4.2. The heated crucible was surrounded by a heat reflecting shield constructed from a cylinder of stainless steel covered with a further quartz tube. Screening the space between the source and substrate, there was a hot-wall consisting of a pyrex cylinder with a heating element wrapped around it. The length and the diameter of this pyrex cylinder were 22.5 cm and 14 cm respectively. A shutter could be inserted below the substrate holder to interrupt

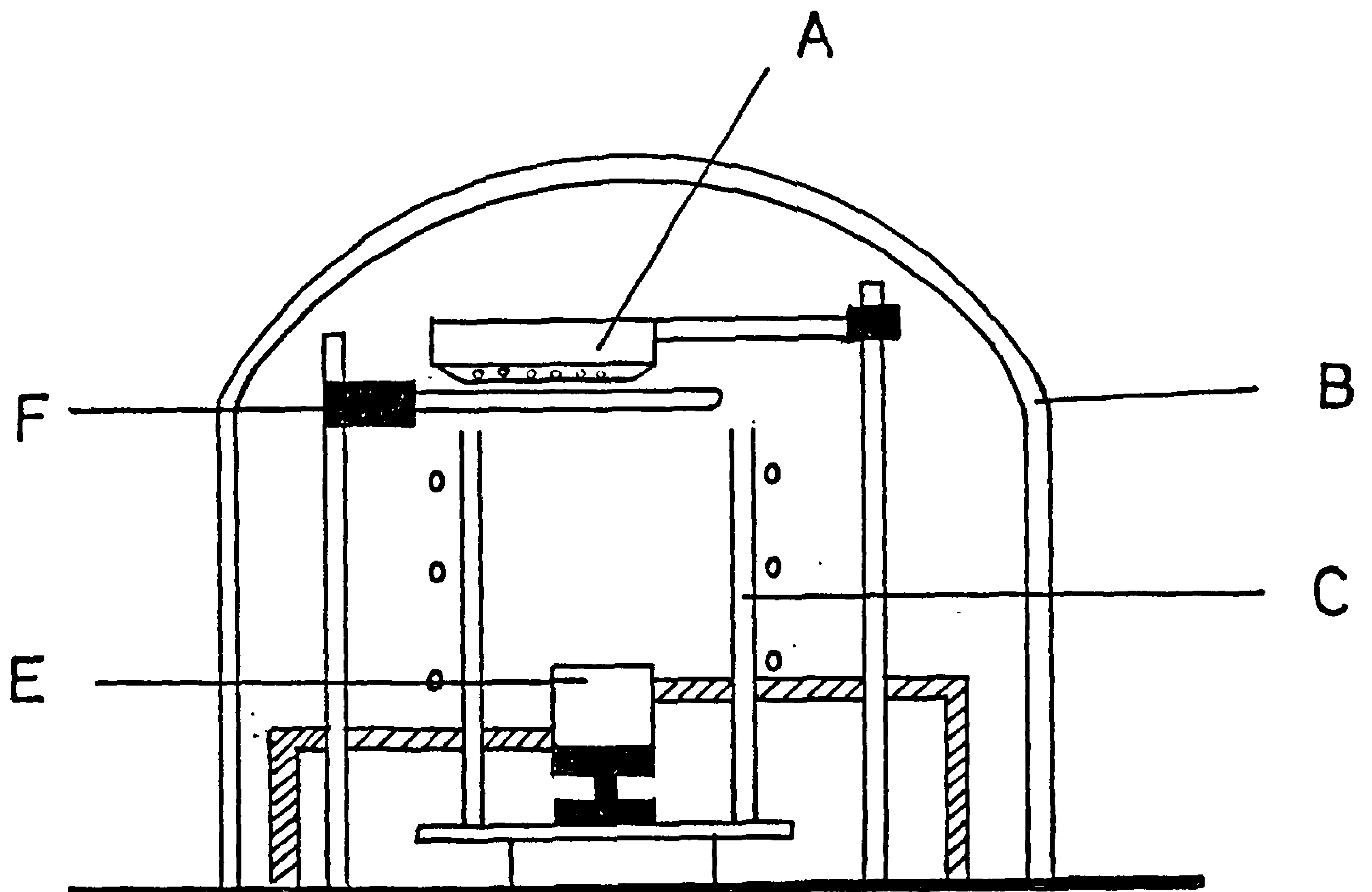

Fig.(4.1) Apparatus for the deposion of CdS
A: Substrate holder and heater
B: Bell jar
C: Hot-wall
F: Shutter
E: Source container and heater

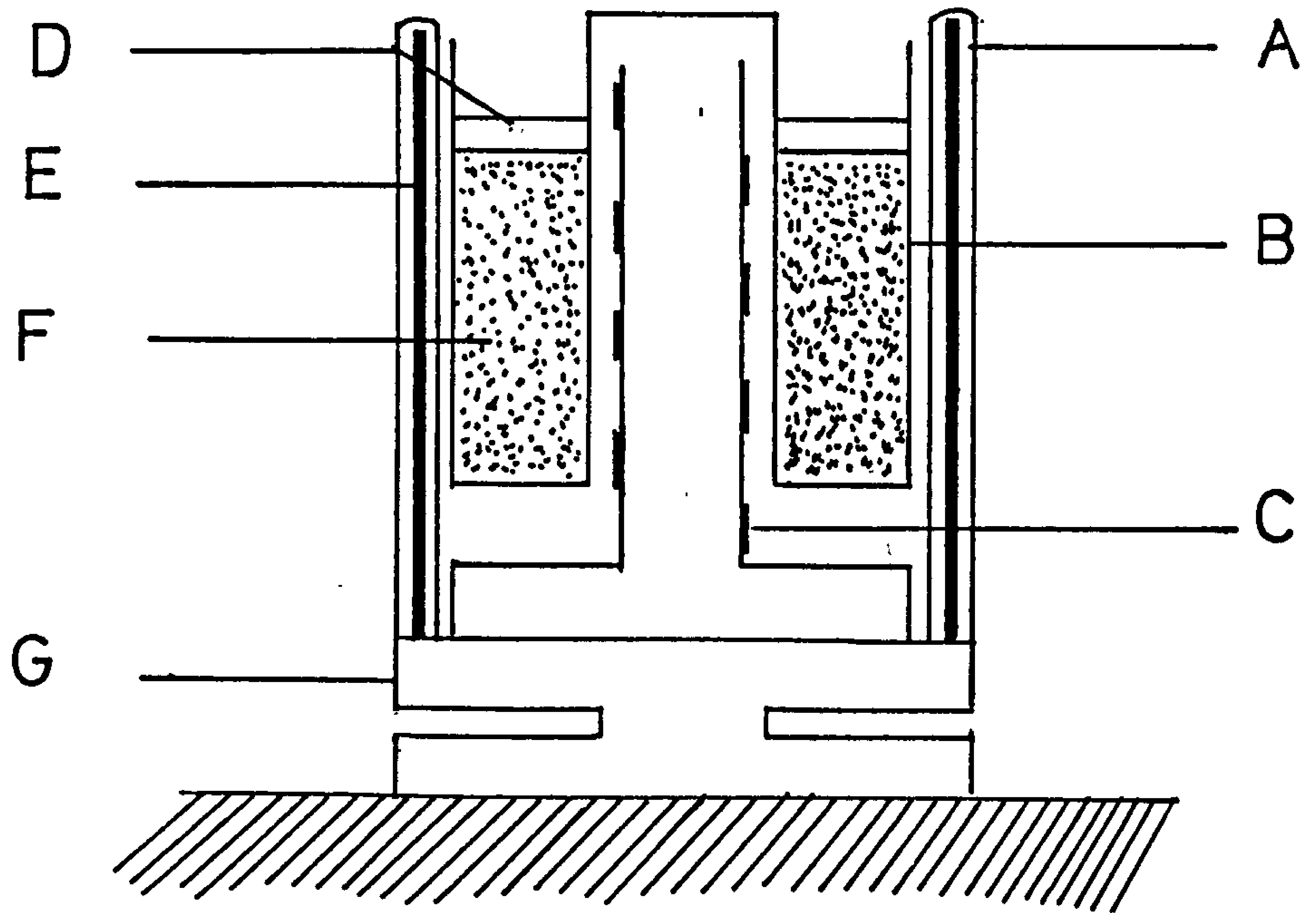

Fig.(4.2) Source container and heater
A. Quartz tube
B. Quartz crucible
C. Molybdenum heating element
D. Quartz wool
E. Stainless steel shield
F. CdS powder
G. Stand (pyrofolite)

the vapour steam between the source and the substrate, as required.

4.1.2 Substrate preparation

Before any material can be used successfully as a thin film support, it must be adequately cleaned. The proper cleaning technique depends on the nature of the substrate, the nature of the contaminants, and the full role of the substrate in the final structure. In this project, copper sheet was used as the substrate material. In its initial form, the surface was assumed to carry contaminants from manufacturing procedures and human contact including dust and grease particles. To provide a substrate suitable for use in a photovoltaic cell it was not only necessary to make the surface clean enough to ensure good adhesion of the CdS layer but also to provide a good, low resistance electrical contact to this layer. To ensure that both requirements were met, great care was taken over the substrate surface preparation. The copper foil was first cut into sheets of approximately 5 x 4.5 cm^2 in area and immersed in a beaker of carbon tetrachloride solution. This was put into an ultrasonic bath for a few minutes. The substrate sheets were then rinsed in hot distilled water and subsequently etched in dilute nitric acid for 1 minute. After rinsing and drying in distilled water and nitrogen gas respectively, the copper sheets were transferred to the vacuum system for coating with zinc. The zinc material was placed in a molybdenum boat and, after pumping down to 10^{-6} torr, a layer of zinc was deposited with thickness in the range of 0.1 to 0.2 μm in accordance with the results of earlier studies on the conditions necessary to provide a good ohmic contact to the CdS film.

4.1.3 The CdS film deposition process

The deposition of CdS films requires very careful attention as it is particularly important to obtain films with good structural quality as well as with the desired electrical properties. As a result of much experimentation during the course of this project, it was found that the best results were achieved using a source crucible which was half-filled with CdS powder, covered with a thin layer of quartz wool. Using freshly prepared zinc-coated copper substrates, the vacuum system was quickly pumped down to a pressure of less than 10^{-5} torr. The substrate was first heated to 250°C for out-gassing to occur while the shutter still covered the substrate. The hot-wall was also heated up to 250°C while the CdS powder was heated slowly until it became ready for evaporation. During the preliminary heating of the substrate, the hot wall and the source, the pressure in the deposition chamber was initially increased by the out-gassing process but, eventually, the pressure dropped back to less than 10^{-5} torr. The substrate temperature was then reduced to that required for the deposition and the shutter was subsequently opened to allow the CdS vapour to reach the substrate. The hot wall temperature was lowered to 150°C during the deposition to allow preferential condensation of impurities on this wall rather than the substrate. At the end of the deposition of CdS the shutter was replaced back into the closed position and all the heaters were switched off. The system was allowed to cool down to room temperature and then the freshly deposited films of CdS were removed.

Heating the zinc-coated substrate to 250°C before depositing the CdS, has an advantageous effect in addition to promoting out-gassing. As a result of the enhanced interdiffusion of zinc and copper, a brass

layer is formed. This provides high reflectivity for light which reaches the substrate after traversing the Cu_xS and CdS layers in a photovoltaic cell and therefore allows a further useful absorption of photons on the second pass through the Cu_xS layer. The substrate temperature during the deposition of CdS has a strong influence on the properties of the resultant film. The CdS molecules dissociate upon evaporation and should recombine on the substrate. Since the sulphur vapour pressure is slightly higher than cadmium vapour pressure, the deposits will have an excess of Cd. The lower the substrate temperature the greater the amount of excess Cd in the film and hence the lower resistivity. If the temperature of the substrate is very high, Cd atoms may re-evaporate before recombining with sulphur atoms so that the stoichiometry of the deposited CdS thin film depends not only on the stoichiometry of the CdS powder in the crucible but also on the substrate temperature and the evaporation rate (84). The CdS films formed by vacuum evaporation have a wurtzite hexagonal structure with the preferred growth direction being such that the C-axis lies perpendicular to the substrate. With increasing thickness of the CdS layer the degree of preferred orientation of the crystallites in the polycrystalline film is increased. This type of oriented growth yields the columnar structure as shown in figure 4.3. The substrate surface texture and the temperature, and evaporation rate, determine the number of nucleation sites, the statistical distribution of the crystallite orientations, and hence the distribution of grain sizes in the final CdS film (194).

During the course of this project it was found that good quality layers could be obtained using a substrate temperature in the range

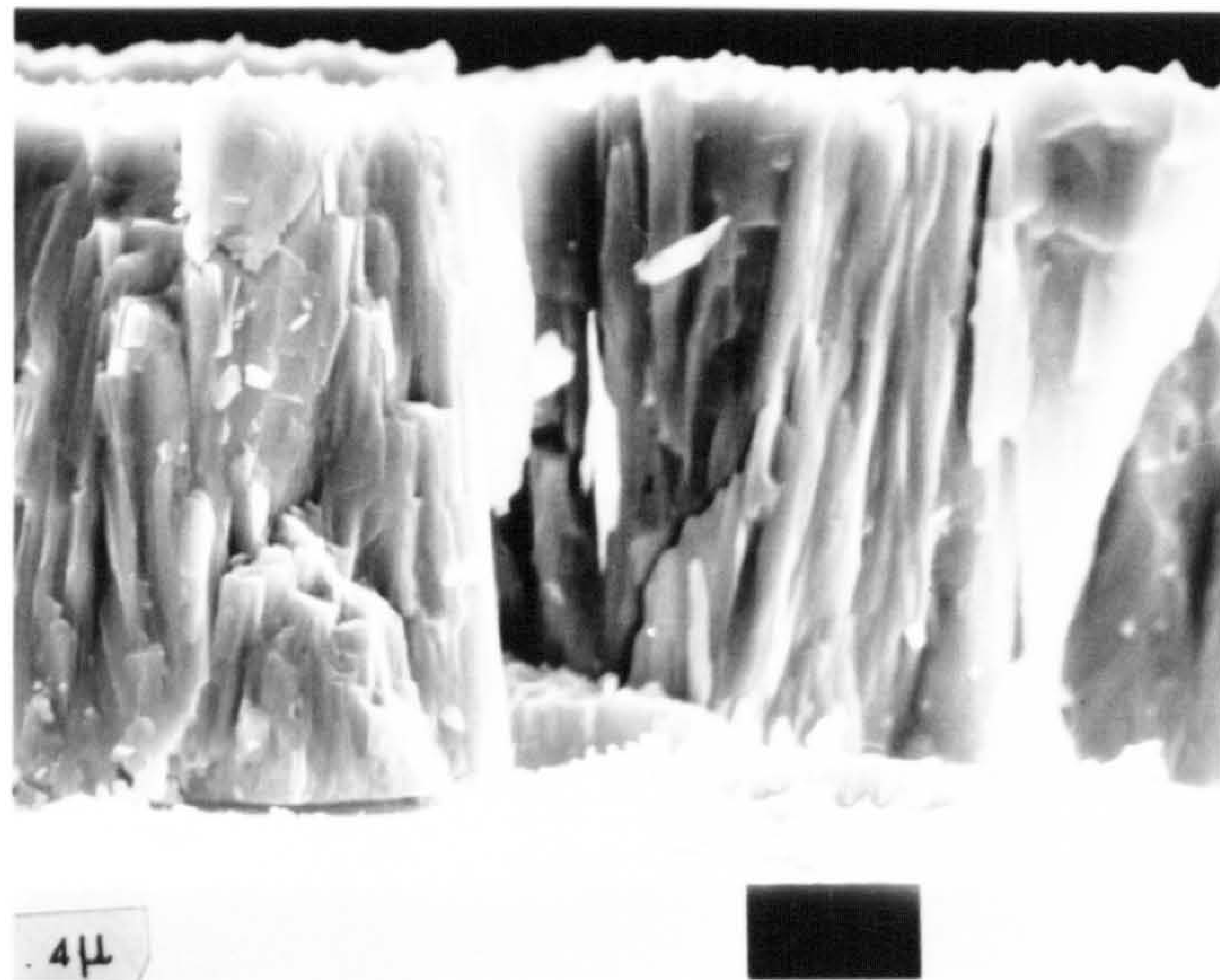

Fig. (4.3): SEM micrograph (cross section) showing vacuum evaporated CdS grain structures, with columnar grains lying approximately perpendicular to the copper substrate.

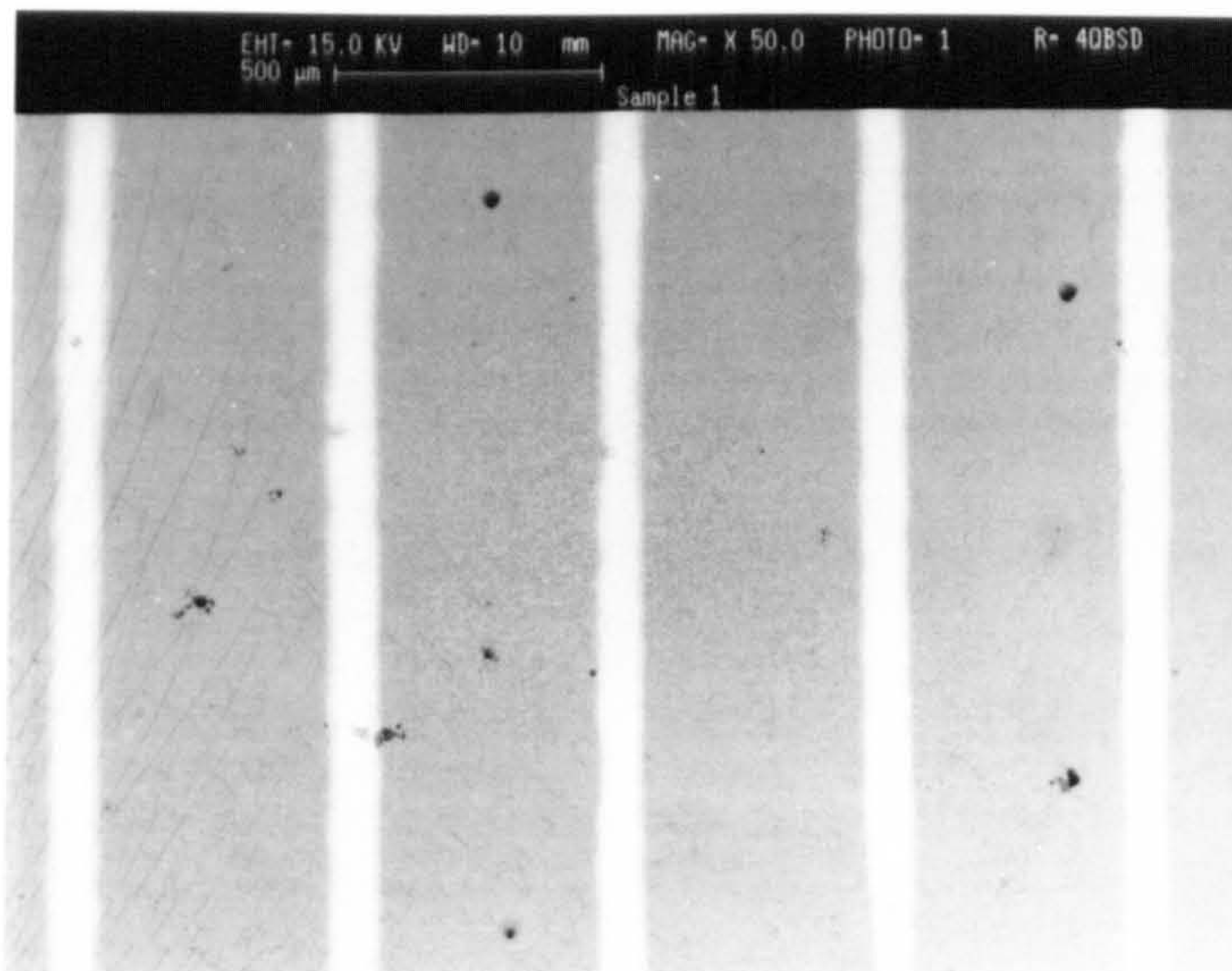

Fig. (4.4): SEM micrograph showing evaporated gold grid (20 line/cm) on the surface of the Cu_xS layer. The line width and spacing distance are ∿ 100 and ∿ 400 μm respectively.

200-250°C with film deposition rates of approximately 1 μm per minute. More information on the evaporation conditions are given in chapter 5.

4.2 Electrical characterisation of CdS layers

The electrical properties which were routinely determined prior to selection of CdS films for solar cell fabrication or associated experiments included resistivity and carrier concentration.

To measure the resistivity of the freshly deposited films of CdS, indium dots were evaporated onto the unetched CdS surface through a mask having several circular apertures with diameters of the order of 1 mm. The total resistance R_T between each indium top contact and the copper substrate was measured directly using a digital multimetze, and the average value for the film R_T was recorded. The resistivity of the CdS layer was then determined from the relation $\rho = R_T \frac{A}{d}$ where A is the contact area and d is the thickness of the CdS layer. (The latter was obtained from measurements of the weight of the substrate before and after the CdS deposition, to determine the mass of CdS in the film.) C-V measurements were made to measure the carrier concentration and the diffusion potential as discussed in section 3.5. Gold dots of approximately 1 mm diameter were evaporated onto the CdS surface. A d.c. power supply was used to provide a reverse bias voltage and the capacitance was measured using a Boonton (model 72B) capacitance meter. By plotting $\frac{1}{C^2}$ against reverse bias voltage the carrier concentration was determined from the gradient of the resultant graph as indicated by the relationship (3.5.13).

4.3 Formation of copper sulphide layers

The p-n heterojunction was formed by immersing the pre-etched CdS in a hot CuCl bath at 95°C for a few seconds to produce a thin film of Cu_xS. The CdS was etched in concentrated HCl for 3 seconds, which was sufficient to reveal the grains by opening up the grain boundaries. This increased the junction area and the light absorption, due to the reduced reflectance of the light resulting from increased roughness of the CdS surface. The formation of Cu_xS takes place by exchange of two Cu^+ ions for every Cd^{++} ion according to the reaction:

$$CdS + 2\ CuCl \ \rightarrow\ Cu_2S + CdCl_2 \qquad (4.2.1)$$

It is well known that the CuCl bath preparation and dipping process is extremely important for the fabrication of efficient solar cells for which the copper sulphide must have a Cu/S atomic ratio > 1.995 (182). Departure from ideal stoichiometry dominates the electronic properties of Cu_xS with both the minority carrier transport and majority carrier conductivity being controlled by the copper deficiency. The deviation from stoichiometry is affected by the presence of small amounts of Cu^{++} incorporated during growth, or by the formation of either cuprous oxide, Cu_2O or cupric oxide, CuO due to exposure to air subsequent to film growth. The divalent copper Cu^{++} ions can be introduced into the CuCl solution by oxidation of Cu^+ by dissolved oxygen as follows:

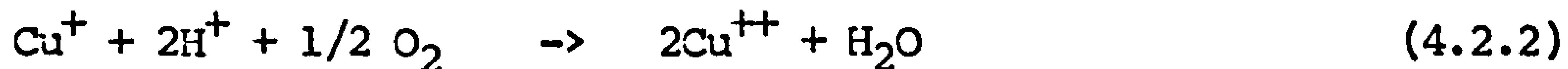

$$Cu^+ + 2H^+ + 1/2\ O_2 \ \rightarrow\ 2Cu^{++} + H_2O \qquad (4.2.2)$$

In order to inhibit this reaction, the CuCl bath was prepared in the following careful manner. Distilled water was used with nitrogen gas bubbling through it for up to 2 hours prior to application. Approximately 100 ml of water was heated to boiling temperature and then reduced to 80°C while 11 ml Hydrazine, 13 ml Hydrochloric acid,

and Ø.5 g of purified CuCl were added. With the aid of a pH meter, the solution was adjusted to pH = 4 and after allowing the temperature to stabilize at approximately 95°C the CdS layers were etched in concentrated HCl for 3 seconds, washed in distilled water and then dipped into the hot CuCl bath. After further washing to remove unwanted reaction products from the surface, using oxygen-free distilled water, the films were dried in nitrogen gas. In general the growth of Cu_xS at high bath temperatures yields higher Cu/S ratios, partly due to the solubility of oxygen being a decreasing function of temperature, and to the solubility of CuCl increasing with temperature. A further measure needed to avoid the presence of the unwanted cupric ions, in the chemiplating solution concerns the purifying of the CuCl powder prior to use. To remove any cupric ions, the powder was first dissolved in a concentrated solution of HCl. This was then decanted and precipitated in a large volume of oxygen free distilled water. The pale green solution associated with the unwanted cupric ions was removed and fresh water was added to the deposit which was again allowed to settle. This process was repeated several times until the green colour and traces of HCl had been totally removed leaving clear liquid above a clean white powder. Finally this white CuCl powder was rinsed in alcohol and dried under vacuum.

4.4 Characterisation of copper sulphide layers

4.4.1 Sheet resistance measurements

The copper sulphide - cadmium sulphide heterojunction plays the role of an insulating layer between the Cu_xS layer and the CdS layer, which facilitates the measurement of the sheet resistance of the Cu_xS layer. The sheet resistance of this layer was measured by using a linear four-point probe technique as shown in figure 4.5. Four grid lines were evaporated onto the surface of the Cu_xS layer of width L. A current was passed through the outer two grids, and the voltage was measured across the inner two grids which were separated by a distance s. With V as the measured voltage and I the current, the sheet resistance R_s of the Cu_xS layer was deduced from $R_s = \frac{LV}{sI}$.

4.4.2 Electrochemical analysis for determination of thickness and stoichiometry

The thickness and the stoichiometry of the copper sulphide layers were determined electrochemically by cathodic stripping using a cell of the type:

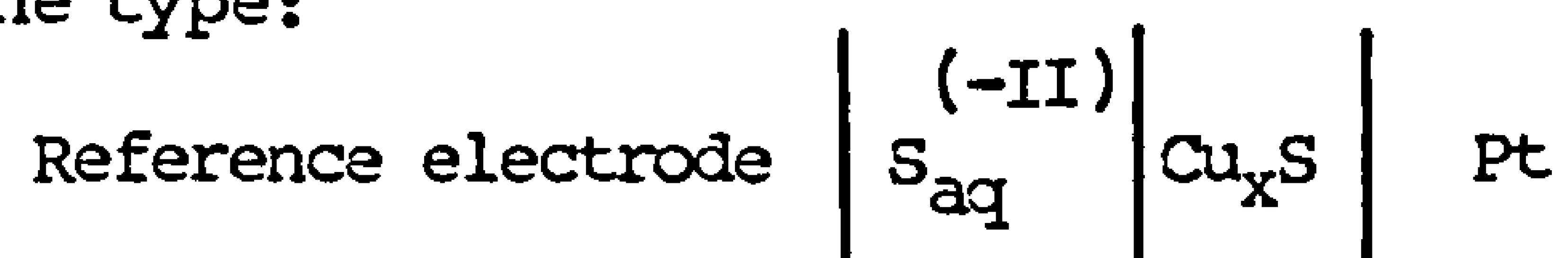

$$\text{Reference electrode} \;\Big|\; S_{aq}^{(-II)} \;\Big|\; Cu_xS \;\Big|\; Pt$$

where $S^{(-II)}$ represents sulphur in a state of oxidation -II dissolved in an aqueous solution of neutral electrolyte. The method was similar to that employed by Castel and Vedel (181) who used a 0.1 M sodium acetate solution having a pH = 8.8 with nitrogen gas bubbling through it to remove dissolved oxygen. The experimental arrangement is shown in figure 4.6. A d.c. power supply produced a constant current between a platinum electrode and the Cu_xS test electrode while the potential of the test electrode relative to a saturated calomel electrode was simultaneously recorded. The reduction takes place in a

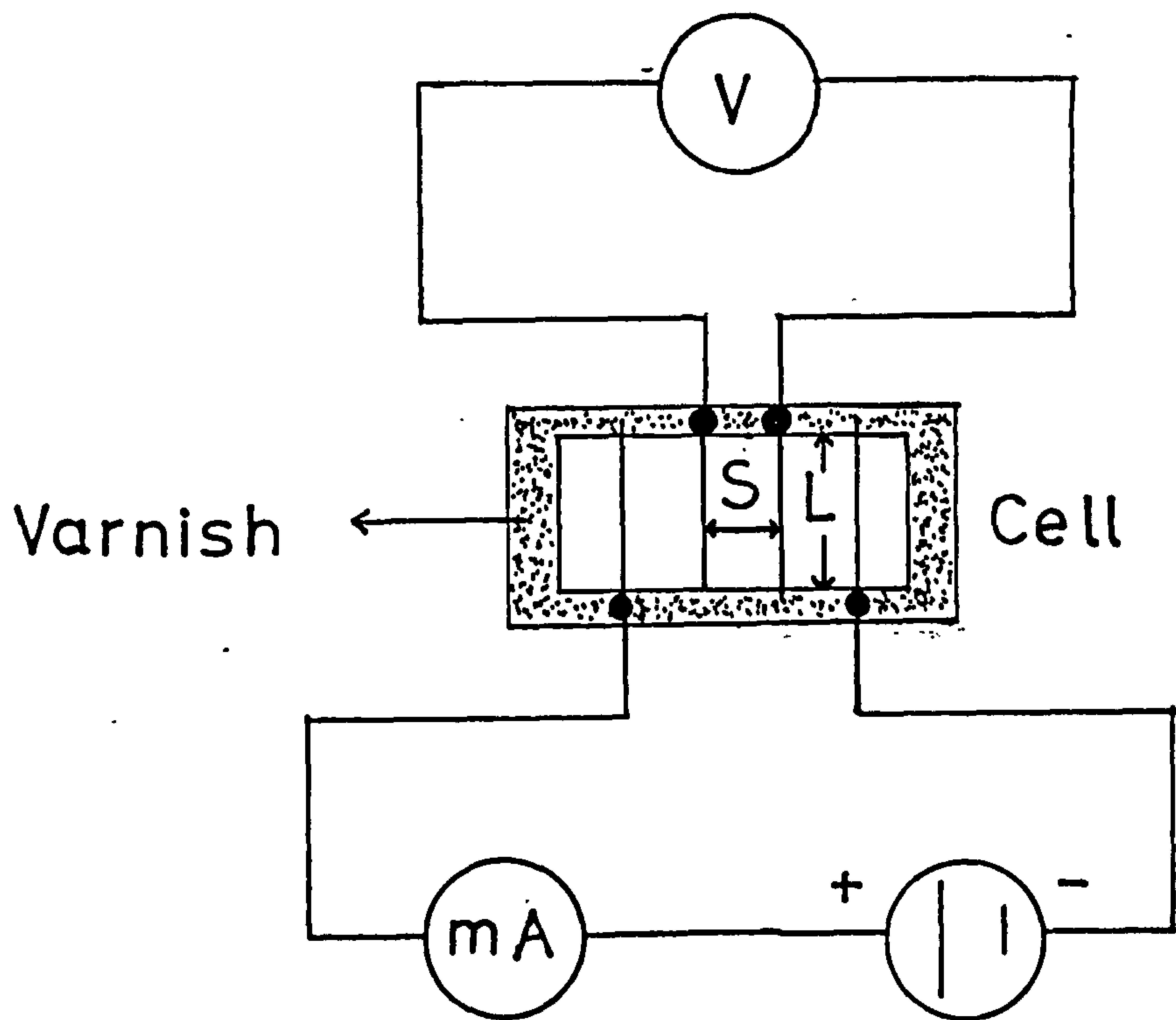

Fig.(4.5) Arrangement for sheet resistance measurement of a copper sulphide layer.

series of steps as can be seen in a typical record of the electrode potential as a function of time as shown in figure 4.7. In the absence of a surface oxide layer, the first step is associated with conversion of Cu_xS to Cu_2S:

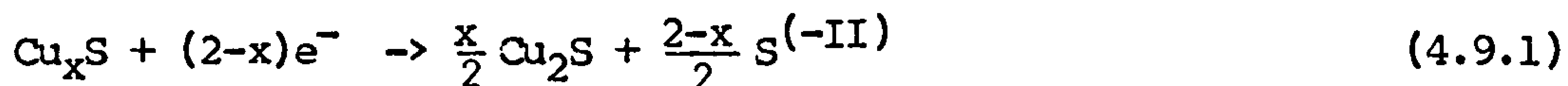

$$Cu_xS + (2-x)e^- \rightarrow \frac{x}{2} Cu_2S + \frac{2-x}{2} S^{(-II)} \quad (4.9.1)$$

The next step is the subsequent reduction of chalcocite to copper as:

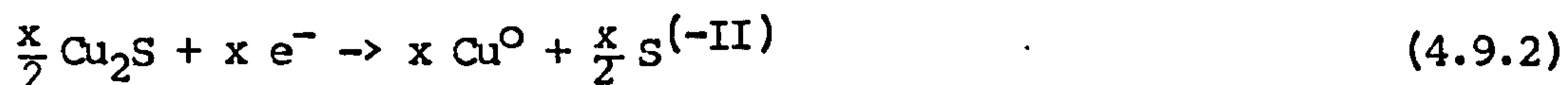

$$\frac{x}{2} Cu_2S + x\, e^- \rightarrow x\, Cu^o + \frac{x}{2} S^{(-II)} \quad (4.9.2)$$

At the end of the first reduction step (4.9.1) the current can be increased by some factor α in order to speed up the process. The deviation of the stoichiometry of the Cu_xS layer can then be calculated from the quantities of charge q_1 and q_2 required to complete the above two reduction steps. Making use of the known increase in current after the first reduction step, the deviation in stoichiometry is given by:

$$\sigma = 2 - x = \frac{2q_1}{q_1+q_2} = \frac{2t_1}{t_1+\alpha t_2} \quad (4.9.3)$$

where t_1 and t_2 represent the time taken for the first stage reduction (4.9.1) and second stage (4.9.2) to be completed. By determining the total amount of charge required to complete the reduction process, the equivalent planar thickness, $\bar{d}$ of the cuprous sulphide layer is calculated from the relation:

$$\bar{d} = \frac{\alpha\, I\, t_2 M}{2F\, \rho\, A} \quad (4.9.4)$$

where M is the molecular weight of Cu_2S, F is Faraday's constant, ρ is the density of Cu_2S taken to be 5.6 g/c.c., and A is the exposed area of Cu_xS. In figure 4.7 which shows a typical titration record

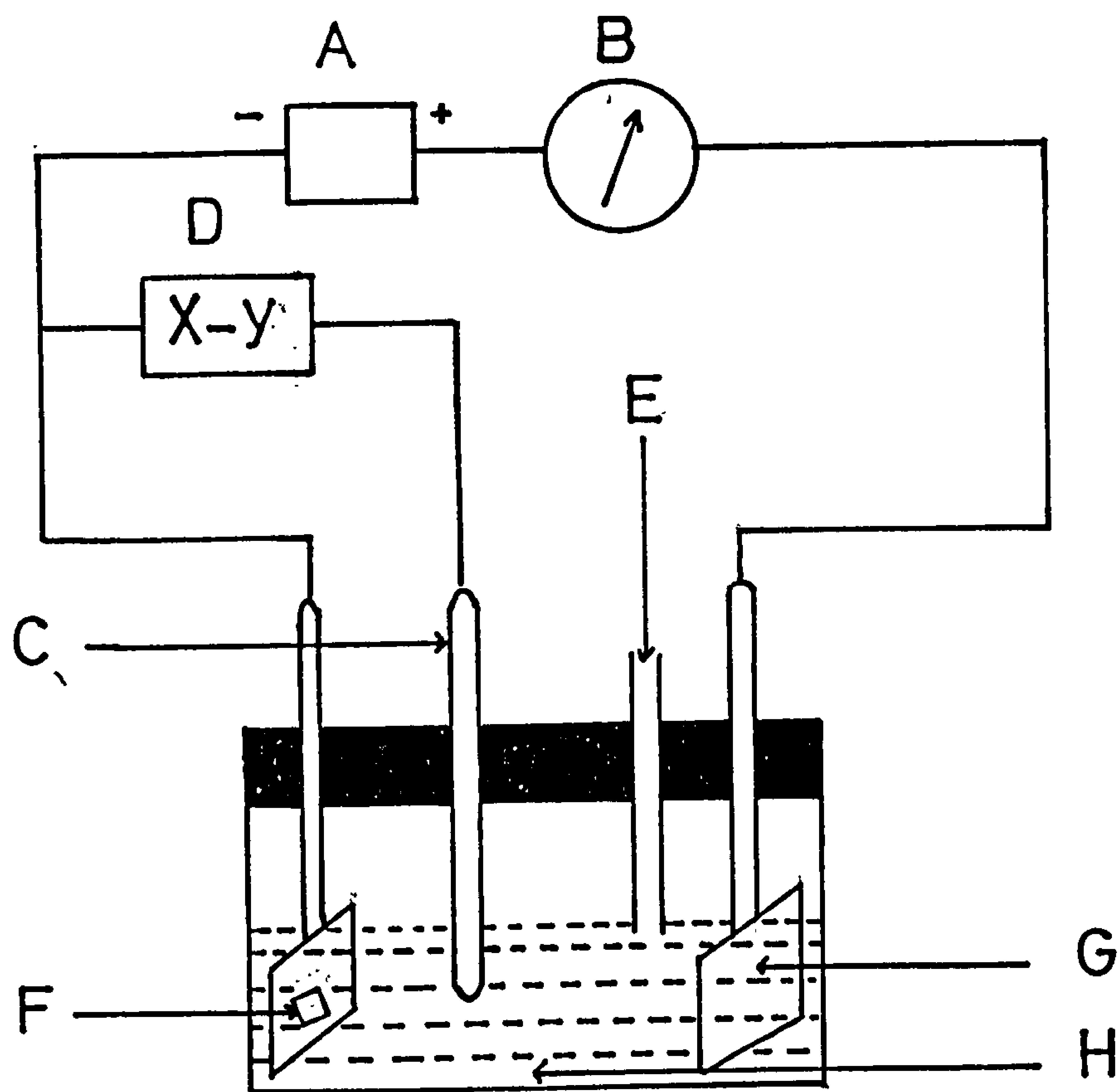

Fig.(4.6) Electrochemical reduction technique for analysis of copper sulphide films.

A. D.C. Voltage supply (300V)
B. Digital multimeter
C. Coloured reference electrode
D. X-Y recorder
E. Nitrogen gas
F. Exposed area of Cu_xS film (cathode)
G. Platinum anode
H. Sodium acetate solution

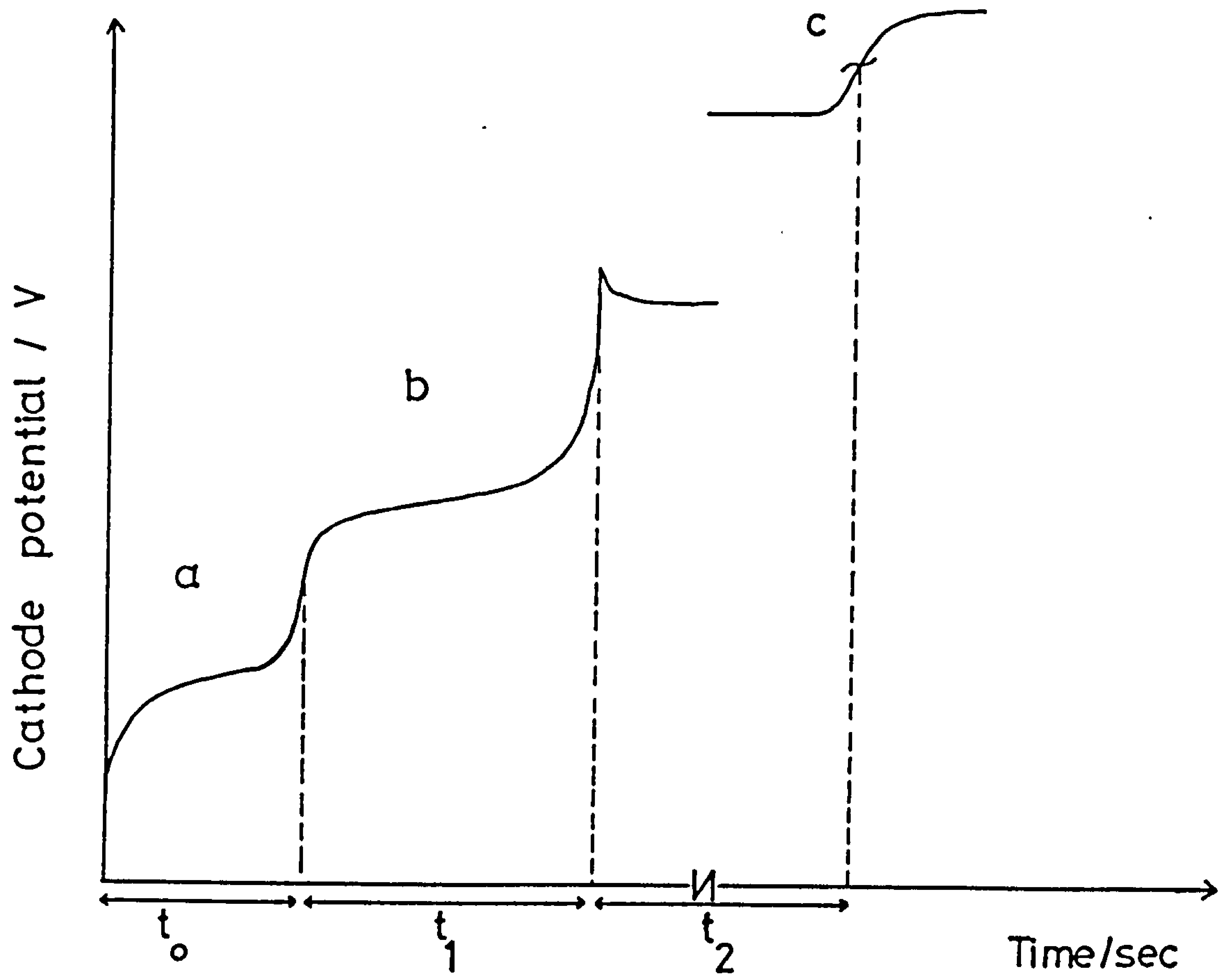

Fig.(4.7) Typical solid state coulometric analysis titration obtained for Cu_xS formed on vacuum evaporated CdS.

obtained for Cu_xS by the process described in section (4.2) on vacuum evaporated CdS, the reduction processes (4.9.1) and (4.9.2) are indicated by the steps (b) and (c). These steps are generally preceded by a step (a) due to the presence of an oxide layer, the reduction of which requires a charge $q_o = I\ t_o$. The relative amounts of oxide and sulphide in the layer are thus given by the fraction $t_o/(t_1 + \alpha\ t_2)$. It is clear that this factor and the deviation from stoichiometry (equation 4.9.3) both depend upon a ratio of measured times. After some trial runs which allow a suitable cell current to be chosen, it is possible to determine the times t_o, t_1 and t_2 with an accuracy of better than 5%. As t_2 is generally much greater than t_1 it can be shown that $\frac{\Delta\sigma}{\sigma} \simeq \frac{\Delta t_1}{t_1} + \frac{\Delta t_2}{t_2}$ so that the deviation from stoichiometry σ can be obtained with an error less than 10%.

Equation (4.9.4) shows that in calculating the effective thickness of the copper sulphide layer $\bar{d}$, the exposed area of the layer must be measured. In practice this exposed region was defined by painting an insulating varnish over the test sample leaving a window with an area ~ 5 mm^2. The dimensions of the exposed window area were determined using a travelling microscope and great care was needed in both the sample preparation and travelling microscope measurements in order to achieve accuracies consistent with those for the reduction times.

4.5 Formation of front contacts

The front contacts to the cells were made by evaporating gold grids onto the Cu_2S surface through a mask yielding approximately 20 lines per cm. A SEM micrograph of the resultant grid structure on the

surface of a CdS film is shown in figure 4.4 indicating a line width of 100 μm and a spacing of ~ 400 μm. The final gold grid lines were connected together by means of a silver paste bus bar attached by using a fine brush. The mask used for the grid evaporation was constructed from thin copper foil which had been etched in dilute nitric acid (30%) for 5 seconds and rinsed in distilled water and trichlorethylene ($CHCl-CCl_2$) before being dried in nitrogen gas. A layer of positive (Shipley AZ-1350) photoresist was spread uniformly over the copper foil and put in a furnace at 80°C for 30 minutes. After cooling down to room temperature a negative print which had been taken from a large scale drawing of the grid design, was placed over the copper foil in front of a UV light and exposed for 2 minutes. This was subsequently developed in (Shipley AZ-351) developer diluted with distilled water for 1 minute. The resultant copper-grid print was baked at 80°C for 10 minutes. Varnish was painted over the area surrounding the grid print before etching away the exposed copper regions in ferric chloride solution. The layer of varnish was then removed by using acetone and the final grid structure was fixed onto the frame onto which a total of six similar grid masks could be mounted.

4.6 Optional cell fabrication and post-fabrication processes

4.6.1 Annealing in different atmospheres

After the formation of the heterojunction between Cu_xS and CdS it is generally found to be necessary to anneal the cell to improve the power output for these devices. Three different annealing atmospheres (hydrogen, vacuum and air) were studied during the course of this project. The annealing atmospheres were found to produce

significantly dissmilar I-V characteristics for the Cu_xS/CdS solar cells. The best results were obtained after annealing in a H_2 atmosphere for between 6-8 hours at 200°C. The hydrogen annealing was carried out in a quartz tube which could be inserted into a furnace which was preset to the required temperature. Prior to insertion into the furnace the quartz tube was connected to a hydrogen supply cylinder via a valve to control the flow rate. In most cases the flow rate was maintained at 2 litres/min during the annealing cycle. After annealing, the quartz tube was pulled out from the furnace and allowed to cool down to room temperature under flowing H_2 before the samples were removed. The vacuum annealing was carried out at a pressure of less than 10^{-5} torr. The Cu_xS/CdS cells were once again mounted in a quartz tube but this was connected to a standard two-stage pumping system. After pumping down to 10^{-5} torr the quartz tube was inserted into a furnace which had been pre-heated to the required temperature. After annealing, the quartz tube was drawn out of the furnace to permit the samples to cool down to room temperature under vacuum. The air annealing was done by putting the samples directly into an oven which was set to the required temperature.

4.6.2 Ion implantation

The ion-implantation technique is employed to dope, in a very controlled way, the near surface regions of a semiconductor, thereby modulating its electrical properties. The system which was used for ion-implantation in this project is illustrated in figure 4.8. The required ion beam was first generated in the ionisation chamber A where a vapour of the desired element was ionised by impact from energetic electrons produced by a hot tungsten filament. (An axial

Fig.(4.8) The implantation system
A. Ion source (Arc chamber)
B. Constant field accelerating tube
C. Magnetic separation.
D. Slit
E. Electrostatic quadrupole triplet lens
F. X and Y shift/scan
G. Primary target
H. Positioning aperture
I. Accelerating column
J. Neutral beam trap
L. Final target at maximum voltage of -200kV

magnetic field constrains the plasma of ions and electrons to travel in spiral trajectories which leads to an increase in the flight path.) The desired ion species was separated from its isotopes and other unwanted ions in the magnetic analyser C. The trajectories of the ions depend upon two parameters, energy and the ratio of mass/charge. As all ions emerged from the source chamber with the same energy, the selection was detemined by the charge mass ratio only. The ion beam thus passed through a slit D which rejected unwanted ions and the remainder were collimated by means of an electrostatic quadrupole triplet lens E. Subsequent electrodes F allowed X and Y shifts before the beam finally passed through a mask to strike the target in the primary target chamber G, if an ion energy of 100 KeV or less was required. The ions could be accelerated further by passing through another set of equipotential planes I to a second target chamber L at a potential up to -200 kV relative to earth. The system allowed samples to be implanted at temperatures in the range 4.2-500K, but in this work the implantation was performed at room temperature.

4.7 Characterisation of Cu_xS/CdS solar cells

4.7.1 The current-voltage characteristics

The I-V characteristics of Cu_2S-CdS solar cells were measured with the aid of a circuit as shown in figure 4.9. The bias voltage was varied manually with the cell either in the dark or under illumination from a light source consisting of a 1000W tungsten lamp with a water filter to provide an approximation to the solar spectrum (195). A Bryans 2600 X-Y recorder was used to record the voltage across the cell and the corresponding current which was obtained by

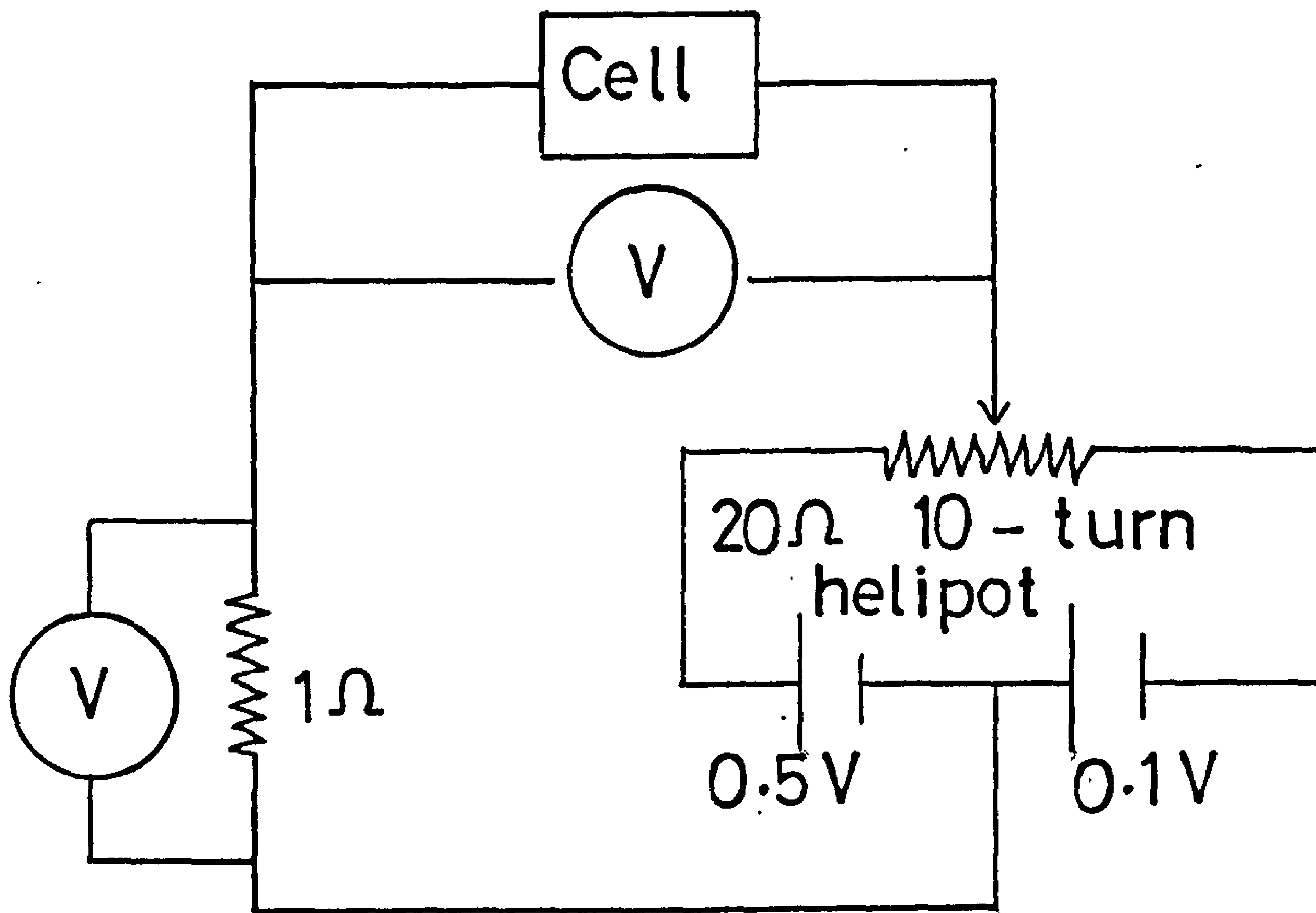

Fig.(4.9) Circuit for measuring current-voltage characteristics.

monitoring the voltage generated across 1 ohm standard resistance. The light intensity was calibrated by means of a standard silicon solar cell.

4.7.2 Scanning electron microscopy

The scanning electron microscope SEM is an electron-optical instrument. The useful application of the SEM ranges from surface studies to bulk analysis and to device fabrication. The history of electron-optical instruments is marked by a number of basic developments including those of Thomson (196) who discovered the existence of the electron, de Broglie (197) who introduced his hypothesis on the wave nature of material particles, and Bush (198) who showed that electric and magnetic fields possessing axial symmetry can act as lenses for electrons and other charged particles. In this work a Cambridge Scientific Instruments stereoscan 600 SEM was used. This provides magnification ranging from X20 to X50,000 representing a scanned area on the sample ranging from 6 mm x 5 mm to 2.4 μm x 2 μm. The samples were cut down to an area $\simeq 2 \times 2\ mm^2$ and fixed by silver paste onto a holder which could be positioned at any angle between $0-90^o$ relative to the electron beam. After pumping down to 10^{-5} torr the electron gun was focused onto the surface of the sample producing an image of the surface on the video screen. This image could be recorded photographically. In this project the SEM was used to study the grain size, grain structure and the surface texture of CdS films and the formation of the Cu_xS layers.

4.7.3 Photovoltaic spectral response measurements

The photocurrent spectral response measurements were carried out by using a Bausch and Lomb diffraction grating monochromator and a 60

W tungsten light source. The Cu_xS/CdS solar cell was placed in front of the monochromator exit slit and connected to a 1 ohm standard resistance. The voltage across this resistance was fed to a low-noise amplifier (Brookdeal type 450) and passed on to a phase sensitive detector (type 411). The output from which was coupled to a potentiometer recorder. The cell was illuminated normally by light in the wavelength range 0.4 μm to 1.1 μm. This was modulated by passing through a light chopper unit (Rofin model 7501). A Wratten 88A filter was used to eliminate second order illumination for wavelengths higher than 0.78 μm. For monitoring the spectral response of the open-circuit voltage the Cu_xS/CdS solar cell was directly connected to the chart recorder. The photovoltaic spectral response measurements could be performed with no background illumination but for some experiments a controlled secondary excitation source was employed. This was provided by an unmodulated tungsten lamp in conjunction with a second Bausch and Lomb monochromator.

4.7.4 The cathodoluminescence system

The system which was used to excite and detect the luminescence from various Cu_xS/CdS samples is shown in figure 4.10. The cathodoluminescence was excited using 5 μA cm^{-2}, 10 keV electron beam from an electron gun positioned at an angle of 45° relative to the sample surface. The samples were placed in an evacuated chamber on a rotating metal finger which could be cooled with liquid refrigerants. The emission from the surface of the sample passed through a window in the cryostat and was focussed by two quartz lenses onto an adjustable mirror which reflected the light through 90° onto the entrance slit of a Hilger and Watts Monospek monochromator. This had a focal length of

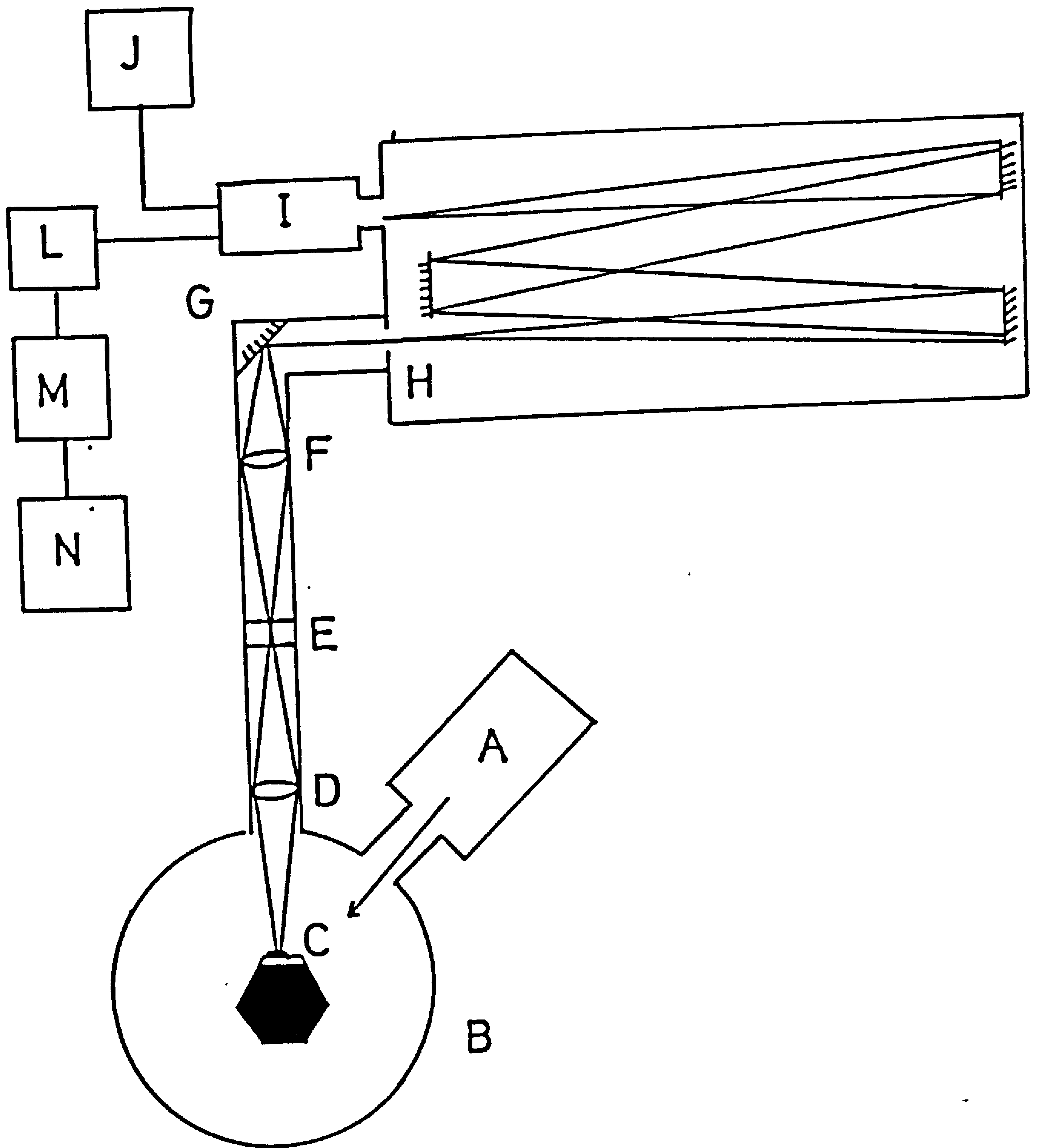

Fig.(4.10) The optical system used for the excitation and detection of luminescence

A. Electron gun
B. Cryostat
C. Sample
D.F. Collecting lenses
E. Programmable chopper unit
G. Mirror
H. Spectrometer entrance slit
I. Photomultiplier tube
J. Photomultiplier EHT supply
L. Low-noise, wide-band amplifier
M. Phase sensitive detector
N. Recorder

1 m and employed a 600 line mm^{-1} grating which was blazed at 1 μm and had a resolution of 8 A° for green and 16 Å for infra red emission, for a slit width range 1-2 mm. The light which passed through the monochromator was detected by a photomultiplier, the output of which was fed into a Brookdeal low-noise wide band width amplifier and then into a Brookdeal phase sensitive detector. Photomultiplier types EMI 9553 and EMI 9684B were used for the green edge and infra red emissions respectively. All the spectra were recorded at 77 K.

4.7.5 Rutherford backscattering technique

Rutherford backscattering (RBS) is a fast and nominally non-destructive technique for analysing the nature and distribution of elements in the near-surface region of a sample. The technique requires the use of a beam of light, positively charged monoenergetic particles. In this study, 400 keV protons were used. The protons striking the sample surface undergo a series of energy loss processes. Firstly, they interact with the electron clouds surrounding the target nuclei and are slowed down without being deflected. Secondly, when in the vicinity of a nucleus, the Coulomb repulsive force between the charged particles will cause the proton to be deflected with an energy which is dependent on the size of the target nucleus and the scattering angle. It is this feature which makes it possible to identify the atoms involved. For a head-on collision, it can be shown that the protons are deflected back along their incident path with an energy E_1, given by:

$$E_1 = E_o \left(\frac{M - m}{M + m}\right)^2$$

where E_o is the incident energy of the protons and M and m are the mass of the target nucleus and proton respectively. Clearly, the larger the mass of the target nuclei, the larger the energy of the backscattered protons. Finally there is a further loss of energy as the protons move back to the sample surface before being collected.

The RBS facility in this department (figure 4.11) consisted of a 400 keV van de Graaff proton accelerator capable of producing up to 10 μA of protons (before collimation). The beam energy was stabilised at ± 2 keV by a feed back system and the collimated beam could be directed at varying angles of incidence onto the surface of test samples mounted in the scattering chamber under high vacuum. Protons which were backscattered from the target were detected by a thermoelectrically cooled annular silicon surface barrier detector. Proton induced x-rays could be monitored with a Si(Li) detector. After pulse shaping and amplification, the spectrum was displayed on a Canberra 8100/e multichannel analyser (MCA), and the output could then be stored in a computer or transferred to a plotter. Before mounting a Cu_xS/CdS test cell in the (RBS) chamber, it was first fixed to an aluminium disc with silver paste. The disc was then mounted onto the sample holder on a three-axis goniometer and the system was then vacuum pumped to less than 10^{-6} torr. The proton beam current normally used was in the range of 10-30 nA.

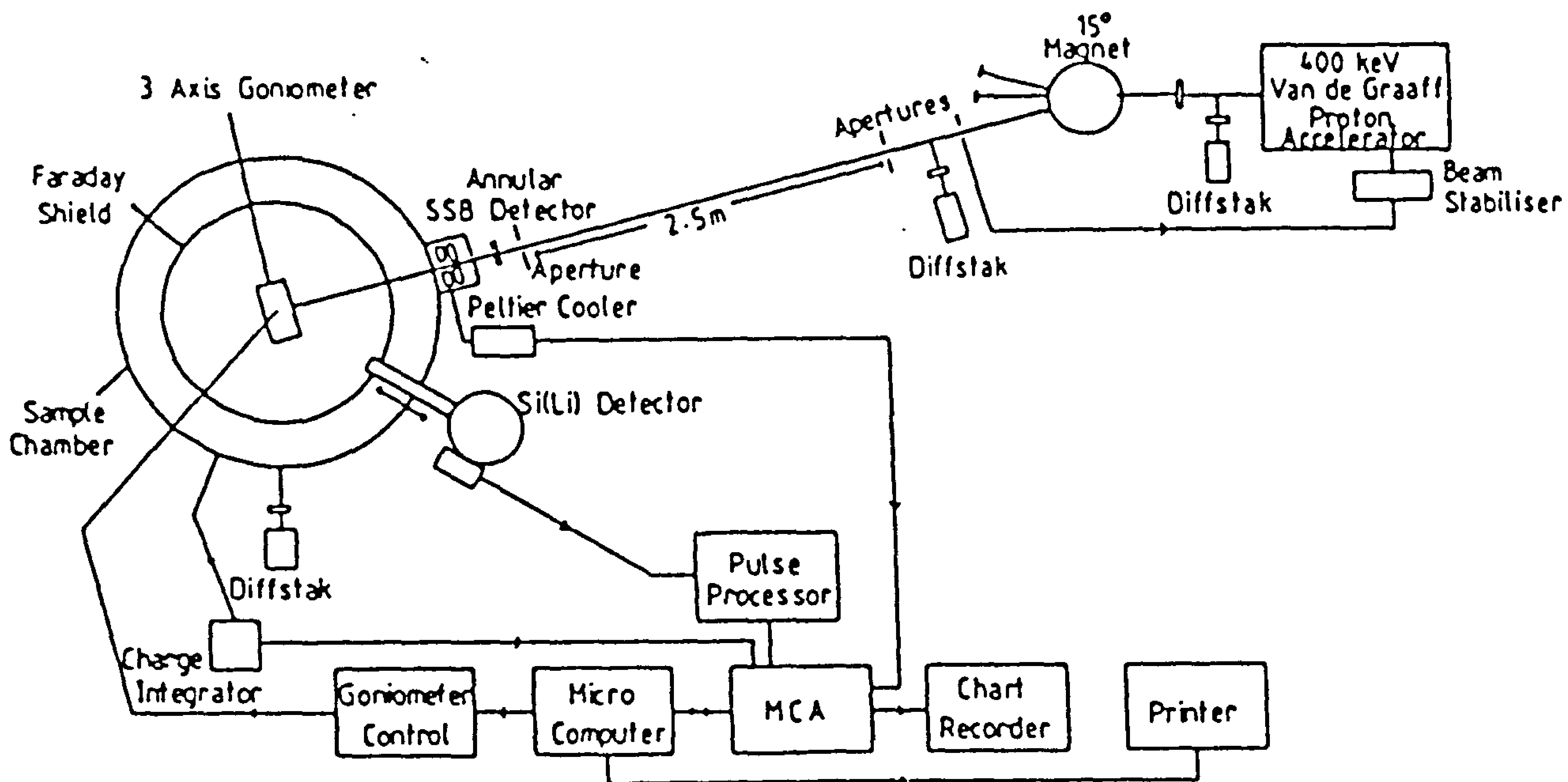

Fig.(4.11) Rutherford backscattering technique (RBS).

CHAPTER FIVE

EXPERIMENTAL RESULTS AND DISCUSSION

5.1 Structure and properties of the CdS layer

5.1.1 Substrate preparation

On several occasions in the earlier sections of this thesis, attention has been drawn to the sensitivity of the Cu_xS/CdS cell characteristics to the structure and properties of each individual component of the cell. In the case of the metal substrate, this component plays a passive and relatively minor role in the operation of the cell, but it became clear during the early stages of work on this project that the substrate is very important in determining the eventual properties of the cell. As this is the foundation on which the cell is constructed, it is not surprising to find that any defects present on the substrate surface tend to generate defects in the subsequently deposited layers and these adversely affect the cell performance and reproducibility. As this study has involved comparisons between cells subjected to different treatments, great importance has been attached to the development of fabrication techniques capable of providing cells with reproducible characteristics. Substrate preparation is of course, the first stage of the cell fabrication process.

As noted in chapter 4, the substrate material employed for this project was zinc-coated copper foil. Details of the basic procedure for cleaning and etching the copper foil and for evaporating a layer of zinc were given in section 4.1.2. This procedure was based on practices developed during the course of earlier studies in this department and modified in the light of experience gained during the

early part of the programme now being described. The major problem associated with the substrate preparation procedure revealed itself by the presence of clearly visible defects in some of the subsequently deposited CdS layers. Under an optical microscope, these defects appeared as a random distribution of black dots over the sample surface. At first, it was not known if these defects arose from the substrate or were due to some impurity which was incorporated during the CdS deposition. In order to determine this, a CdS deposition run was made with glass and other substrate materials placed in the substrate holder as well as Zn/copper foils. Subsequent examination of the CdS surfaces revealed no sign of the black dots for the CdS films deposited on glass indicating that the problem was associated with the copper/zinc substrate. When the copper foil was examined under a microscope, numerous narrow lines were found on the surface probably due to damage created during the foil fabrication process. Believing that this damage, could be a source of impurity, an attempt was made to eliminate the problem by more careful preliminary cleaning. This was unsuccessful and the black shiny dots remained even after the substrate was given a polish with Brasso before being washed and etched in nitric acid for different lengths of time. The problem was finally traced to the Zn layer. The problems of achieving a uniform distribution of zinc over a large substrate area had previously been noted and great care was required during the zinc evaporation process in order to ensure uniformity when very thin layers were being deposited. It became apparent that for a thickness between 0.1 and 0.2 μm which gave the appearance of uniformity there were probably many small pin holes. During a subsequent deposition of CdS, it is assumed that these pin holes allowed a reaction to occur

between the copper and the sulphur vapour to form filaments of copper sulphide giving rise to the appearance of black dots.

In order to test this proposition, a CdS deposition was made using a zinc-coated copper substrate which had been deliberately scratched in order to form an obvious discontinuity in the zinc layer. The resultant CdS film was found to have a black mark following the line of the scratch. Following this evidence the problem was subsequently found to be eliminated by use of a thicker layer of zinc in the range of 0.2 to 0.3 μm. This resulted in the consistent production of CdS films with smooth surfaces and no black dots. The CdS layers were found to be well adhered to the substrate which provided a good, low resistance ohmic contact.

5.1.2 Effect of different CdS source materials

During the process of developing reliable and reproducible procedures for fabricating Cu_xS/CdS cells, many different types of CdS source material were used for the vapour deposition of the CdS base layers. High purity CdS powders were obtained from the Koch-Light company, General Electric (GE) and Reidel de-Häen, while CdS in tablet form was obtained from Merck. Details of the evaporation procedure have been given in chapter 4 (section 4.1.3) and the effect of variations in the deposition parameters are discussed in the following section (5.1.3). The main problems associated with fabrication of good quality CdS films using the powder sources were associated with fine powder particles being carried directly from the CdS source crucible onto the substrate surface, together with the vapour stream, producing a random distribution of solid particles embedded in the CdS layer. The problem could be diminished by using a slower deposition rate but with the finest powders (particularly the

Reidel de Häen source), some particles were still found in layers deposited at the slowest rate employed (5.5×10^{-3} µm/minute). Greater success in eliminating this problem was achieved as a result of a modification to the heater of the CdS source crucible. Instead of having a heater coil with a uniform density of turns along the axis of the crucible (figure 4.2), the coil was rewound to provide a gradually increasing density of turns towards the top of the crucible. This was to ensure that the rate of evaporation from the CdS source was always greatest in the upper part of the crucible so that the resulting vapour could escape without passing through the remaining powder. A further precaution was a thicker layer of quartz wool to occupy the top third of the quartz crucible. Using this source assembly, and following the deposition procedure outlined in section 4.1.3, the resultant CdS layers were found to have no powder fragments deposited on them using deposition rates up to a certain limit dependent on the particle size in the powder being used. In the case of Reidel de Häen powder, the upper limit was ~ 0.5 µm/minute.

In addition to the differences in particle size and evaporation behaviour, further differences between the various CdS sources were indicated from the luminescence emitted by these sources. Typical cathodoluminescence spectra are shown in figure 5.1 where curve A is for the Reidel de Häen (RH) material, curve B is for a sample of GE powder, and curve C was obtained from a Merck tablet source (MT). Corresponding spectra (A,B,C) obtained for CdS layers produced from these different sources are shown in figure 5.2. These spectra display a number of features which are commonly associated with CdS. The shortest wavelength emission around 490 nm is referred to as the blue edge emission which has been identified as being due to radiative

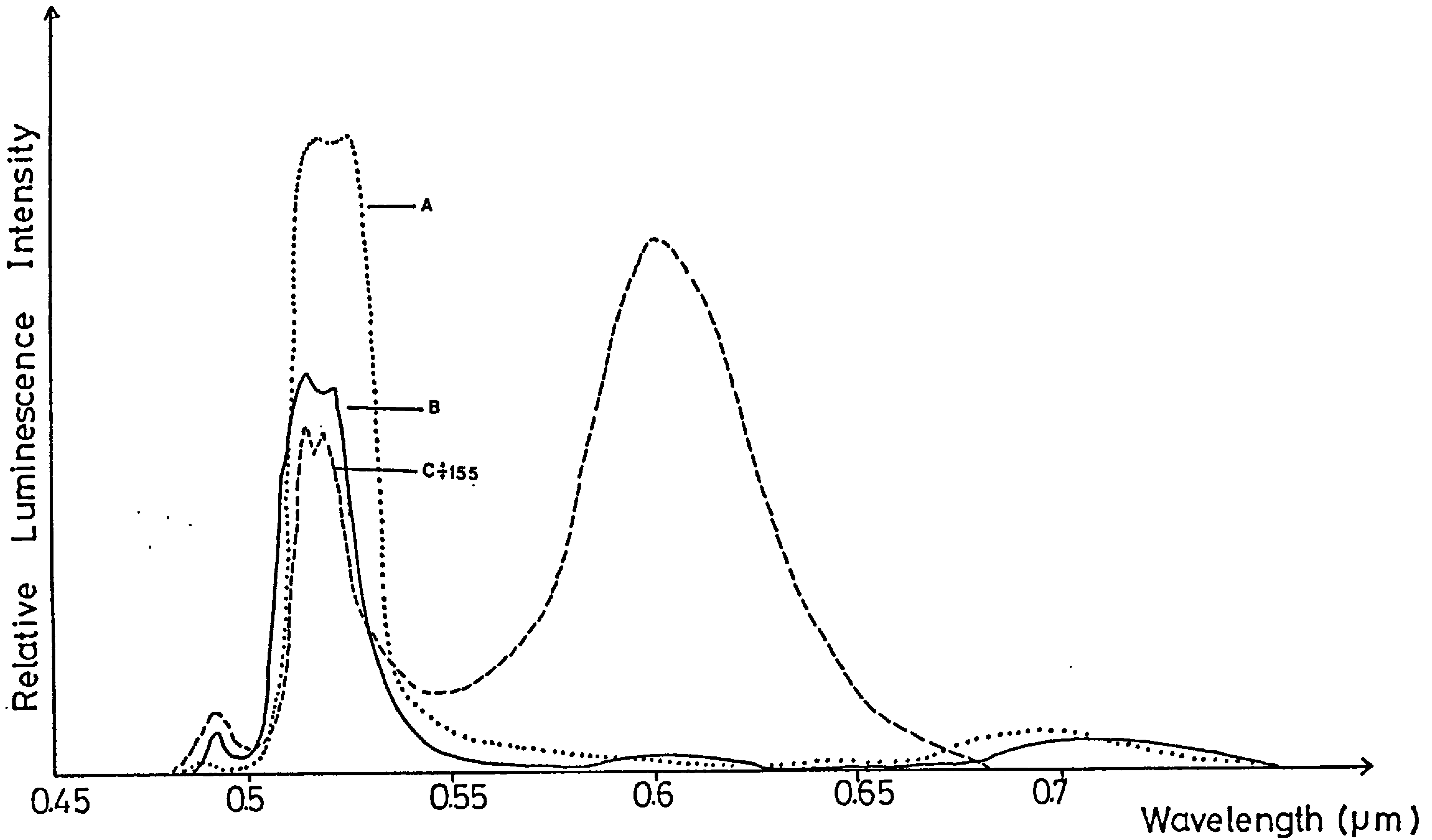

Fig.(5.1) Typical cathodoluminescence spectra for as-received powders of CdS; Curve A represents the emission spectrum for the Reidel de-Haen material, curve B is for the GE powder and curve C is for the Merck tablets.

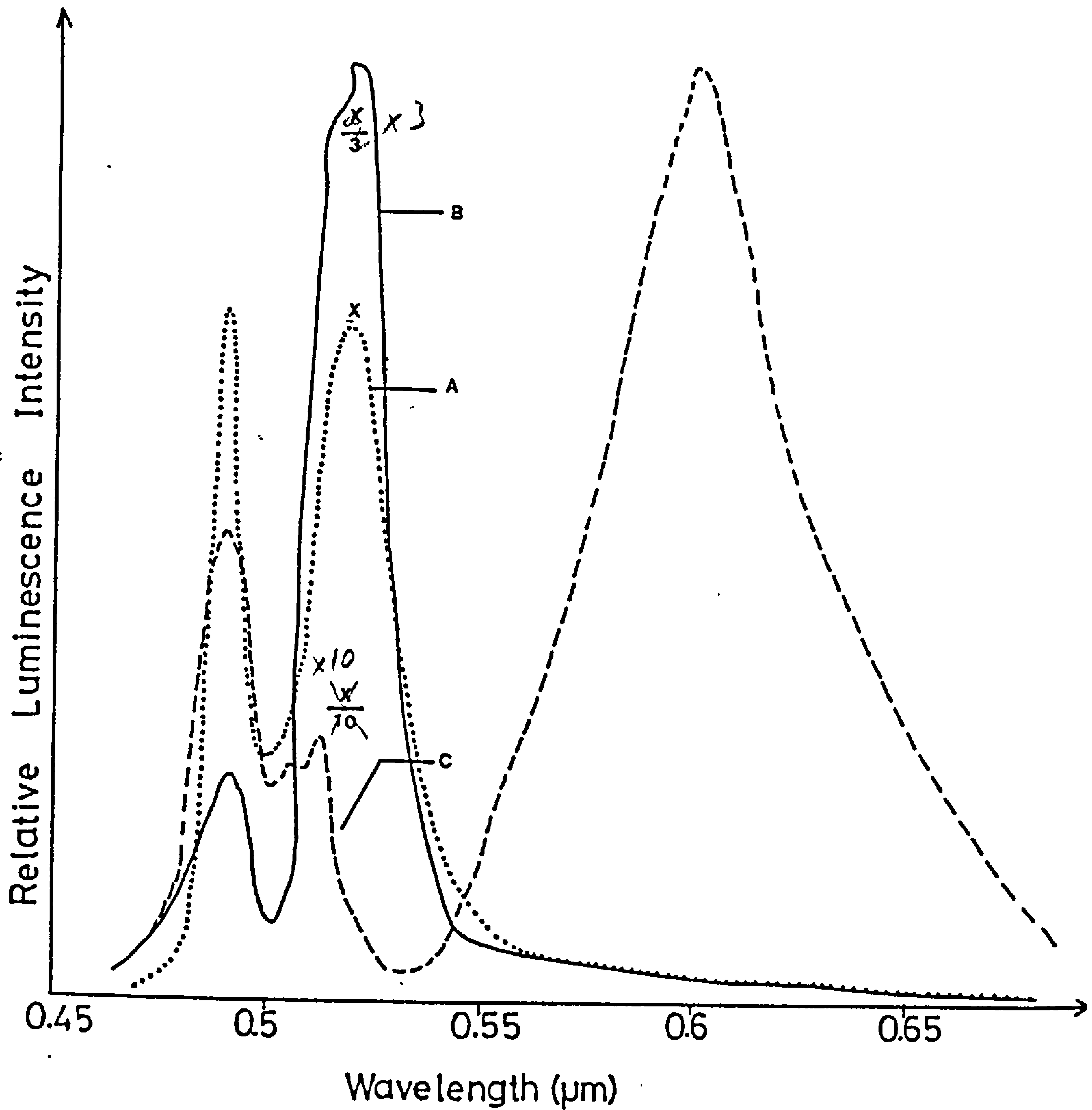

Fig.(5.2) Cathodoluminescence spectra for CdS layers deposited at similar substrate temperatures (200-240°C), using three different source powders. Curve A for film deposited from Reidel de-Haen powder, curve B for film from GE powder and curve C for film from Merck tablets.

bound exciton recombination (199,200). The second strong feature in the vicinity of 520 nm is the green edge emission which has been attributed to recombination of a free electron with a hole bound to a shallow acceptor (201) (native defect, probably the Cd vacancy, or an impurity) or the donor-acceptor pair recombination (202). The longer wavelength broad emission band at ~ 610 nm has been observed in Cd-rich samples (203), and in samples which have been irradiated with electrons of energy sufficient to displace Cd atoms from their regular sites in the CdS lattice (204). Finally, the other broad emission band (centred at ~ 720 nm) is usually associated with a defect-impurity complex centre (205).

Use of the defect assignments referred to above suggests that the MT source, giving a pronounced emission at 610 nm in figure 5.1, contains a stoichiometric excess of Cd as compared with the GE and RH sources. This excess appears to be carried over into the deposited CdS film which also generates a dominant 610 nm emission band (figure 5.2). As it is known that the evaporation of CdS proceeds in such a way as to remove preferentially any excess component (206), it might be expected that the dominance of the 610 nm peak in the emission from the deposited layer might diminish with time, but this was not investigated. The remaining differences between the spectra from these films are less clear and may not be significant in relation to the final properties of cells constructed from them. However, it should be noted that the RH CdS film has the strongest edge emission suggesting that the crystal structure of these films is relatively free of defects, and the emission in the vicinity of ~ 720 nm seen for both the RH and GE powders (figure 5.1) was not present in the spectra from the corresponding evaporated CdS films (figure 5.2), suggesting

an element of purification in the process. Finally, it is interesting to note that those films which display weak edge emission (e.g. curve C, figure 5.2) generally result in low efficiency cells in agreement with Hall (207) and Humenberger's (208,209) observation that cadmium rich CdS films yield poor efficiency.

Of course, for the purpose of constructing photovoltaic cells, it is the electrical properties of these CdS layers which are of most concern. A detailed investigation into the electrical properties of vapour deposited layers and their dependence on the CdS evaporation source was carried out previously in this department (96). This related primarily to GE and KL powders but in subsequent work during the present project, it has been found that different batches of material from the same supplier do not always give exactly similar results so that it is always necessary to carry out a series of tests with a new batch of material and to adjust the deposition conditions as necessary in order to achieve the required properties.

Typical results for films produced from 3 different CdS sources are shown in table 5.1.

Table 5.1 Electrical characteristics of CdS layers formed using 3 different source powders. (Deposition rate 0.4 μm/min; substrate temperature 240°C)

	Resistivity (Ω cm)	Carrier concentration (cm^{-3})
Koch-light CdS (KL)	6020	1×10^{15}
Sintered CdS (GE)	3.5	2×10^{17}
Reidel de Häen CdS (RH)	4	7×10^{17}

Although the results in table 5.1 were obtained for layers produced under identical conditions (with a deposition rate of 0.4 μm/min and a substrate temperature of 240°C) it is clear that the films produced from the different source materials have very different electrical properties. In fact, the table shows differences in the resistivity of approximately 3 orders of magnitude. The variations in resistivity seem to be clearly related to changes in the free carrier concentration which similarly cover a wide range of nearly 3 orders of magnitude. While this suggests that the carrier mobility is not strongly influenced by the source material (indicating that the films involved have a similar structure, at least for the deposition parameters used here) it must be remembered that the measured resistivity is an average value for the full thickness of the film, whereas the carrier concentration is measured at the upper surface. As these films have very non-uniform structures throughout their depth, as discussed in section 3.2.3., use of the relationship $\sigma = ne\mu$ yields only an effective or average value for μ which is expected to be controlled by the more disordered region of the film close to the substrate.

5.1.3 The effect of film deposition conditions

The electrical properties of the evaporated CdS films were found to be very strongly influenced by the deposition conditions. This can be seen very clearly in table 5.2 which shows the effect of the deposition rate on the electrical resistivity and carrier concentration of films deposited onto a substrate maintained at a temperature 240°C from a Reidel de Häen CdS source.

Table 5.2 Carrier concentration and electrical resistivity of CdS films prepared at different deposition rates with substrate temperature at 240°C.

Deposition rate (μm/min)	Resistivity (Ω cm)	Carrier Concentration (cm^{-3})
0.15	6	1×10^{17}
0.35	4	5×10^{17}
0.55	2	1.1×10^{18}
0.75	1	5.85×10^{18}
1.0	0.8	1.07×10^{19}

Table 5.2 shows a steady reduction in the electrical resistivity and a corresponding increase in the carrier concentration as the deposition rate increases. However in this case, the reduction in the average resistivity does not match the 2 order of magnitude increase in carrier concentration for these films. This may be due to a lower average mobility resulting from the increased disorder in the grain structure at higher deposition rates with RH powder as discussed in the previous section.

The influence of the substrate temperature on evaporated layers of CdS, is demonstrated by the results shown in table 5.3 for films produced from a GE CdS source.

Table 5.3 Effect of substrate temperature.

Mean substrate temperature °C	Deposition rate (μm/min)	Resistivity (Ω cm)	Carrier concentration (cm^{-3})
210	1.55	0.4	2.5×10^{18}
260	1.55	205	1×10^{16}

The results in table 5.3 show very significant changes in resistivity and carrier concentration for a relatively small change in substrate temperature of 50°C. For these results, it is particularly necessary to be cautious in comparing the actual magnitudes of these changes in resistivity and carrier concentration. It has been noted previously that the former parameter is an average value over the thickness of the film while the latter is the value at the film surface, but for the results in table 5.1 and 5.2 care was taken to ensure that the films were of similar thickness (≈ 30 μm). However, at substrate temperatures in excess of 250°C, the process of reevaporation of CdS from the growing film becomes sufficiently efficient to prevent the formation of layers of the required thickness. Thus, the thickness of the CdS layers deposited at the high and low substrate temperatures in table 5.3 were 21 μm and 30 μm respectively. In summary, the observed trends in carrier concentration and resistivity under various deposition conditions are in general agreement with results previously obtained in this department (96) and with the reports of some other workers (210, 174). While an opposite trend has been observed in the case of the dependence of film resistivity on deposition rate (84), this observation related to films of less than 5 μm thickness and therefore, as discussed in section 3.2.3, these films are not strictly comparable with the thicker films employed in the present study due to their substantially different grain structure.

5.1.4 CdS surface topography and effects of etching

Although the evaporated layers of CdS have a polycrystalline structure, as discussed in section 3.2.2., the surfaces of freshly deposited layers have a smooth appearance when viewed by eye and, even when examined under an electron microscope, the granular structure is

not very clearly apparent. However, the polycrystalline structure can be revealed by fracturing a layer along a direction perpendicular to its plane and examining the edge of the layer under an electron microscope. As the film tends to break along grain boundaries, the grain structure can be clearly observed and an SEM micrograph for such a fractured layer has previously been shown in figure 4.3. This figure shows very clearly the grain structure with the characteristic columnar grains lying approximately perpendicularly to the substrate. Some indication of the grain size is also provided by such views of the film. However, more satisfactory information concerning the distribution of grain widths across the film can be provided by forming a layer of Cu_2S in the usual way (by dipping the film in a solution of CuCl) and then removing this Cu_2S layer by dissolving it in KCN solution. As previously explained (section 3.3.3) the Cu_2S layer forms preferentially at grain boundaries causing deep protrusions of Cu_2S between the CdS grains. When the Cu_2S is dissolved in KCN solution, the separated grains of CdS can be clearly seen when the surface is examined at normal incidence in a SEM. A typical micrograph indicating an average grain width of $\approx$ 2 μm is shown in figure 5.3.

The deep protrusions of Cu_2S clearly help to trap the light which falls onto a cell during operation and this, correspondingly, increases the current which can be generated. However, additional improvements in the light collection efficiency of the cell can be achieved by further surface texturing. This can be provided by etching the CdS surface in HCl prior to dipping in CuCl solution. The effects of such etching have been investigated by several different

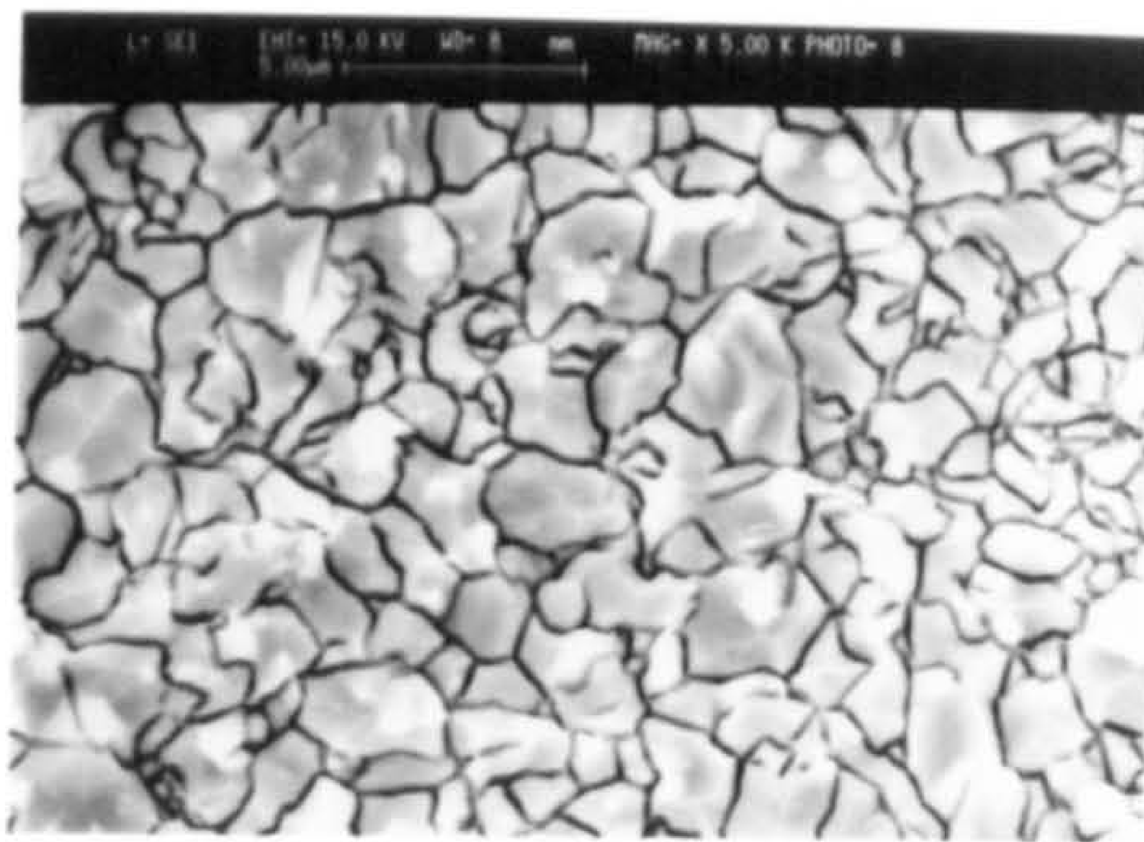

Fig. (5.3): SEM micrograph for Cu_xS-CdS cell after removing the Cu_xS layer by dissolving in KCN solution. The micrograph shows the deep protrusions due to preferential Cu_xS growth in the CdS grain boundaries.

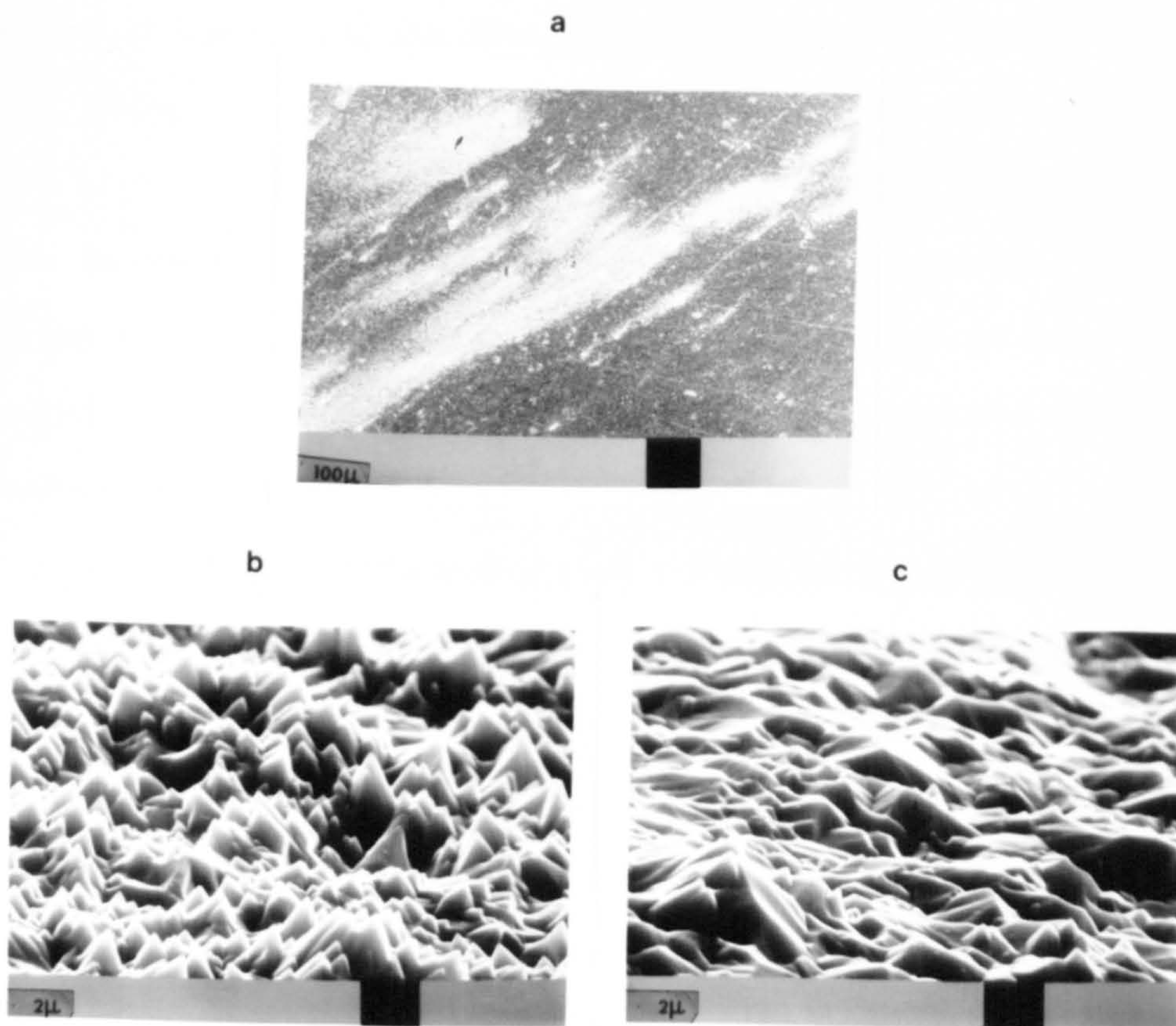

Fig. (5.4): SEM micrographs showing effects of etching for a non-uniform CdS film.
(a) low magnification view showing general patchy appearance (b) high magnification view of the bright region (c) high magnification view of the dull region.

groups (88,211,152,212). The acid attacks the CdS surface anisotropically forming pyramid shaped structures on the upper surface of the crystallites. The rate of attack and the resulting surface topography appears to be dependent on the crystal structure of the initial CdS film as can be seen in figure 5.4 which shows SEM micrographs for a film with a clearly non-uniform structure. The non-uniformity of this film was apparent immediately after etching. When viewed by eye, it was seen to have a patchy appearance and this can also be observed in the micrograph shown in figure 5.4(a) taken at low magnification. Figures 5.4(b) and (c) show higher mangification pictures of the bright and dull regions respectively of the surface in figure 5.4(a). Here it can be seen that the bright area is associated with a higher density of sharply pointed pyramids while the darker region is composed of fewer, larger and flatter pyramids. CdS films with clearly non-uniform surfaces of the type described here were not selected for cell fabrication as they could not be relied upon to give reproducible characteristics.

Figure 5.5 shows the results of a study of the effects of etching for different lengths of time. These scanning electron micrographs are for CdS films which had been etched in a concentrated HCl acid for 0, 3, 10 and 20 seconds at room temperature. In addition to the surface texturing, these films display a relatively large number of deep etch pits. It is clear that the etch pit width at the CdS film surface increases with increasing etch time as observed by Shirland (88) who also found that the depth of penetration of the etch pits increased substantially with time. The appearance of etch pits probably results from structural defects in the CdS films which, in turn could be caused by surface features on the underlying substrate.

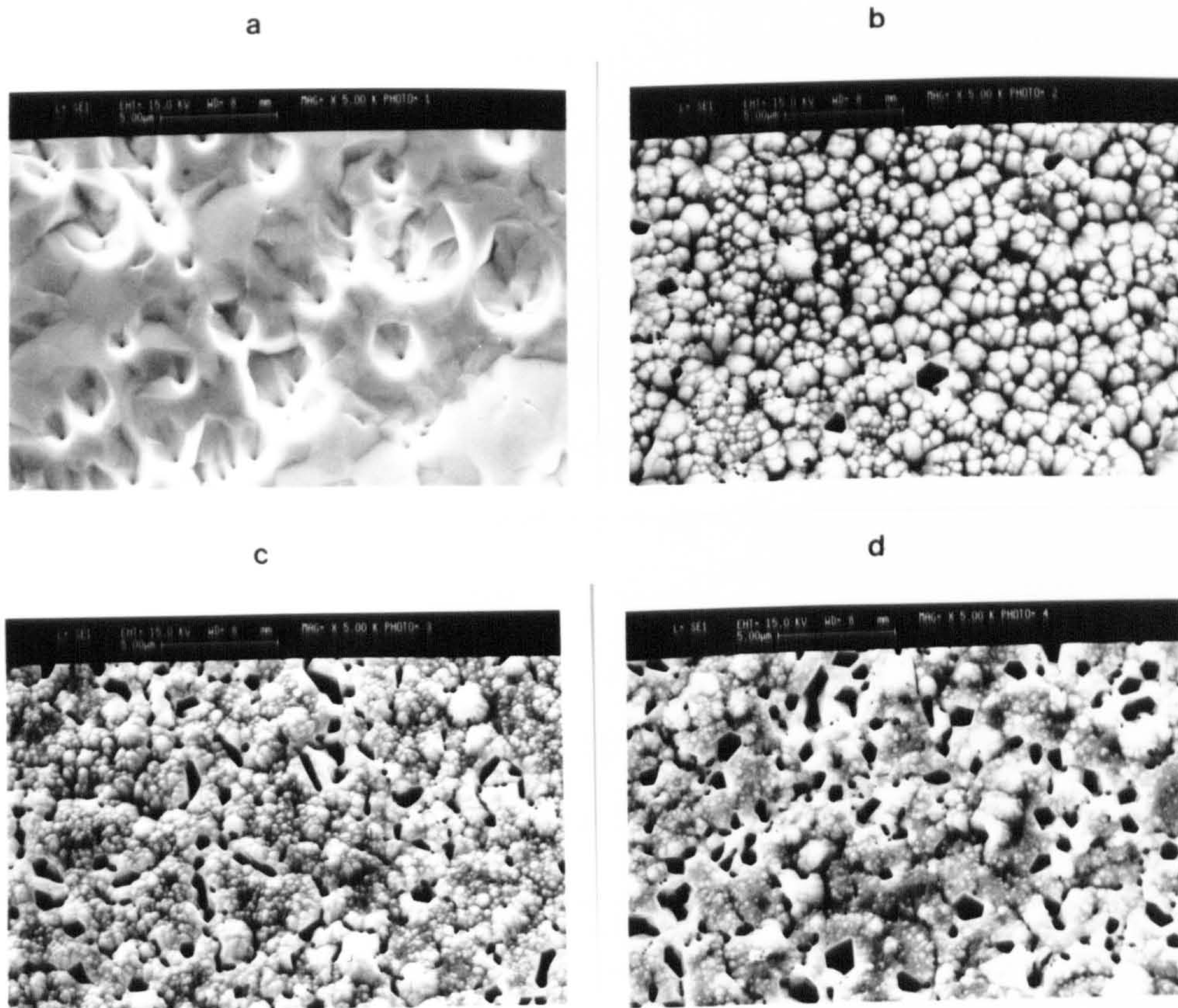

Fig. (5.5): SEM micrographs for CdS film which had been etched in concentrated HCl acid for different times. (a) the surface of CdS film before etching (b) after 3 seconds (c) after 10 seconds (d) after 20 seconds.

Fig. (5.6): SEM micrograph for a film which had been formed on a smooth substrate of copper, after etching CdS film for 5 seconds. (Viewing angle ∿ 30°)

Indeed, it has been found that for CdS evaporated onto a copper foil substrate with a very smooth surface, a significantly different crystallite structure is produced with less etch pits as can be seen in figure 5.6 which shows the SEM micrograph for a film which had been etched for 5 seconds. The difference is also observed in the cross section of the CdS layers. Those layers grown on a smooth substrate have a very well ordered growth of crystallites (figure 4.3) while the cross section for the layers grown on a rough surface has a poorly ordered crystal structure as shown in figure 5.7. These results from figure 5.7 and figure 4.3 indicate very clearly that the degree of roughness of the copper substrate has a strong influence on the etching behaviour of the CdS films, but the film growth conditions can also have an influence, as illustrated in figure 5.8 and 5.9. These SEM micrographs show that the etched surfaces of films grown at two different substrate temperatures (210°C and 260°C). While both samples were etched for the same length of time (3 seconds) and both display the characteristic rounded pyramid type surface structure, it is clear that the sample grown at the lower temperature is more highly textured with a greater density of pyramid features than the sample produced at the higher temperature. It is significant that these samples were from the same growth runs as the samples listed in table 5.3 (previous section) which were found to have very different electrical properties.

A quantitative indication of the degree of surface texturing by etching has been obtained from C-V measurements carried out with Schottky contacts to the CdS layers. For example, figure 5.10 shows results for 2 similar samples which had been etched for different

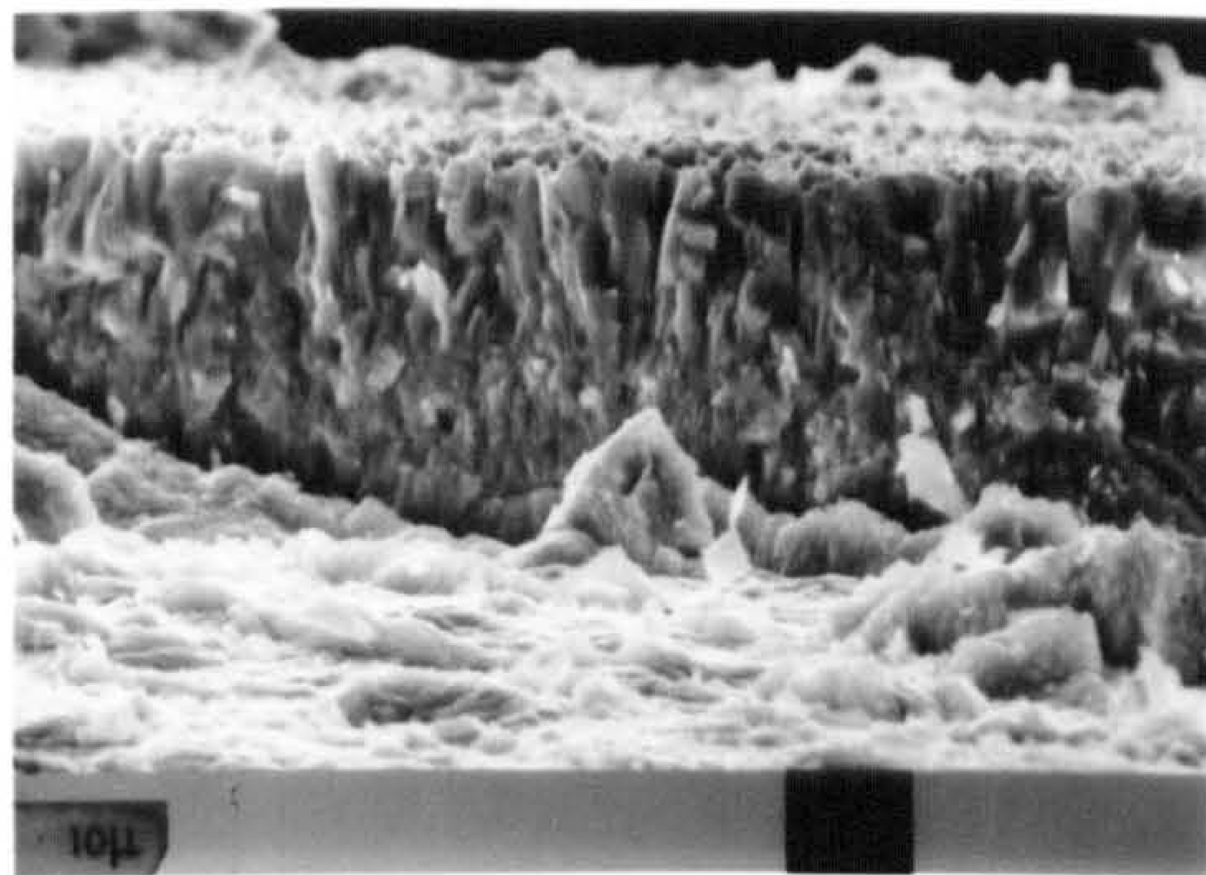

Fig. (5.7): SEM micrograph (cross section) for a CdS layer grown on a rough copper surface.

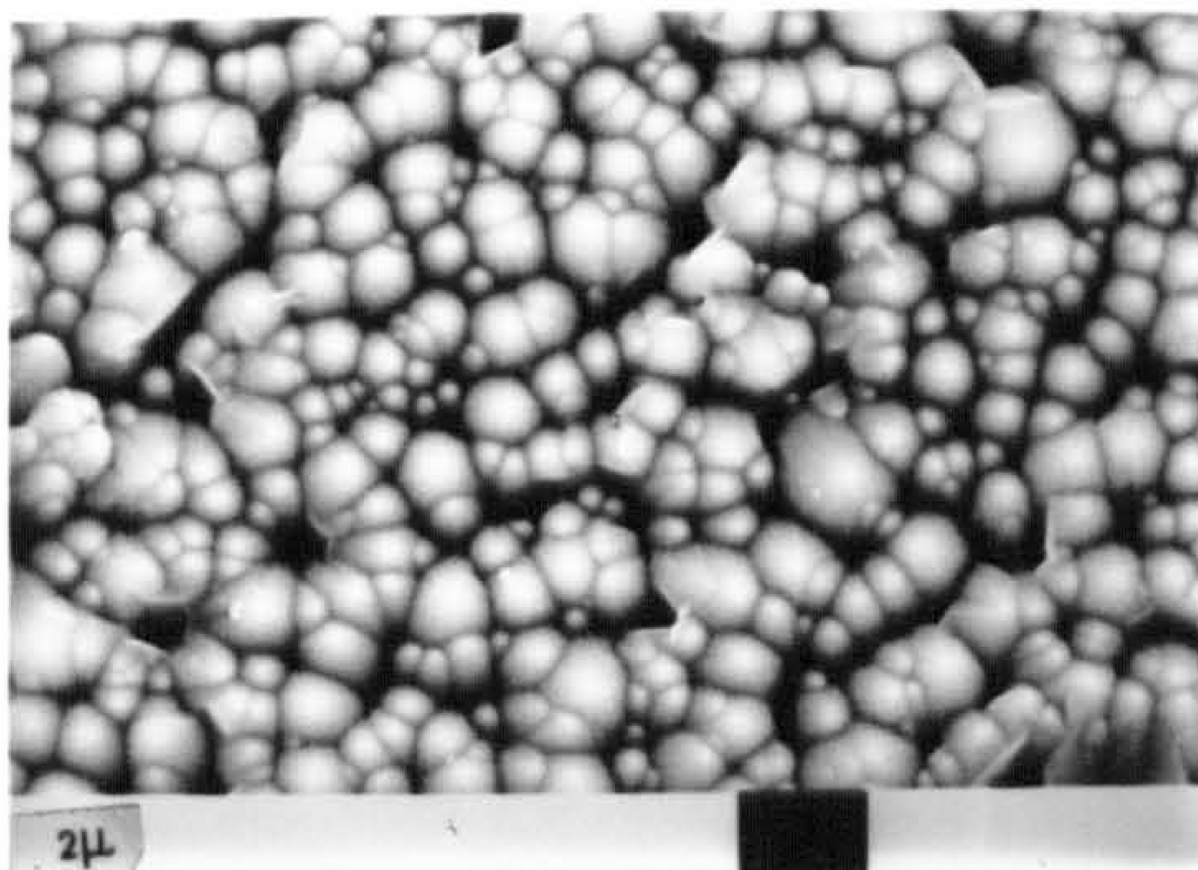

Fig. (5.8): SEM micrograph for a CdS layer which was etched in HCl for 3 seconds. The CdS layer was deposited at a substrate temperature 180-240°C.

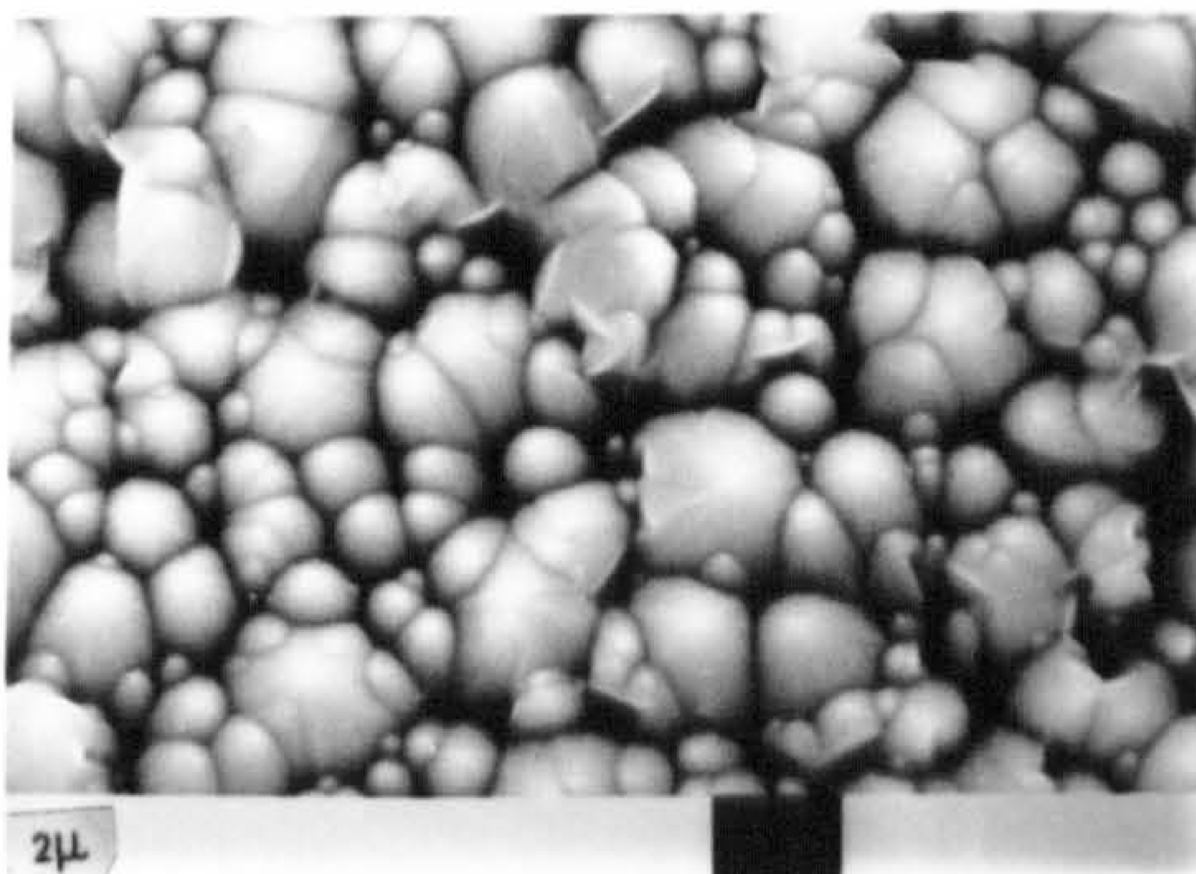

Fig. (5.9): SEM micrograph for a CdS layer which was etched for 3 seconds. This CdS film was deposited at a substrate temperature 220-300°C.

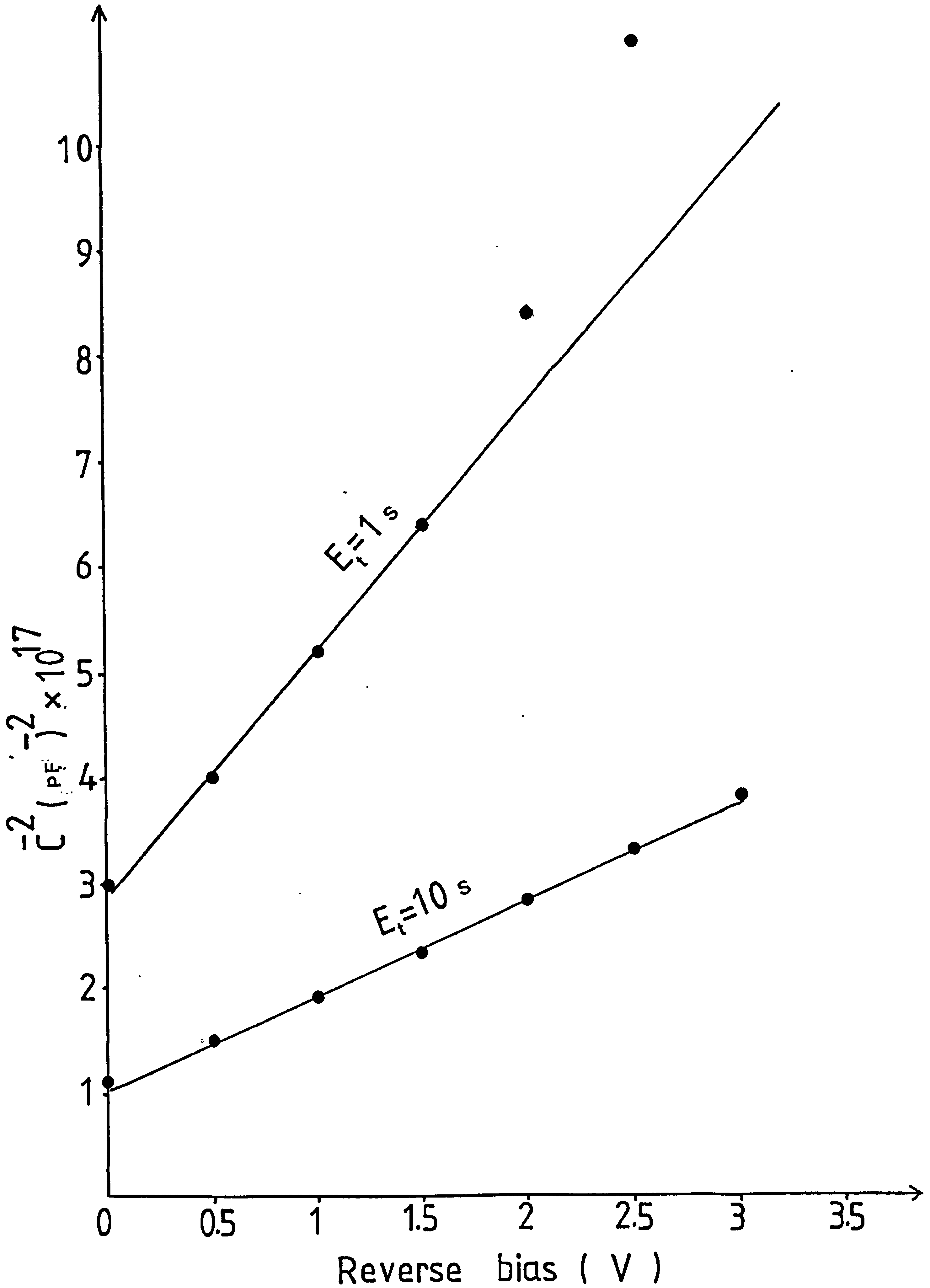

Fig.(5.10) $1/C^2$ against reverse bias V for two similar CdS layers with different etching times of 1 and 10 seconds.

lengths of time (1 second and 10 seconds). The plots of C^{-2} against reverse bias V produce straight lines with slopes giving carrier concentrations for the two CdS films of $1 \times 10^{18}/cm^3$ and $2.5 \times 10^{18}/cm^3$ respectively. However, if it is assumed that the carrier concentration for the two layers are the same (as they were deposited under identical conditions, in the same growth run) the different C^{-2}/V slopes could be attributed to different junction areas between the CdS and the deposited gold contact, due to the different surface texturing. This leads to the conclusion that the 10 seconds etch produces an effective area which is 1.6 times higher than the surface area resulting from the shorter etching time.

5.1.5 Effect of ion implantation

In an earlier study of the use of ion implantation in the fabrication of Cu_xS-CdS solar cells (213), it was found that the presence of implanted copper in the CdS prior to formation of the Cu_xS layer had a significant influence on the growth properties of this layer. The investigation reported here was intended to provide further information concerning these effects and to determine whether there was any associated influence on the stability of the resultant cells. This section gives the results of a brief examination of the effect of ion implantation on the luminescence characteristics of the CdS layer while section 5.3.4 describes the effects on the resultant cell characteristics.

The CdS layers used for implantation studies were produced using Merck tablets as source. These layers were etched for 3 seconds in a concentrated HCl, before being implanted with Cu^+ ions at various energies in the range between 50 and 250 KeV. As implantation is accompanied by damage to the lattice, it is necessary for this to be

removed by annealing. In this case, the post-implantation treatment was carried out for 1/2 hour at 300°C in vacuum. Figure 5.11 shows the CL emission spectrum for an unimplanted film (curve A) together with those for films implanted with 5 x 10^{14} ions/cm^2 at various energies (curves B-F). The spectrum for the unimplanted samples shows the three distinct luminescence bands which were discussed in section 5.1.2 with the band at 610 nm being the dominant feature, as seen in figure 5.2 for films produced from Merck tablets of CdS. It is clear from figure 5.11 that the effect of ion implantation is to reduce the intensity of all three peaks and this effect is seen to become more pronounced as the ion energy is increased.

A similar pattern of behaviour has previously been observed for Cu-implanted CdS films, but for comparative purposes a second set of CdS films was implanted with Zn ions using identical ion energies while maintaining the same constant ion flux. The results are shown in figure 5.12, while figure 5.13 shows the effects of Zn ion implantation using 50 KeV ions for ion doses in the range 10^{14} to 10^{16} ions/cm^2. It is very clear from figures 5.11 and 5.12 that the effects of the implantation (as far as can be seen from the cathodoluminescence) are not dependent on whether Cu or Zn ions are implanted. Thus, it appears that the process of implantation leads to some structural change to the lattice which remains even after post-implantation annealing. The associated effects on later stages of cell fabrication and cell characteristics are discussed in section 5.3.4.

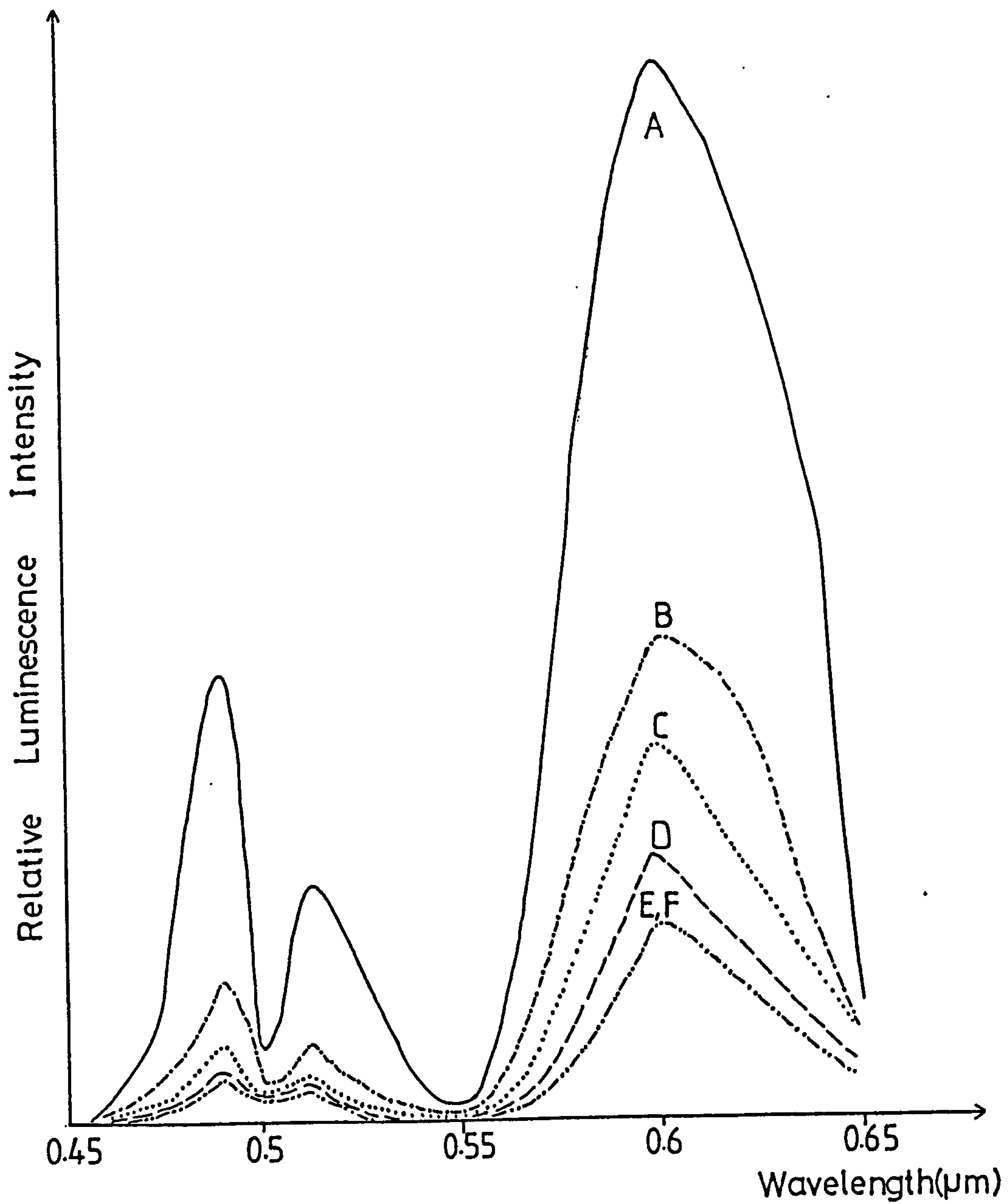

Fig.(5.11) CL emission spectrum for an unimplanted film (curve A) and Cu-implanted CdS films with $5x10^{14}$ ions/cm^2 at 50keV (curve B), 100keV (curve C), 150keV (curve D), 200keV (curve E) and 250keV (curve F).

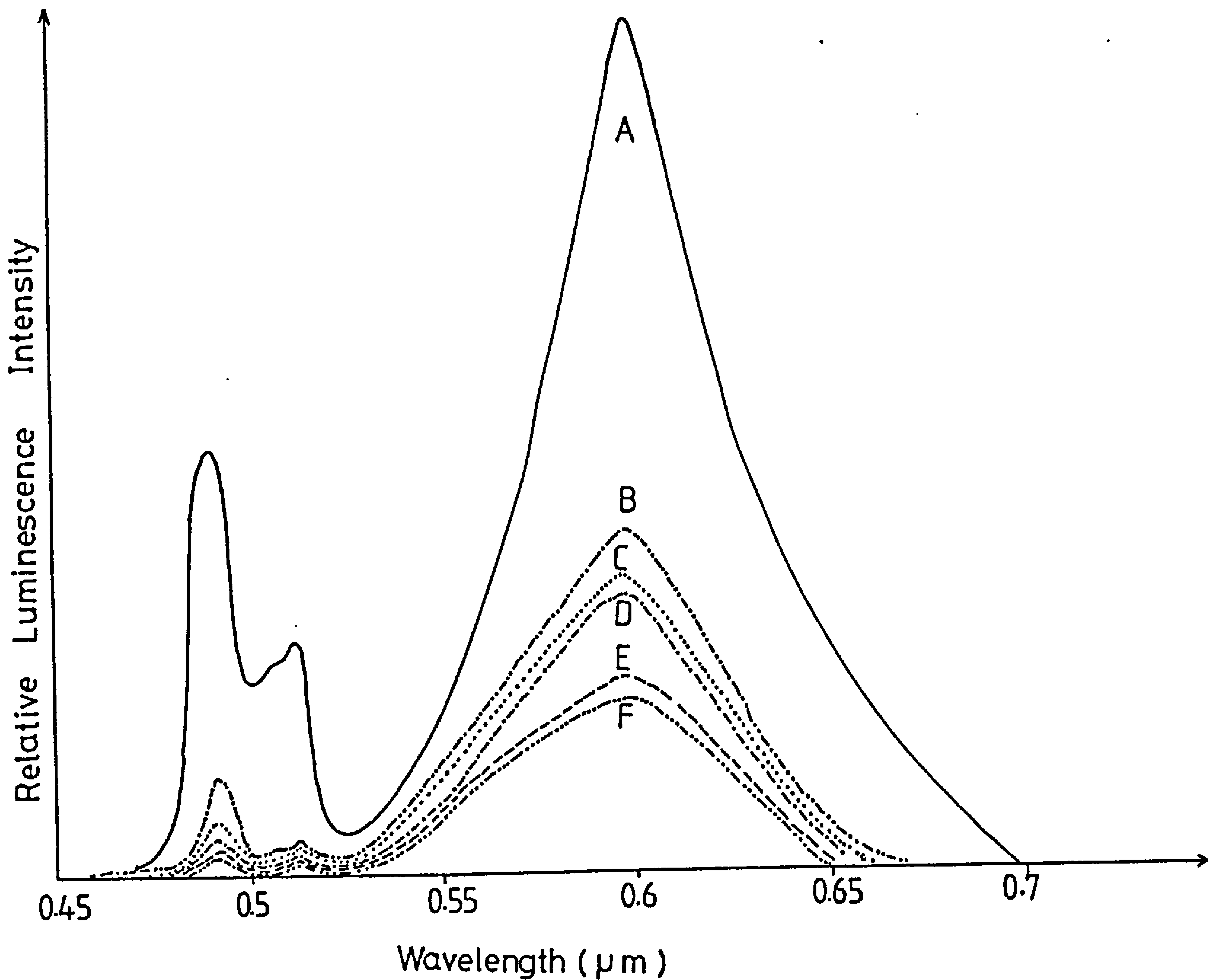

Fig.(5.12) CL emission spectrum for an unimplanted film (curve A) and Zn-implanted CdS film using constant ion dose ($5x10^{14}$ ions/cm^2) at 50keV (curve B), 100keV (C), 150keV (D), 200keV (E) and 250keV (F).

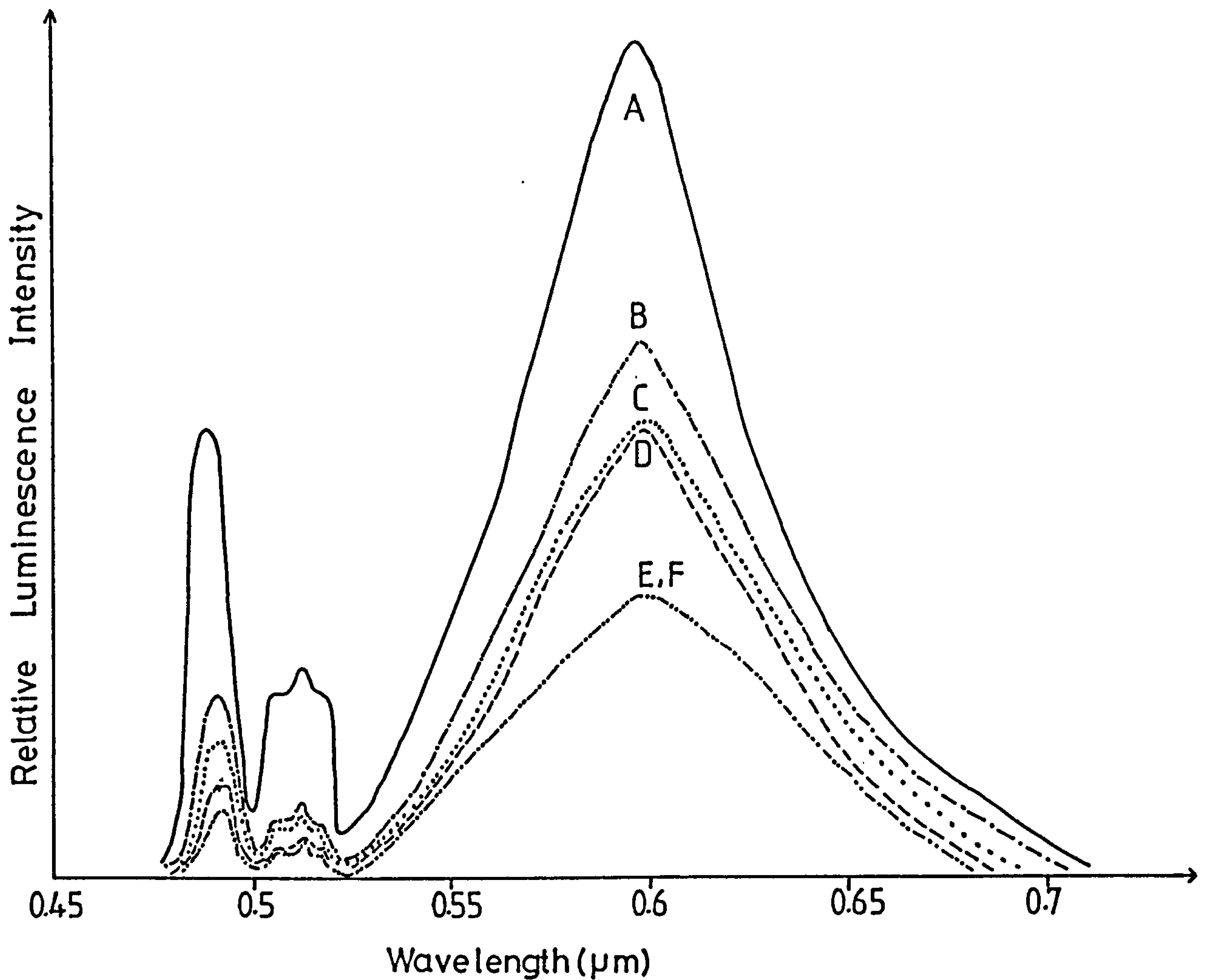

Fig.(5.13) CL emission spectrum for an unimplanted film (curve A) and Zn-implanted CdS film using ion doses of 10^{14} ions/cm^2 (curve B), $5x10^{14}$ (curve C), 10^{15} (curve D), $5x10^{15}$ (curve E) and 10^{16} (curve F) at a constant energy (50keV).

5.2 Formation and properties of the copper sulphide layer

5.2.1 Production of Cu_xS layers

As there have been several previous studies concerning the growth of Cu_xS on CdS, using the Clevite technique (147,214,82) it was not intended that further studies of this subject should form a major part of the research project described here. However, as with every other aspect of the Cu_xS-CdS cell fabrication process, some experimentation was necessary in order to establish the fabrication procedure necessary to yield the required characteristics in a reproducible way. In the case of the Cu_xS layer which is the main photonabsorber in the cell, the control of its structure and properties was of special concern and in the course of considering how these factors are influenced by the Cu_xS growth process, some new ideas relating to the growth kinetics have emerged. It is well known that the growth of Cu_xS on polycrystalline CdS is strongly affected by the surface topography of the CdS film due to the growth taking place both on the top of the CdS grains and in the grain boundaries. Of course the resultant Cu_xS layer has a very non-uniform thickness but, in this work, the ECA technique has been used to determine the thickness of the Cu_xS layer and, as described in section 4.4.2, this gives the effective planar thickness $\bar{d}$. By taking a set of CdS samples from the same deposition run and making measurements of $\bar{d}$ for different growth times for the Cu_xS layer (formed by immersion in CuCl solution), a graph showing the rate of formation of the Cu_xS layer can be constructed. For example in figure 5.14 the full line shows the results obtained for a particular set of CdS films which had been etched for 3 seconds before immersion in the CuCl solution (containing 3g/l of CuCl) at 95°C. Allowing for experimental errors (mainly

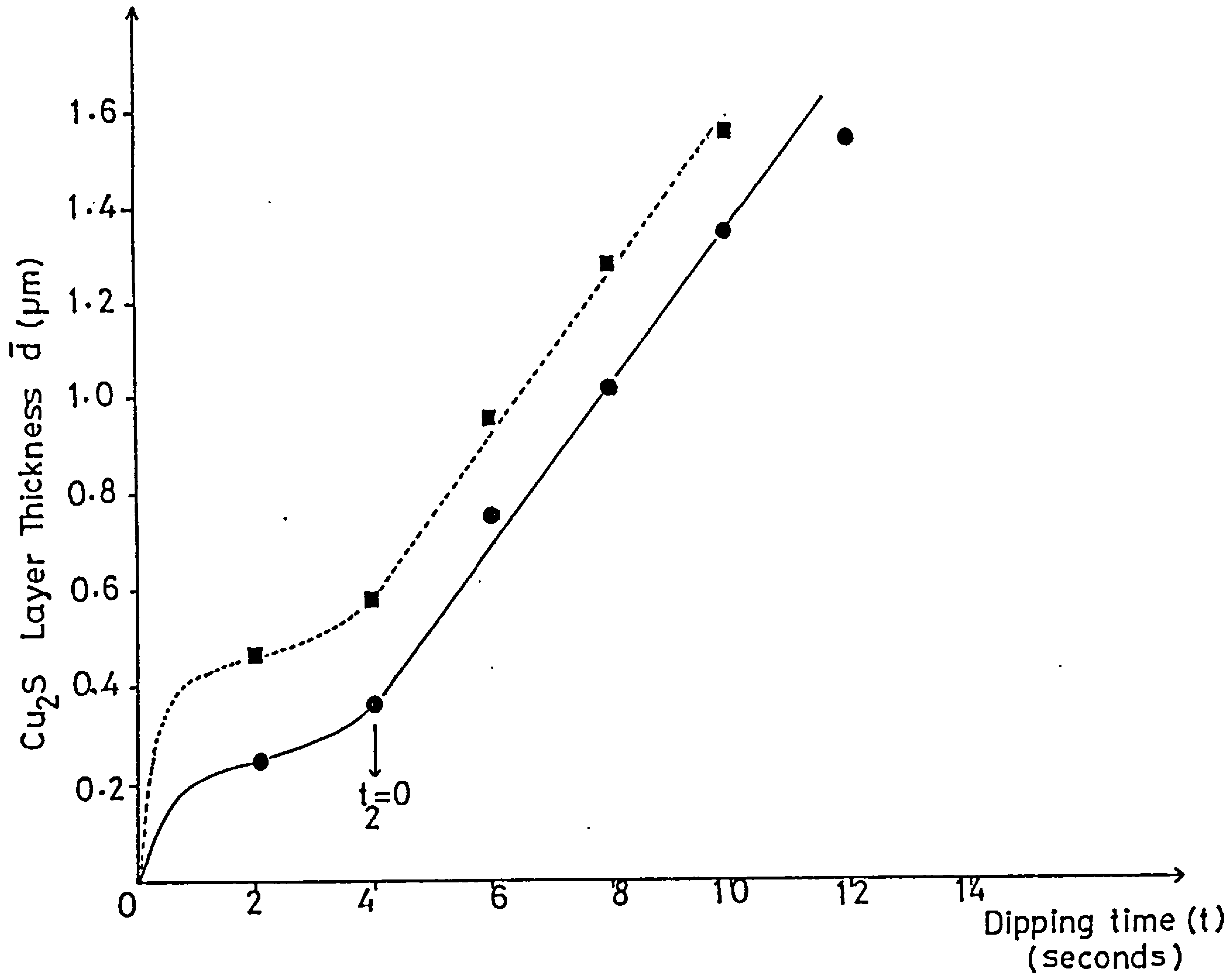

Fig.(5.14) Average Cu_2S layer thickness against dipping time using different concentrations of CuCl (full line 3g/l of CuCl and dashed line 5g/l).

associated with the CdS samples not being perfectly similar, in spite of being prepared under identical conditions), this data alone might have been presented as a straight line. However, reference to similar sets of data (e.g. the set shown by the dashed line in figure 5.14) confirms that there is a definite non-linearity in the relationship in the Ø-6 seconds region (for the conditions used here). This non-linearity is consistent with the results obtained by others (147,214,82) and can be explained in general terms by taking account of the clearly demonstrated different rates of growth at the grain surface and at the grain boundaries. The growth of Cu_xS on single crystal CdS surfaces has been found to follow a parabolic law (215,216) as would be expected for a diffusion limited process. A similar growth process would be expected to occur over the upper surface regions of the individual crystallites in a CdS film. In addition to this, a faster, more linear growth process is found to occur in the grain boundaries giving rise to the characteristic, deep protrusions of Cu_xS on polycrystalline films. While a detailed analysis of the growth rate in a practical cell would be difficult, in view of the non-uniformities associated with the CdS structure and the resulting Cu_xS film, idealised models have been employed in order to develop a mathematical analysis to account for the main features observed. For example, Rothwarf (214) has used a simple flat top cylindrical grain model of the form shown in figure 5.15, while Salkalachen and co-workers (147) chose a more realistic hexagonal model with a pyramidal top. However, neither of the mathematical treatments based on these models is entirely satisfactory, mainly due to the assumptions made concerning the diffusion process in the grain

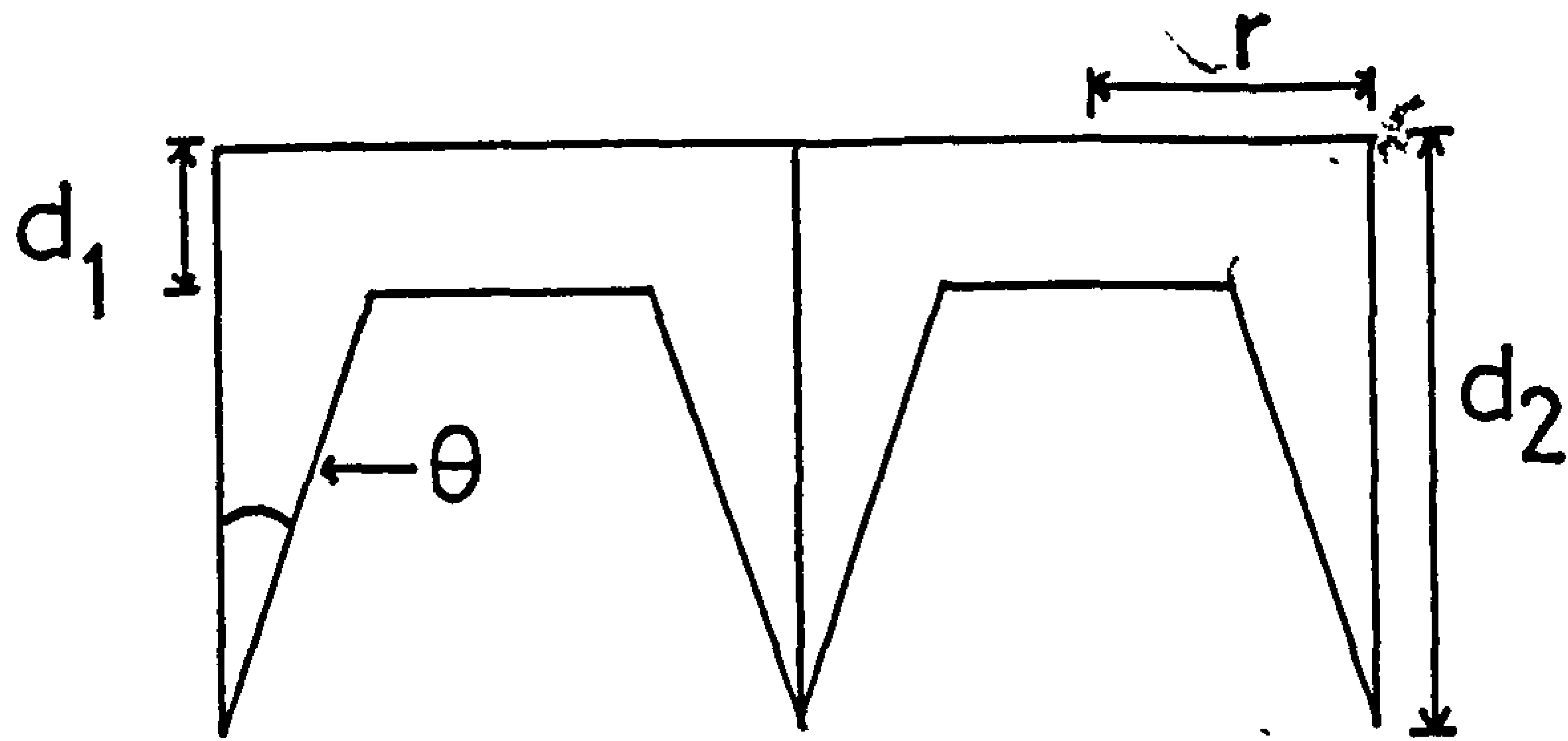

Fig.(5.15) Flat top cylindrical grain model which was discussed by Rothwarf (214).

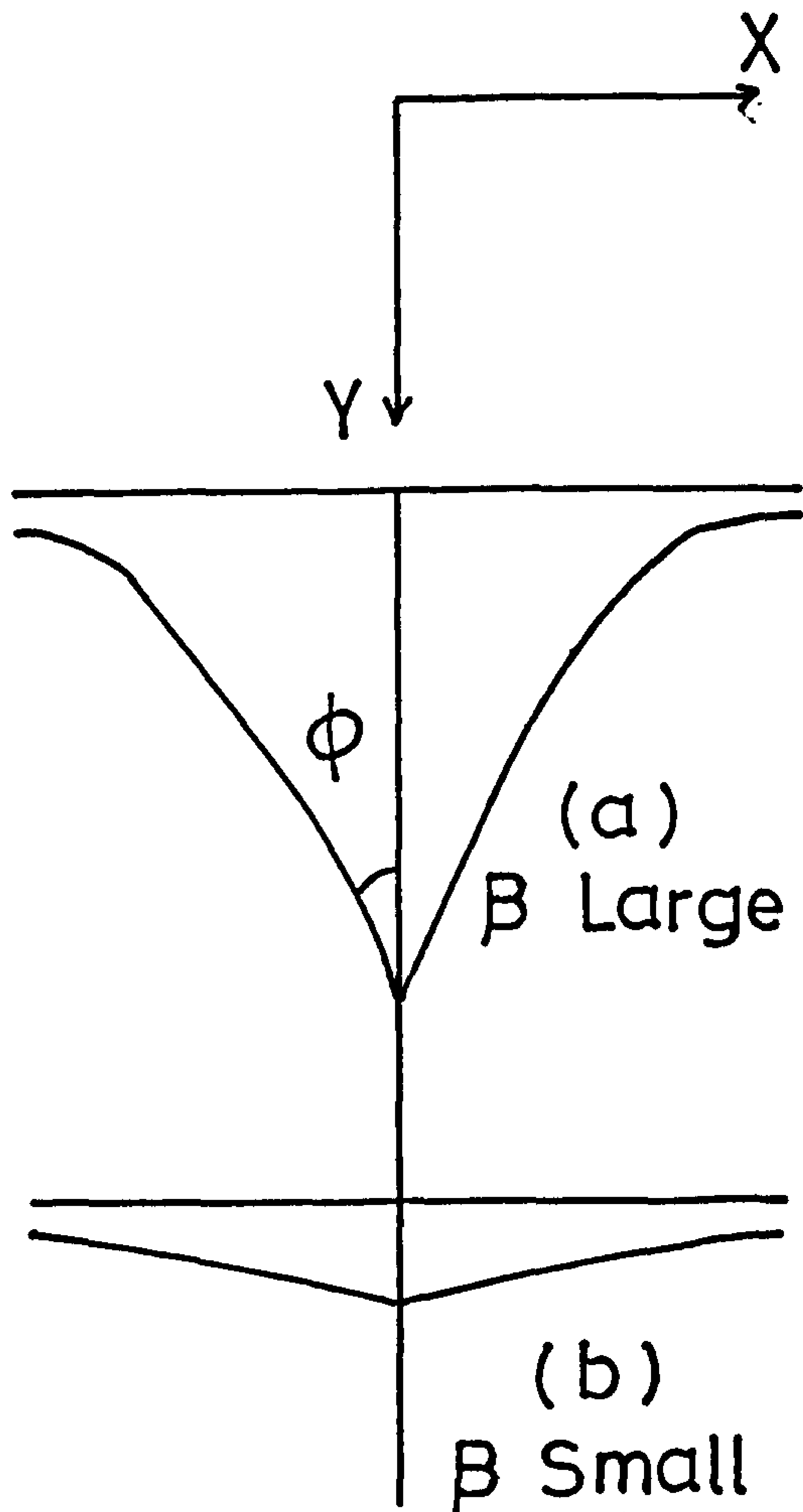

Fig.(5.16) Typical shapes of constant concentration contours in region of a grain boundary for large β (a) and small β (b).

boundaries. In the former case, the growth processes at the grain surface and at a boundary are both assumed to be diffusion limited and, accordingly are expressed in similar terms. Thus the thickness at the upper surface, d_1 as a function of time t is given by $d_1 = c_1t^{1/2}$ while the depth of penetration at the grain boundaries d_2 is given by $d_2 = c_2 t^{1/2}$ with the assumption that $c_2 \gg c_1$. This appears to be an over simplification of the growth mechanism in the boundary region which will involve transfer of atoms between the grain boundary and the crystal interior in a direction parallel to the film surface as well as along the grain boundary itself.

In the second treatment (147), d_1, is again assumed to have the form $d_1 = c_1 t^{1/2}$ while d_2 is expressed as $d_2 = c_2t$ without justification.

As discussed in chapter 2 (section 2.6), the grain boundary diffusion problem has been examined in some detail by Le Claire (41). For the idealised model described in section 2.5, assuming a constant surface concentration of the diffusion species, equation (2.6.5) gives the depth dependence of the average concentration of the diffusant as would be measured by a standard depth profiling technique. Assuming that the formation of Cu_2S on CdS layers immersed in CuCl solution is a diffusion limited process, a depth profile of the average concentration of copper through the layer should follow the 6/5 power law as discussed in section 2.5. Such a relationship has been observed experimentally (42) over a region of the profiles well removed from the free surface. This result supports the proposition that the reaction between the CuCl solution and the CdS can be described in terms of effective diffusion coefficients D_g for the grains and D_{gb} for the grain boundaries.

However, during the investigation now being discussed, it was not the depth profile which was measured but the effective planar thickness $\bar{d}$ of the Cu_2S layer and, in order to predict the rate of growth of $\bar{d}$ in terms of the model in figure 5.15, it is the time dependence of d_2 which requires to be established. This, again, can be approached using the theory developed by Whipple (217) and Leclaire (41). As illustrated in figure 5.16, the constant concentration contours have a form which is very sensitive to the parameter $\beta = (\frac{\dot{D}}{D} \frac{\frac{1}{2}\sigma}{(Dt)^{\frac{1}{2}}})$. When β is large (> 10), the grain boundary angle ϕ is very small and it is clear that diffusion into the grains on either side of a grain boundary is predominantly in the x direction rather than in the y direction as at the free surface. For the conditions under which Cu_2S–CdS solar cells are prepared using the Clevite model, it is well established, that the Cu penetration along the grain boundaries is very large in comparison with the diffusion in the mid-grain regions so that ϕ must be very small corresponding to a large value of β .

In order to examine how the Cu penetration varies with time, use can conveniently be made of Leclaire's graphical representation of Whipple's solution as shown in figure 5.17. This shows the concentration in the grain boundary relative to the surface concentration as a function of $\eta\beta^{-\frac{1}{2}}$ where η is given by $\frac{y}{(Dt)^{\frac{1}{2}}}$. The curves here are shown for β ranging from 0.1 to 100 but for β > 100 the results cannot be distinguished from the β = 100 curve. In fact, it can be seen that for β > 10, C/Co effectively becomes a function only of $(\eta\,\beta^{-\frac{1}{2}})$. Thus, the progression of any fixed concentration contour (such as that corresponding to the concentration

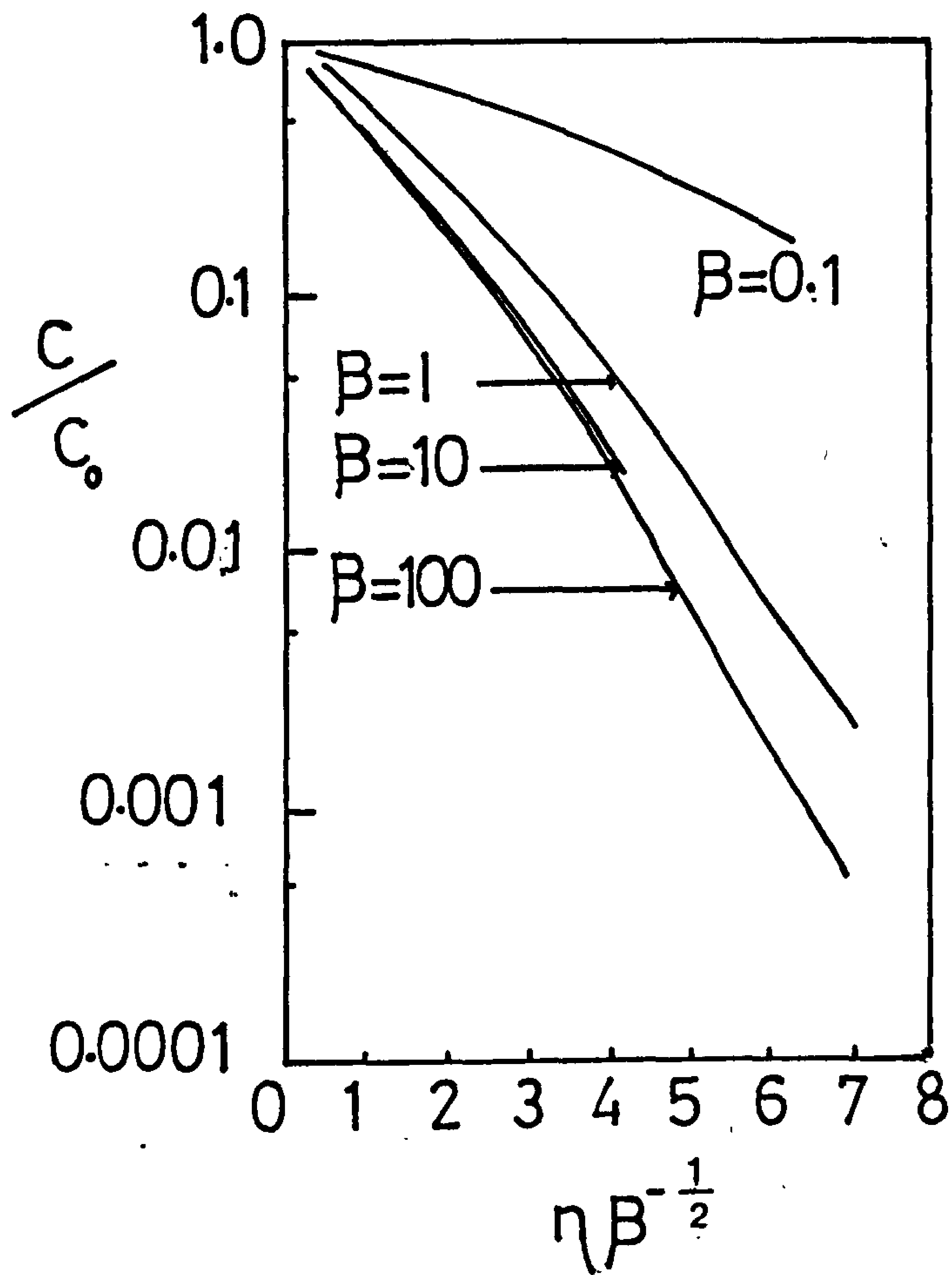

Fig.(5.17) Relative concentration in the grain boundary as a function of $\eta\beta^{-1/2}$ as given by Le Claire (41).

at the tip of a Cu_xS protrusion) is such that $\eta\beta^{-\frac{1}{2}}$ remains constant provided that β is sufficiently large. Thus

$$\eta\beta^{-\frac{1}{2}} = \left[\frac{y}{(Dt)^{\frac{1}{2}}} \cdot \frac{D}{\dot{D}} \cdot \frac{(Dt)^{\frac{1}{2}}}{\frac{1}{2}\sigma} \right]^{\frac{1}{2}} = \text{constant}$$

and it follows that $y \propto t^{\frac{1}{4}}$ or, in terms of the notation for the model in figure 5.15, $d_2 \propto t^{\frac{1}{4}}$. For the grain model represented in figure 5.15, the value of the average planar thickness is given by:

$$d = \frac{\text{total volume of } Cu_2S}{\text{planar surface area}} = d_1 + \frac{d_1 d_2}{r} \qquad \text{for } d_2 \gg d_1$$

Assuming that d_1 is proportional to $t^{\frac{1}{2}}$ and d_2 is proportional to $t^{\frac{1}{4}}$ as discussed above, it follows that:

$$\bar{d} = a\, t^{\frac{1}{2}} + b\, t^{\frac{3}{4}} \qquad (5.2.1)$$

where a, b are constants. In figure 5.18 the data of figure 5.14 is redrawn and compared with theoretical curves obtained using equation (5.2.1). In order to do this, it was first necessary to determine values for the constants a and b. The value of a was obtained by assuming that the initial growth is dominated by the reaction at the free surface where the growth proceeds according to $d_1 = a\, t_1^{\frac{1}{2}}$. Thus the constant a was determined to be 0.17 by using the experimentally observed thickness at time $t_1 = 2$ seconds. The second parameter b was calculated to be 0.21 by use of the relation $d_2 = b\, t_2^{\frac{3}{4}}$, where d_2 was determined by the difference between the experimentally observed $\bar{d}$ and the calculated value of d_1 given by $a\, t_1^{\frac{1}{2}}$. However, in order to obtain a good fit between the experimental and theoretically obtained data, it was necessary to assume that d_2 remained effectively zero for the first 4 seconds. Accordingly, the value of b was obtained using $d_2 = \bar{d} - d_1$ where the growth process in the grain boundaries, expressed by $d_2 = bt_2^{\frac{3}{4}}$ was assumed to begin ($t_2 = 0$) at time $t = t_1 = 4$ seconds. Thus b was evaluated at $t = t_1 = 6$ seconds corresponding

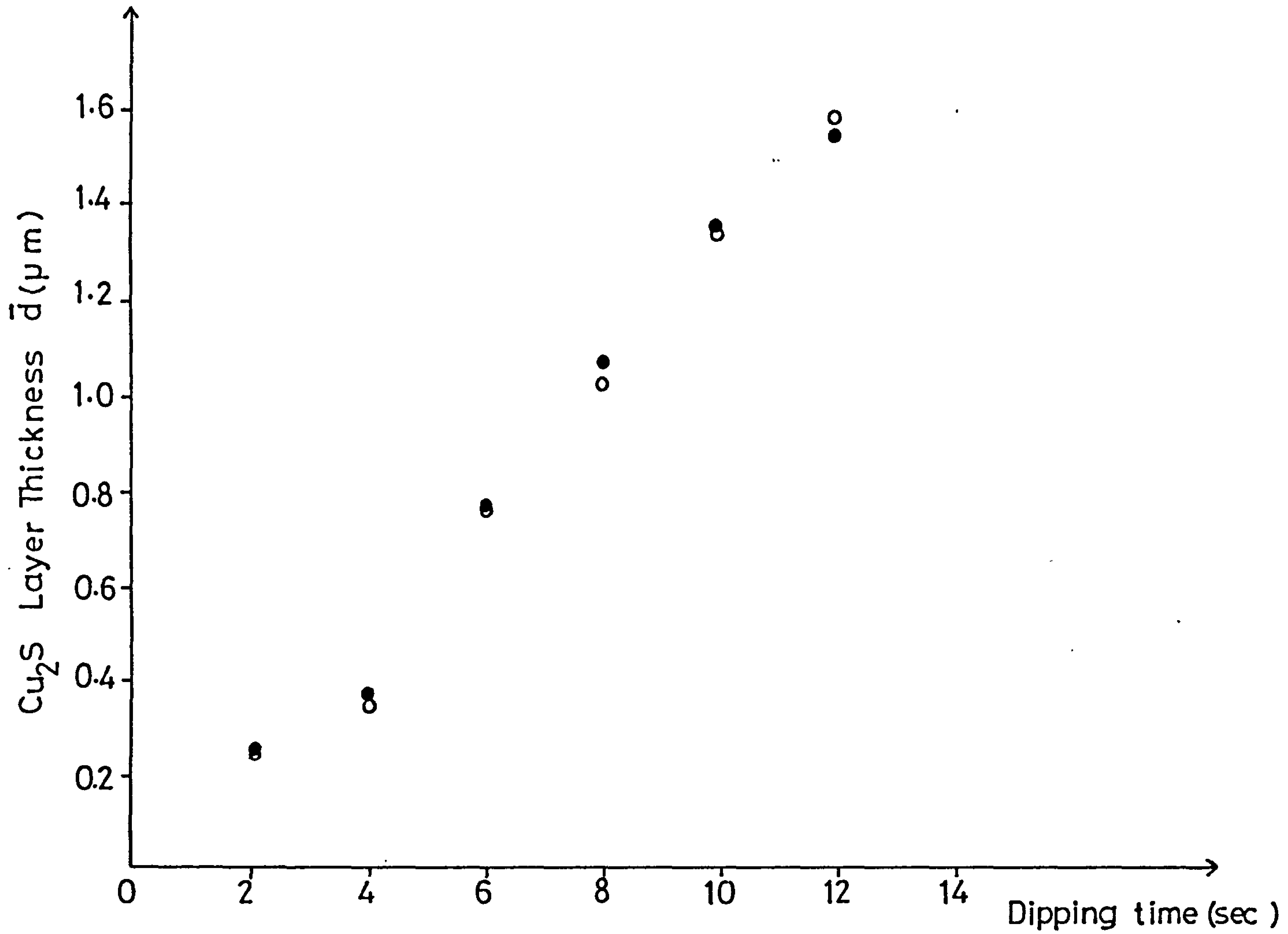

Fig.(5.18) The average Cu_2S thickness against dipping time in CuCl bath.
●: Experimentally observed values of Cu_xS thickness using ECA. O: Theoretical thickness values of Cu_xS layers using equation (5.2.1).

to $t_2 = 2$ seconds. By using the parameters a = 0.17 and b = 0.21 the theoretical values of $\bar{d}$ were calculated and these are represented by the open circles in figure 5.18. It can be seen that these values provide an excellent fit to the experimental values. In order to test the effectiveness of the above analysis under very different Cu_xS growth conditions, use has been made of data provided by Salkalachen (147) who employed a CuCl solution with pH = 4.6 to obtain much thinner layers over the same time scale as that used in this study. The experimentally obtained values of thickness $\bar{d}$ against dipping time are shown in figure 5.19 together with calculated values obtained using the same procedure as that described above, except that, in this case d_2 was assumed to remain at zero until t = 9 seconds. Once again a good fit to the experimental values is achieved. It is clear that the thickness of Cu_xS is very dependent on the time of delay before growth in the grain boundaries begins and this is discussed further in the next section. Independent evidence for the extensive growth of Cu_2S in the CdS grain boundaries has come from the junction capacitance measurements for different dipping times as shown in table 5.4.

Table 5.4 Capacitance measurements for Cu_2S-CdS junctions with different dipping times. (CdS etched for 3 seconds)

Dipping time (seconds)	Capacitance p.F/mm^2
2	1040
4	1490
6	2200
8	2430

It is clear from table 5.4 that the formation of Cu_2S on CdS results in a junction capacitance which increases significantly with Cu_2S

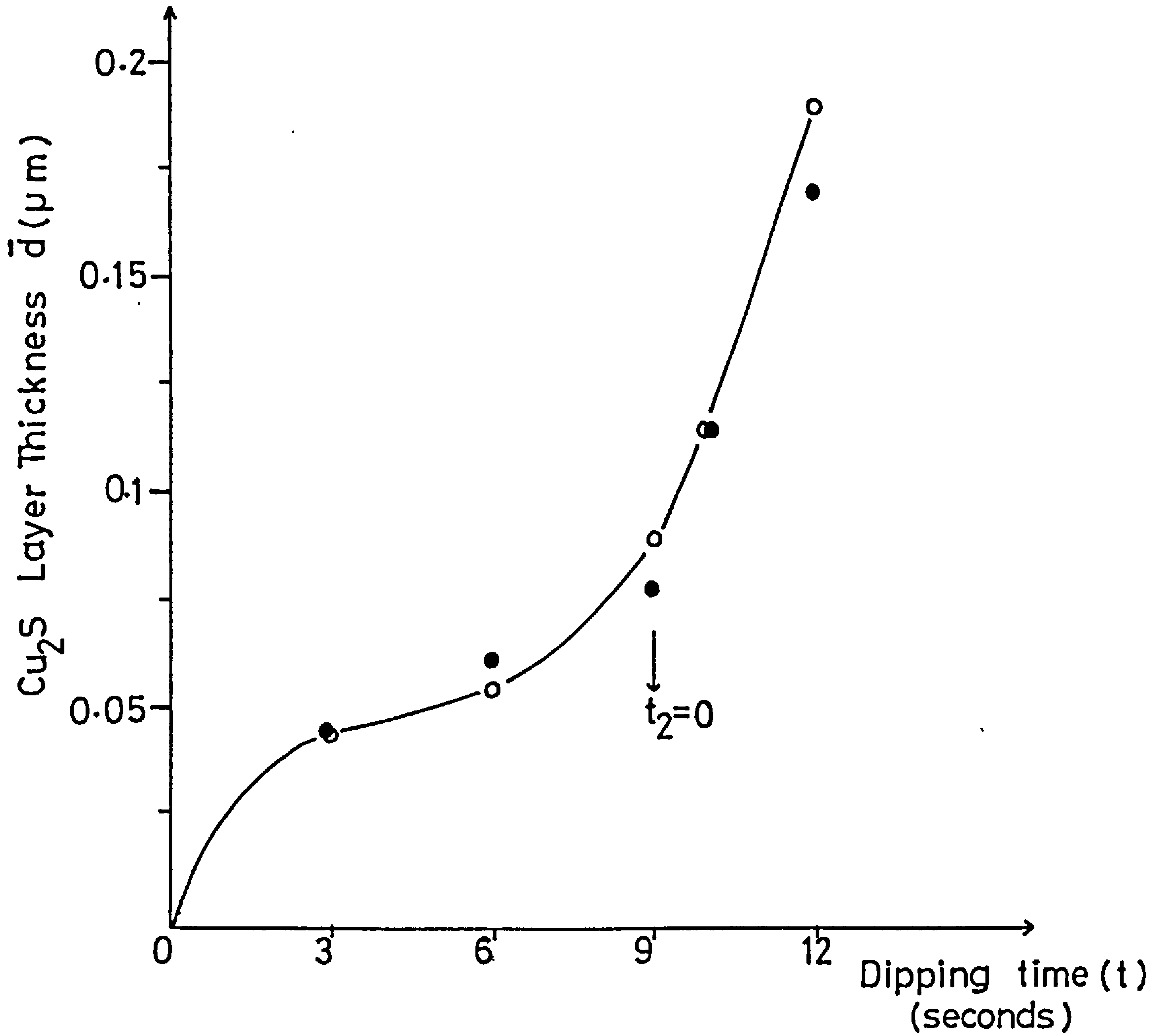

Fig.(5.19) The average thickness of Cu_xS layer against different dipping times.
O: Data obtained experimentally by Salkalachen (147).
●: Theoretical values of Cu_xS layer thickness using equation (5.2.1).

growth time. If the effect of longer dipping was simply to increase the thickness of Cu_2S on the surface of the film, no such increase in capacitance would be expected but due to growth along grain boundaries and the resulting increase in junction area with increasing of dipping time, a corresponding increase in junction capacitance can be understood. Unfortunately, these measurements do not allow an accurate determination of the junction area (and associated grain boundary penetration) to be made due to variations in the junction structure with dipping time. However an estimate of the thickness of the surface film of Cu_2S can be made by leaching the Cu_2S layer from the CdS layer using KCN solution as described previously (82). In figure 5.3 SEM micrographs show the surface topography of a CdS layer from which the Cu_xS had been leached in KCN after dipping for 8 seconds. As indicated in the model of the dipped CdS layer in figure 5.15, the full width of a Cu_2S grain boundary protrusion at the upper surface is $2d_1$. Thus by measuring the width of the grain boundary regions after removing the Cu_xS layer (as revealed by SEM micrographs such as that in figure 5.3) an estimate could be made of the thickness of the Cu_xS layer d_1 on the upper surface of the CdS film. Making use of the SEM to measure the width of the grain boundaries at many different points across the film surface, an average grain boundary width was obtained. For the system shown in figure 5.3, the result was found to be 224 ∓ 10 nm. This film had been dipped for 8 seconds. For a similar CdS film which had been dipped for 2 seconds the average value was 110 ∓ 10 nm. Thus the thickness of Cu_xS at the top of the grains was calculated to be 55 ∓ 5 and 112 ∓ 5 nm for dipping times of 2 seconds and 8 seconds respectively. In figure 5.20 these values for the thickness of Cu_xS over the surface of the CdS grains d_1 are

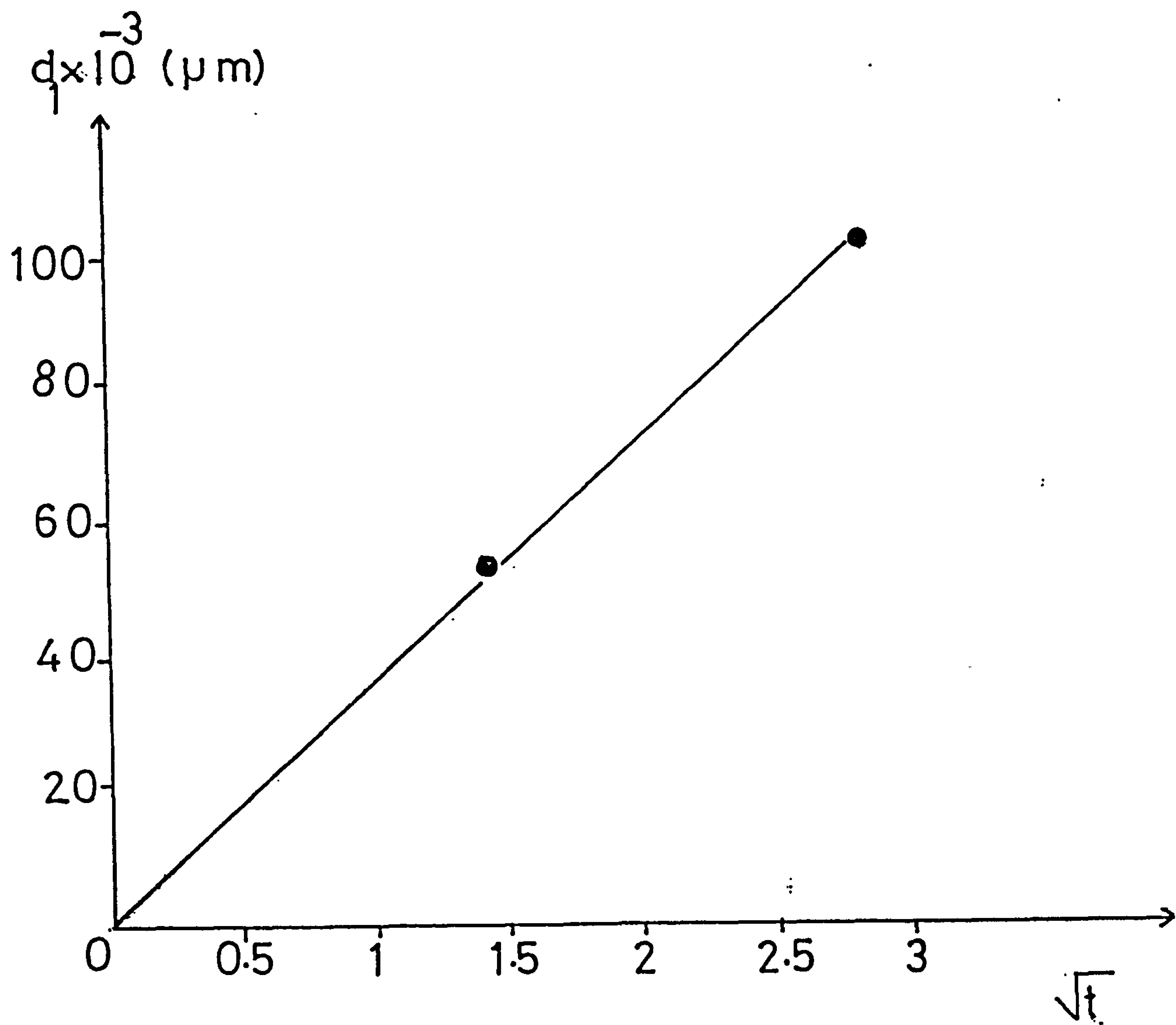

Fig.(5.20) Surface thickness of Cu_2S layer d_1 against the square root of dipping time t.

plotted against the square root of dipping time t. The plot shows a straight line which confirms that the formation of Cu_xS on the top surface of the CdS grains follows a $t^{1/2}$ law.

5.2.2 Growth of Cu_xS on annealed CdS substrates

The properties of CdS thin films are known to be very sensitive to changes in surface stoichiometry and to surface contamination from the ambient gas. The effect of absorbed oxygen on the electrical properties of CdS in both single crystal and thin film form has been found to be especially significant (218,219,220). For example, it is well known that oxygen is chemisorbed at the surface of CdS, forming strong bonds with the surface atoms (221,222) and this causes an increase in the CdS resistivity by reducing both the electron mobility and the density of free carriers (223). In order to determine how the surface condition of the CdS layer influences the formation and properties of the Cu_xS layer grown over it, a series of Cu_xS growth experiments were performed using CdS films which had been annealed in different atmospheres after deposition. The annealing atmospheres employed were hydrogen, vacuum or air and the annealing was carried out after first etching the CdS films in HCl acid. This was in order to ensure that Cu_xS layer formed on the annealed films could be properly compared with those formed on unannealed CdS films which are normally etched prior to the formation of a Cu_xS layer. Before discussing the effect of these treatments on subsequently formed Cu_xS layers, consideration will be given to some supplementary experiments which were introduced to provide information on the surface characteristics of the CdS layer after the different annealing treatments. This information was provided by comparative studies of

the cathodoluminescence spectra and the surface carrier concentration as deduced from C-V measurements using a gold Schottky contact. Figures 5.21 and 5.22 show the cathodoluminescence spectra obtained for one set of CdS films before and after annealing at 300°C in each of the three different atmospheres for 1/2 hour. The spectra in figure 5.21 all show the characteristic strong emission peaks in the region of the CdS band gap energy which is associated with films of good structural quality, as discussed previously in section 5.1.2. Annealing in hydrogen is seen to have only a small effect on this spectrum but there is significant reduction in the intensity of these peaks after annealing in vacuum and a much greater reduction after annealing in air. It is clear that structural changes occur at the CdS surface as a result of the latter annealing conditions which must lead to non-radiative or alternative radiative recombination processes. Figure 5.21 indicates one such process by the appearance after air annealing of a broad, long wavelength emission peak centred at ~ 680 nm. A similar effect due to air annealing has recently been reported by Achour and Talat (224) who attributed this red emission band to the development of neutral complex $\left[V_{Cd}^{2+}\ V_S^{2+}\right]$ centres. However, it is unlikely that these broad emission bands are associated with any single type of defect and a variety of native defect-impurity complexes are possible. For example, Humerberger and coworkers (208) and also Susa et al (203) have suggested that V_{Cd} associated with Cl_S is responsible for a red emission band centred at 730 nm. It seems reasonable to expect that vacancies can be generated by annealing in air. Oxygen can interact with the CdS films to form CdO, SO_2 and $CdSO_4$ (225) so that the out diffusion of Cd and/or S

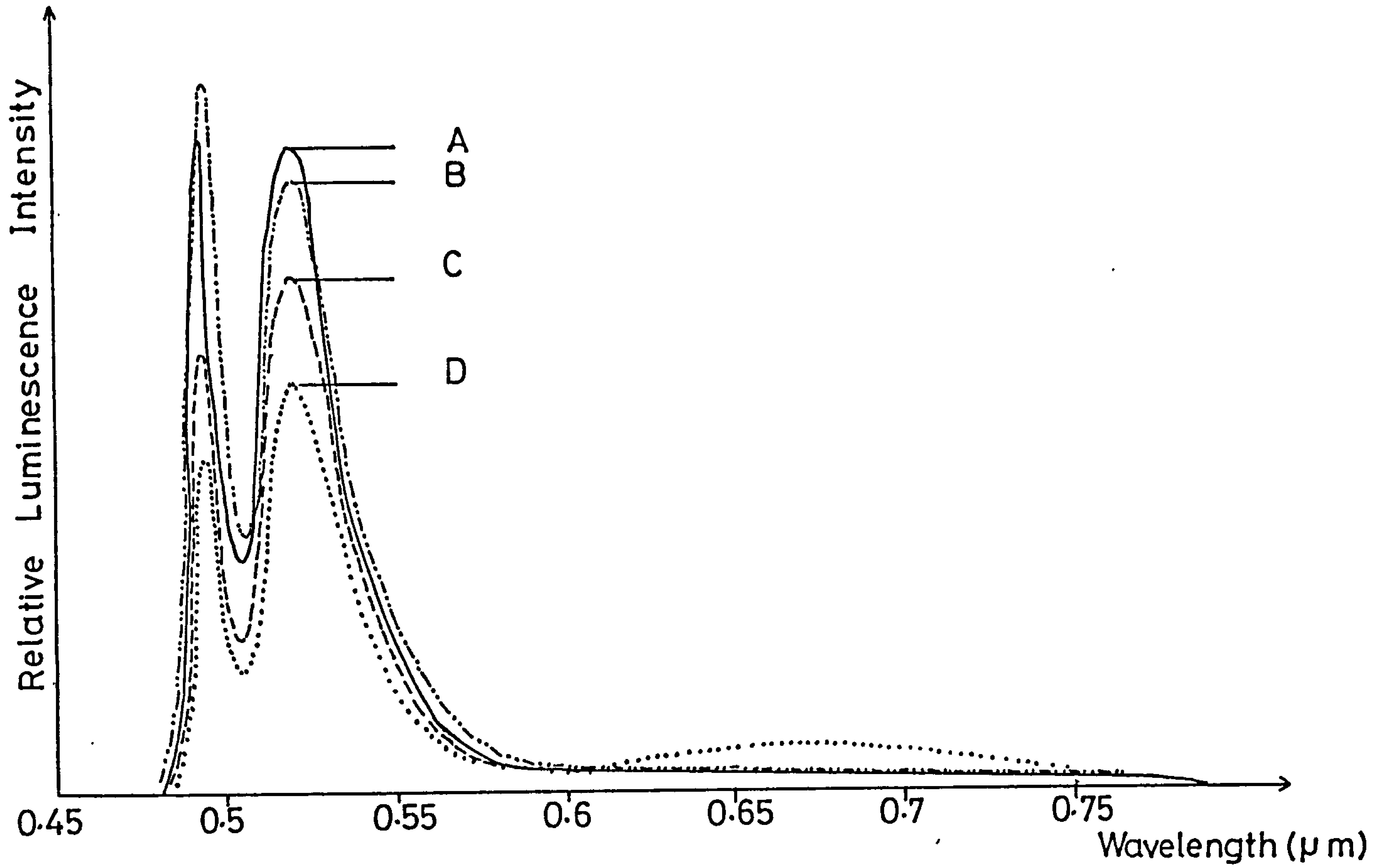

Fig.(5.21) The cathodoluminescence spectra for unannealed and annealed CdS films using different atmospheres at 300°C for 30 minutes. A, before annealing; B, CdS film annealed in hydrogen; C, CdS film annealed in vacuum; D, CdS film annealed in air.

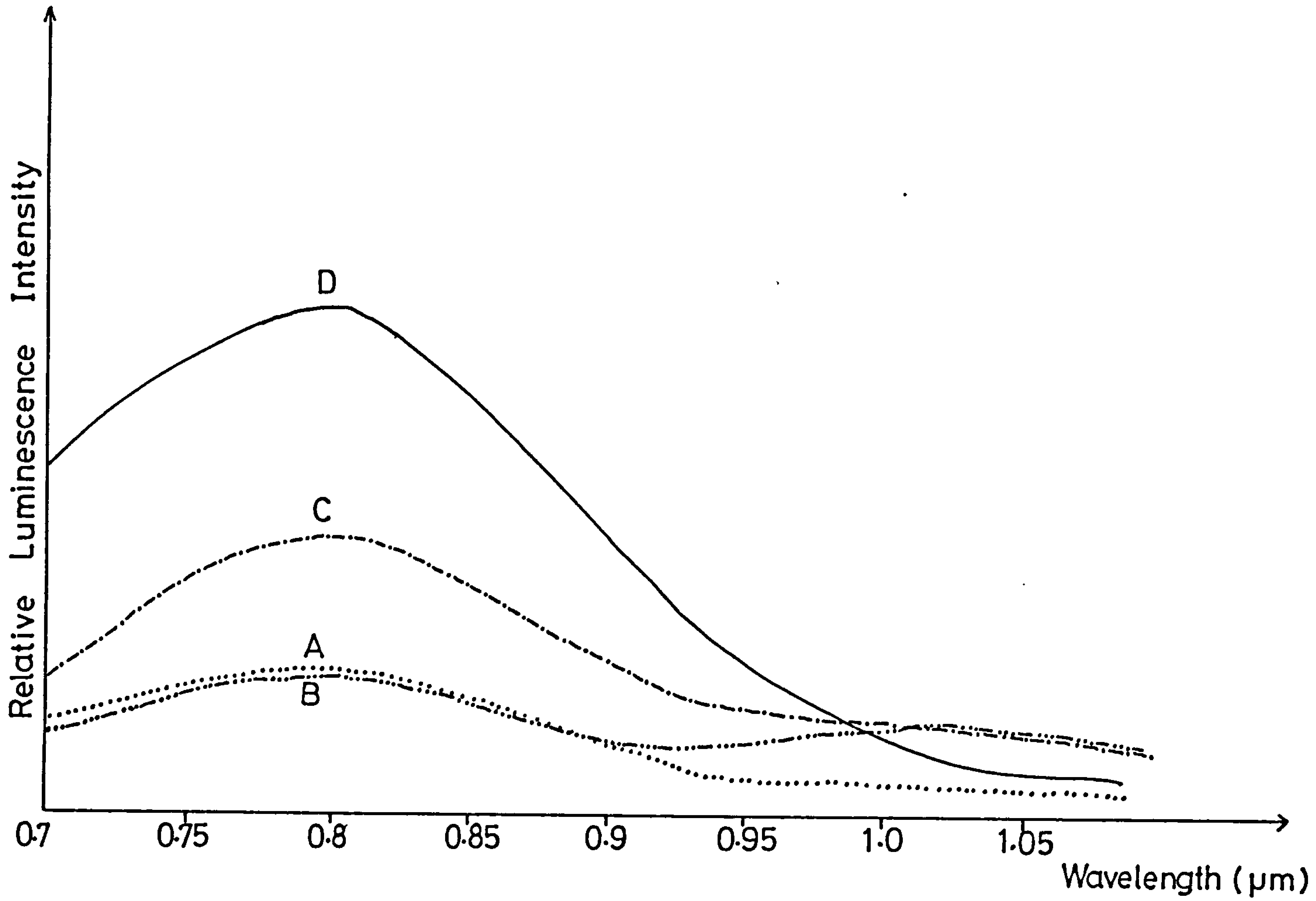

Fig.(5.22) The cathodoluminescence spectra for unannealed and annealed CdS films using different atmospheres at 300°C for 30 minutes. A, unannealed CdS film; B, CdS film annealed in hydrogen; C, CdS film annealed in vacuum; D, CdS film annealed in air.

atoms to the surface of CdS, during thermal annealing in air can be expected and, in polycrystalline films the diffusion process is expected to be especially fast along the grain boundaries. In fact, in thermally evaported layers which are slightly rich in Cd, the grain boundaries and surface are likely to be regions where excess Cd atoms can accumulate. This excess would be rapidly depleted by annealing in air and Cd vacancies might eventually be formed to generate the complex centres which contribute to the peak at 0.68 μm. Another broad emission band which is commonly observed in both single crystals and thin films of CdS with a peak at ~ 800 nm can be seen in figure 5.22 which shows the cathodoluminescence emission in the 700-1100 nm region. This peak, again, is clearly enhanced by annealing in air but relatively unaffected by annealing in hydrogen. Although the origin of the luminescence emission in this region of the spectrum has been discussed by a number of authors (205, 226, 227, 203, 228), much uncertainty still remains. Some evidence has been presented (228) to suggest that the centres responsible for this emission occur preferentially at grain boundaries, but it is seen in single crystals as well as in polycrystalline films. Grillot (227) observed a broad peak centred at 820 nm in CdS crystals doped with Cu and some subsequent workers (229, 230) have also attributed this emission to copper impurities but results obtained by Susa and coworkers (203) indicated that native defects might have an important role. The effects of different annealing treatments, as illustrated in figure 5.22, support the latter view but do not rule out the possibility of copper involvement. Of course the CdS is not intentionally doped, but copper could be present as a result of diffusion from the substrate or as a result of its presence as a residual impurity in the CdS source

material. The possible role of Cu in the luminescence emission is discussed again in section (5.2.4). Accompanying these changes in the luminescence emission, the surface free carrier conentration was also found to be modified as can be seen in figure 5.23 where the electron concentration (as determined from C-V data) is plotted as a function of annealing time in each of the three different atmospheres. The annealing was carried out in 1 hour stages and a fresh gold contact was evaporated onto the exposed CdS film surface after each stage of the annealing process. It can be clearly seen that the carrier concentration for films annealed in air decreased with increasing annealing time (as would be expected to occur as result of absorption of oxygen to occupy previously vacant S sites or the removal of excess Cd as discussed above). Annealing in vacuum appeared to have the opposite effect possibly as a result of incorporation of excess Cd at the surface into the underlying CdS lattice. Consistent with the lack of any change in the luminescence following hydrogen annealing, the carrier concentration was found to remain constant with increasing annealing time in hydrogen. In comparing luminescence emission and carrier concentration data, it should be noted that different regions of the film are monitored by the two techniques. The C-V data gives the free carrier density at the edge of the depletion region which, in these samples, was ~ 0.038 μm wide whereas the cathodoluminescence data related to a depth of the sample corresponding to the penetration depth of the electrons which, for 10 KV electrons, is ~ 0.4 μm. Therefore, in the samples used here, the C-V method is more sensitive to changes very near to the surface.

When the CdS films which had been exposed to the three different

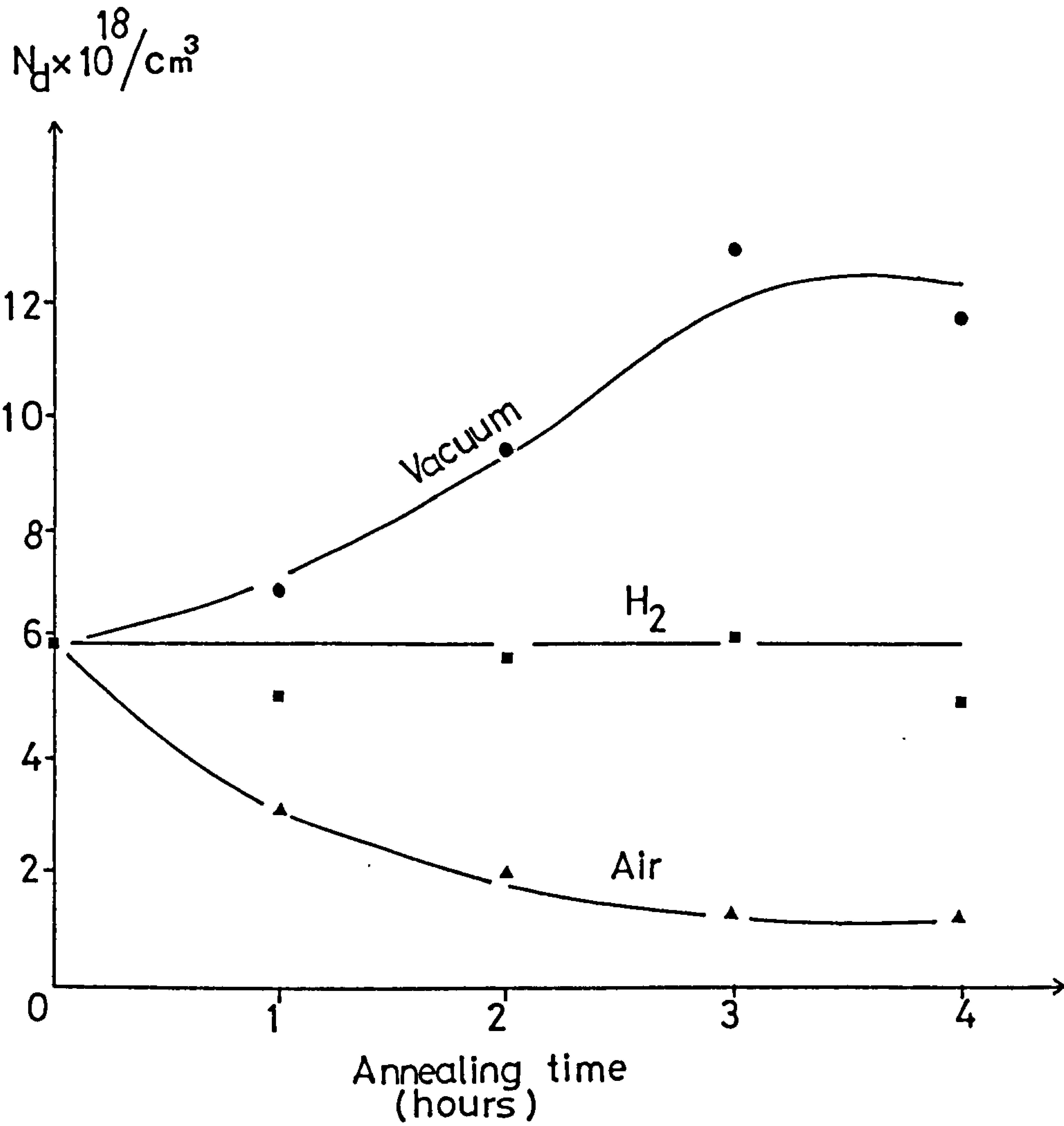

Fig.(5.23) The carrier concentration as a function of annealing time for CdS layers annealed in different atmospheres (hydrogen, vacuum and air).

annealing treatments (hydrogen, vacuum, air) were used to form Cu_xS layers by dipping into a standard CuCl solution, clear differences in the rate of Cu_xS formation were observed. This is demonstrated by the results in table 5.5 which lists the mean thickness of Cu_xS (as determined by electrochemical analysis) for a dipping time of two seconds.

Table 5.5 Mean thickness of Cu_xS formed in 2 seconds on CdS layers annealed at 300°C for 1/2 hour.

Annealing atmosphere	Mean thickness of Cu_xS (μm)
Non-annealed	0.4
Hydrogen	0.41
Vacuum	0.62
Air	2.9

As might have been expected from the observations described above concerning the changes in luminescence emission and the surface carrier concentration, the process of annealing the CdS layer in hydrogen has very little effect on the Cu_xS formation rate while that of annealing in vacuum or air has a clearly measurable effect. In fact, the air annealing is seen to increase the rate of formation to a remarkable extent leading to a mean thickness of nearly 3 μm in just 2 seconds whereas, for these particular CdS layers, a Cu_xS thickness of ~ 0.4 μm was obtained for CdS films which had not been given any initial annealing treatment. The experiment on air annealing was repeated for a different set of CdS layers (using a lower annealing temperature (200°C) and, although the result was not quite so dramatic, a significant increase in Cu_xS formation rate was again observed. This time, the effect of different annealing times was

investigated and the results can be seen in figure 5.24 which shows the mean Cu_xS thickness (for a dipping time of 2 seconds) as a function of the initial CdS annealing time in air. This graph indicates an almost linear dependence of the Cu_xS thickness on pre-annealing time.

A possible explanation of the observed dramatic influence of the air annealing is provided by the analysis of the Cu_xS growth kinetics described in section 5.2.1. While the growth of Cu_xS is known to take place both at the free surface of the CdS layer and at the grain boundaries, it was found that a theoretical fit to the experimental data could be best achieved by assuming that penetration into the grain boundaries is delayed by a period of time which appears to be dependent on the acidity of the solution. As the growth of Cu_xS in the grain boundary region proceeds at a much faster rate than the growth at the free surface, any variation in the delay time, before grain boundary attack, can clearly have a large influence on the total Cu_xS formation in a short dipping time. Thus, if annealing in air has the effect of changing the structure at the free surface edges of the grain boundaries in such a way as to promote a quick start to the reaction in these grain boundary regions, a rapid increase in average thickness of the Cu_xS film will result. The observed changes in the luminescence spectra discussed above give some support to the suggestion that annealing in air does have a significant effect on the structure of the grain boundaries. In relation to the enhancement of the red emission bands following air annealing, attention was drawn to the mechanism proposed for vacancy generation in which an important role is played by the grain boundaries in providing a path for the rapid diffusion of Cd and S atoms to the surface where they become

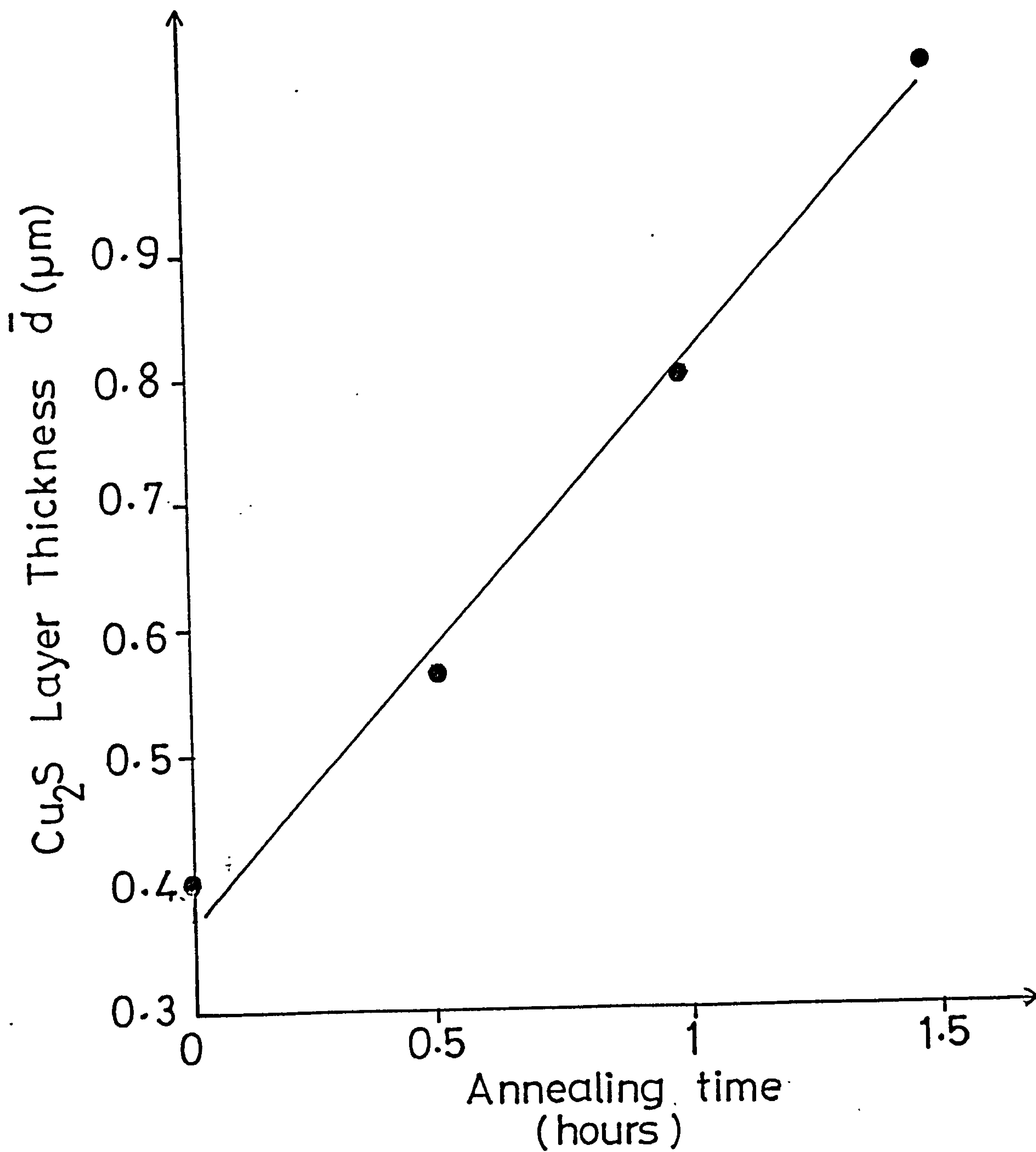

Fig.(5.24) The mean Cu_xS layer thickness (for a dipping time of 2 seconds) as a function of the initial CdS annealing time in air.

oxidized. In addition there is independent evidence to suggest, that the emission which is enhanced by air annealing is due to centres which arise predominantly at intergranular regions (228). Finally, it is clear from other results obtained during the course of the present investigation, that the excess thickness of Cu_xS associated with air-annealed CdS films lies mainly in the grain boundaries. These results will be presented in sections (5.2.4).

5.2.3 Copper sulphide stoichiometry

In addition to determining the thickness of the Cu_xS layer as discussed in the previous section, the ECA technique has been used to determine the deviation from the ideal Cu_2S stoichiometric composition for a variety of different growth conditions and post-growth treatments. For example, in figure 5.25, the parameter x is plotted as a function of dipping time for the same group of samples for which the layer thickness is given in figure 5.14. It is clear that x increases with dipping time (corresponding to increasing thickness) as would be expected from the model put forward by Vedel (153) and discussed in section (3.3.3).

Of course the stoichiometry is very sensitive to post formation treatments such as the annealing treatments which are required to form the Cu_2S-CdS interface barriers and to provide good photo-electric properties for the completed cells.

The effect of annealing in a vacuum or in a hydrogen atmosphere is shown in figure 5.26. It can be seen that the stoichiometry factor for the Cu_xS layer increased steadily with increasing annealing time in H_2 while annealing in a vacuum leads to an increase in x for short annealing times but, with increasing annealing time, the stoichiometry

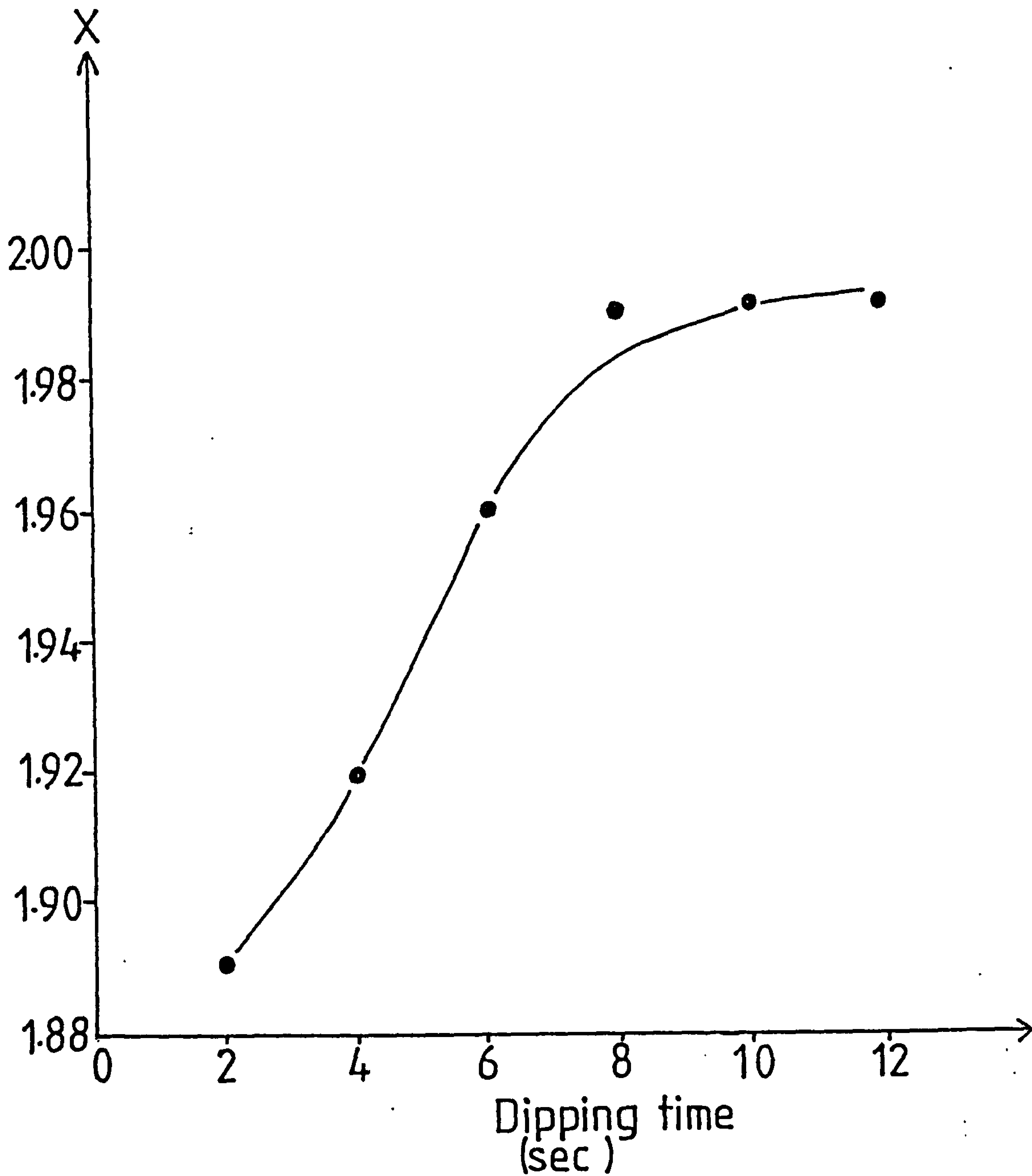

Fig.(5.25) The stoichiometry parameter x of the Cu_xS layer as a function of dipping time.

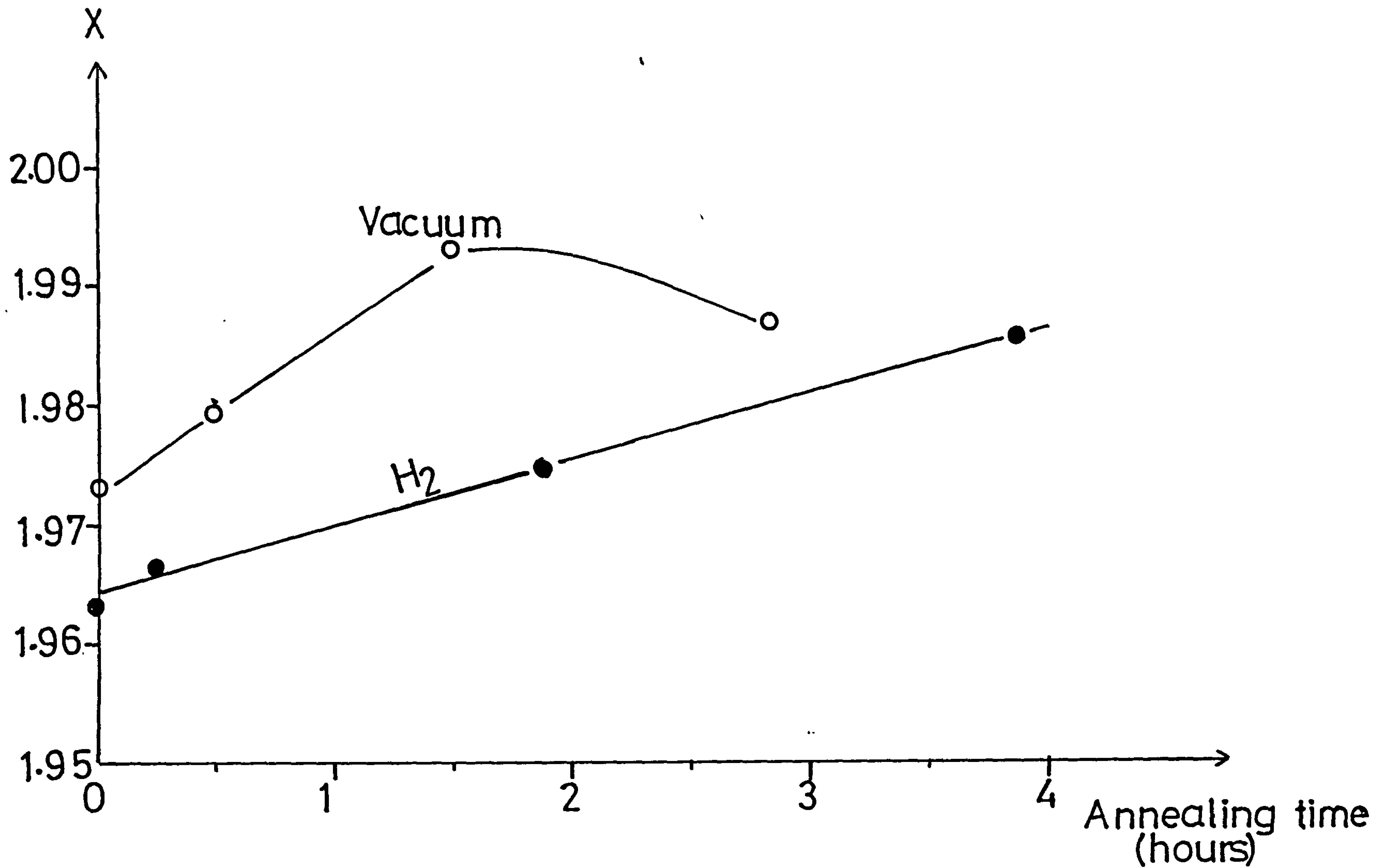

Fig.(5.26) The stoichiometry parameter x of the Cu_xS layer as a function of annealing time in hydrogen and vacuum at 200°C.

of Cu_xS seems to saturate or to slightly decrease. The changes in oxide thickness at the surface of Cu_xS layers involved in figure 5.26 were measured and are shown in figure 5.27. It can be seen that the oxide layer at the surface of the Cu_xS layers annealed in H_2 was removed completely after ~ 4 hours, while vacuum annealing seems to have little influence on the oxide thickness. In general, it has been found that long annealing times in a hydrogen atmosphere has a beneficial effect on the Cu_xS layer and on the photovoltaic properties of the completed photo cells. Similar results have been obtained using other reactive atmospheres such as carbon monoxide (174) and H_2 - argon mixtures (14).

The effect of air annealing appears to be more complicated being dependent on the annealing time and the structure of the layers. This is demonstrated in figure 5.28 where the stoichiometry of the Cu_2S layer is plotted as a function of annealing time in air at 200°C for two different samples A and B. The stoichiometry factor x for sample A (with a high initial value of x) was found to reduce steadily with increasing annealing time in air, while the x factor for sample B (with the lower initial x value) was found to increase for the first 5 minutes in air and then to reduce slowly with increasing annealing time. The sample A, with the initial high stoichiometry factor (x ~ 2) was fabricated in the usual manner for good cell production (by dipping for 2 seconds into a CuCl bath at 95°C with pH = 4 and with nitrogen gas bubbling through it). In contrast, sample B, with the lower initial stoichiometry factor (x ~ 1.96) was formed by dipping the CdS layers for 2 seconds into a bath of CuCl which was expected to contain a higher concentration of divalent copper ions.

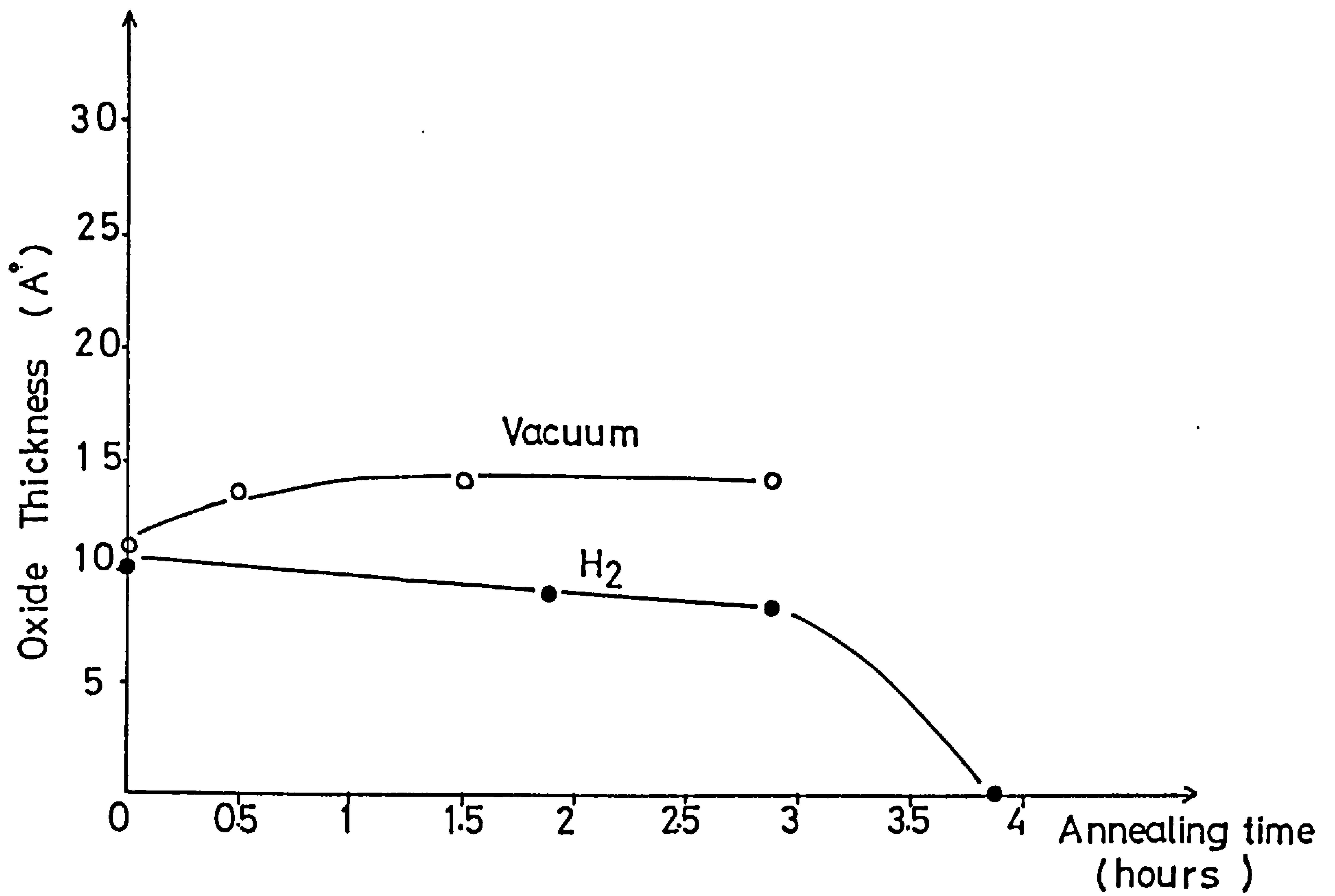

Fig.(5.27) The oxide thickness at the surface of Cu_xS-CdS cells after annealing in hydrogen and vacuum for different lengths of time at 200°C.

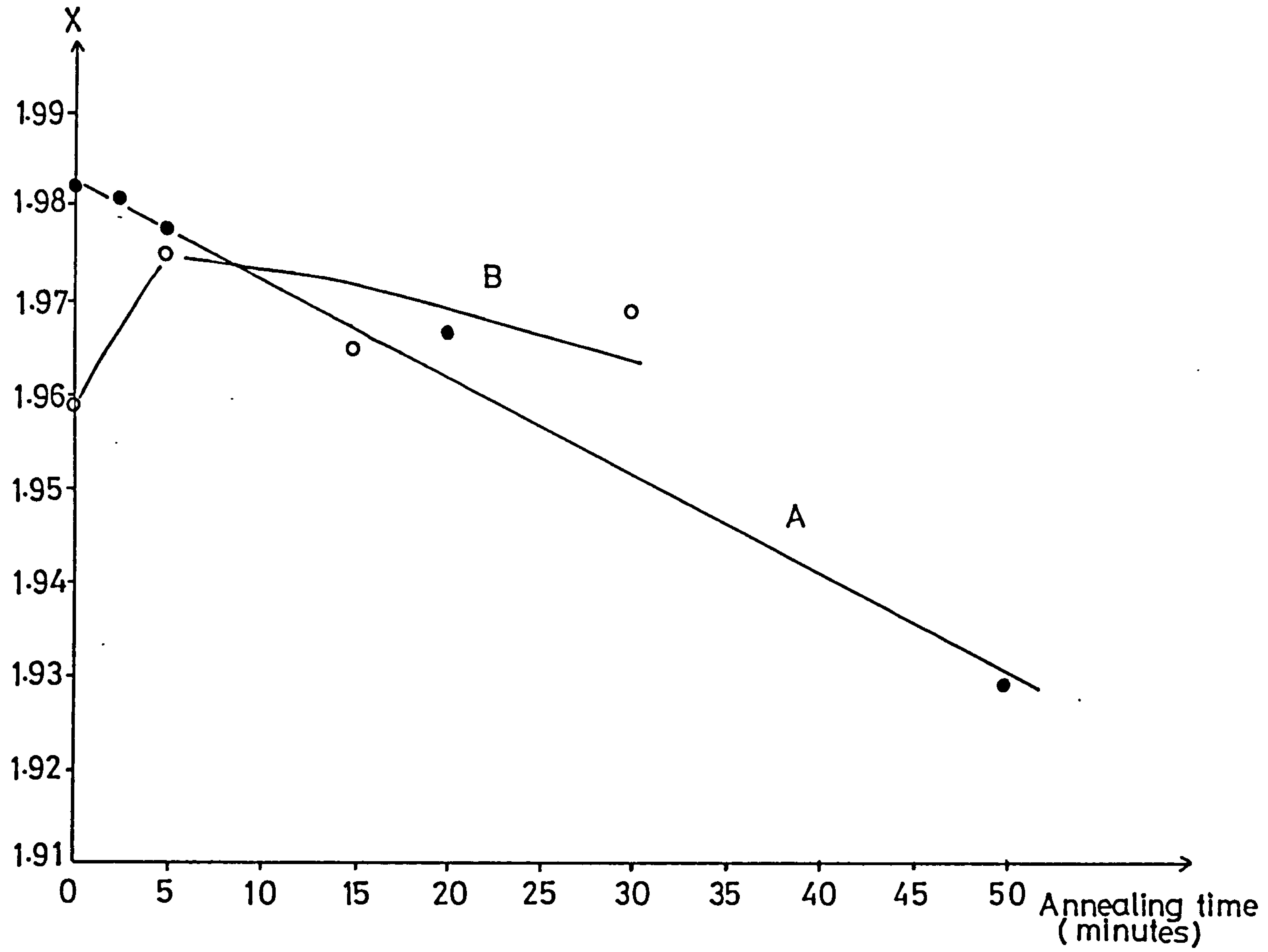

Fig.(5.28) The stoichiometry parameter x of the Cu_xS layer as a function of annealing time in air at 200°C.

As has been previously discussed (section 4.3), the Cu^{++} ions can be introduced into the CuCl solution as a result of oxidation of Cu^{+} ions by dissolved oxygen in the CuCl solution. By not supplying nitrogen gas to the CuCl solution, dissolved oxygen is not so effectively removed from the bath. Such a bath was used for sample B. It has previously been shown (182) that high concentrations of Cu^{++} ions in the bath can reduce significantly the formation rate as well as the x value of the Cu_xS layer. This is confirmed by the results in figure 5.29 which shows the initial Cu_xS layer thickness to be 0.51 μm for sample A but only 0.21 μm for sample B.

A difference in air annealing behaviour similar to that shown in figure 5.28 has been found by Salkalachen and coworkers (231) who used two different solutions (with pH values of 2 and 4.6) to create Cu_xS layers with different values of x. They attributed the different behaviour to different concentrations of free Cu^{++} ions trapped at the Cu_xS-CdS interface which became redistributed in the Cu_xS layer during the annealing process. However, it should be noted that this mechanism was inferred from changes in the depth profile of Cu and Cd making use of XPS. As the different layers were formed using solutions of different acidity (pH = 2, pH = 4.6), it is expected that the structures of the layers were quite different (in relation to grain boundary penetration), as discussed in section 5.2.1) and this must seriously affect the interpretation of the depth profile data.

One mechanism for the reduction in x value associated with extensive air annealing in all samples is of course an oxidation process, and increases in the oxide thickness are clearly observed, as shown in figure 5.30 for samples A and B of figure 5.28. The growth of an oxide layer at the surface of a solid material is frequently

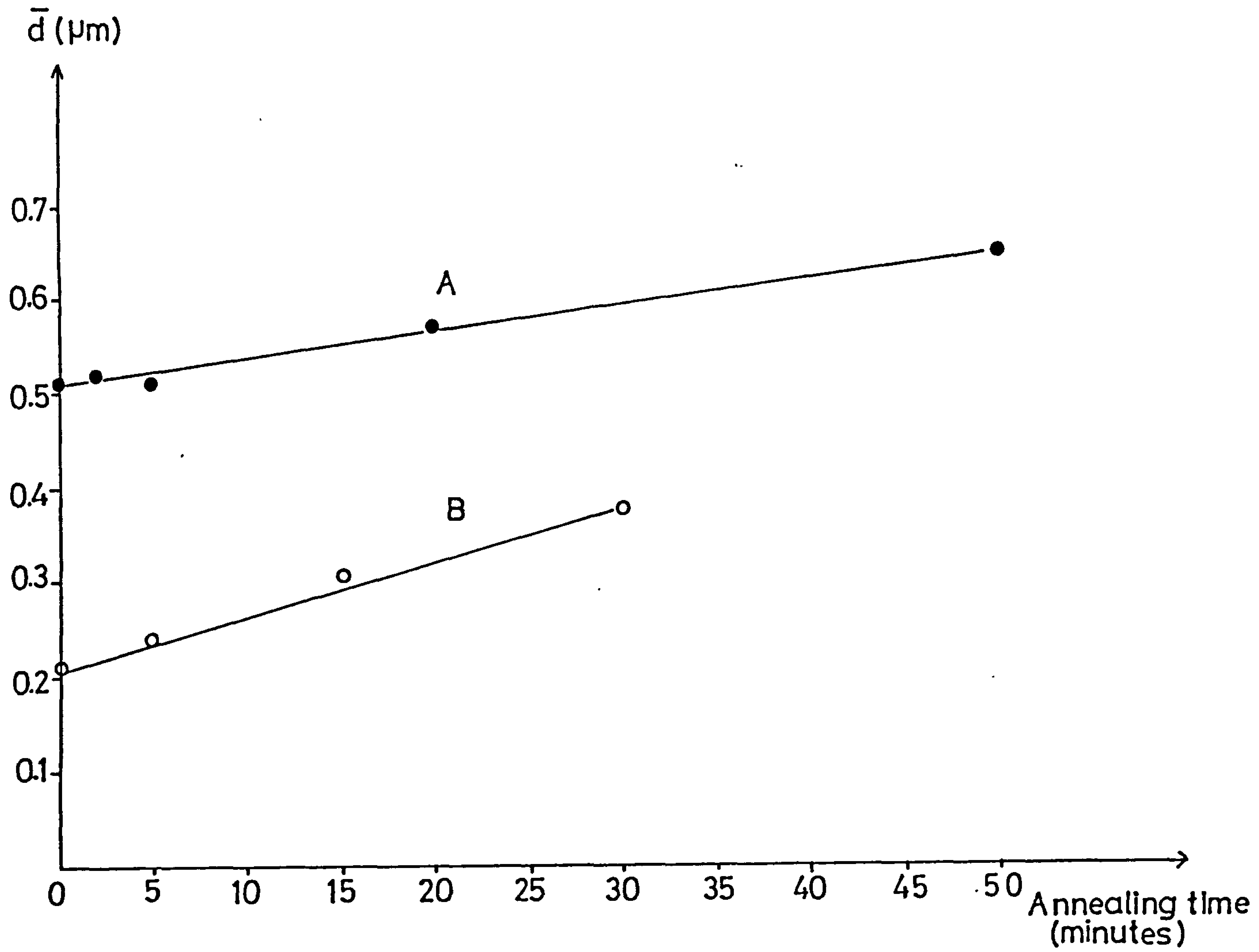

Fig.(5.29) The variation of Cu_xS layer thickness as a function of annealing time in air at 200°C.

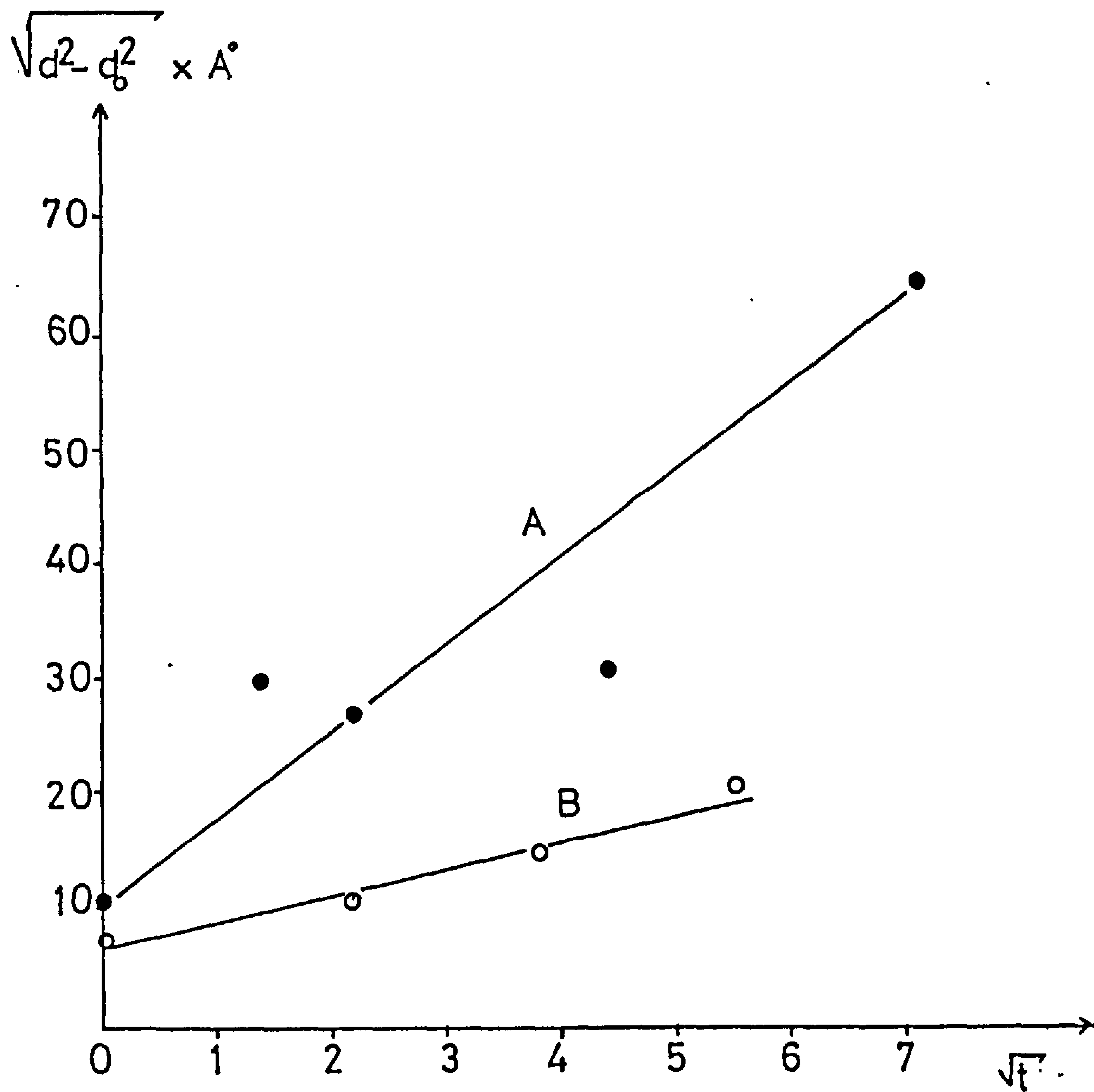

Fig.(5.30) The growth of oxide thickness at the surface of two different thicknesses of Cu_xS layer. (0.51µm for line A and 0.21µm for line B), as a function of annealing time in air.

found to follow a parabolic law as a result of the process being diffusion limited. Such a process appears to be involved in this case as can be seen in figure 5.30, where the oxide thickness d is plotted in the form $(d^2 - d_0^2)^{1/2}$ against the square root of annealing time in air, where d_o is the thickness of oxide at the surface of Cu_xS layer before annealing in air. The results in figure 5.29 show that, as the oxidation proceeds, the thickness of the Cu_xS layer also increases with increasing annealing time. Such a result would not be expected if it was assumed that oxidation involved only the removal of Cu from the Cu_xS layer. However, experimental evidence has been provided (178, 166, 183) to indicate that oxides of cadmium as well as copper are formed, as a result of out-diffusion of Cd from the CdS layer. The overall reaction proposed by Florio (178) can be described by equation (3.4.1) as discussed in section (3.4.3). It is clear that such a process leads to an increase in the thickness of the Cu_xS layer at the expense of the underlying CdS (183). Since the total content of Cu is unchanged, there is a corresponding reduction in x as confirmed by the data in figure 5.28. This degradation of the Cu_xS layer can be reversed by annealing in hydrogen, as can be clearly seen by the data in table 5.6. This table gives the thickness and stoichiometry factor x for a CdS-Cu_xS cell before and after annealing for 10 minutes in air. As discussed above, this has the effect of increasing the Cu_xS layer thickness and reducing x. Subsequent annealing in hydrogen for a much longer time (5 1/2 hours) restores both the thickness and x parameters to magnitudes close to their original values. It is interesting to note, however, that the effect of annealing in hydrogen alone for the same length of time does

not have such a significant impact on these parameters.

Table 5.6: Thickness, stoichiometry and sheet resistance for unannealed and annealed Cu_xS-CdS solar cells in hydrogen and air atmospheres at 200°C.

	Thickness of Cu_xS (μm)	x	Sheet resistance (Ω)
Unannealed Cu_xS-CdS	0.49	1.99	-
Cu_xS-CdS annealed in air 10 minutes	0.68	1.97	464
Cu_xS-CdS annealed in air 10 minutes and in H_2 for 5 1/2 hours	0.45	1.98	4844
Cu_xS-CdS annealed in H_2 for 5 1/2 hours	0.50	1.99	5444

Due to the ECA technique being a destructive technique, measurements which involve comparison between film properties associated with different treatments, depend upon the availability of many samples which are initially identical. For polycrystalline materials like those used in this project, it is very difficult to achieve exactly identical samples in large numbers and it is for this reason that some scattering of the points occurs in the results such as those presented in figures 5.28 - 5.30. Fortunately, there are other non-destructive, techniques which can provide information concerning the Cu_xS layer characteristics. One such technique involves the measurement of the sheet resistance. With x values close to 2 in Cu_xS layer the sheet resistance is very high. Deviations from ideal stoichiometry associated with diffusion of copper into the CdS layer or oxidation at the Cu_2S surface lead to an increase in the concentration of copper vacancies and consequently to an increase in the free hole concentration. The sheet resistance of the Cu_xS layer

is therefore reduced as illustrated by the data included in table 5.6. Sheet resistance measurements for Cu_xS layers of the same two types as those presented in figure 5.28 are shown in figure 5.31. Here, again, the results are plotted as a function of annealing time in air. These results appear to indicate that the sheet resistance increases for the first 5 minutes and subsequently reduces. However, the values of the sheet resistance for low annealing times cannot be considered to be reliable. When first formed (prior to annealing), the CdS space charge region at the junction between the Cu_2S and CdS layers is very narrow so that the junction impedance is very low due to electron tunnelling through the barrier. Under these condition accurate sheet resistance measurements for the Cu_xS layer are prevented by a substantial leakage current flowing through the CdS layer and back contact. However, following a short annealing time, the diffusion of Cu into the CdS leads to the formation of acceptor states which compensate the donors in the region near to the junction. This causes a reduction in the space charge density and to a corresponding increase in space charge width which prevents tunnelling and therefore, increases the barrier impedance so that the leakage current is cut off. For annealing times in air of more than 5 minutes a steady reduction in the sheet resistance of the Cu_xS layer is observed. This is consistent with the reduction in the stoichiometry factor x for these layers as observed in figure 5.28. It should be noted that the greater sheet resistance for sample B and its apparent greater sensitivity to the influence of air annealing can be attributed to the Cu_xS layer for sample B being much thinner than that for sample A, as indicated by the results in figure 5.29. Sheet resistance measurements carried out on Cu_xS layers formed on air

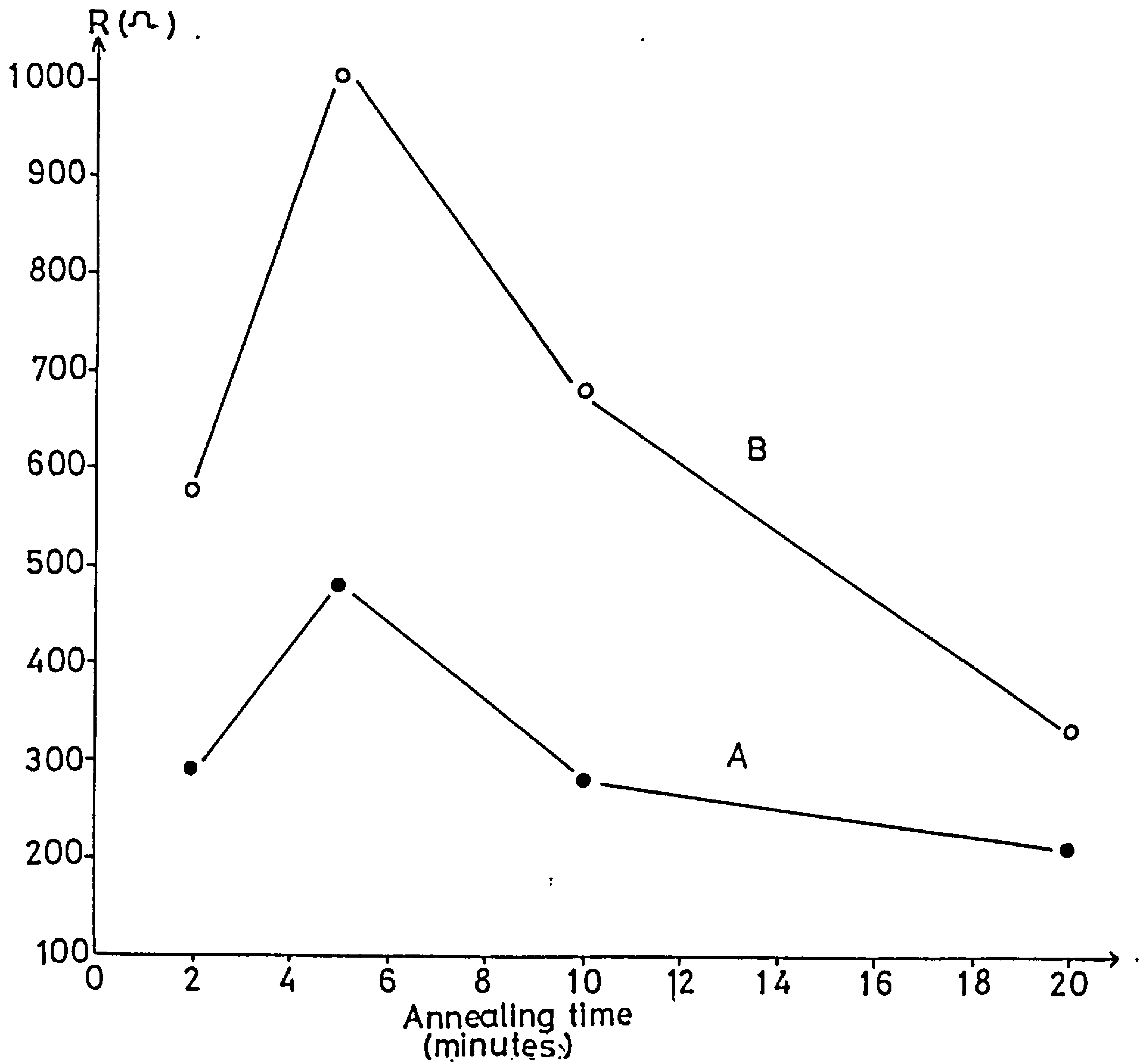

Fig.(5.31) The sheet resistance measurements for Cu_xS layers of different initial thickness (curve A: 0.51 μm and 0.21 μm curve B), as a function of annealing time in air.

annealed CdS layers have provided some additional information concerning the structure of these layers using identical samples of CdS to figure 5.21. Cu_xS layers were formed after etching the CdS layers for 3 seconds and annealing in air for different lengths of time at 200°C. The CdS layers were dipped for 2 seconds and subsequently annealed in vacuum for 1/2 hour at 200°C. The resultant sheet resistance of the Cu_xS layers are shown in figure 5.32 as a function of the initial CdS air annealing time. It can be seen from figure 5.32 that the sheet resistance of the Cu_xS was decreased by this treatment, as was expected in view of the known increase in Cu_xS layer thickness, as determined from the ECA data (figure 5.24). However, while the ECA data showed a rapidly increasing Cu_xS layer thickness with increasing CdS air annealing time, the measurements in figure 5.32 do not indicate a corresponding steady fall in sheet resistance. Instead, following an initial rapid reduction, there is a subsequent, much more slowly varying resistance after 1 hour pre-annealing. This is consistent with the Cu_xS layer in these samples forming predominantly in the CdS grain boundary regions rather than over the upper surface. Further evidence for this structure is presented in section 5.2.4.

5.2.4 Luminescence characteristics

Following the work of Hwang et al (232) on luminescence from Cu_xS layers, it was established that the chalcocite phase gives rise to a characteristic emission band at 0.96 μm and that the emission intensity falls sharply as the x value decreases below 2. Accordingly, it was suggested that cathodoluminescence could be used

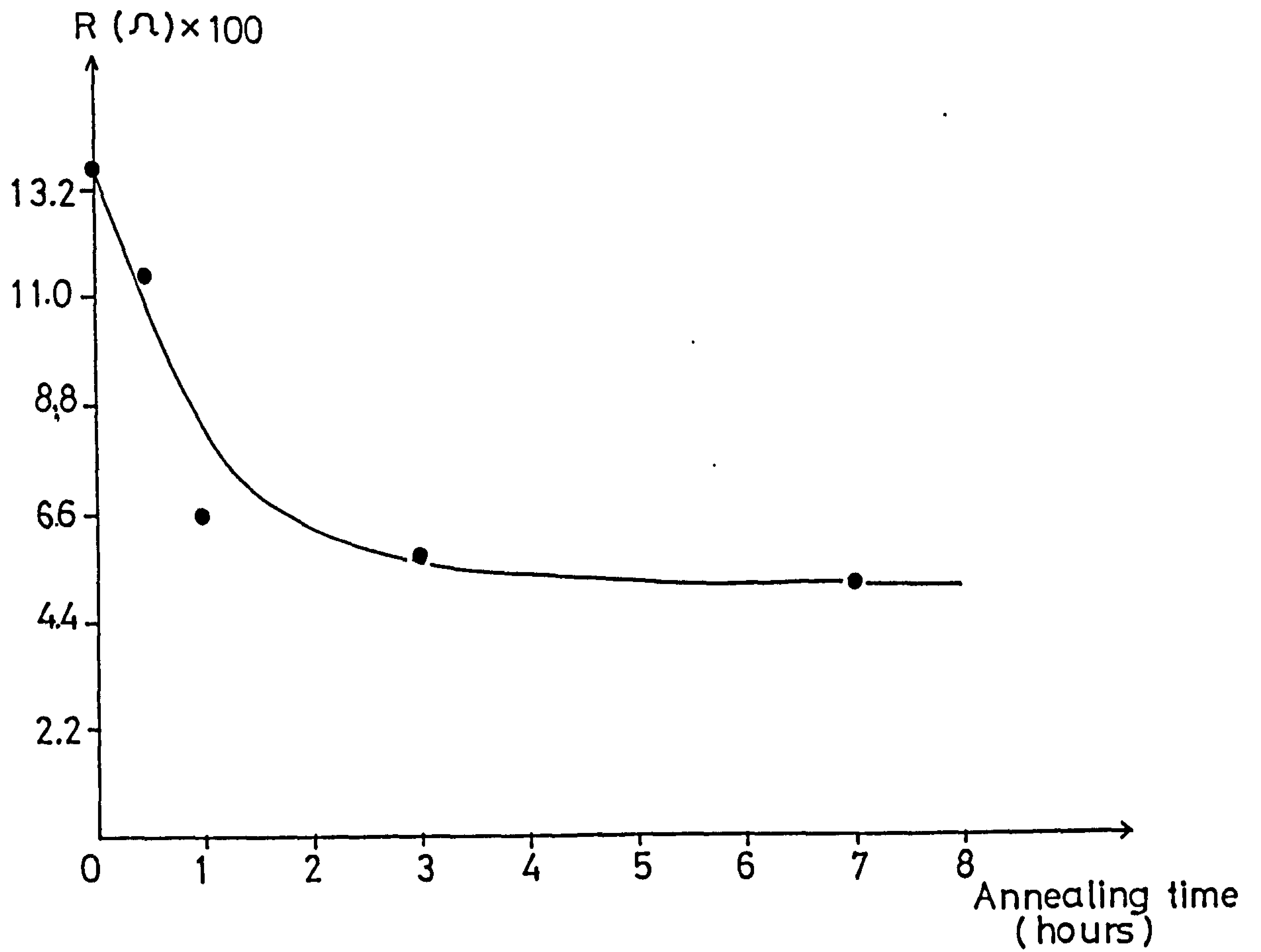

Fig.(5.32) The sheet resistance measurements of Cu_xS layers against time of initial annealing given to the preetched CdS layers in air at 200°C (dipping time was 2 seconds).

as an effective non-destructive technique for characterising the Cu_xS layers formed during cell fabrication. For the purposes of the present study of Cu_xS-CdS cells, in which the stability of the cells was to be a major concern, a non-destructive contactless technique for monitoring changes in stoichiometry of Cu_xS layer presented clear advantages to both the ECA and sheet resistance methods. Therefore, a study of CL emission spectroscopy was begun. A typical spectrum is shown in figure 5.33. This is for a sample in which the Cu_xS had been prepared using standard conditions (CdS etched for 3 seconds and dipped in CuCl for 2 seconds). Unlike the spectra obtained by Hwang and coworkers (232) for pure chalcocite layers, which consist of a single narrow peak centred at 0.96 μm, the spectrum in figure 5.33 clearly shows two broad features, one centred just below 0.8 μm with a shoulder at ~ 0.9 μm and the other at ~ 1.0 μm. Attempts to generate the chalcocite related 0.96 μm peak by annealing samples of this kind in hydrogen for long periods proved to be unsuccessful. It was assumed at this stage that any emission from the Cu_xS layer was being masked by stronger emission from the CdS and so some single Cu_xS layers (evaporated onto glass substrates) were examined before and after prolonged hydrogen annealing. These produced no detectable emission probably due to these layers being very thin (~ 0.2 μm). As the Cu_xS layer on the CdS/Cu_xS sample in figure 5.33 had a similar thickness, it was therefore assumed that all the emission seen in this figure 5.33 was associated with the CdS rather than the Cu_xS layer. As the penetration depth for the 10 k eV electrons is ~ 1 μm (233) it is clear that both the CdS and Cu_xS are excited by the cathode beam. In order to improve the chances of observing luminescence emission from Cu_xS formed by the Clevite method, some very thick layers were

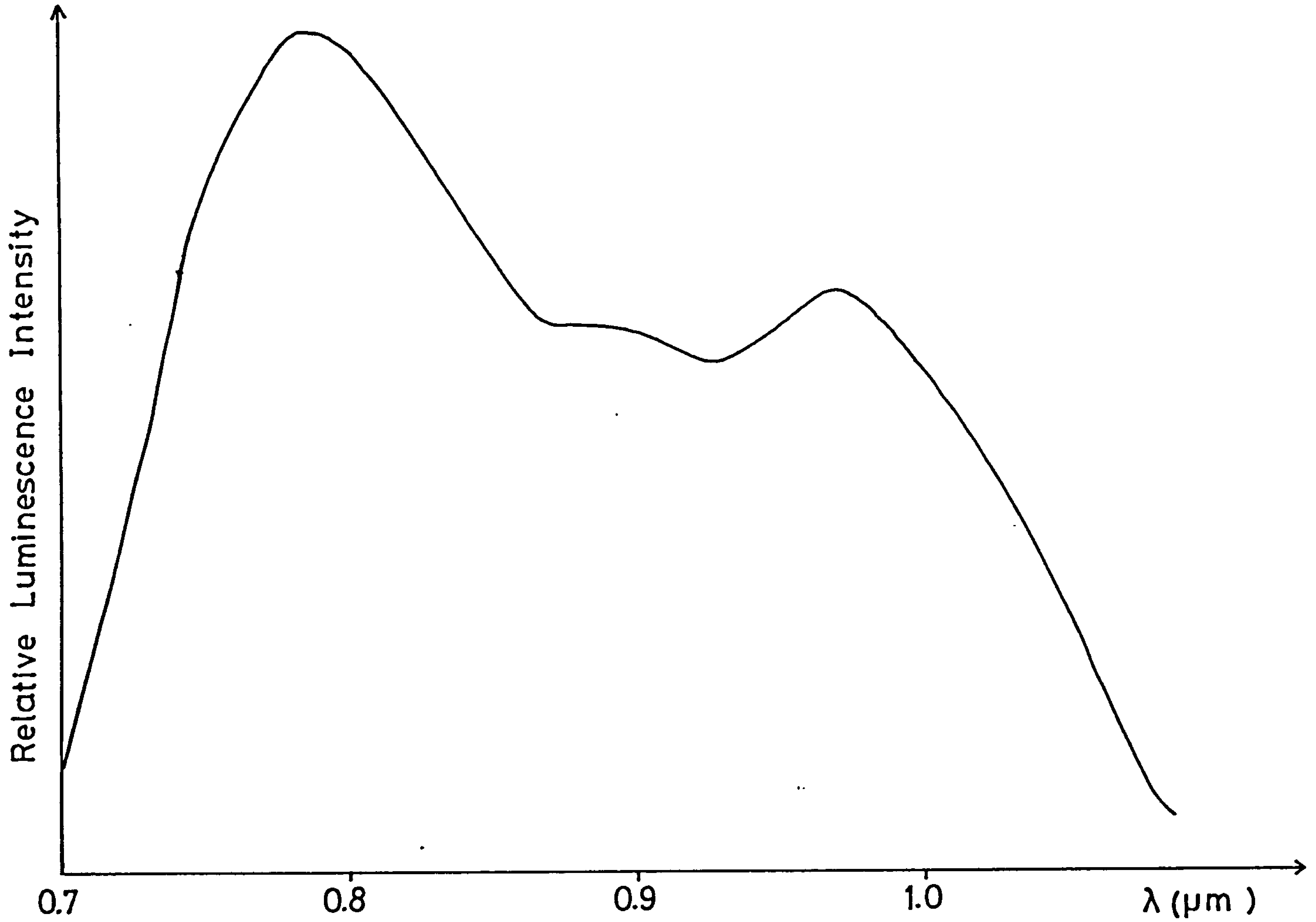

Fig.(5.33) Typical cathodoluminescence spectrum for Cu_xS-CdS cells annealed in vacuum for 30 minutes at 200°C.

formed by dipping for a much longer time than usually employed. Following the conclusions reached in the previous section concerning the effect of different annealing treatments on the copper sulphide stoichiometry, the thick Cu_xS layers were annealed for an extensive period in hydrogen with a view to increasing the fraction of chalcocite. This process was successful in producing CL specta with a peak which could be attributed to chalcocite as can be seen in figure 5.34 (curve A) which shows the emission for a CdS film which was etched for 3 seconds and dipped for 2 minutes in a standard hot CuCl bath. This sample was subsequently annealed in H_2 for 17 hours. The first thing to note in figure 5.34 is the large noise signal indicating that the whole emission spectrum is very weak in comparison with the luminescence emerging from the Cu_2S/CdS samples in figure 5.33. The second point to note from figure 5.34 is that the emission spectrum displays two peaks (in the vicinity of 0.97 µm and 1.03 µm) and the peak at 0.97 µm is very close to that observed in chalcocite by Hwang as mentioned above. As a further confirmation of this, the spectrum is compared in figure 5.34 with the emission from a sample of pressed powder of Cu_2S, again after annealing in H_2 for 17 hours (curve B). This clearly provides a single peak at the same wavelength (0.97 µ m). The peak in the neighbourhood of 1.03 µm was also discovered by Loferski et al (234) in polycrystalline pressed bars of chalcocite which had been doped with Cd. Therefore, it is apparent that the Cu_2S layers formed by the Clevite, copper-cadmium exchange method contain a significant concentration of Cd. The weakness of the emission from these Cu_2S samples supports the earlier suggestion that the emission from the Cu_xS/CdS samples prepared in the normal way was

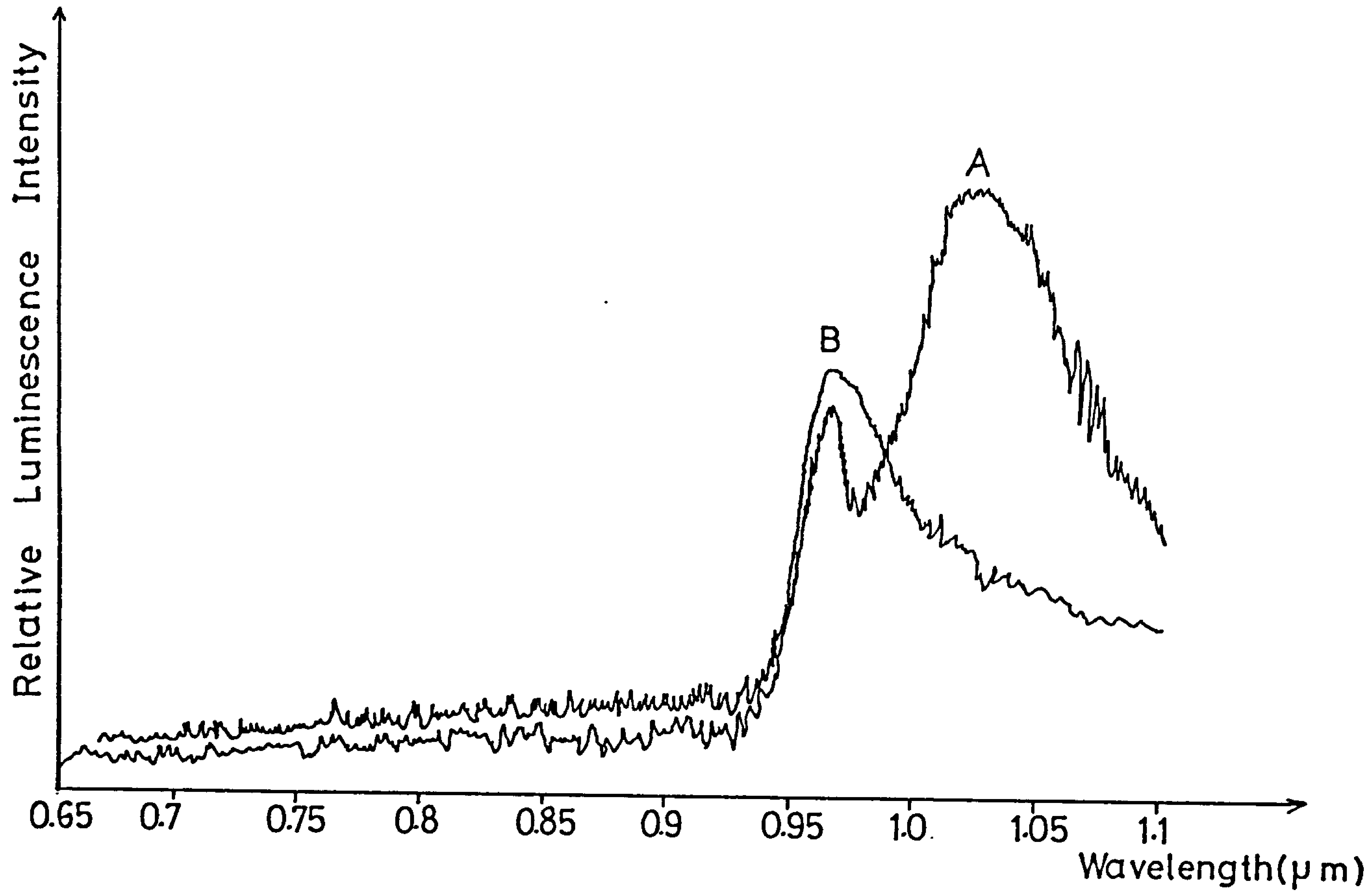

Fig.(3.34) Curve A - the emission spectrum for a CdS film which was etched for 3 seconds and dipped for 2 minutes in standard CuCl bath. The sample was subsequently annealed in hydrogen for 17 hours at 200°C. Curve B - the emission spectrum for a pressed powder of Cu_2S after annealing in hydrogen for 17 hours.

dominated by emission from the CdS layer. More detailed consideration was therefore given to CdS films without a Cu_xS layer.

Previous reference has been made to an emission peak at 0.78 μm section (5.1.2) μm being associated with impurity related defects in CdS and it was suggested that residual Cu could play a role. Of course, in the CdS layers covered with Cu_xS, copper is known to diffuse into the CdS film and this could enhance this emission peak. This possibility was examined by comparing the emission from CdS films with and without a thin coating of metallic copper (deposited by evaporation). The results are shown in figure 5.35. Curve A is for a CdS film with 100 Å of copper deposited on its surface and curve B is for a similar film without copper. Both samples were given the same etch treatment and both were annealed for 1/2 hour at 300°C in vacuum to allow the copper to diffuse in the sample A. It can be seen that the peak centred at 0.8 μm is certainly enhanced by the incorporation of Cu and that a new band at ~ 1.0 μm (as appeared in the Cu_xS-CdS sample in figure 5.33) is generated by this treatment. A spectrum with similar characteristics was also obtained from a Cu_xS-CdS sample from which the Cu_xS layer had been electrochemically transformed to Cu during an ECA experiment. The CL spectrum is shown in figure 5.36 for this sample which was annealed in hydrogen for 3 hours before the electrochemical reduction of the Cu_xS layer. The effect of this annealing would be to diffuse Cu from the Cu_xS layer into the CdS base-layer giving a CL spectrum with the same Cu-related emission bands as obtained by the more direct Cu doping process using a thin metallic Cu film.

Although these results confirmed that the observed luminescence

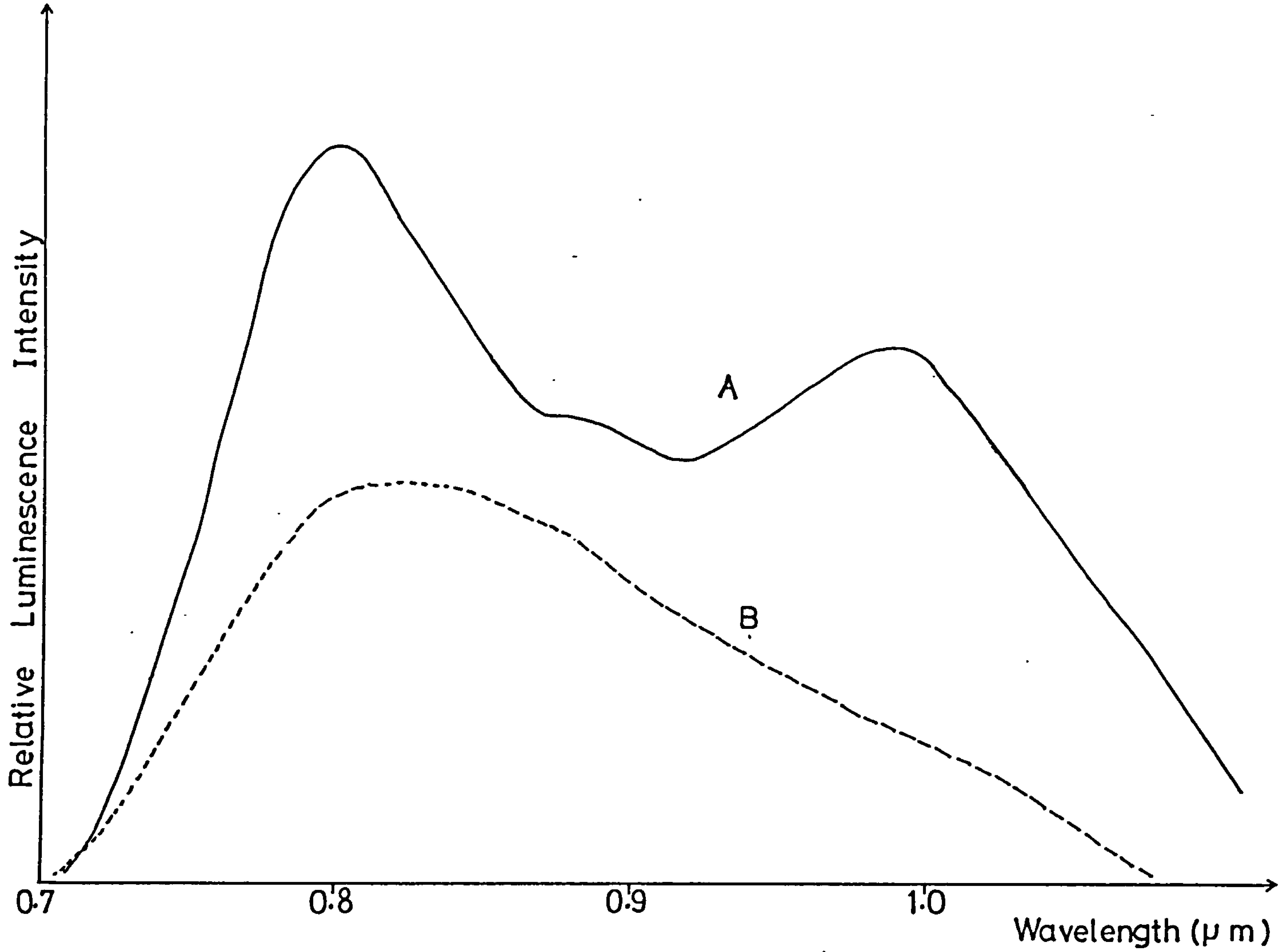

Fig.(5.35) The emission spectra for a CdS film with 100A of copper deposited at its surface (curve A) and for a similar film without copper (curve B).

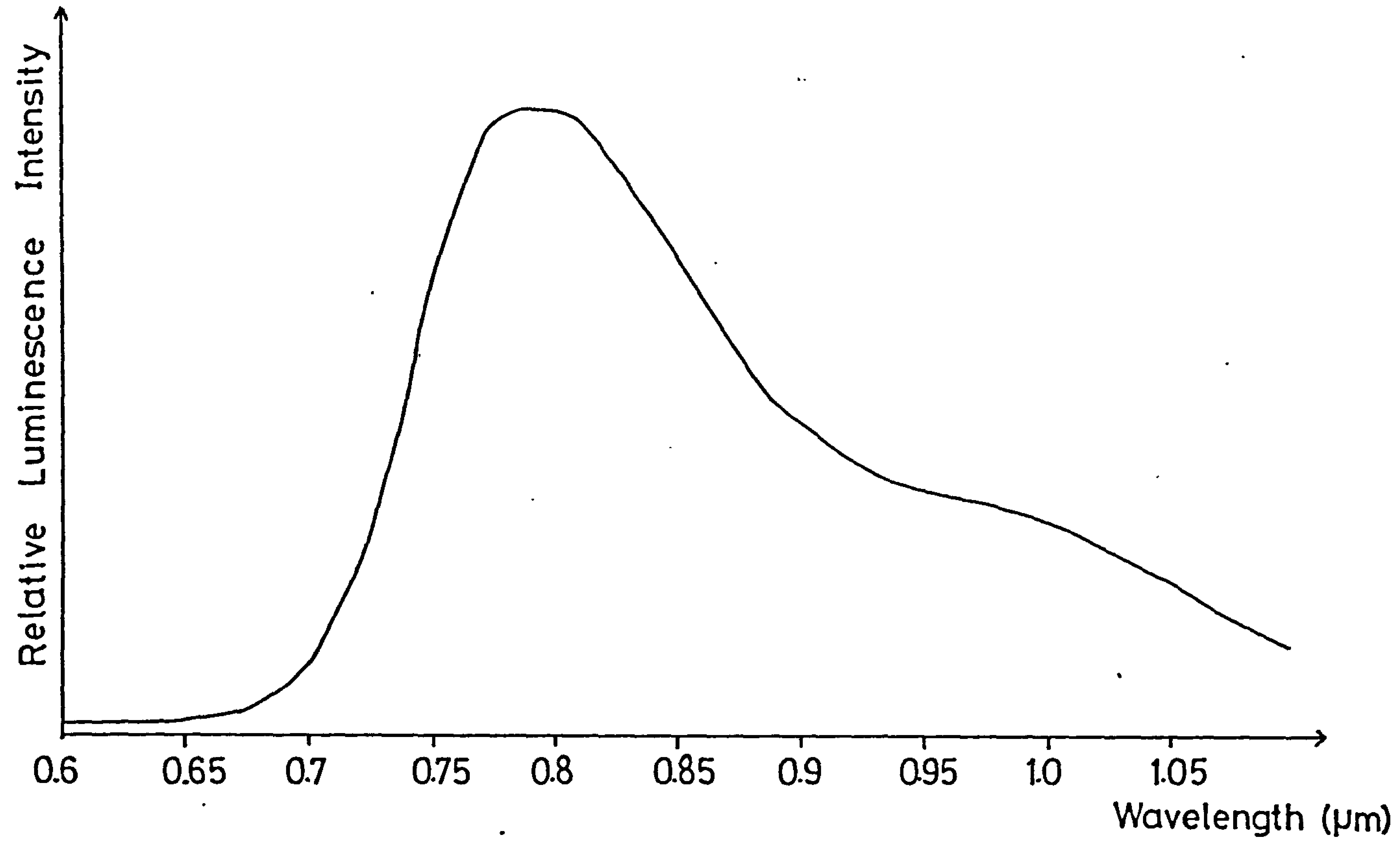

Fig.(5.36) The CL spectrum for a Cu_xS-CdS cell which was annealed in hydrogen for 3 hours before the electrochemical reduction of the Cu_xS layer.

emission was generated solely in the CdS, it was found as a result of further experiments, that useful information concerning changes in the Cu_xS layer properties could be deduced from changes in the observed CL spectrum. This was due to the effect of the Cu_xS layer on the CL emission from the CdS as it passed through the Cu_xS layer. The optical absorption coefficient and its spectral dependence are known to be very sensitive to the stoichiometry of the Cu_xS layer, so that the transmission of the CdS emission would be similarly dependent on Cu_xS thickness and composition. Unfortunately, attempts to measure directly the spectral dependence of the optical transmission for the Cu_xS layers used in this study proved to be unsuccessful. For this purpose CdS layers deposited on glass substrates were used and the measurements were made on a Pye Unicam 200 Spectrophotometer but the results were unsatisfactory due to excessive scattering in the polycrystalline films. A further attempt was made using epitaxial CdS films on single crystal GaAs substrates (grown by MOCVD at RSRE, Malvern, and kindly supplied by M. Halsall) but in this case the absorption in the very thin Cu_xS layer was masked by the greater absorption in the 1 μm thick GaAs layer. However, as discussed in section (3.3.2) many measurements on free standing Cu_xS layers and bulk samples have been made in other laboratories and, making use of such data, an indication is given in figure 5.37 of how the absorption in the Cu_xS layer influences the observed emission from the CdS film. Figure 5.37 shows a typical CL spectrum from a CdS layer together with the absorption coefficient spectral dependence for Cu_2S (as determined by Partain (167)). By calculating the transmission for a 0.2 and a 1.0 μm thick layer of Cu_2S, a modified CL spectrum has been drawn to indicate the emission which would be expected to be observed from a

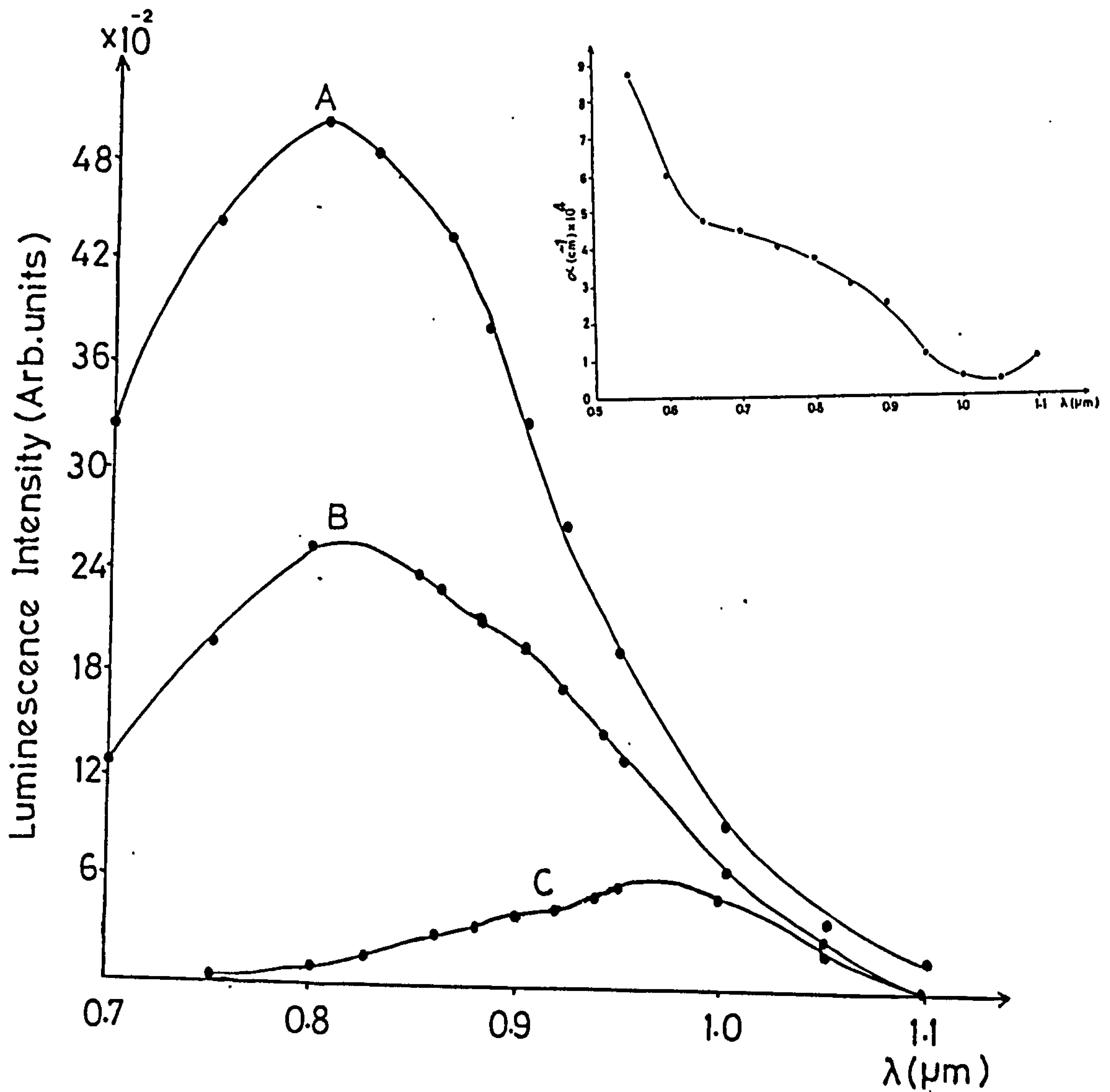

Fig.(5.37) The CL spectum for a CdS film alone (curve A) and the modified CL spectra due to the presence of a Cu_xS layer of thickness 0.2 μm (curve B) and 1.0 μm (curve C). The inset figure shows the absorption coefficient spectral dependence for Cu_2S (as determined by Partain (167)).

CdS layer with an overlayer of Cu_2S with uniform thickness of either 0.2 or 1.0 μm. Clearly, there is a substantial reduction in the 0.85 μm peak and a shoulder appears at ~ 0.9 μm as commonly found in the actual experimental data and as can be clearly seen in figure 5.33.

A large number of CL emission spectra for Cu_xS samples have been investigated and variations in the relative intensity of the luminescence in different spectral regions have been studied for different experimental conditions.

The simplest effect of Cu_xS layer thickness is seen clearly in figure 5.38 where curve A, B and C are the emission spectra for Cu_xS-CdS samples prepared using different dipping times of 2,6 and 12 seconds respectively. The luminescence intensity at 1.0 μm relative to the peak at ~ 0.78 μm clearly increases with increasing dipping time as predicted from the data in figure 5.37 (In fact, this intensity ratio is 2.03 for curve A, 3.5 for curve B and 4.2 for curve C). However, for the practical cells in figure 5.38, the Cu_xS layers do not have uniform thicknesses. The effect of increased dipping time on the structure of the Cu_xS layer was discussed in section (5.2.1) where evidence was presented indicating that with increasing dipping time the formation of Cu_xS layer becomes dominated by the growth at the grain boundaries. The effect on the luminescence coming from the grain boundary regions (with thicker Cu_xS layers to penetrate) would be a greater reduction in the intensity of the 0.8 μm emission relative to that at longer wavelengths. In fact, the CdS layers which were used to obtain the data in figure 5.38 were composed of small crystallites and after etching these layers showed many deep grain

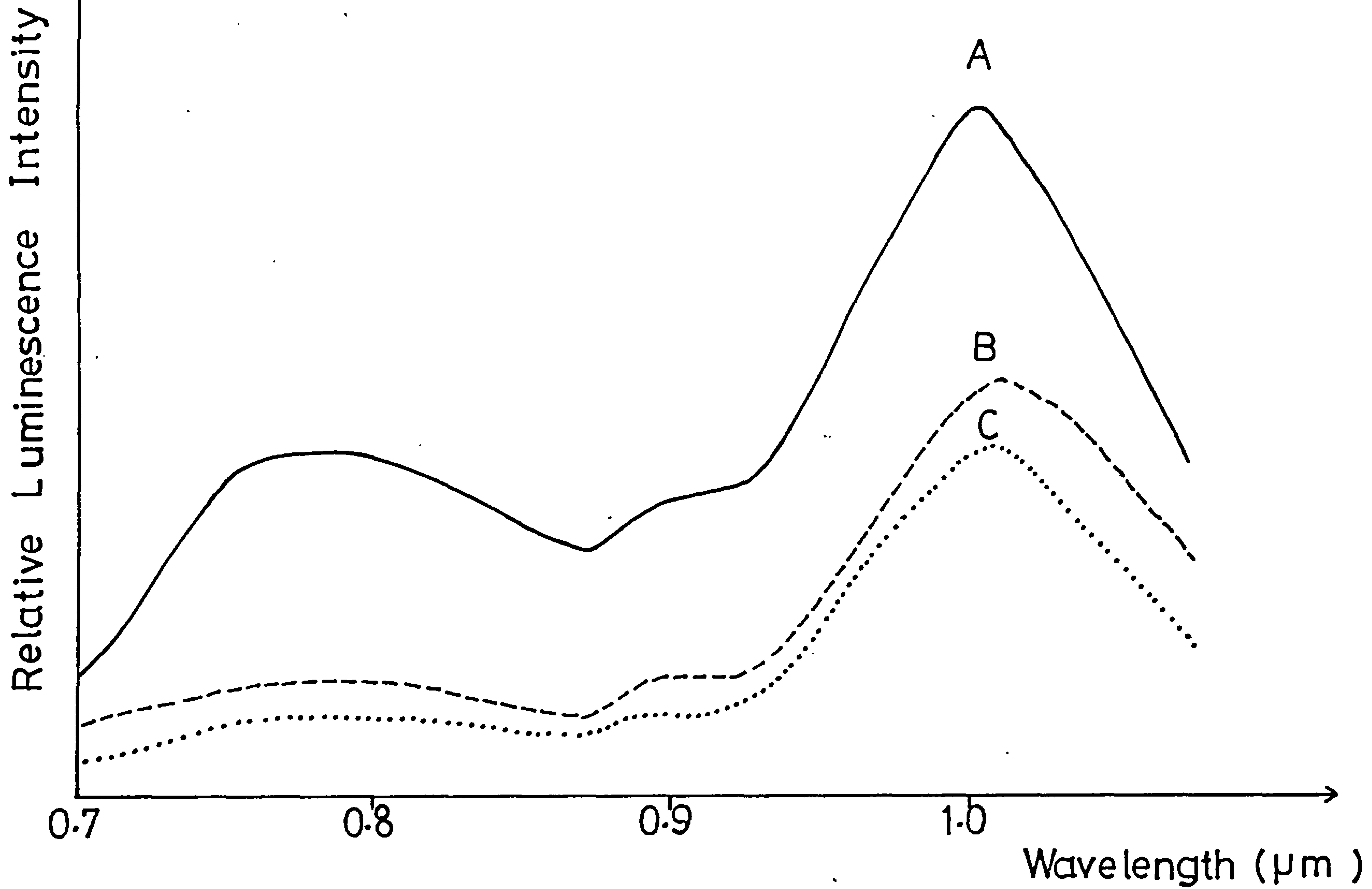

Fig.(5.38) The CL spectrum for Cu_xS-CdS cells prepared using different dipping times of 2,6 and 12 seconds (curve A, curve B and curve C respectively).

boundaries like those seen in figure 5.5(c,d). The effect of the greater density of grain boundaries would be the cause of further reduction in the 0.8 μm/1.0 μm luminescence intensity ratio. This explains why the 1.0 μm emission peak is actually of higher intensity than the 0.8 μm peak for the spectra in figure 5.38 whereas for films with larger crystallites (as used for most of the studies in this report), the 0.8 μm peak was usually the greater. This effect of the grain boundaries on the ratio of emissions at 0.8 and 1.0 μm is further supported by the cathodoluminescence spectrum seen in figure 5.39 where curve A and curve B are for CdS layers which were etched for 5 and 20 seconds respectively prior to dipping both samples for 8 seconds. Curve C is for a CdS layer which had been etched for 5 seconds and then dipped for 2 seconds. It is clear from curves A and B that increased etching time of CdS layers, which opens up more defects and grain boundaries for rapid Cu_xS growth has the effect of increasing the relative luminescence intensity of the peak of ~ 1.0 μm to the 0.8 μm peak. This ratio was 4.1 for curve A in figure 5.39 and increased to 8 for curve B. For curve C, the ratio was significantly less (1.2) as expected for the much lower dipping time.

Although the increased emission at ~ 1.0 μm relative to that at ~ 0.8 μm can be explained in terms of the thicker Cu_xS layer associated with increasing dipping time of CdS, (with the thicker regions of the Cu_xS layer being concentrated at the grain boundaries) the observed effects of greater grain boundary densities on the 1.0 μm to 0.8 μm emission ratio could alternatively be explained by the peak at 1.0 μm being generated with greater intensity at the grain boundary regions. Evidence supporting the suggestion that the 1.0 μm emission is associated with grain boundaries is provided by figure 5.40 which

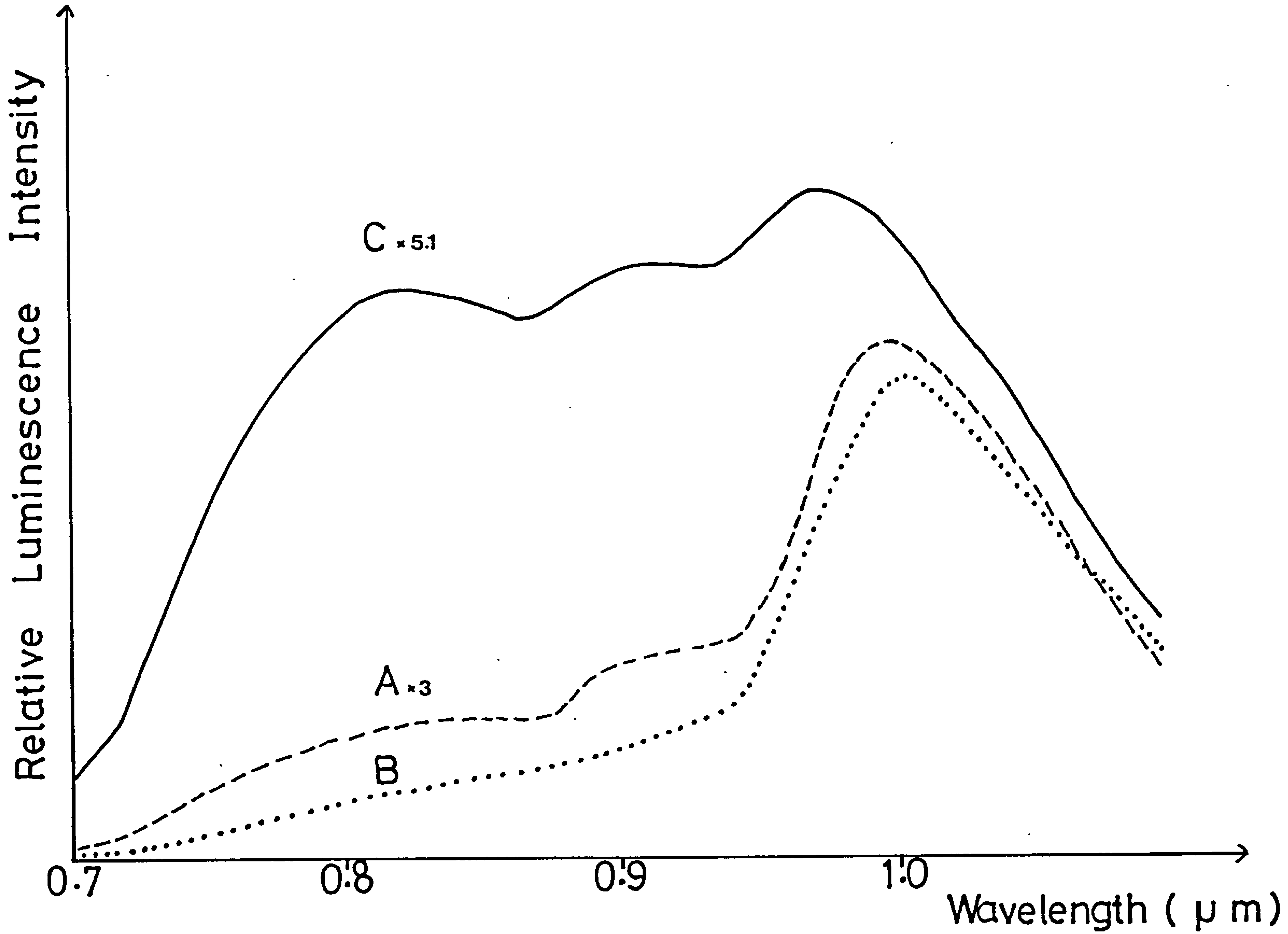

Fig.(5.39) The CL spectra for CdS layers (curves A and B) which were etched for 5 and 20 seconds respectively prior to dipping both samples for 8 seconds. Curve C is the CL spectrum for a CdS layer which had been etched for 5 seconds and then dipped for 2 seconds.

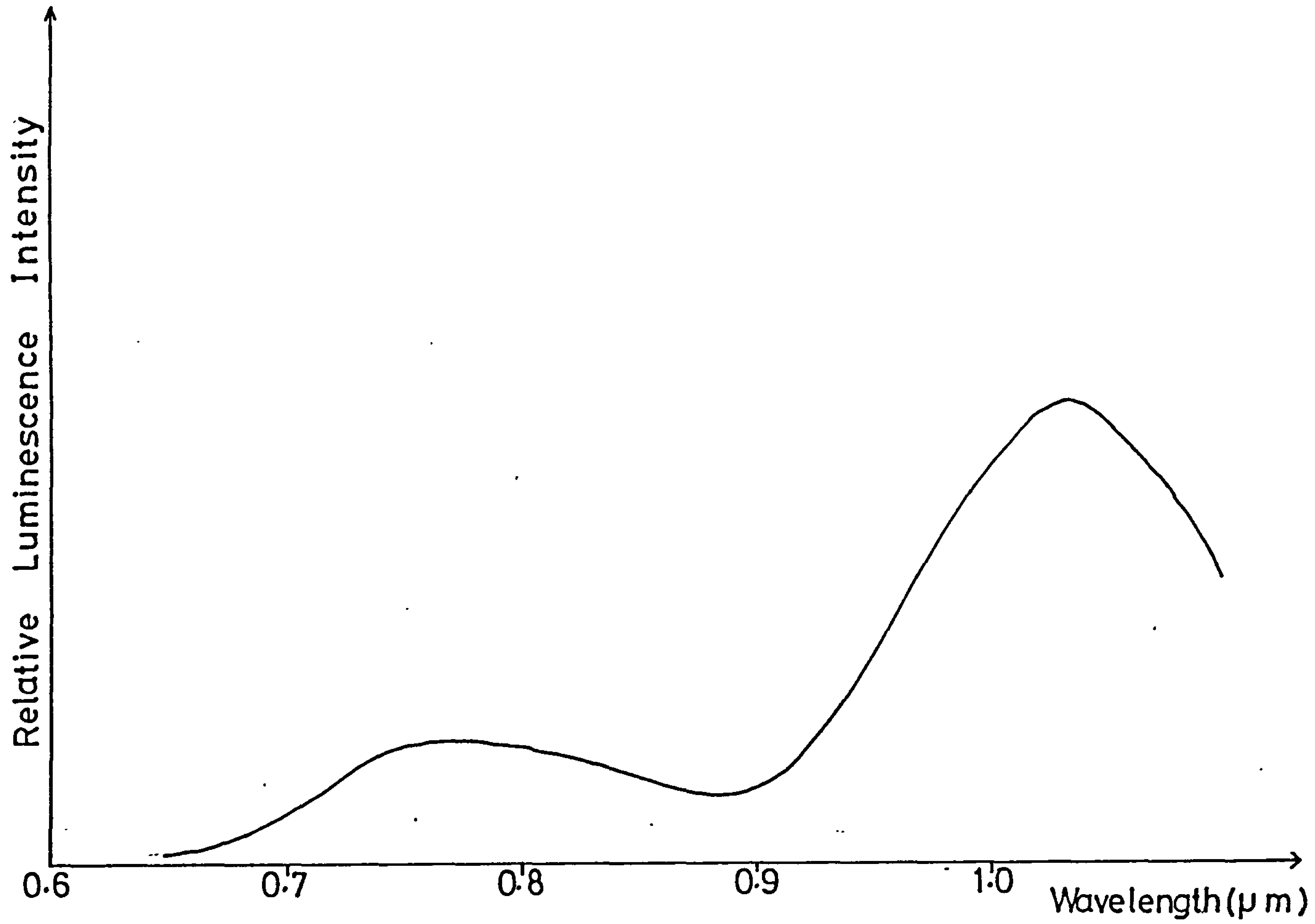

Fig.(5.40) The emission spectrum obtained from a CdS single crystal with a 100Å thick layer of copper deposited onto its surface before it was annealed at 300°C in vacuum for 30 minutes.

shows the emission spectrum obtained from a CdS single crystal with a 100 Å thick layer of copper deposited onto its surface before it was annealed at 300°C in vacuum for 1/2 hour to diffuse in the copper. This CdS single crystal was in the form of a platelet (~ 100 μm thick) with visible striations covering the surface running parallel to the c-axis. Thus, the surface orientation of this single crystal corresponded to grain boundary surfaces along which the Cu_xS layer penetrated in the polycrystalline films. The emission spectrum of figure 5.40 has a peak in the vicinity of ~ 1.0 μm which is of much higher intensity than that at ~ 0.8 μm (similar to those shown in figures 5.38 and 5.39 suggesting that the longer wavelength emission from those samples originates mainly from their grain boundaries. A further piece of evidence has come from work on the epitaxial layers of CdS referred to above. These single crystal layers were grown with the C-axis perpendicular to the plane of the layer, as in the polycrystalline films. The CL emission spectrum from such a sample is shown in figure 5.41 (curve A) together with that for a similar sample which had been dipped in a standard CuCl bath for 2 seconds to form a Cu_xS layer and annealed in hydrogen for 3 hours at 200°C (curve B). Both spectra display a peak at ~ 0.8 μm which is severely distorted by the GaAs absorption. Curve B shows an additional feature at ~ 0.91 μm which is characteristic of absorption within the Cu_2S layer as discussed earlier (figure 5.37), but neither spectrum shows any emission peak in the vicinity of 1.0 μm supporting the view that this emission is due to centres related to grain boundaries lying parallel to the C-axis (as discussed in section 5.1.2). In relation to figure 5.41 it should also be noted that for a GaAs/CdS sample which had been

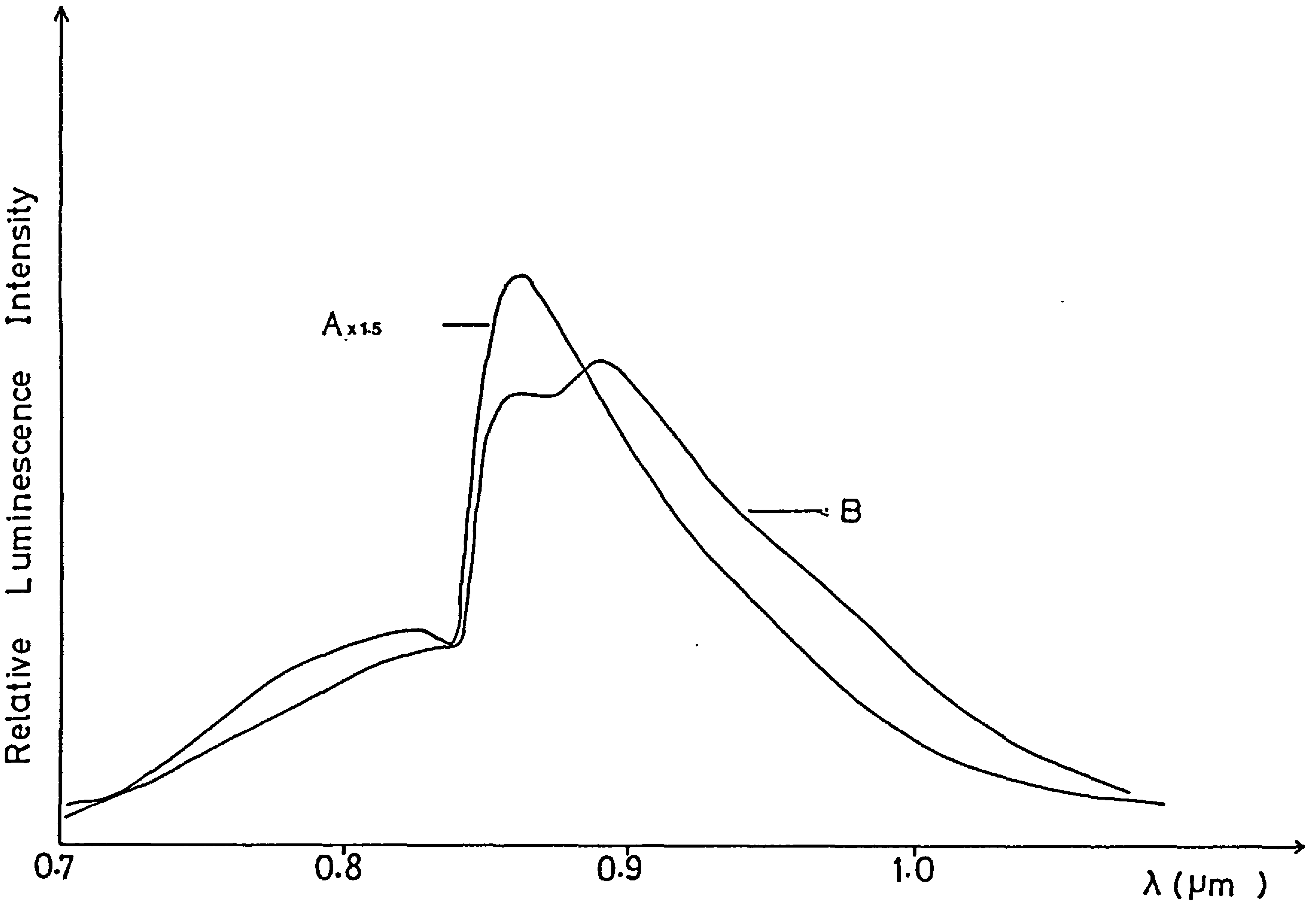

Fig.(5.41) The emission spectrum obtained from a CdS single crystal grown with the C-axis perpendicular to the plane of the layer (curve A) together with that for a similar sample which had been dipped in standard CuCl bath for 2 seconds and annealed in hydrogen for 3 hours at 200°C (curve B).

dipped for 8 seconds, the emission became very weak, as can be seen in figure 5.42. This was probably due to the full thickness of the CdS layer being converted into Cu_2S and is consistent with the earlier conclusion that all the observed emission is created in the CdS layer rather than in the Cu_xS layer.

As discussed in section (5.2.1), variations in Cu_xS layer thickness over the grain surface and grain boundary regions can arise from different predipping or post-dipping treatments rather than different dipping times. For example, figure 5.43 shows the CL spectra for CdS layers given different annealing treatments before dipping for the same length of time (2 seconds). The CdS samples were etched for 3 seconds and annealed in different atmospheres (air, vacuum and hydrogen) for 1/2 hour at 300°C. The annealed CdS layers were subsequently dipped into a standard CuCl bath at 95°C and the resultant Cu_xS-CdS cells were all annealed in vacuum at 200°C for 1/2 hour. The curves A, B and C are the spectra obtained using CdS films which had been pre-annealed in hydrogen, vacuum and air respectively. The thickness variations of Cu_xS layers formed as pre-annealed substrates have been discussed in section 5.2.2. The values of thickness (given in table 5.5) are seen to be increased for CdS which is annealed in air relative to those for vacuum or hydrogen pre-annealing. Similarly, the relative luminescence intensities of the peak at 1.0 μm to that at ~ 0.8 μm are increased as the thickness of Cu_xS layer increases, with values of 0.69, 1.056 and 1.45 for curves A, B and C respectively. It should be noted that according to table 5.5, the Cu_xS layer which was formed on air annealed substrate was very thick (3 μm) in comparison with vacuum and hydrogen annealed substrates. Therefore, at first sight, it is surprising to find that

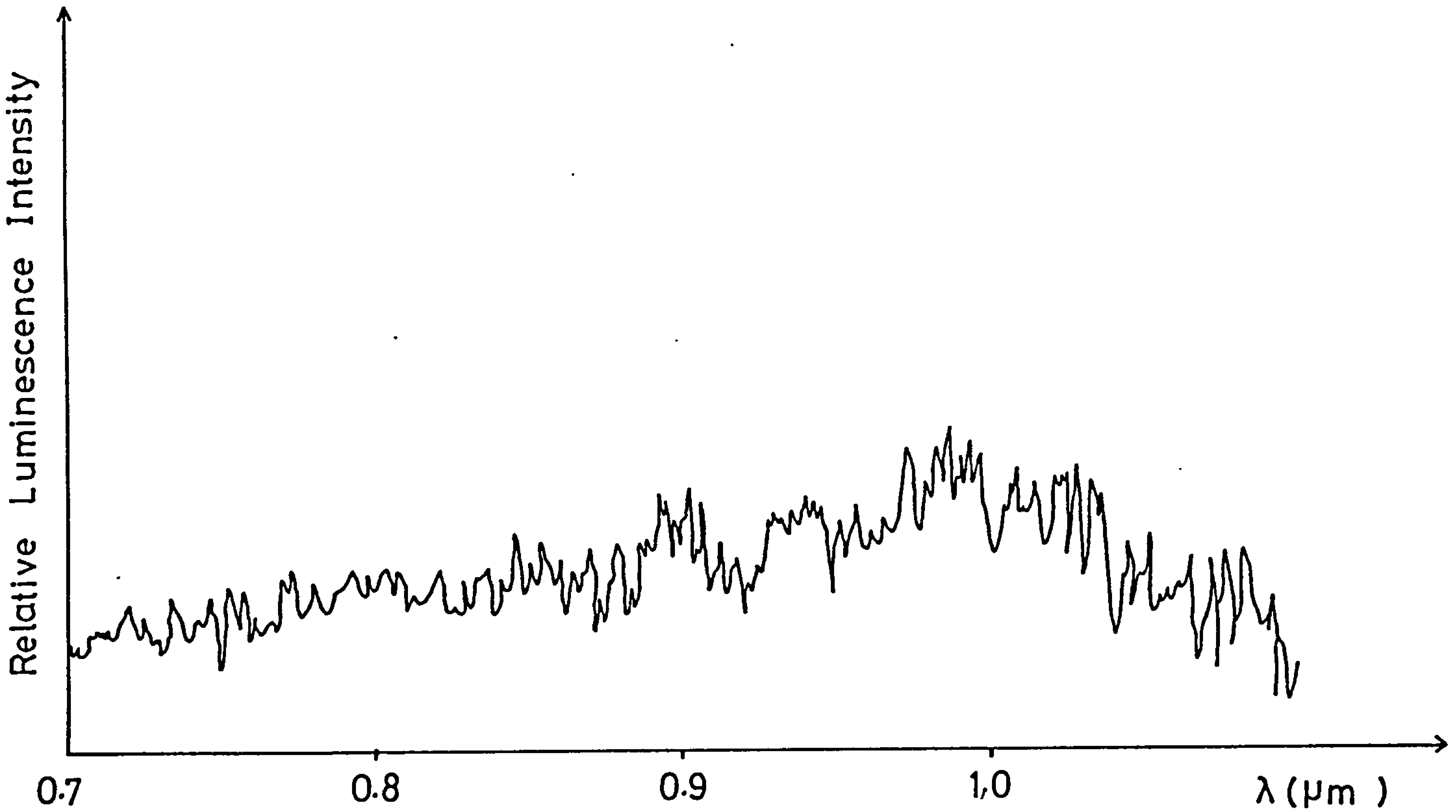

Fig.(5.42) The CL spectrum for GaAs/CdS sample after it had been dipped for 8 seconds and annealed in hydrogen for 4.5 hours at 200°C.

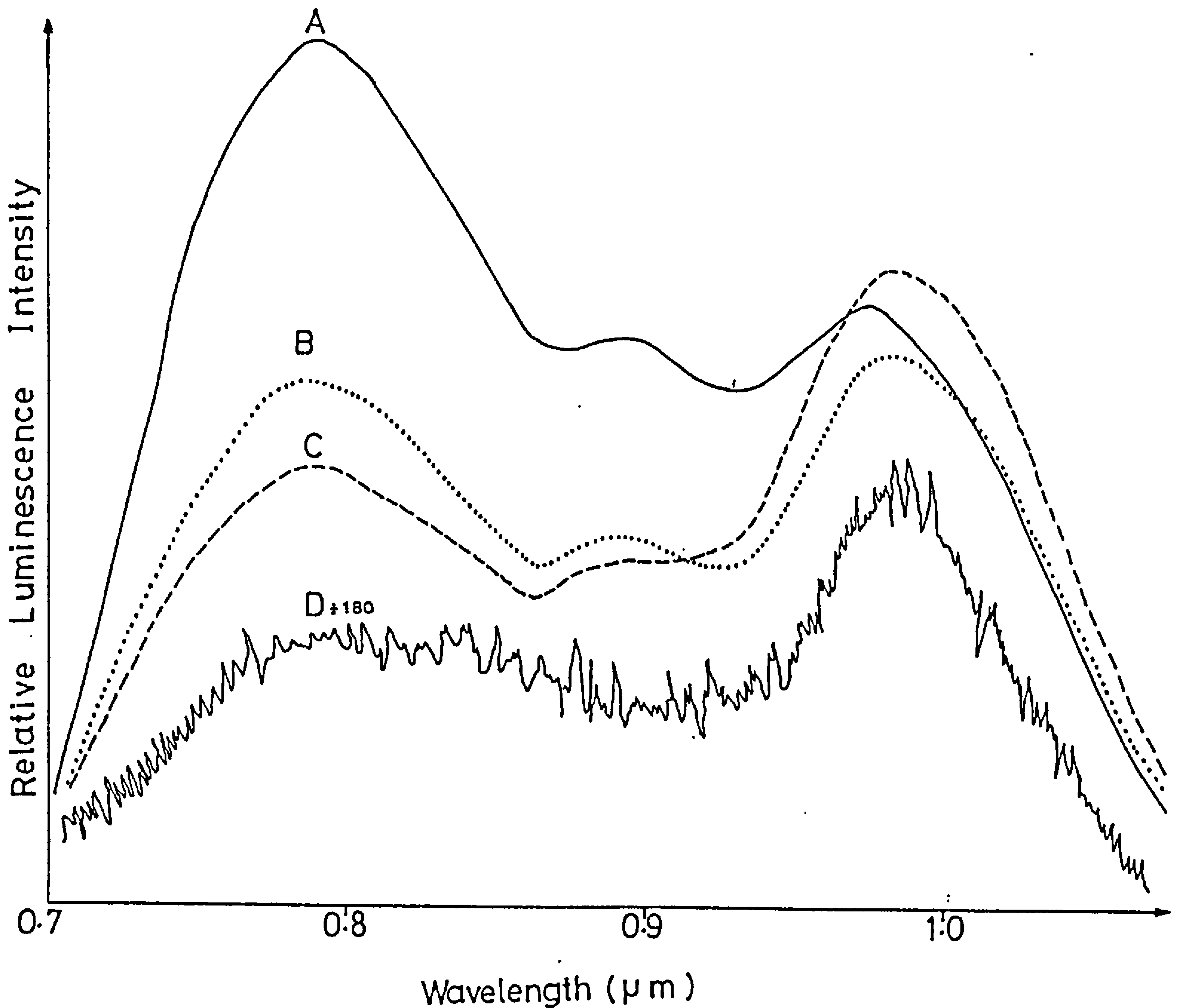

Fig. (5.43) The CL spectra for CdS layers given different annealing treatments in H_2 (curve A), vacuum (curve B) and in air (curve C) before dipping for 2 seconds. (The Cu_xS-CdS cells were given 30 minute anneals in vacuum at 200°C). Curve D represents the spectrum from another sample obtained using an unannealed CdS layer dipped for 24 seconds and annealed in vacuum for 30 minutes at 200°C.

the emission intensities for curves A, B and C in figure 5.43 are reasonably similar. However, an explanation for this is provided by the spectrum from another sample (curve D). Like the sample which had been pre-annealed in air, this sample had a thickness of 3 μm but this was obtained using an unannealed CdS layer and this required a dipping time of 24 seconds to achieve such a thickness of Cu_xS. Clearly the emission spectrum for this sample (curve D) was very weak in comparison with curve C. This supports the earlier suggestion that most of Cu_xS layer which was formed on samples which had been pre-annealed in air was lying in the grain boundary regions with only a relative thin layer covering the upper surface of the cell. However, for the sample of curve D the growth of Cu_xS is known to take place both at the free surface of the CdS layer and at the grain boundaries and by dipping for a very long time (24S) a very thick surface layer of Cu_xS was formed, causing a very big reduction in the emission. Pre-annealing the CdS in hydrogen has very little influence on the formation of the Cu_xS layer as shown by curve A which is similar to the emission spectrum which is obtained from samples for which the Cu_xS layer was formed on unannealed CdS films.

As would be expected, the CdS short wavelength (band edge) CL emission is also reduced by increasing the thickness of Cu_xS layer but an even greater reduction in the intensity occurs due to the larger absorption coefficient for Cu_xS at these wavelengths. An example of the effects of pre-annealing treatments similar to those for samples in figure 5.43 is given in figure 5.44.

The effects of post-dipping annealing treatments are illustrated by figures 5.45, 5.46 and 5.47. In figure 5.45 is shown the Cl

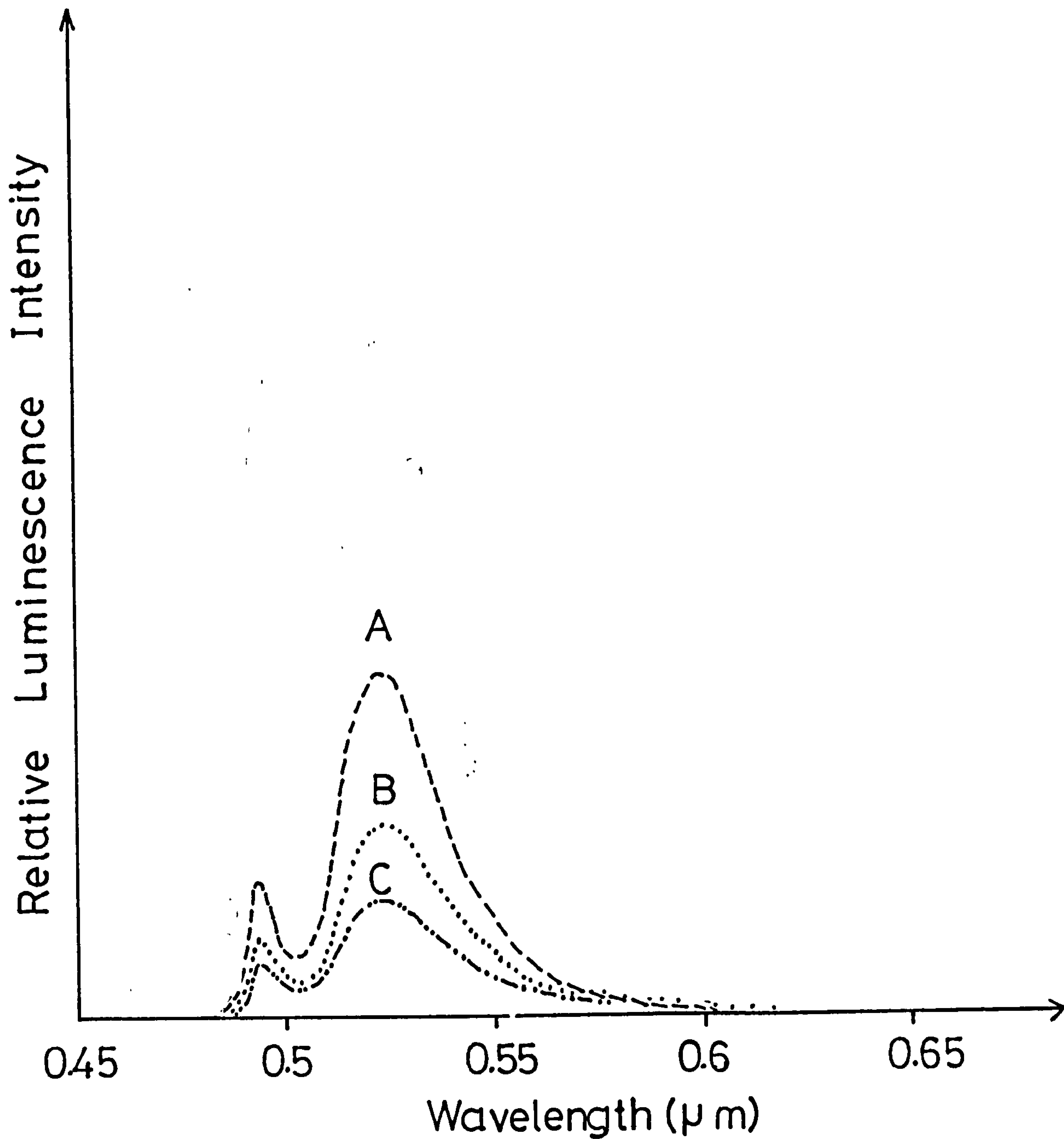

Fig.(5.44) Short wavelength (band edge) CL emission for CdS layers annealed in hydrogen (curve A), vacuum (curve B) and air (curve C) before dipping. Cu_xS-CdS annealed in vacuum for 30 minutes at 200°C.

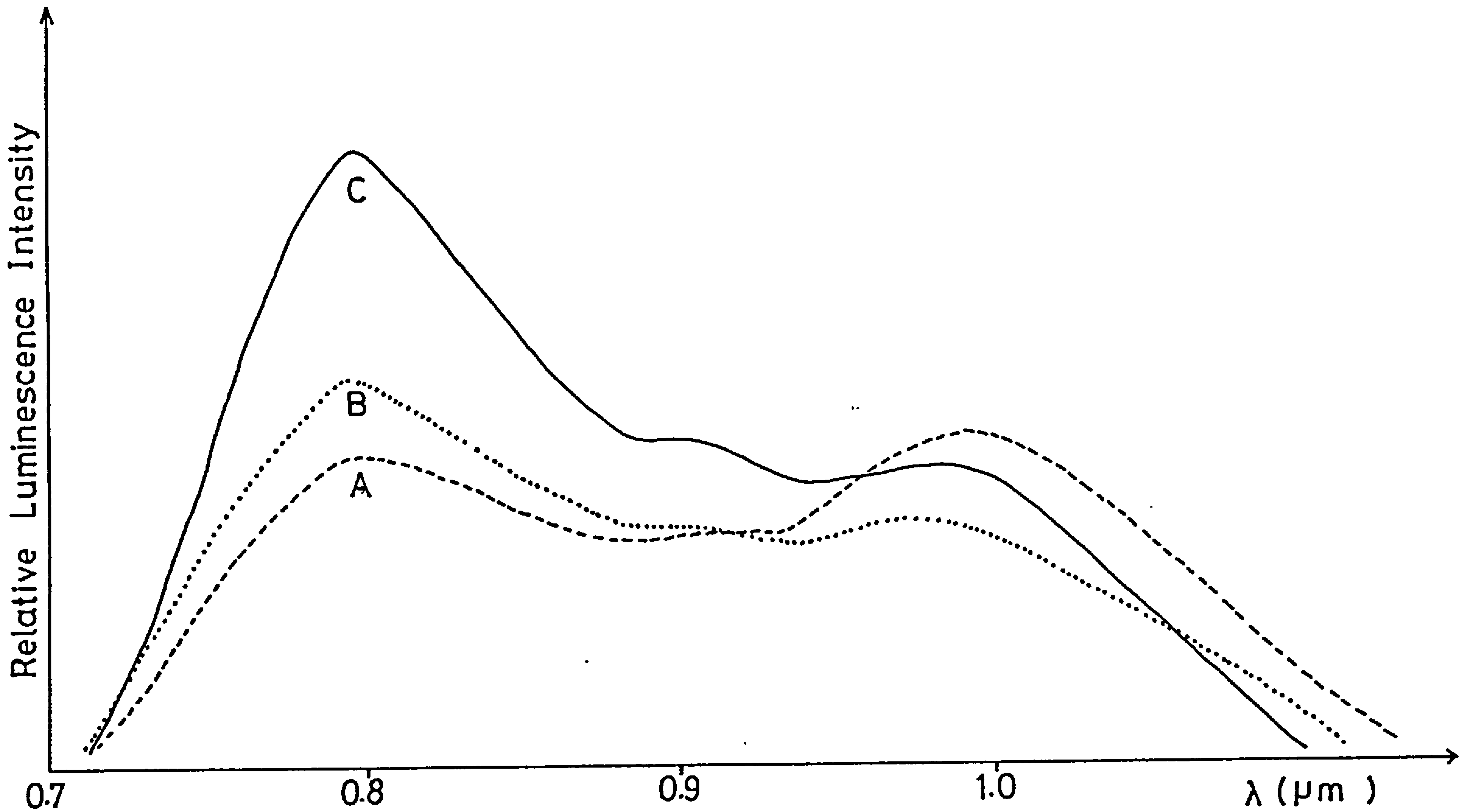

Fig.(5.45) The CL emission for Cu_xS-CdS cells annealed in air for 10 minutes at 200°C (curve A), in hydrogen for 5.5 hours (curve B) and in air for 10 minutes followed by annealing in hydrogen for 5.5 hours (curve C).

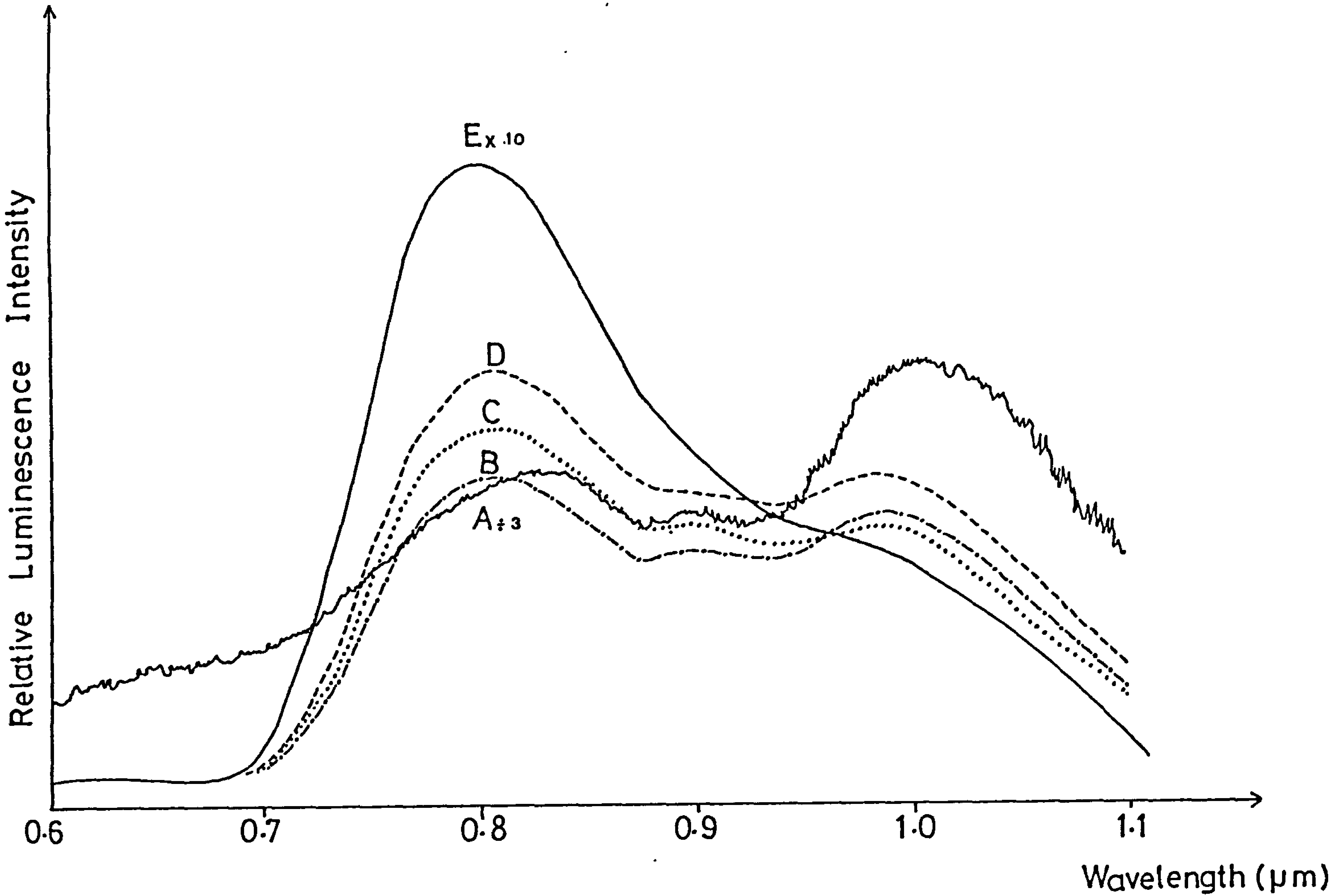

Fig.(5.46) The CL emission for Cu_xS-CdS cells annealed in hydrogen at 200°C for 5, 15, 30, 60 and 21 hours for curves A, B, C, D and E respectively.

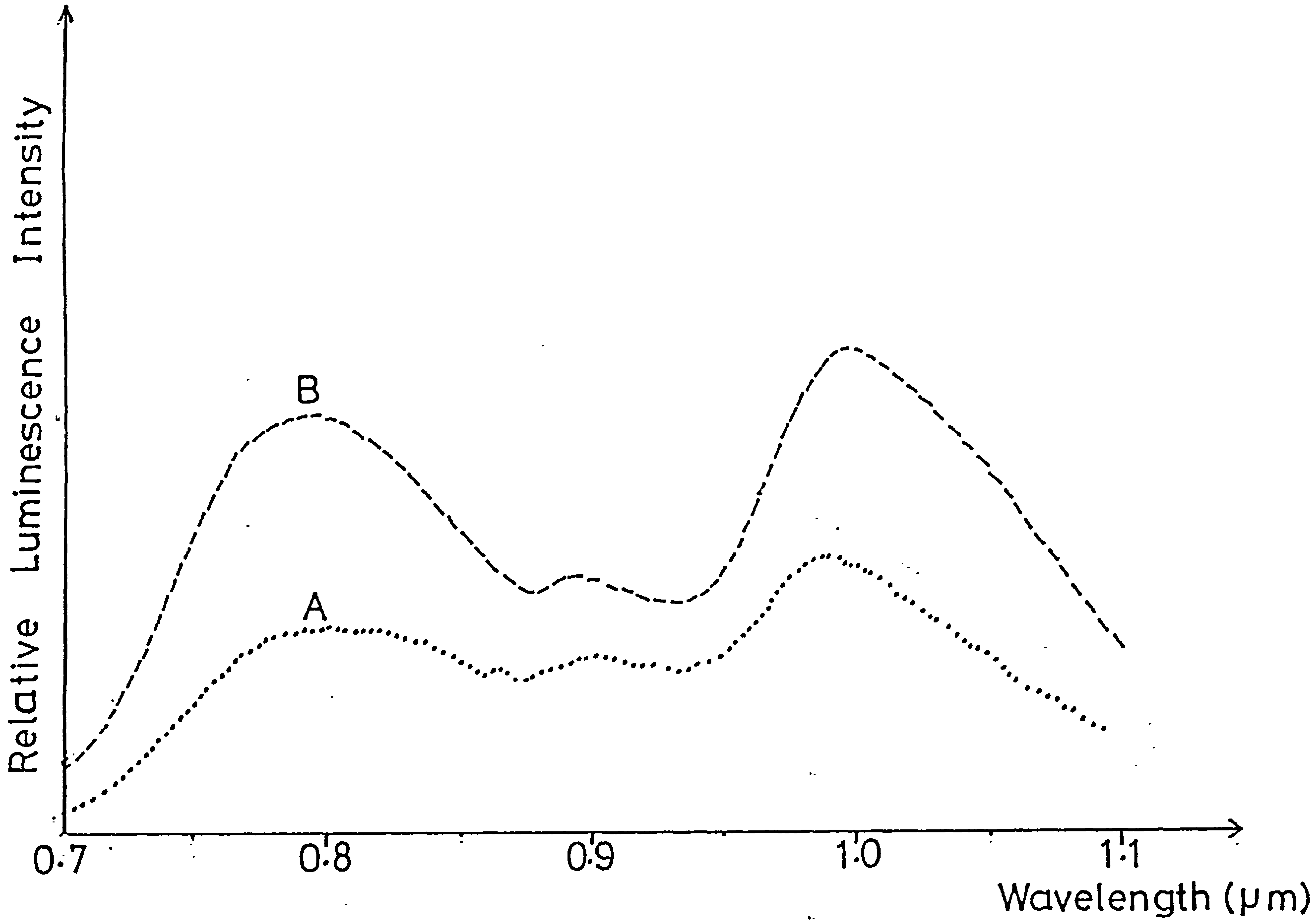

Fig.(5.47) The CL spectra for Cu_xS-CdS cells annealed in hydrogen for 3 hours (curve A) and 21 hours (curve B). A thicker Cu_xS layer was used (dipping time was 8 seconds).

emission for Cu_xS-CdS cells annealed at 200°C in air for 10 minutes (curve A), in hydrogen for 5 1/2 hours (curve B) and in air for 10 minutes followed by annealing in hydrogen for 5 1/2 hours (curve C). Previously described ECA results (presented in table 5.6) have shown that the latter treatment produces a much reduced Cu_xS layer thickness in comparison with that produced by air annealing alone. The CL emission spectra in figure 5.45 are consistent with the ECA data as curve C clearly indicates a reduction in Cu_xS thickness from the reduction in the emission intensity at ~ 1.0 μm relative to that at ~ 0.8 μm. The influence of hydrogen annealing is shown more clearly by figures 5.46 and 5.47, where different annealing times have been used with Cu_xS layers of different thickness. It is clear from figure 5.46 that increasing the annealing time in hydrogen up to 21 hours leads to a steady reduction in the ratio of the emission intensity at ~ 1.0 μm to that at ~ 0.8 μm. This is consistent with a steady reduction in the Cu_xS layer thickness at the grain surface. A similar result is obtained for much thicker Cu_xS layers as shown in figure 5.47, where curve A and B are the emission spectra for Cu_xS-CdS samples annealed in hydrogen for 3 and 21 hours respectively. The ratio of the emission intensities at ~ 1.0 μm and ~ 0.8 μm was found to be 1.3 and 1.2 for curves A and B respectively. It is anticipated that for samples with very large thicknesses (as in figure 5.47) much longer annealing times in hydrogen would be required before substantial changes in transmitted intensity (of the size obtained in figure 5.46) are observed. However, it is clear that even with thick layers, the CL spectra reveal some reduction in Cu_xS thickness as a result of hydrogen annealing. The electrochemical measurements for samples of unannealed Cu_xS-CdS and those annealed in hydrogen for different times

(up to 8 hours) have indicated no consistent reduction in thickness of the Cu_xS layer. This discrepancy between the ECA data and the CL results can again be explained in terms of the non-uniformity of the Cu_xS layer thickness over the CdS film. The ECA technique gives the average thickness of the total Cu_xS film which is distributed over the surface and in the grain boundaries. When there is a large contribution to this value coming from the Cu_xS in the grain boundaries, a small change in thickness of the layer at the upper surface would represent a much smaller fractional change in the overall average thickness so that the electrochemical analysis technique would not be sensitive enough to detect it. However, the CL emission will be strongest in the regions where the Cu_xS layer is thinnest (as at the grain surface) so that the cathodoluminescence method is more sensitive than the electrochemical analysis to changes in the Cu_xS layer at the grain surface.

5.3 Characteristics of complete Cu_xS-CdS cells

5.3.1. I-V characteristics

In order to be able to measure the I/V characteristics of a cell either under illumination or in the dark, it is necessary to complete the cell by forming an ohmic contact to the front face of the Cu_xS layer. At the beginning of this project it was thought that it would be convenient to employ the same contacts as used for the measurement of sheet resistivity of the Cu_xS layer so that changes in the I/V characteristics could be easily correlated with changes in sheet resistivity resulting from different treatments. However, the frequent changes in the connections to the contacts for the two different measurements proved to be inconvenient. More significantly,

it soon became clear that a grid structure with only 4 lines/cm (as employed for the sheet resistance measurements) was unsuitable as the photocell contact if maximum energy conversion efficiency was to be achieved. Because the copper sulphide layer is very thin in front wall cells, its sheet resistance is high and, in order to minimise the series resistance of the cell, the conduction path length for photo-generated carriers must be kept short so that a close-spaced grid structure is required. Using a mask, fabricated as described in section 4.5, a grid contact with 20 lines/cm was formed. This was found to achieve the desired reduction in the series resistance, with associated improvement in the fill factor and conversion efficiency of the cell, as can be seen in figure 5.48. The two cells (a) and (b) were fabricated from CdS films with similar thickness and resistivity. They were both dipped in a CuCl bath for 6 seconds but cell (a) was given a front contact with 20 lines/cm while the contact for cell (b) was 4 lines/cm. Both cells were subsequently annealed in vacuum to optimise their performance. From the steeper slope of the curve under high forward bias, it is clear from figure 5.48 that cell (a) has a substantially lower series resistance than cell (b) giving rise to a better fill factor for cell (a). Thus, although the short circuit current for cell (b) is significantly greater than for (a), probably due to the greater grid shaddowing associated with the higher density grid, the overall efficiency for cell (a) is superior to that for cell (b).

It is expected that with thicker Cu_xS layers (with associated lower sheet resistance), higher fill factors could be obtained without the use of high density grid contacts, but use of increased Cu_xS layer

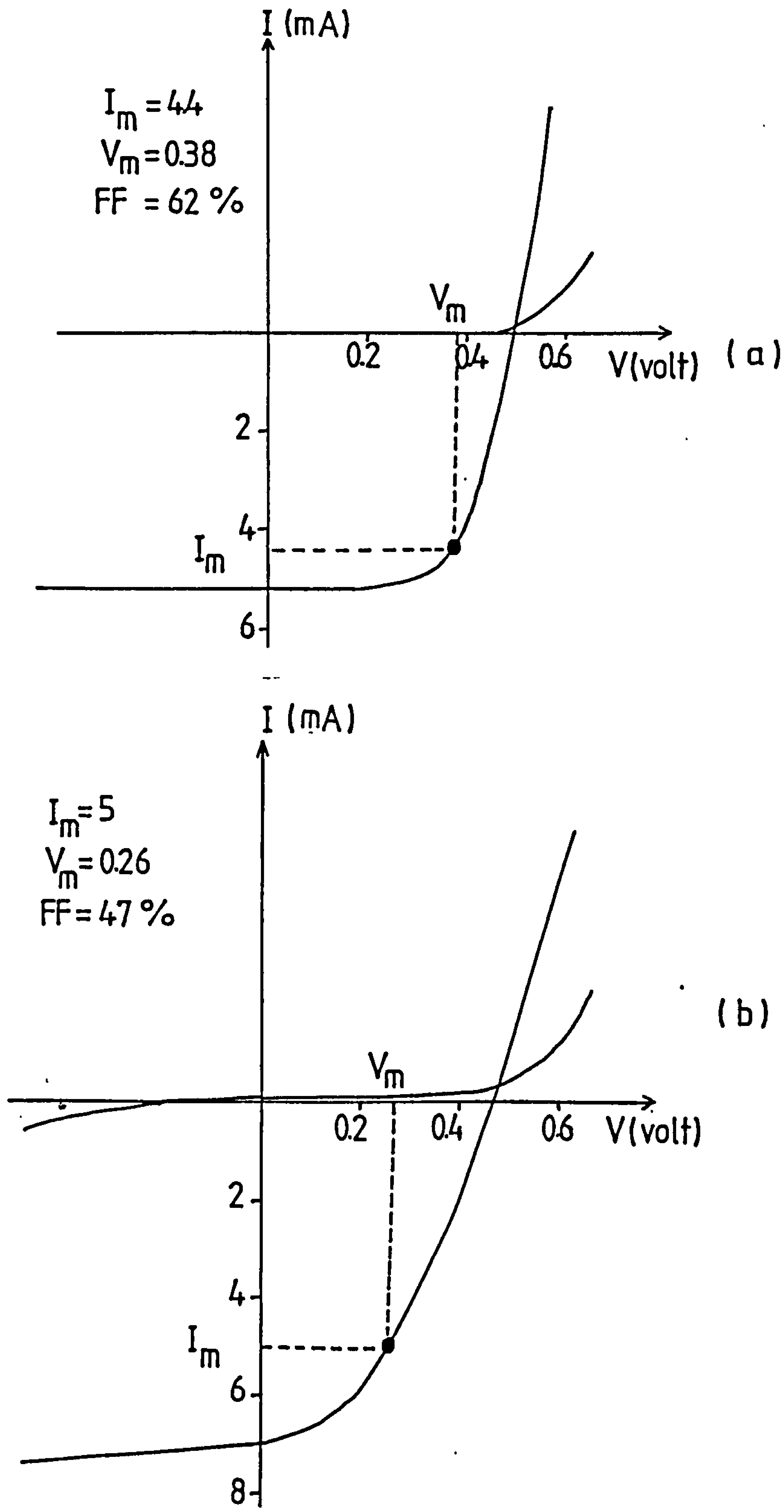

Fig.(5.48) Typical I/V characteristics for similar Cu_xS/CdS cells using different grid structures (a) 20 lines/cm (b) 4 lines/cm.

thickness leads to a lower photogenerated carrier collection efficiency due to the increased recombination within the Cu_xS film before the photogenerated carriers reach the Cu_xS-CdS interface. The effect is illustrated by the data in table 5.7 for a set of samples with 4 grid lines/cm.

Table 5.7: I-V characteristics for Cu_xS-CdS cells (using 4 grid lines/cm) for different thicknesses of Cu_xS layer.

Dipping time(s)	I_{SC}(mA/cm^2)	V_{OC}(volt)	FF%
2	6	0.38	31.5
4	5.37	0.37	40
8	4.87	0.35	43
10	2.75	0.32	58

It is clear that increased Cu_xS film thickness (resulting from longer dipping times) produces a steadily increasing fill factor but this improvement is outweighed by the reduction in short circuit current. This reduction in current is seen to be accompanied by a reduction in the open circuit voltage which can be partly attributed to the increased junction area (in accordance with equation 2.4.6) due to the greater penetration of the Cu_xS into the CdS grain boundaries with longer dipping times, as discussed in section 5.2.1.

It was noted above that, although the use of a greater number of grid lines in the top contact provides the required reduction in series resistance, there is a reduction in the short circuit current due to the increased shadowing of the cell. This is because, the area under the grid itself contributes nothing to current generation due to the fact that all the usable light is absorbed or reflected by the metallic grid. Therefore there is an upper limit to the number and size of the grids which can be deposited for optimum solar cell

performance in any given environment and for given values of the solar cell parameters. Making the width of the grid lines very small increases the optical transmission of the grid structure but this can seriously reduce the conductance of the grid fingers. Clearly a compromise is necessary and the structure described in 4.5 was found to combine a relatively high optical transmission (of 80%) with satisfactory conductance. This grid structure was used for most of the comparative studies of I/V characteristics during this project.

In addition to the effects of the top contact and Cu_xS layer thickness, the cell characteristics are very sensitive to the structure and properties of the CdS base layer and to post-fabriction heat treatment. In order to illustrate the effect of the CdS base layer, the I-V characteristics of the samples of figure 5.2 are shown in table 5.8. In constructing these cells, the as-deposited CdS layers (produced from 3 different sources) were all etched together for 3 seconds and dipped for the same length of time (2 seconds). Similarly, all the cells were given the same post-fabrication heat-treatment which consisted of annealing in H_2 atmosphere for 6 hours.

Table 5.8: Electrical characteristics for cells fabricated using three different sources of CdS but with the same dipping and annealing conditions

CdS source	I_{sc}(mA/cm^2)	V_{oc}(Volt)	η %
Reidel de Häen powder	21.5	0.44	4
GE powder	17.75	0.49	4
Merck tablets	5.25	0.2	0.3

Although the dipping and annealing conditions used for all the cells in table 5.8 were not necessarily the optimum conditions for each type

of cell, it is clear that the cells formed using the Merck tablets CdS source displayed very poor characteristics in comparison with the other two types. As pointed out in section 5.1.2 the MT CdS films displayed weak green edge emission and it has been noted previously (207, 208, 209) that such layers produce cells with poor efficiency. Even after later experiments designed to optimise the performance of the cells made from Merck tablets CdS, (by adjusting the etching and dipping time of CdS layers and the post-fabrication annealing conditions) the best short circuit current and open circuit voltage which could be achieved were I_{SC} = 8 mA/cm^2 and V_{OC} = 0.4 volts respectively but, as described later (in section 5.3.4), much more significant improvements were obtained by exposing the CdS films to ion implantation prior to the formation of the Cu_xS layer. The results presented in section 5.3.4 indicate that the effect of ion implantation is to modify the Cu_xS growth process, to produce a more satisfactory Cu_xS layer geometry and Cu_xS-CdS interface structure. Table 5.8 shows that the cells formed from RH and GE CdS sources produced similar efficiencies but with different short circuit currents and open-circuit voltages. The RH cell has lower V_{OC} suggesting larger junction area possibly due to a more textured surface which would collect more light giving rise to a higher I_{SC} as observed in table 5.8. Clearly the I_{SC} and V_{OC} parameters are dependent on the subsequent annealing conditions.

Although the I-V characteristics are useful for comparing the results of different treatments, particularly as they affect the overall efficiency, information concerning the changes in physical and chemical structure of the cells can best be obtained from other

characteristics (e.g. spectral response, luminescence and junction capacitance). Results of measurements of these characteristics are included in the following sections.

5.3.2 Photosensitivity spectral response

As discussed in section 5.2.4, the spectral dependence of the Cu_xS layer photon absorption coefficient is very sensitive to changes in stoichiometry. As the absorption coefficient controls directly the rate of photogeneration of minority carriers (electrons) in the Cu_xS layer, information concerning changes in stoichiometry can be obtained from observation of changes in the spectral dependence of the cell photocurrent or photovoltage. This is illustrated in figure 5.49 which shows the short circuit current spectral response for two different cells with extremely different characteristics. Curve A is for a cell giving good photo I/V characteristics after being freshly annealed in hyrdogen for 4 hours. The response can be considered in terms of two main regions; one centred at ~ 0.6-0.7 μm and the other at ~ 0.9 μm with a cut-off at ~ 1.0 μm. The latter feature is attributed to absorption in the Cu_xS layer by the chalcocite (Cu_2S) phase (175,235,236) and, as expected, this feature is always found to be strong in cells which have been annealed in hydrogen. The 0.6-0.7 μm peak could be partly due to the presence of other phases of Cu_xS such as djurleite, which has a larger bandgap (1.8 eV) than chalcocite. However, such a contribution is not expected to be significant after hydrogen annealing and it is more likely that this peak results from absorption in the CdS layer close to the Cu_xS-CdS interface, due to the presence of band gap states in the CdS some of which are associated with the diffusion of copper from the Cu_xS layer (237). The small shoulder of the response at ~ 0.52 μm corresponds

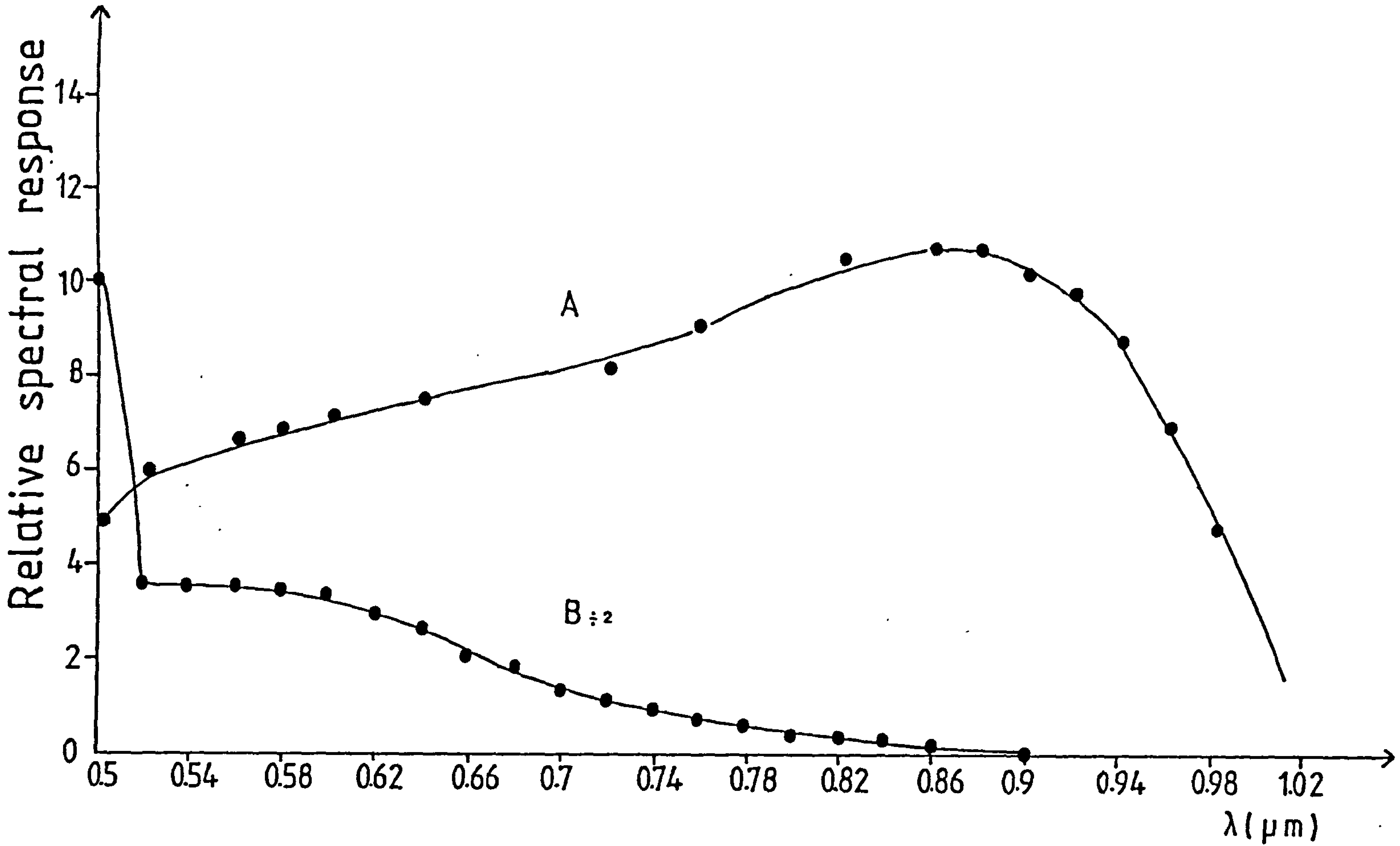

Fig.(5.49) The short circuit current spectral response for two different cells with extremely different characteristics. Curve A is for a cell annealed in H_2 for 4 hours (dipping time was 6 sec.). Curve B is for a cell with a thin Cu_xS layer (dipping time was 2 sec.) which had degraded after a long exposure to air 1 year.

to band to band excitation in the CdS layer.

Curve B in figure 5.49 is for a cell with a thin Cu_xS layer which had degraded after a long exposure to air. The cell gave poor photo I/V characteristics and as can be seen in figure 5.49 the response was generally much weaker than that for cell A. However, it is particularly noticeable that the longer wavelength feature in the curve for cell A is absent for cell B indicating the absence of the chalcocite phase in the Cu_xS layer. With absorption in this thin Cu_xS layer being relatively weak, the response for wavelengths less than 0.52 μm due to absorption in the CdS layer becomes significantly more important as can be seen in figure 5.49.

It should be noted that the long wavelength response for curve A in figure 5.49 is only observed when the measurement is made using a short wavelength bias light. This is a commonly observed characteristic for Cu_xS-CdS solar cells (34, 238, 239, 240) and is due to the low electric field strength at the junction resulting from the presence of copper related deep acceptor centres compensating the shallow donors in the CdS layer close to the interface. As discussed in chapter 2, in relation to equation 2.4.3, the interface collection factor for photogenerated electrons depends upon the relative rates at which the carriers transfer or recombine at the interface. If the space charge density is reduced by the presence of copper acceptor centres, the electric field is weakened and a greater proportion of the carriers recombine at the interface and therefore do not contribute to the photocurrent. For samples given a long annealing treatment (as in the case of cell A above) significant copper diffusion across the Cu_xS-CdS interface occurs and the electric field

is reduced sufficiently to make the interface collection factor effectively zero for carriers produced in the Cu_xS layer by long wavelength radiation. However, with the use of shorter wavelength radiation (< 0.7 μm), the light penetrating to the CdS layer is of sufficient energy to ionize the deep levels (copper centres and other defect states) in the near surface region of the CdS film. This leads to an increase in the positive space charge density and a corresponding increase in the electric field strength at the junction. It follows that the interface collection factor is increased so that the carriers excited in the Cu_xS layer can generate a photocurrent. For the case of carriers excited in the Cu_xS layer by long wavelength radiation, it is clearly necessary for a secondary short wavelength radiation to be provided to maintain a suitably high junction field for the effect of the primary carriers to be observed.

5.3.3 Effects of annealing

It has already been noted several times that the photovoltaic performance of Cu_xS-CdS solar cells can be significantly improved by a post-fabrication annealing process. Indeed, it is often found that for cells studied immediately after fabrication, little or no photovoltaic effect at all is observed so that an annealing process is essential. Such cells display a nearly ohmic I/V relationship due to the existence of a narrow depletion barrier on the CdS side of the Cu_xS-CdS interface due to the relatively high density of shallow donors (usually in excess of 10^{18} cm^{-3}). The dominant electron transport mechanism across these narrow barriers is due to tunnelling so that little rectification is observed. When the cells are annealed, copper can diffuse from the Cu_xS layer into the CdS layer forming acceptor centres which compensate the shallow donors and thereby increase the width of the depletion layer. This prevents tunnelling through the barrier and good rectifying I-V characteristics are then observed. This is accompanied by good photovoltaic behaviour when the cell is illuminated.

In addition to its influence on the CdS barrier layer structure, the annealing process has a significant influence on the Cu_xS layer as a result of effects occuring at the Cu_xS-CdS interface and at the free surface. These interfacial diffusion processes and surface oxidation/reduction processes lead to changes in the stoichiometry of the Cu_xS layer, as discussed in section 5.2.3, and have a direct impact on the photovoltaic properties of the cells. For example, changes in the photon absorption efficiency of the Cu_xS layer produce corresponding changes in the photogenerated current and variations in

the spectral dependence of the optical absorption coefficient (discussed in section 5.2.4) can be seen in the photocurrent spectral response for the cell. What is less clear is the effect of the annealing environment on the rate of copper diffusion from the Cu_xS layer into the CdS. In an earlier investigation employing AES profiling (241) it was found that the copper penetration was much faster when annealing in air compared with annealing in vacuum or hydrogen for similar times at the same temperature. In these studies, it was not possible to obtain precise quantitative information about the diffusion characteristics due to the difficulty of separating the bulk diffusion and grain boundary diffusion contributions. Quantitative studies have been made by other workers (242, 243) for the case of copper diffusion in bulk single crystal materials but the results have shown widespread disparity possibly because of the dominant influence which dislocations and other defects can have on the diffusion processes (38). In view of this sensitivity of the diffusion in single crystals to the structural properties of the crystals, it is to be expected that polycrystalline layers would not only behave differently from single crystals but would also show a strong dependence on the manner in which they had been formed. The added sensitivity of the diffusion in such layers to the ambient atmosphere, which has been discussed by Bryant and coworkers (241), suggests that great care is required in the determination of reliable diffusion characteristics.

The approach taken in the present investigation was to examine the effect of the diffusion process on the CdS space charge, as seen through its effect on the junction capacitance. It is clear from the

analysis in chapter 2 (section 2.5) that any reduction in space charge density in the near surface region of the CdS layer, due to the formation of copper acceptor centres in this layer, is expected to have a significant effect on the total width of the depletion layer. This has already been noted in relation to the effect on the I/V characteristics and spectral response but, as shown in the analysis of section 2.5, there is a corresponding effect on the C-V characteristics. Thus, it was intended to use the information relating to the changes in the C-V characteristics to monitor the penetration of copper into the CdS and, thereby, to obtain estimates for the diffusion coefficient under different annealing conditions.

Due to the narrow width of the space charge region for freshly made cells, the junction capacitance per unit area is very high and, for a complete test cell was too large to be measured accurately on the Boonton meter. Therefore, it was necessary to construct test samples with much smaller area. This was done by defining a set of windows in a CdS film using a varnish (and a fine tipped paint brush) before dipping the film in CuCl solution.

In this way, a set of 6 or 8 small area cells (~1.5 mm^2) were produced on a single 1 cm^2 sample. A gold top contact could then be provided to cover each of the test areas as required (either before or after annealing). This arrangement had the advantage that the set of test cells were all being created on a single 1 cm^2 sample so that they would have very similar initial properties. The main disadvantage was that the areas of the test cells were all slightly different and great care was needed to measure accurately each of these areas. A travelling microscope was used for this purpose.

Figures 5.50 and 5.52 show plots of C^{-2} against reverse bias

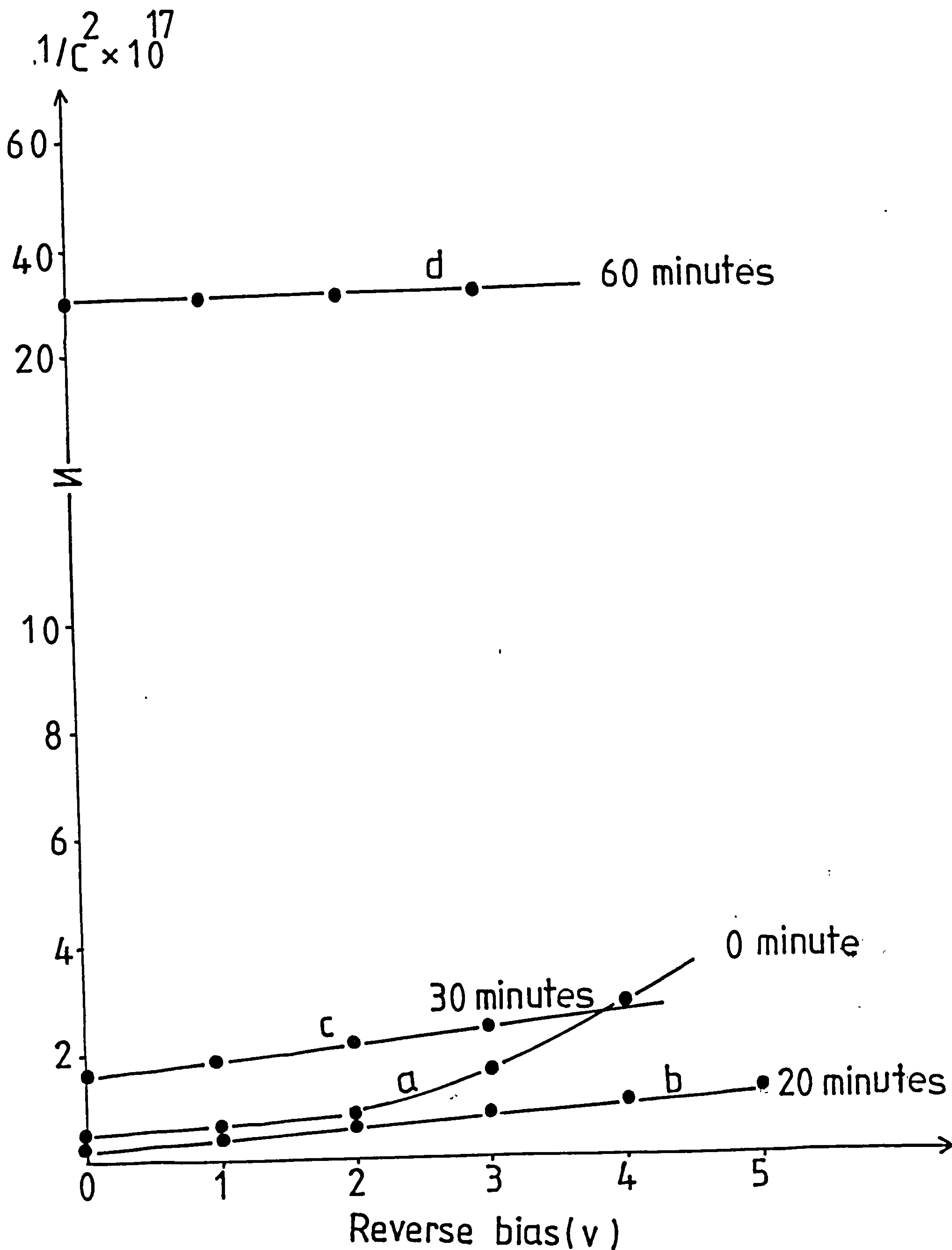

Fig.(5.50) $1/C^2$ against reverse bias voltage V for Cu_xS-CdS cell before and after annealing in hydrogen.

voltage V for samples before and after annealing in hydrogen and air respectively.

Both samples before annealing show a non-linear relationship for voltages above 2V which is indicative of reverse bias breakdown probably associated with tunnelling as the barrier would be very narrow with these CdS films having a high shallow donor concentration. Using the slope of the linear region at low bias voltages to obtain a value for this shallow donor concentration provided a magnitude of $3.4.10^{18}$ cm^{-3} for the sample in figure 5.50, consistent with results obtained using gold Schottky contacts on these CdS layers. After annnealing for 20 minutes in hydrogen (the non linear region was removed for bias voltages up to 5 V as seen in figure 5.50 (curve b). This is consistent with copper diffusing into the CdS layer from the Cu_xS to compensate the shallow donors and to widen the space charge region and reduce the tunnelling effect. According to the theory in chapter 2 (equations 2.5.17), establishment of an insulating layer of width d_2 should increase the voltage axis intercept from V_D to $(V_D + \frac{q}{2\varepsilon} N_3 d_2^2)$ where N_3 is the shallow donor conentration deep inside the CdS layer. In the case of curve b in figure 5.50, it is clear that the line intercepts with the voltage axis at a smaller voltage than for curve a suggesting some non-ideality in the behaviour of this sample. This is not surprising as the theory assumes a planar structure whereas the polycrystalline system has a very non-planar structure. However, after further annealing (for 30 minutes), curve c shows a clear reduction in the capacitance values suggesting a deeper diffusion of Cu into the CdS layer and a corresponding increase in the width of the compensated region which is

close to the junction. It is expected that with increasing annealing time, the voltage intercept would be increased due to the increasing width of the insulating region d_2 according to the relationship which was mentioned above (equation 2.5.17). However, as expected, the slope of the line C is changed very little from the slopes of lines a and b as the slope is controlled by the shallow donor concentration N_d at the edge of the space charge layer in the uncompensated CdS region even if there is a more insulating layer at a shallower depth. After further annealing (60 minutes), the second term of the equation 2.5.17 becomes dominant (due to a further increase in d_2) so that the capacitance becomes less sensitive to voltage. This is clearly seen in curve d of figure 5.50 (note change of scale on the c^{-2} axis).

The calculated values of d_2 (from voltage axis intercepts) are shown in table 5.9 for the different times of annealing in flowing hydrogen.

Table 5.9: Capacitance-voltage characteristics for Cu_2S-CdS cells annealed in hydrogen for different times

Area (m^2)	Time (mins)	$N_d(m^{-3})\times10^{24}$	V_D(volt)	d_2(μm)	W(μm)
1.44×10^{-6}	0	3.4	2.0	0.021	0.029
	20	3.4	1.8	0.017	0.021
	30	2.4	6.0	0.052	0.051
	60	-	107	0.23	0.22

It is clear from table 5.9 that the width of the compensated layer d_2 was increased significantly by increasing the annealing time in hydrogen. While the values of d_2 for up to 20 minutes annealing represent only a portion of the total space charge width w (calculated from the value of the zero bias capacitance), d_2 becomes an increasing

fraction of the total width with increasing annealing and clearly dominates the space charge region for annealing times greater than 30 minutes. Under these conditions, when the insulating region d_2 becomes equivalent to the depletion layer thickness, thereby controlling the capacitance, it is expected that (for this diffusion controlled process) both d_2 and I/C should be proportional to the square root of the diffusion time $t^{1/2}$, as discussed in section 2.5. Figure 5.51 (curve A) shows the relationship between d_2 and $t^{1/2}$ for the data in table 5.9 but it is clear that the expected proportionality is not observed.

Corresponding data for air annealed samples is shown in figure 5.52. It is clear that there is a similar trend in behaviour for successive annealing cycles, but the changes are much more significant for air annealing than for hydrogen annealing. After 10 minutes annealing, a substantial reduction in capacitance occurred as can be seen by curve b in figure 5.52. Once again, the slope of the relationship for the annealed sample is close to that for the linear part of the unannealed sample, consistent with theoretical analysis (section 2.5). However, after 30 and 60 minutes annealing in air, the more insulating region (associated with the diffusion of copper) is dominating the space charge region and the capacitance appears to be independent of voltage. The dominance of the insulating region is confirmed by the data in table 5.10. Once again, when the width of the insulating region d_2 is plotted as a function of the square root of the diffusion time, $t^{1/2}$, a superlinear relationship is obtained as can be seen in figure 5.51 (curve B).

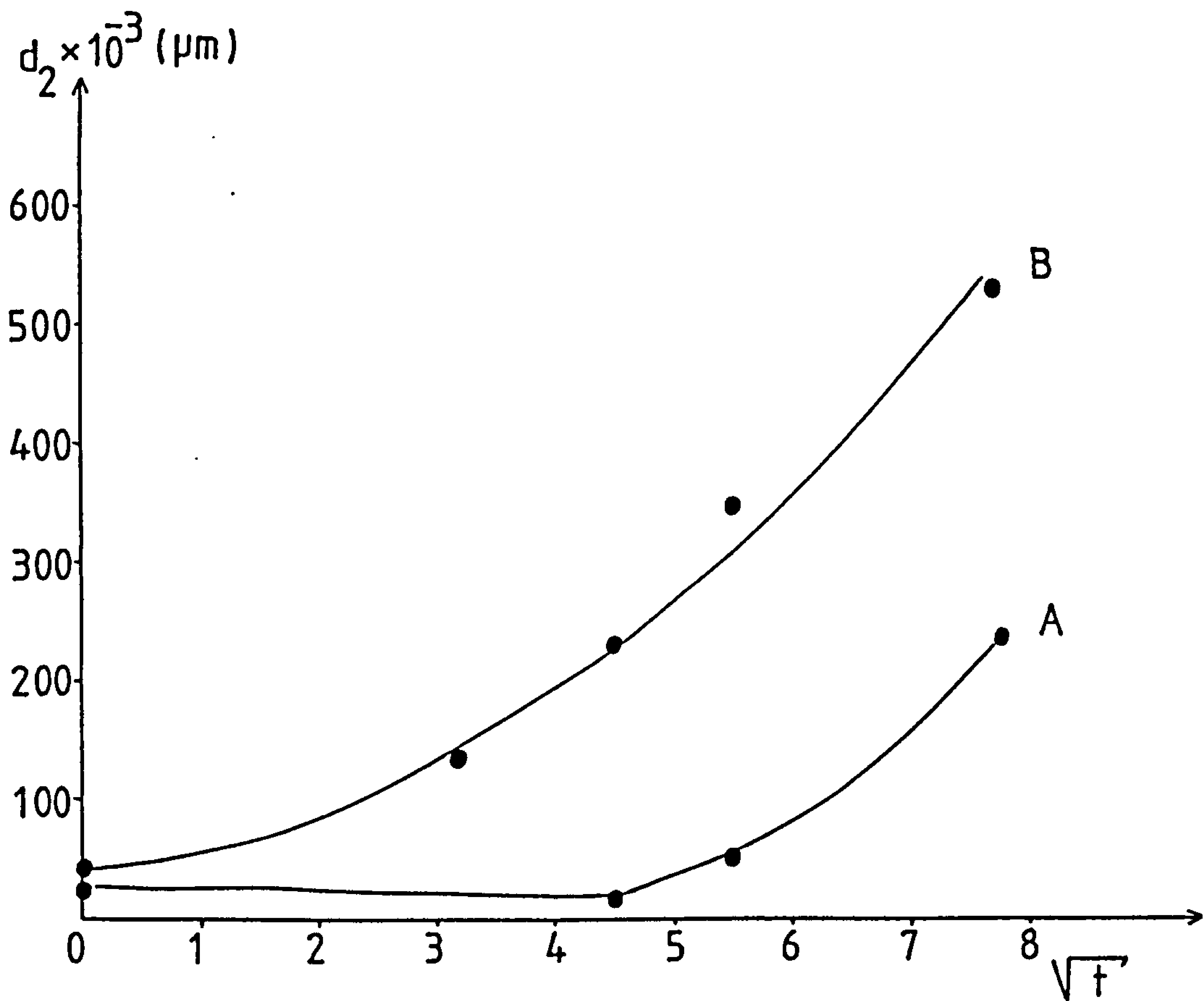

Fig.(5.51) The compensated layer d_2 against the square root of the diffusion time $t^{1/2}$, for hydrogen (curve A) and air (curve B) annealing.

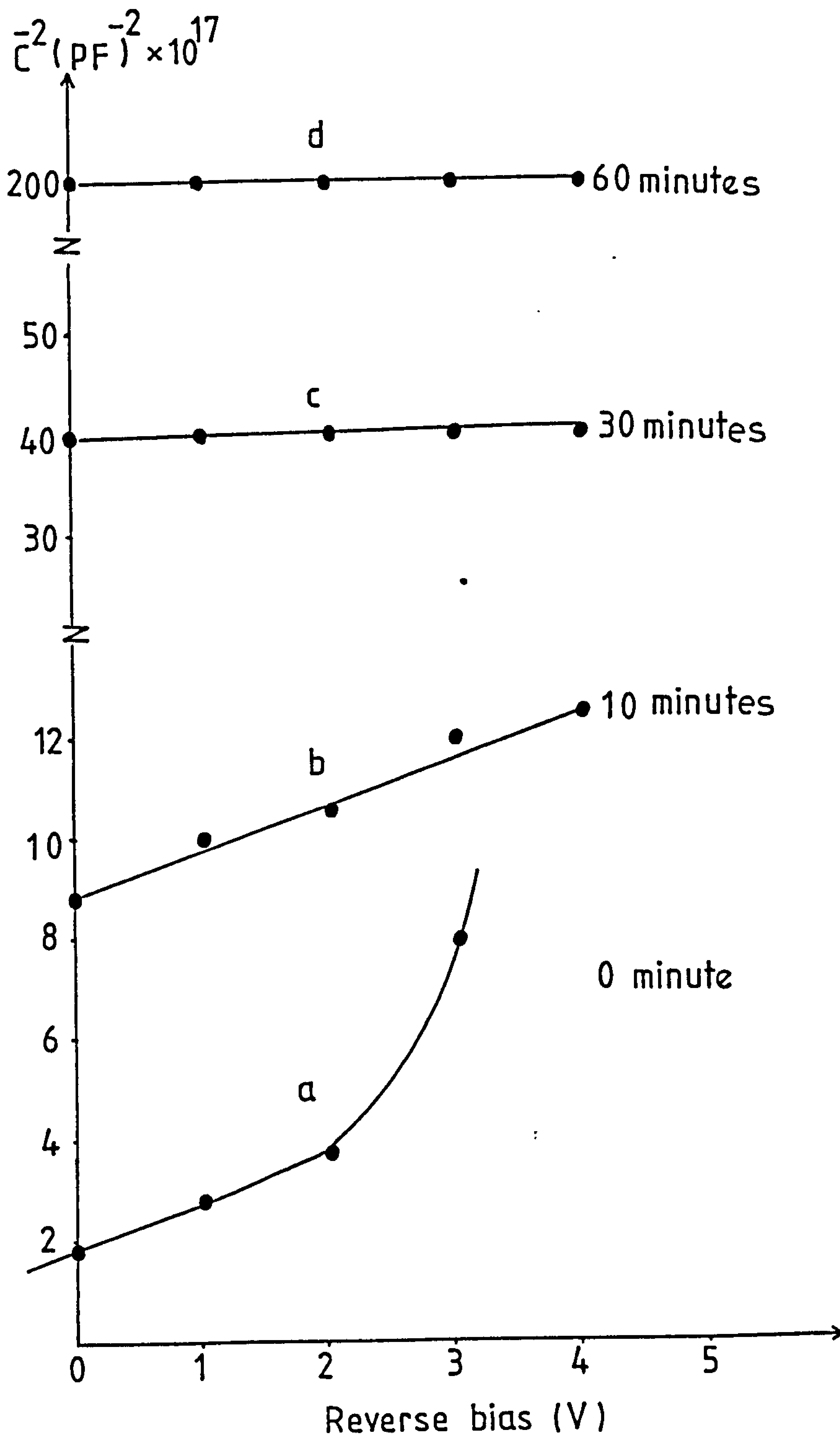

Fig.(5.52) $1/C^2$ against reverse bias voltage V for Cu_xS-CdS cell before and after annealing in air.

Table 5.10 Capacitance-voltage characteristics for Cu_xS-CdS cells annealed in air for different times.

Area (m^2)	Time (mins)	$N_d (m^{-3}) x10^{24}$	V_D(Volt)	d_2(μm)	W(μm)
$1.2x10^{-6}$	0	1.2	2.5	0.04	0.05
	10	0.96	8.6	0.09	0.11
	30	-	41.7	0.23	0.24
	60	-	222	0.53	0.52

A similar superlinearity has been observed by Hall and Singh (37) who suggested that this could be due to a change in the effective area of the junction as a result of diffusion related changes in the structure of the junction particularly in the grain boundary regions. However, in spite of this non-ideal behaviour, it is clear from figure 5.51 that the rate of diffusion of copper into the CdS film is faster when the annealing process is performed in air than in a hydrogen atmosphere. Making use of equation 2.6.3 an estimate for the diffusion coefficient D can be obtained by setting $x^2 = d_2^2 = 4Dt$. Using the data for 60 minutes annealing time in tables 5.9 and 5.10 yield values for D of 3.7×10^{-14} cm^2 s^{-1} and 2.0×10^{-13} cm^2 s^{-1} for hydrogen and air annealing respectively. Although these values are subject to a large uncertainty they are of comparable magnitude to the value ($D \approx 10^{-13}$ cm^2 s^{-1}) obtained by Sullivan (38) for single crystal CdS samples annealed at the same temperature under vacuum.

It should be noted that the data provided in figure 5.50 and table 5.9 for the case of annealing in hydrogen were all obtained using the same test element in a cell with 6 small area elements, as described above. A thin gold contact was evaporated over this element after formation of the Cu_xS layer and measurements were made using

this contact after each stage in the subsequent series of annealing cycles. The same experimental arrangement applied for the results shown in figure 5.52 and table 5.10 for air annealing. It is clear from the very different results obtained for the two different annealing environments that the contacts involved were sufficiently thin to allow interaction between the cell and the ambient atmosphere but in order to check that the contact was not affecting this interaction additional measurements were made using different test elements on the cell with a new contact applied to a different element after each stage of annealing. The results are listed in tables 5.11 and 5.12 for hydrogen and air annealing respectively.

Table 5.11: Capacitance-voltage characteristics for Cu_xS-CdS cells annealed in hydrogen for different times using different areas (contact applied after annealing).

Area (m^2) x 10^{-6}	Time (mins)	N_d (m^{-3}) x 10^{-24}	V_D (volt)	d_2 (μm)	W (μm)
1.44	0	3.4	2.0	0.021	0.029
1.6	10	5.9	1.0	0.007	0.031
1.08	20	9.31	2.4	0.015	0.04
1.44	30	2.8	8.0	0.057	0.058
1.92	60	-	395	0.42	0.523

It is clear that the results in tables 5.11 and 5.12 show similar trends to those described above but the increases in the actual values of d_2 and w are significantly larger than those given in tables 5.9 and 5.10. However, the values derived in tables 5.11 and 5.12 are less reliable due to the use of different elements with areas subject to additional measurement errors.

Table 5.12: Capacitance-voltage characteristics for Cu_xS-CdS cells annealed in air for different times using different areas (contact applied after annealing).

Area $m^2 x 10^{-6}$	Time (mins)	N_d (m^{-3}) $x 10^{-24}$	V_D (volt)	d_2 (μm)	W(μm)
1.2	0	1.2	2.5	0.04	0.05
2.56	10	0.41	6	0.13	0.15
2.25	20	0.25	7	0.18	0.23
2.0	30	-	28	0.37	0.34

5.3.4 Effects of ion implantation

For each of the investigations concerning the effects of ion implantation, samples from a set of CdS films produced in the same evaporation run were all given the same preliminary etch treatment (typically 3 seconds in cold concentrated HCl). All but one of these samples was then implanted with ions, using a different ion flux or different ion energy for each separate sample. As discussed in section 5.1.5, the process of ion implantation is accompanied by lattice damage and in order to remove this damage, the implanted samples were annealed in vacuum at 300°C for 1/2 hour. A layer of Cu_xS was subsequently formed on all the samples (including the unimplanted sample) by dipping in CuCl for the same length of time using the standard procedure described previously. Finally, all the cells were given the same post-fabrication annealing treatment and, if electrical measurements were to be made, a gold grid was evaporated to provide a top contact for each cell.

A typical set of results is presented in table 5.13 for CdS films implanted with 50 keV Cu^+ ions at various fluences in the range 10^{14}-

10^{16} ions/cm^2. These cells were formed by dipping in CuCl solution for 6 s and annealing in vacuum for 20 minutes.

Table 5.13: The I/V characteristics of Cu_xS/CdS cells annealed in vacuum for 20 minutes. (CdS was implanted with 50 keV Cu^+ ions at various ion doses.)

Ion dose/cm^2 at 50 keV	I_{SC}(mA/cm^2)	V_{OC}(volt)	Cu_xS thickness d(μm)	x
Unimplanted	8.125	0.48	0.33	1.91
10^{14}	-	0.47	0.34	1.95
5×10^{14}	7.17	0.45	0.51	1.96
10^{15}	6.736	0.45	0.58	1.98
5×10^{15}	6.25	0.45	0.71	-
10^{16}	5.46	0.46	0.78	1.99

The electrochemical analysis data in table 5.13 indicates a steadily improving x factor and steadily increasing d for the Cu_xS layer with increasing ion fluence while the open circuit voltage V_{OC} and short circuit current I_{SC} both reduce. This decrease in photovoltaic response can be directly attributed to the increases in the values for d and x which would result in the photogeneration of carriers at greater distances from the Cu_xS/CdS interface and consequent increase in recombination losses.

In a previous study of the use of ion implantation in the fabrication of Cu_xS/CdS solar cells (213), an increase in x with increasing Cu ion fluence, as seen in table 5.13 was observed. However in contrast to the results in table 5.13, the thickness d of the Cu_xS layer was found to fall as the ion fluence was increased over the same range as that used in the present case. The explanation for

the disagreement between these two sets of results is assumed to be related to the different sets of CdS films used on these two different occasions and this suggests that the film structure is very important in determining the overall effect of ion implantation. A sensitivity to film structure was confirmed by subsequent work on different types of CdS films during the course of this project.

The mechanisms by which the implanted copper ions influence the growth rate and other properties of the Cu_xS layer are not clear, especially as the depth of implantation, at the ion energies used here, is relatively small in relation to the total thickness of the Cu_xS layer which is subsequently formed. Table 5.14 gives the projected ranges R_p and standard deviations ΔR_p for 50, 100 and 200 keV Cu ions in CdS, calculated according to LSS theory as discussed by Dearnaley (244).

Table 5.14: The projected ranges R_p and standard deviations ΔR_p for implantation of Cu^+ ions into CdS at energies 50, 100 and 200 keV

Energies of ions (keV)	Projected range R_p(Å)	Deviation ΔR_p(Å)
50	270	133
100	477	240
200	934	415

Using $(R_p + \Delta R_p)$ as a measure of the effective penetration depth for the ions, it is clear that at 50 keV this is nearly an order of magnitude below the values for the Cu_xS layer thickness given in table 5.13. However, from the peak implanted density at a depth R_p, there will be a tail in the distribution of Cu ions, with significant

concentrations at much greater depths. In addition, as the implanted layer is annealed to remove the lattice damage, diffusion processes will lead to enhanced Cu ion concentrations at even greater depths. Of course these diffusion processes will be influenced by the crystal structure of the CdS film, with the grain boundaries playing an important role. The resulting distribution of Cu ions, particularly in the region of the grain boundaries would be expected to influence the growth rate of the Cu_xS layer. Thus, in view of the results discussed in section 5.2.1 concerning the influence of the grain boundaries on Cu_xS growth mechanism, it is not surprising to find different responses to Cu ion implantation associated with CdS layers having different grain structures. Unfortunately, there was insufficient time to allow a detailed investigation of the Cu_xS growth rate variations with thickness for layers given different implantation treatments, to provide further information on the relative contributions from mid-grain and grain boundary growth. However, some effects of the different Cu_xS layers resulting from different implantation conditions can be seen in figures 5.53 and 5.54 which show two sets of long wavelength cathodoluminescence emission spectra. Figure 5.53 shows the results for different ion energies at a constant fluence of 5.10^{14} cm^{-2}. It is clear that the emission intensity is increased for all the implanted samples relative to the unimplanted sample. This could be due to the Cu_xS layer being thinner for the implanted layers but, in view of the results presented in table 5.13, this is unlikely to be the case. More likely the enhanced emission arises from the increase in Cu concentrations in the CdS resulting from the implantation and annealing process. The feature of particular interest in figure 5.53 is the significant difference in

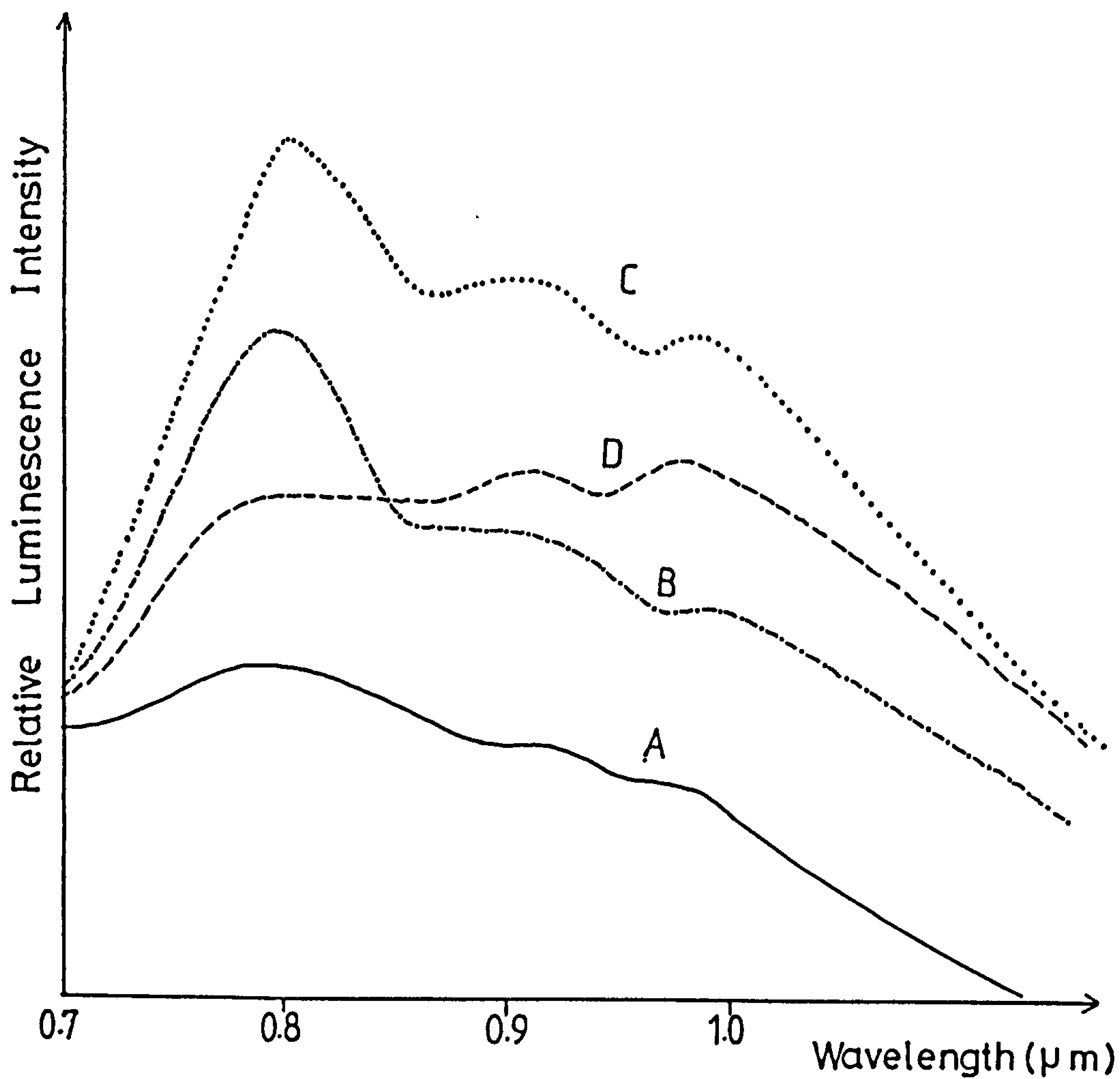

Fig.(5.53) The cathodoluminescence emission spectra for umimplanted curve (A) and Cu^{+} - implanted CdS at constant fluence of $5x10^{14}cm^{-2}$ with different ion energies, 50keV (curve B), 100keV (curve C) and 200keV (curve D). ($Cu_{x}S/CdS$ annealed in vacuum for 30 minutes at 200°C).

shape between the spectrum for the cell implanted at 200 keV (curve D) and that for the two lower energies (curve B and C). In quantitative terms the luminescence intensity at 1.0 μm relative to that at 0.8 μm is 1.09 for curve D, reducing to 0.77 and 0.59 for curves C and B respectively. This reduction could be due to the Cu_xS layer for sample D being of greater thickness than for samples B and C (Possibly resulting from enhanced grain boundary growth) or to a higher x factor. Either of these possibilities or a combination of both would lead to enhanced absorption in the Cu_xS layer with more pronounced absorption at 0.8 μm relative to that at 1.0 μm. This mechanism is consistent with the data in figure 5.54 which shows how the shape of the spectrum is affected by a change in the fluence at a constant ion energy of 50 keV, as for the data in table 5.13. The curves in figure 5.54 indicate a reduction in the luminescence intensity at 1.0 μm relative to 0.8 μm, from 0.58 for an implantation flux of 10^{16} ions/cm^2 (curve C) to 0.54 for 5.10^{15} ions/cm^2 (curve B). Although this is only a small change, suggesting a small reduction in thickness of the Cu_xS layer, the data in table 5.13 shows a corresponding reduction in Cu_xS layer effective thickness from 0.78 μm for 10^{16} ions/cm^2 to 0.71 μm for 5.10^{15} ions/cm^2.

Further results, which could be of use in relation to the uncertainty concerning whether ion implantation increases or decreases the parameters x and d, are presented in table 5.15. Here, the I-V characteristics and the ECA derived parameters x and d are listed for CdS films implanted with 5.10^{14} Cu^+ ions/cm^2 at energies from 10 to 50 keV. Unfortunately, the set of CdS films used for this experiment were evaporated from a CdS source in tablet form and, as mentioned

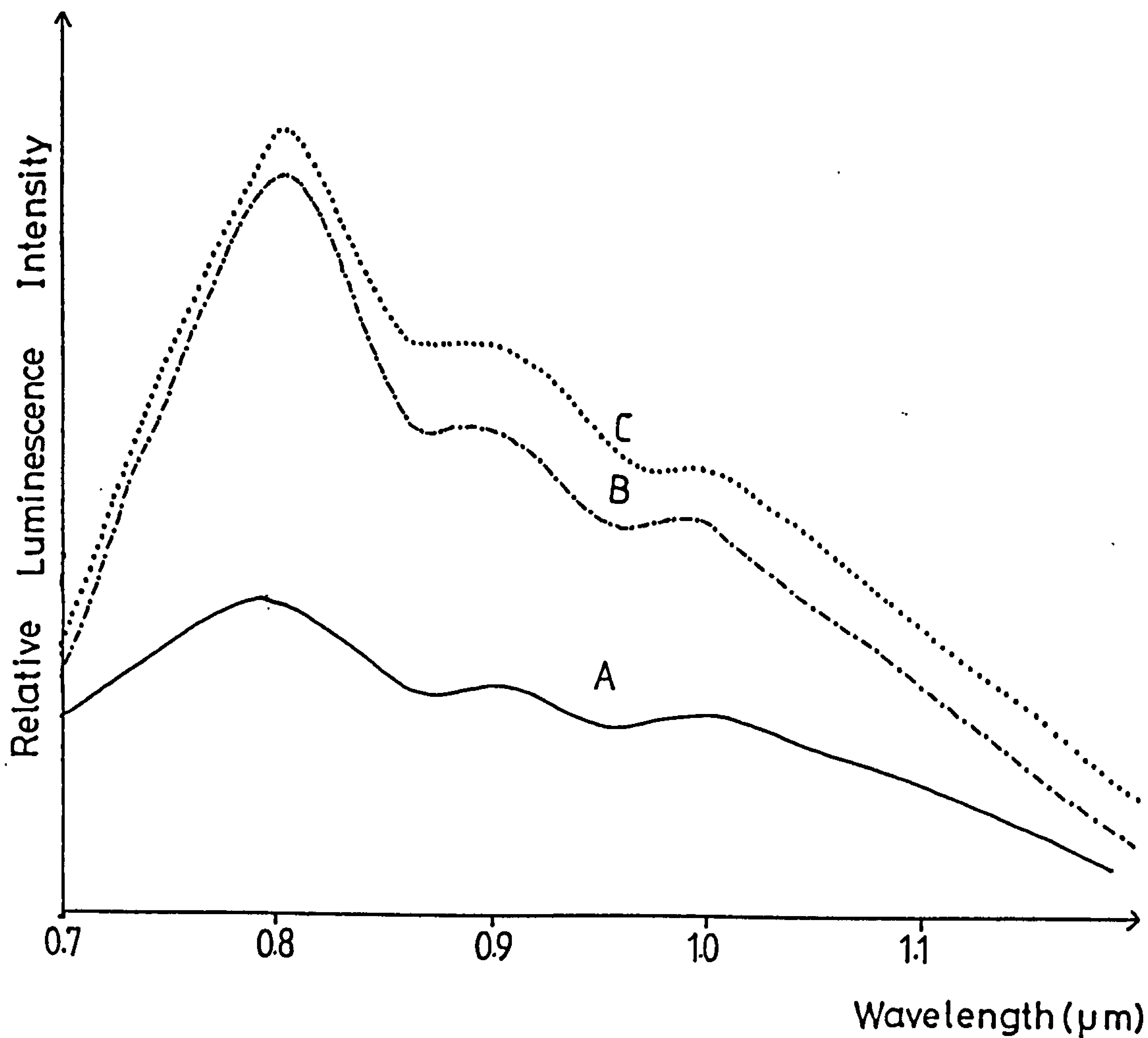

Fig.(5.54) The CL emission spectra for unimplanted (curve A) and Cu^{+} - implanted CdS at constant energy 50keV with different ion fluences of $5x10^{15}$ ions cm^{-2} (curve B) and 10^{16} ions cm^{-2} (curve C).
($Cu_{x}S$/CdS annealed in vacuum for 30 minutes at 200°C).

previously (section 5.1.2), such films have poor crystal structure and form cells with poor efficiency. This is demonstrated in table 5.15 which gives the efficiency for the unimplanted cell as only 1%. However, what is of interest in this set of results is the apparent reversal in the changes to the values for x and d as the ion energy increases. The initial reduction and subsequent increase observed suggests that, in general, the observation of an increase or decrease in x and d will depend upon the values of the ion implantation parameters employed as well as on the structure of the CdS films involved.

Table 5.15: Photovoltaic characteristics of Cu_xS/CdS cells annealed for 6.25 hours in hydrogen. (The CdS layers were implanted with 10-50 keV Cu ions at a constant dose 5×10^{14} ions/cm^2.)

Ion energies (keV)	I_{sc} (mA/cm^2)	V_{oc} (volt)	d (μm)	X	η %
Unimplanted	13.1	0.28	0.54	1.96	1
10	11.56	0.43	0.35	1.94	1.5
20	11.87	0.4	0.34	1.93	2.4
30	15.87	0.47	0.29	1.91	4.3
40	10.3	0.4	0.22	1.87	2
50	7.8	0.4	0.47	1.91	0.9

Although the I/V parameters listed in table 5.15 show significant scatter (due to the poor uniformity of these particular layers) it is clear that ion implantation leads to a significant improvement in their performance. In particular, there is a substantial increase in the open circuit voltage suggesting that the effective junction area of the cells might be substantially reduced by ion implantation. This

could result from less grain boundary penetration during the growth of the Cu_xS layer. As discussed in section 5.2.1 the amount of grain boundary growth has a strong influence on the resultant effective thickness of the Cu_xS layer. Thus, a reduction in the grain boundary penetration would lead to reduced effective thickness and, as the results in table 5.15 show, this is what occurs for these particular cells. These effects result in a substantial improvement in the overall photovoltaic performance of these cells, with the efficiency being increased to be 4.3% for implantation at 30 keV.

Finally, in addition to the results for copper implanted cells, it is worth mentioning the results of a brief investigation using zinc ions. The CdS films used for this study were of poor quality, coming from the same batch as those for the cells in table 5.15. However, the use of similar films does mean that the results of the Zn implantation can be compared directly with the results in table 5.14 for Cu implanted cells. As 30 keV ions provided the best result for Cu ions, the same energy was employed for the Zn ions with the fluence varying from 10^{14} - 10^{16} ions/cm^2. The results are presented in table 5.16.

It was surprising to find that Zn implantation into these cells produced very similar effects to those resulting from Cu implantation. However, this supports the view that the main effect of implantation is on the crystal structure of the CdS film and that this has an influence on the growth process for Cu_xS during subsequent dipping (particularly at the grain boundary regions). Although the results for the Zn implanted cells show some random variations (again, due to the poor quality of these films), it is interesting to note from

tables 5.15 and 5.16 that the highest efficiency is reached under similar implantation conditions for the Zn and Cu implanted cells (both sets of cells giving the best results for 30 keV ions at 5.10^{14} ions/cm^2). With limited data available, this correspondence in behaviour between Zn and Cu implanted cells could be fortuitous, but it is expected that the Cu and Zn ions (with similar penetration depths into CdS film) would have similar effects on the crystal structure of these films.

Table 5.16: The I-V characteristics for Cu_xS-CdS cells after annealing in hydrogen for 8 hours. (The CdS films were implanted with Zn ions at a constant energy of 30 keV with ion dose in the range of 10^{14}-10^{16} ions/cm^2

Ion dose/cm^2	V_{oc} (volt)	I_{sc} (mA/cm^2)	η %
Unimplanted	0.28	13.1	1
10^{14}	0.44	9.37	2.4
5×10^{14}	0.47	20.6	5.4
5×10^{15}	0.46	13.1	2.6
10^{16}	0.48	18.75	3.4

However, it has become clear that there is a need for further study of the effects of implantation with different ions and different types of CdS films.

5.4 Stability of Cu_xS-CdS cells

5.4.1 Variation of cell characteristics with time

As has been previously mentioned (e.g. in section 3.4.2) the freshly formed Cu_xS-CdS cells generally display poor I/V characteristics, and some form of heat treatment is usually necessary

to optimise the performance of these devices. However, if the cells are subsequently exposed to the atmosphere, structural and chemical changes can occur, causing deleterious effects on the cell behaviour and a consequent reduction in the photovoltaic conversion efficiency of these devices. This efficiency degradation process is clearly seen in figure 5.55 which shows the I/V characteristics for a Cu_xS-CdS immediately after post-fabrication annealing in hydrogen (curve A) and subsequent exposure to air for 10 days (curve B), for 32 days (curve C) and for 159 days (curve D). The general trend in behaviour, seen in figure 5.55 is commonly observed but it is important to note that not all cells behave in exactly the same way. For example, for the case shown in figure 5.55, there is a steady reduction in both the short circuit current and open circuit voltage as the time in air is increased but, for some cells, the initial reduction in short circuit current is accompanied by a small increase in open circuit voltage. Such an effect has been observed by Te Velde (161) who attributed it to the effect of oxygen diffusing to the Cu_xS-CdS interface causing an increase in the potential barrier at the CdS side of the junction. Support for this mechanism comes from the observation that the increase in V_{OC} is reversed by further annealing in hydrogen, which would be expected to assist the removal of oxygen from the interface.

The initial reductions in I_{SC} and V_{OC}, seen in figure 5.55 (curves A and B) are found to be accompanied by an improvement in the fill factor from 0.55 to 0.59. This is consistent with a reduction in the series resistance of the cell which would be expected to arise from a loss of copper from the Cu_xS layer and a consequent reduction in sheet resistance of this layer as discussed in section 3.3.2. For some cells, the fill factor continues to improve for very long

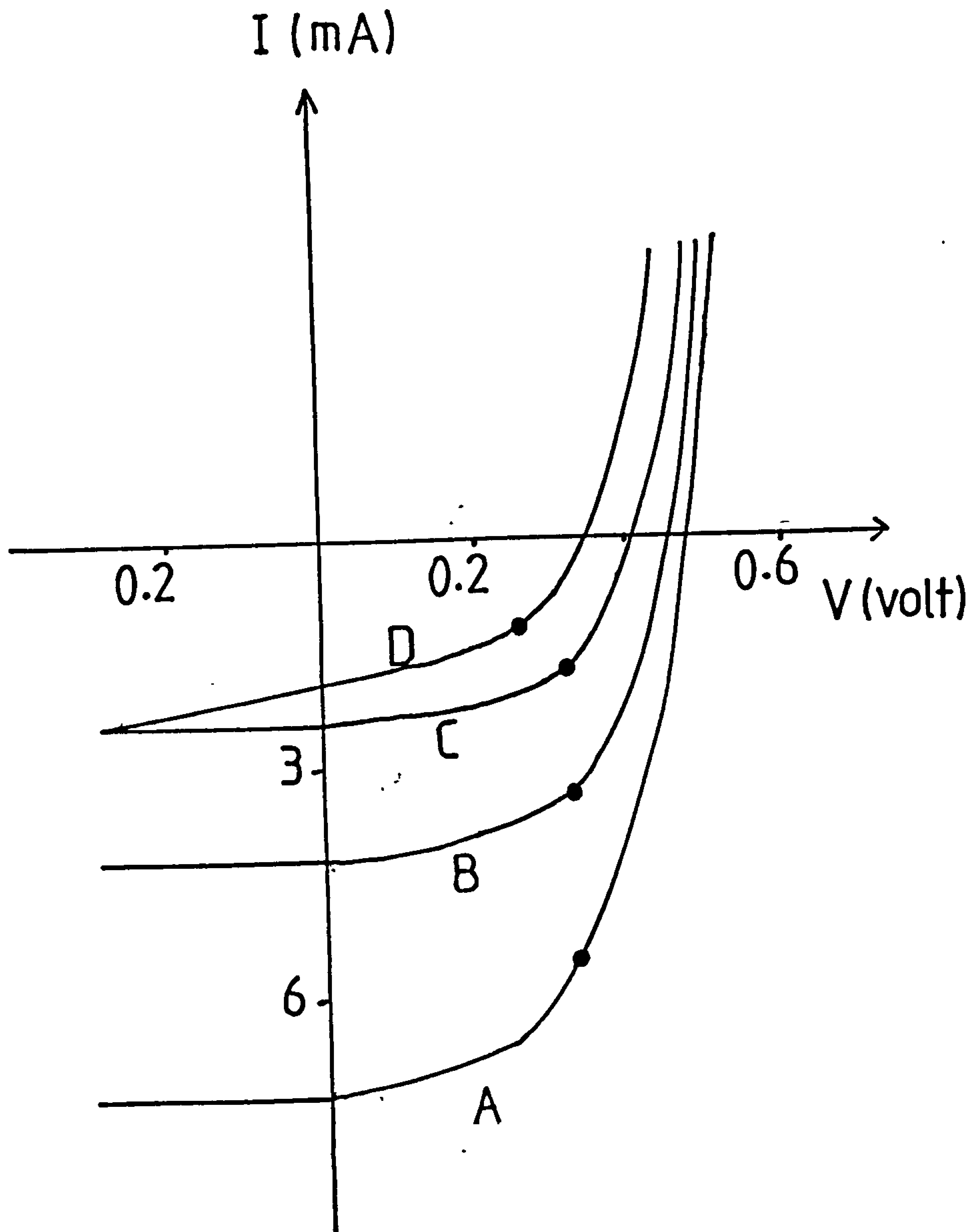

Fig.(5.55) The I/V characteristics for a Cu_xS - CdS cell immediately after post-fabrication annealing in hydrogen for 30 minutes (curve A) and subsequent exposure to air for 10 days (curve B), for 32 days (curve C) and for 159 days (curve D).

exposure times in air, but for the cell in figure 5.55, this trend is not maintained and it is clear from the change of shape for curve D that an additional degradation mechanism is contributing to the reduction in fill factor to 0.5. This is thought to be due to a reduction in shunt resistance caused by diffusion at grain boundaries. In order to obtain further information about the various processes contributing to the observed degradation effects seen in figure 5.55, corresponding effects on other characteristics need to be studied. For example, figure 5.56 shows the spectral response for a cell immediately after annealing for 6 hours in hydrogen (curve A) together with the corresponding response after exposing the cell to air for 115 days (curve B). It is clear from figure 5.56 that the whole spectral response was decreased by exposing the cell to air, but it is also significant that the contribution to the cell current associated with the longer wavelength region of the spectrum suffered a greater reduction than the short wavelength region. As discussed in section 5.3.2, such an effect is consistent with a reduction in the stoichiometry factor x for the Cu_xS layer, and corresponding reductions in the Cu_xS sheet resistance values have been observed.

The effects of copper diffusion from the Cu_xS layer into the CdS layer during operation can most easily be detected from changes in the junction capacitance, as previously described in section 5.3.3. A typical result, showing how the junction capacitance varies with the air exposure time is given in figure 5.57. In accordance with the discussion in section 5.3.3, a reduction in junction capacitance with increasing time in air, could be attributed to diffusion of copper into the CdS layer causing an increase in the width of the compensated

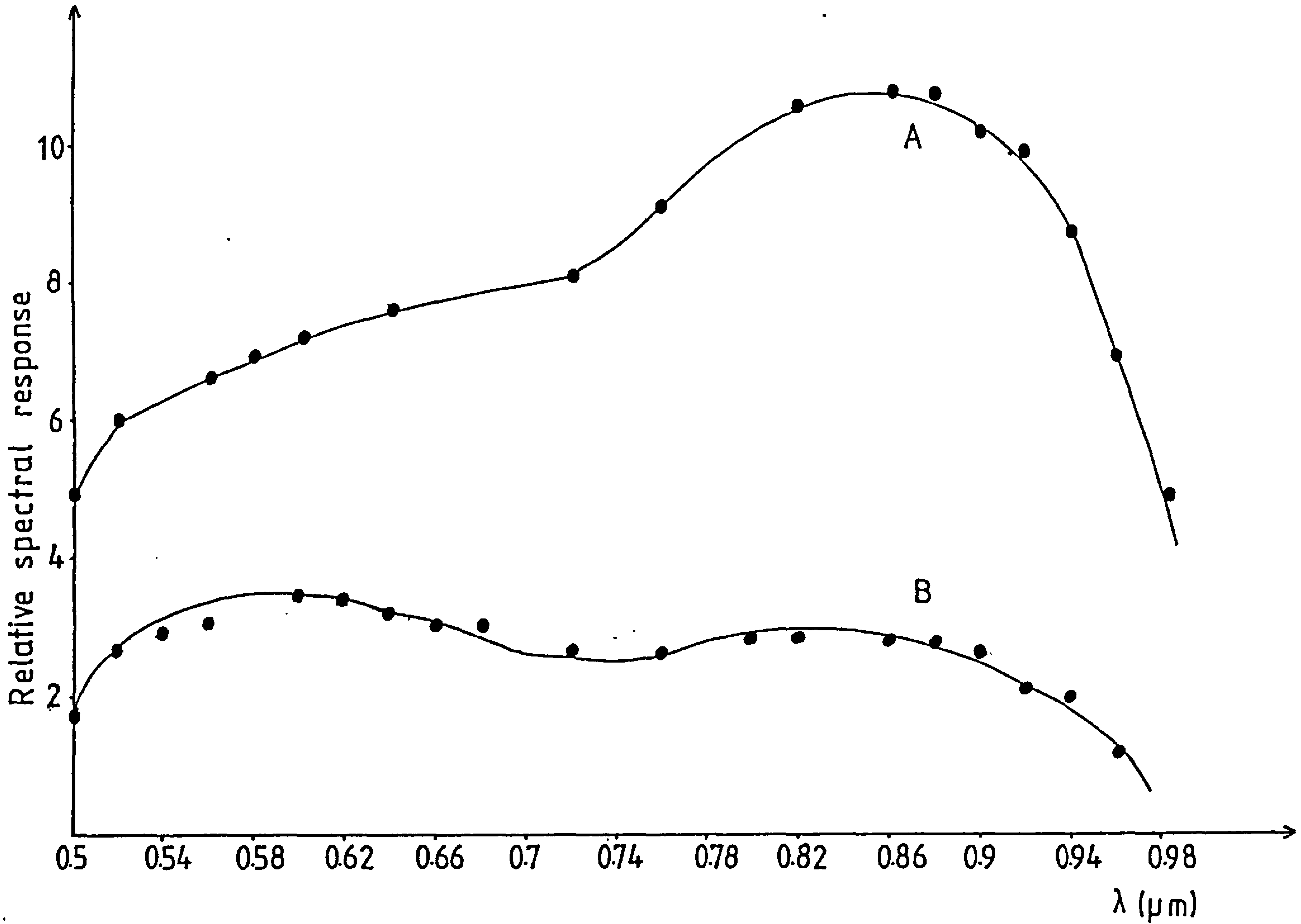

Fig.(5.56) The spectral response for a cell immediately after annealing for 6 hours in hydrogen (curve A) and after exposure of the same cell to air for 115 days (curve B).

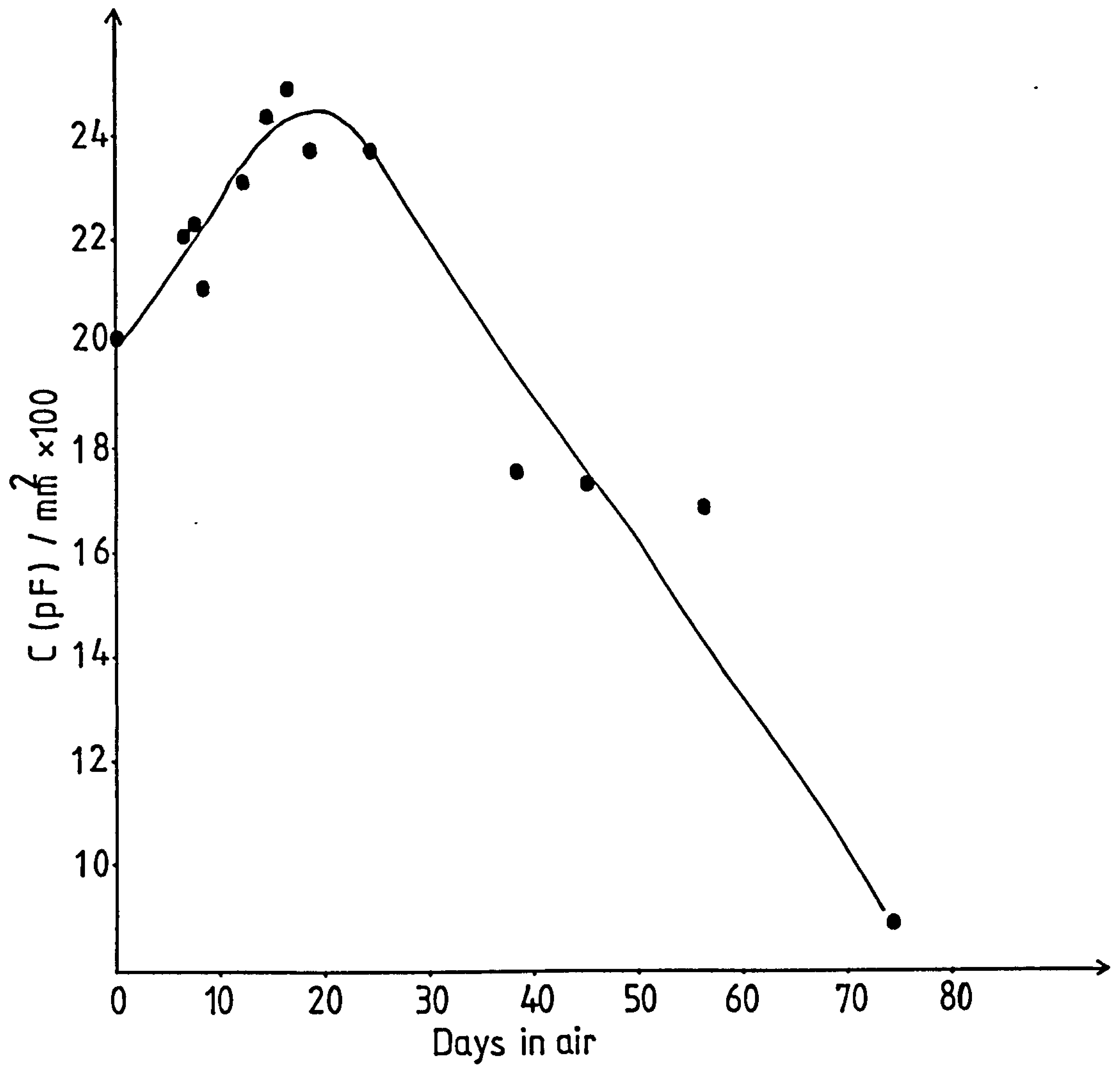

Fig.(5.57) Typical junction capacitance for Cu_xS - CdS cell against air eposure in days.

region close to the Cu_xS-CdS junction. However, the time variation seen in figure 5.57 appears to be more complicated than the behaviour expected to result from this single diffusion process and further consideration is given to the interpretation of this data in section 5.4.3.

It is clear from the examples given in figures 5.55, 5.56 and 5.57 that a number of different processes are involved in changing the characteristics of cells during operation. The efficiencies of cells exposed to air degrade rapidly, mainly as a result of a decrease in the stoichiometry factor x for the Cu_xS layer. This reduction in x is assumed to be due partly to oxidation at the top surface of the film and partly to interfacial diffusion of Cu into the CdS layer, with the diffusion process leading to additional deleterious effects. However, it is also clear that these degradation processes depend very strongly on the structural properties of the cell, involving the crystallite structure of the CdS film, the Cu_xS thickness and topography, and the post fabrication annealing conditions.

A more detailed discussion concerning these factors is given in the next sections which present the results of experiments designed to provide information on the relative significance of the different degradation processes which can occur in different types of cells and possibilities for stabilization of cell characteristics.

5.4.2 Processes associated with Cu_xS-CdS interface

In the previous section, the main degradation processes referred to were diffusion processes between the CdS and Cu_xS layers, oxidation at the Cu_xS surface and the associated changes in composition of the Cu_xS layer. As the Cu_xS layer is very thin, its properties are very sensitive to any loss of copper via either the oxidation or diffusion

mechanisms. However, the diffusion processes are of particular importance as they lead to significant changes in structure and characteristics of the Cu_xS-CdS interface as well as affecting the composition of the Cu_xS layer. The problem is made particularly complex by the fact that diffusion occurs into or out from the interior of the CdS grains and also along the grain boundaries at different rates. Furthermore, although these diffusion processes are considered here as degradation processes, it must be remembered that the cells are usually given a post-fabrication annealing treatment in order to promote a diffusion process across the Cu_xS-CdS interface so as to form a wider depletion layer in the CdS next to the interface. In order to examine whether this effect would occur naturally by slow diffusion at room temperature, an experiment was performed using a set of unannealed cells, with measurements being made on their I/V characteristics as a function of time. For this work, a set of small area cells were fabricated on a single 1 cm^2 CdS sample, as described for capacitance studies in section 5.3.3. Using varnish to define small windows of CdS of area ~ 5 mm^2, four samples were dipped into a hot bath of CuCl for different times (2,4,6 and 8 seconds). A gold contact was then evaporated to cover one of the small areas in each of the samples and the cell current was measured as a function of voltage applied to each of these contacts. After leaving the cells exposed to air for 65 days, a further contact was provided to one of the exposed areas on each of the samples and the I/V relationship was determined for these elements. This was repeated several times, with new contacts being applied to each of the cell elements after exposure to air for different lengths of time. The results of the measurements of

the I/V characteristics as a function of time are shown in figures 5.58, 5.59, 5.60 and 5.61. These figures show that, in general, non-rectifying behaviour was observed and that the dark I/V characteristics became more linear with longer ageing times in air. As the diffusion of copper across the Cu_xS-CdS interface, into the CdS layer, would widen the space charge region and make the I/V characteristics more rectifying, the results in figures 5.58-61 suggested that this diffusion process is not the dominant process at room temperature. The more important process appears to be the diffusion of copper along the grain boundaries causing the junction area of the cells to be increased and the junction resistance to be reduced, depending on the time in air before a contact is formed. The effects are summarized in table 5.17 which gives the zero bias resistance for all curves in figures 5.58-61.

Table 5.17: The zero bias resistance for unannealed Cu_xS-CdS cells as a function of time of exposure to air

	Junction resistance (Ω)			
Time in air (days)	Dipping time (2 seconds)	Dipping time (4 seconds)	Dipping time (6 seconds)	Dipping time (8 seconds)
0	4000	1000	120	100
65	160	100	90	90
100	40	24	30	30
143	30	20	13	1.7
180	30	20	5	5
198	4	4	2.5	40

It is clear from table 5.17 that the initial junction resistance R_j

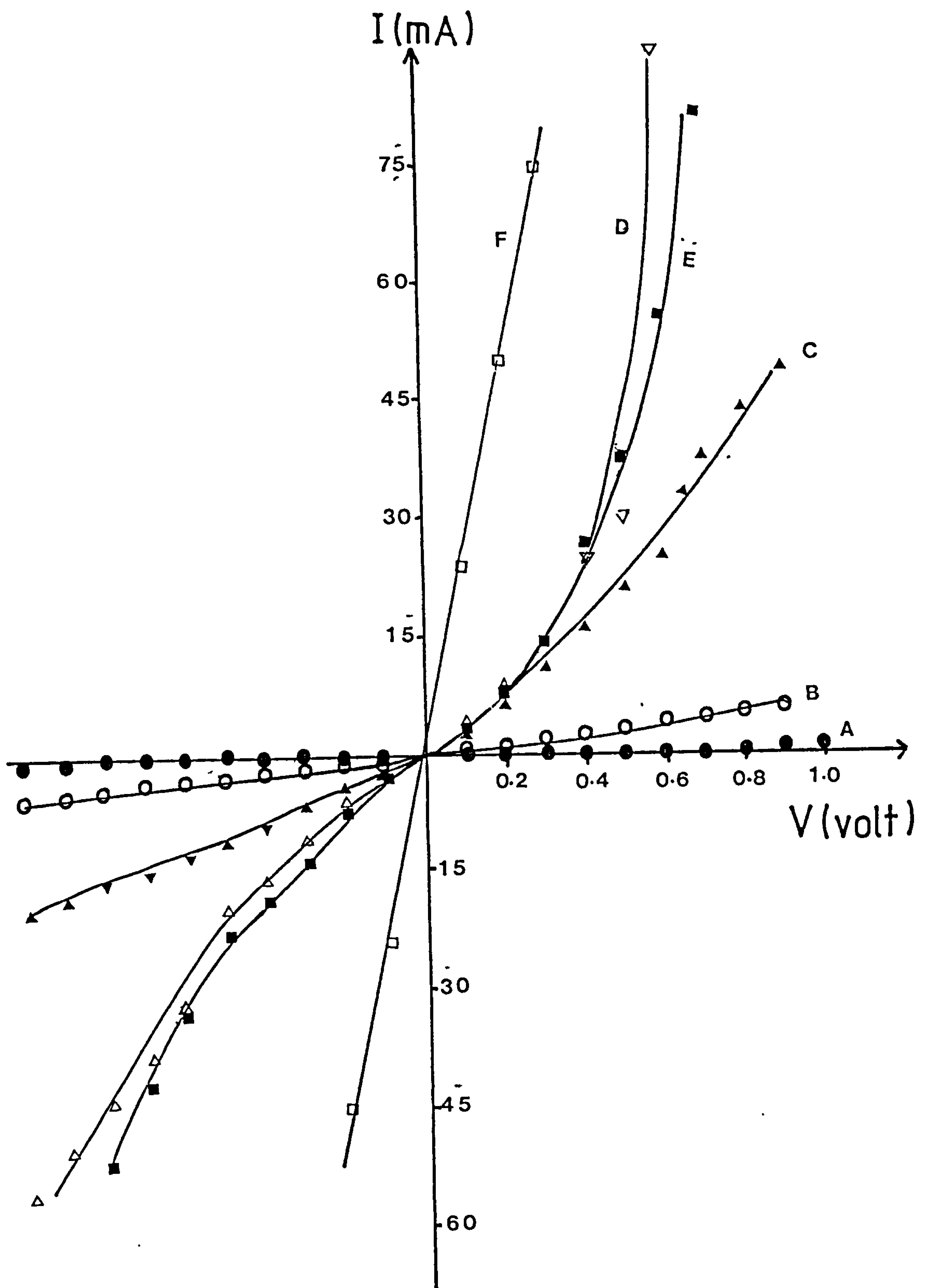

Fig.(5.58) The dark I/V characteristics for the as-formed Cu_xS - CdS cell (curve A) and after exposure to air for 65 days (curve B), 100 days (curve C), 143 days (curve D), 180 days (curve E) and 198 days (curve F). (Dipping time was 2 sec.)

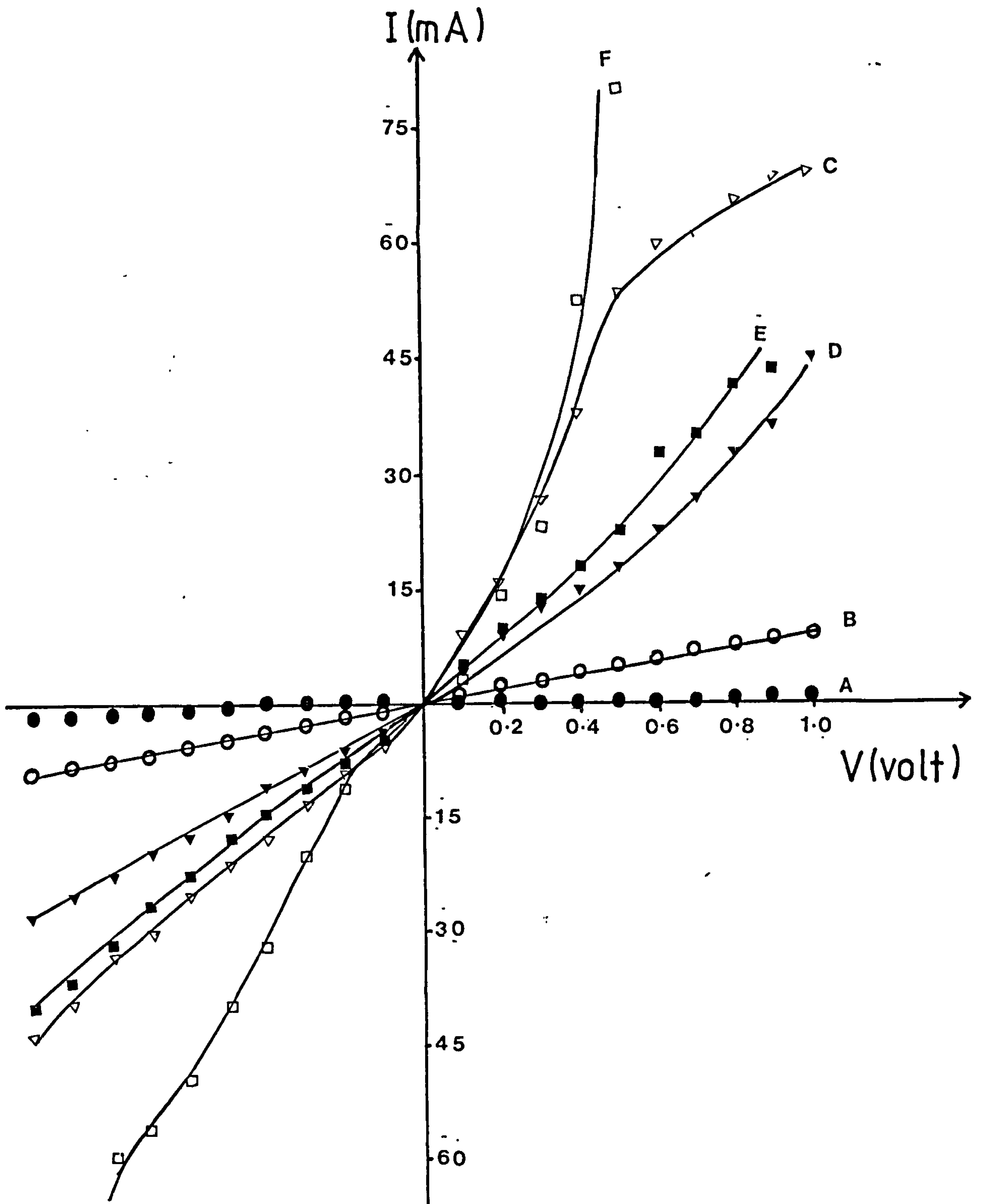

Fig.(5.59) The dark I/V characteristics for the as-formed Cu_xS - CdS cell (curve A) and after exposure to air for 65 days (curve B), 100 days (curve C), 143 days (curve D), 180 days (curve E) and 198 days (curve F). (Dipping time was 4 sec.)

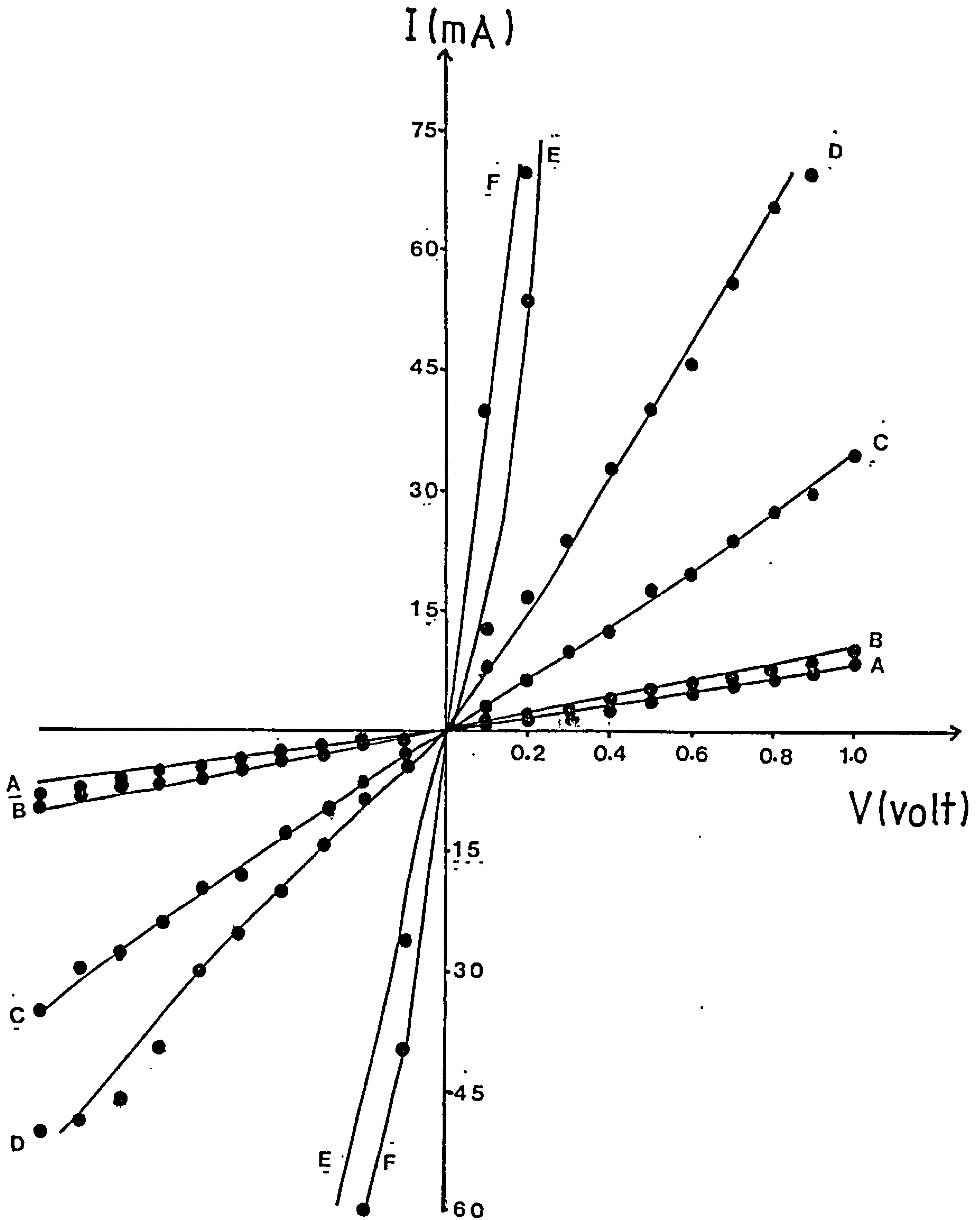

Fig.(5.60) The dark I/V characteristics for the as-formed Cu_xS - CdS cell (curve A) and after exposure to air for 65 days (curve B), 100 days (curve C), 143 days (curve D), 180 days (curve E) and 198 days (curve F). (Dipping time was 6 sec.)

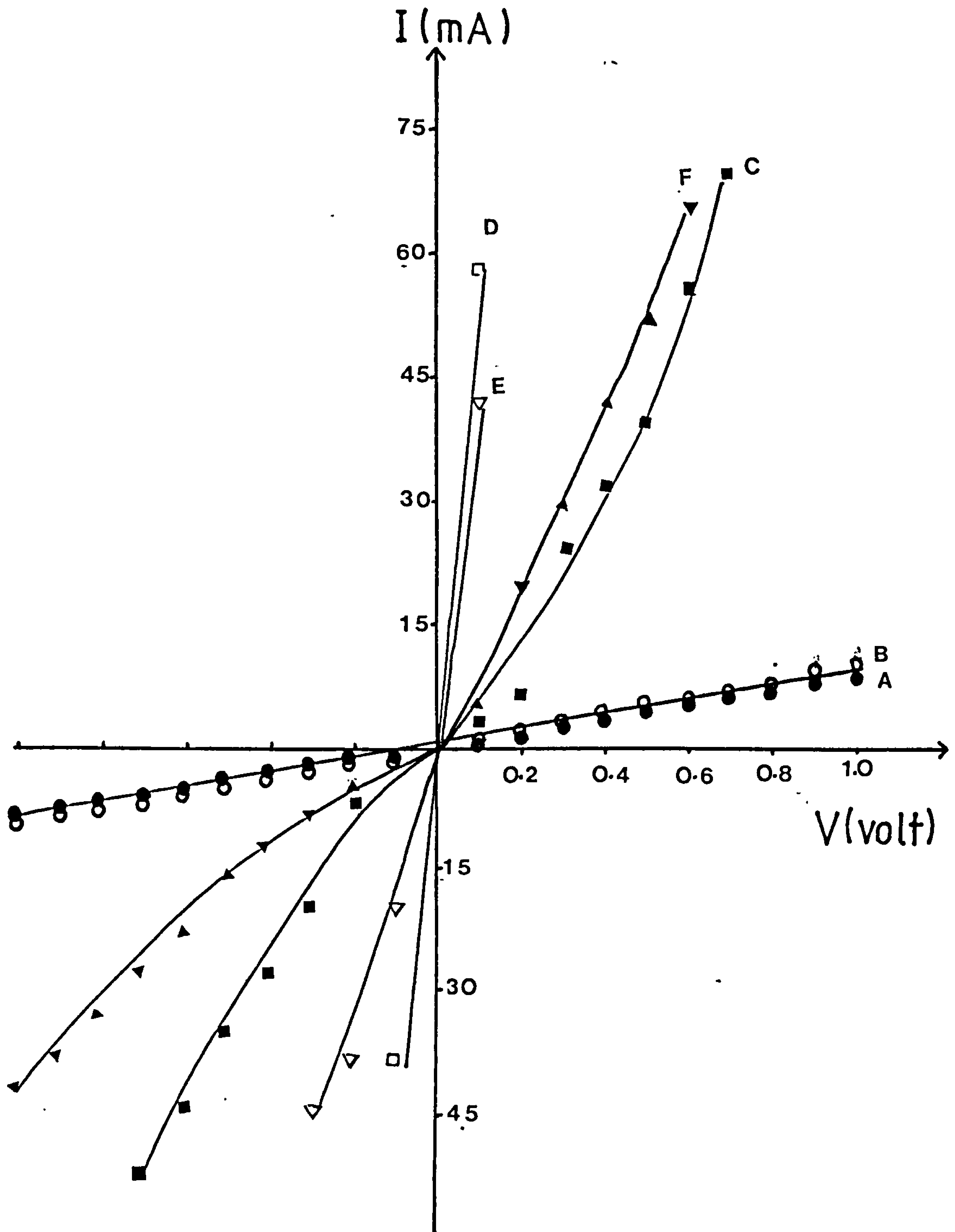

Fig.(5.61) The dark I/V characteristics for the as-formed Cu_xS - CdS cell (curve A) and after exposure to air for 65 days (curve B), 100 days (curve C), 143 days (curve D), 180 days (curve E) and 198 days (curve F). (Dipping time was 8 sec.)

falls with increased dipping time. As discussed in section 5.2.1, longer dipping times cause greater penetration of Cu_xS layer into the grain boundaries, thereby increasing the Cu_xS-CdS junction area. This would have the effect of reducing the effective junction resistance, as is observed. The table also shows that for each of the cells (independent of dipping time) the junction resistance falls with increased air exposure time. This is assumed to be due to the diffusion of copper along the grain boundaries as explained above, but for a dipping time of 8 seconds, there is some hint of increase in R_j for the period from 143 to 198 days in air. The trend towards an increase in R_j after a long time in air at room temperature was confirmed by re-examining all junctions after a further 108 days following the last measurements in table 5.17 when several cells showed a small increase in R_j from their previously recorded values. Further evidence for a reversal in the direction of changes in R_j with time was obtained using a different batch of samples fabricated in the same way as for the samples in figures 5.58-61 but with CdS films from a different deposition run. The results are shown in figure 5.62 where curves A, B, C, D, E and F represent the I/V characteristics before and after ageing the cell in air for 0, 18, 41, 83, 135 and 269 days respectively. It is clear from figure 5.62 that there is an initial reduction in junction resistance but after 41 days in air the slope of the I/V characteristics curves were reduced with increasing time and after 269 days (curve F) there is a very substantial increase in the effective junction resistance. It seems reasonable to conclude that after long periods of time, the properties of the junction begin to be dominated by diffusion across the interface

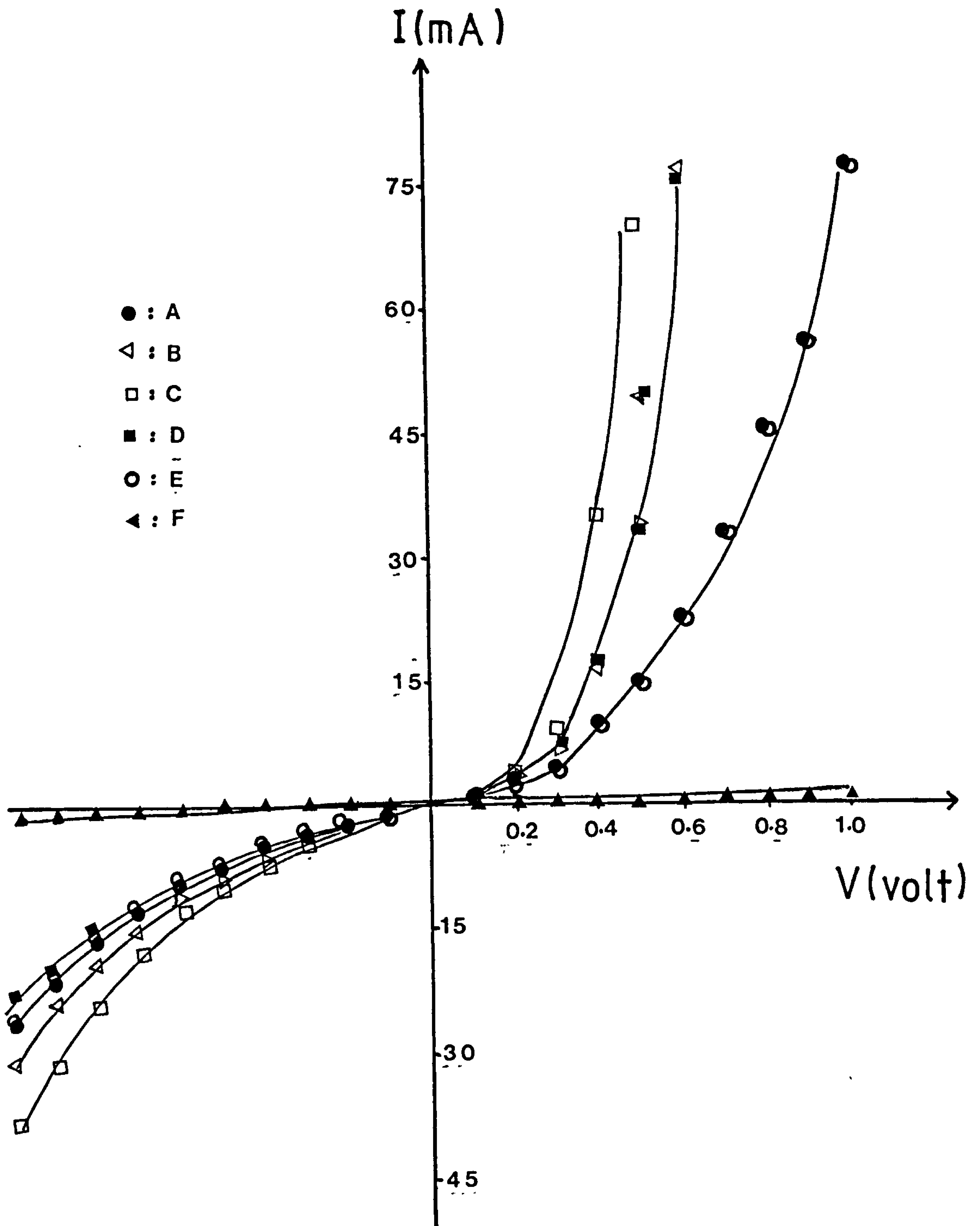

Fig.(5.62) The dark I/V characteristics for the as-formed Cu_xS - CdS cell (curve A) and after aging the cell in air for 18 days (curve B), 41 days (curve C), 83 days (curve D), 135 days (curve E) and 269 days (curve F). (Dipping time was 4 sec.)

rather than along the grain boundaries. This trend appears to be enhanced by annealing which has the effect of increasing the junction resistance and reducing the capacitance. After 306 days at room temperature all the samples of figures 5.58-61 were annealed in vacuum for 1/2 hour, and the subsequent I/V characteristics for one set of cells are shown in figure 5.63. Corresponding capacitance measurements for all the cells are given in table 5.18.

Table 5.18: Capacitance measurements at V=0 for different dipping times (2,4,6 and 8 seconds) after annealing in vacuum for 1/2 hour at 200°C (the samples were in air for 306 days before annealing).

Dipping time (seconds)	Capacitance (PF/mm²)					
	Cell 1	Cell 2	Cell 3	Cell 4	Cell 5	Cell 6
2	356	271	110	350	400	463
4	-	-	405	490	111	417
6	451	462	382	467	375	368
8	357	423	417	385	417	417

The I/V characteristics of figure 5.63 clearly show much reduced current densities in comparison with their values prior to annealing and very similar characteristics, showing that good rectification was obtained for all the samples which were investigated (i.e. with dipping times of 2,4,6 and 8 seconds). While the capacitance measurements before annealing were difficult to make, due to the high conductance for all the cells. It is interesting to note from table 5.18 that after annealing, the capacitance values for all the samples were very similar indicating that similar junction areas were finally obtained. Unfortunately, as mentioned above, the high electrical

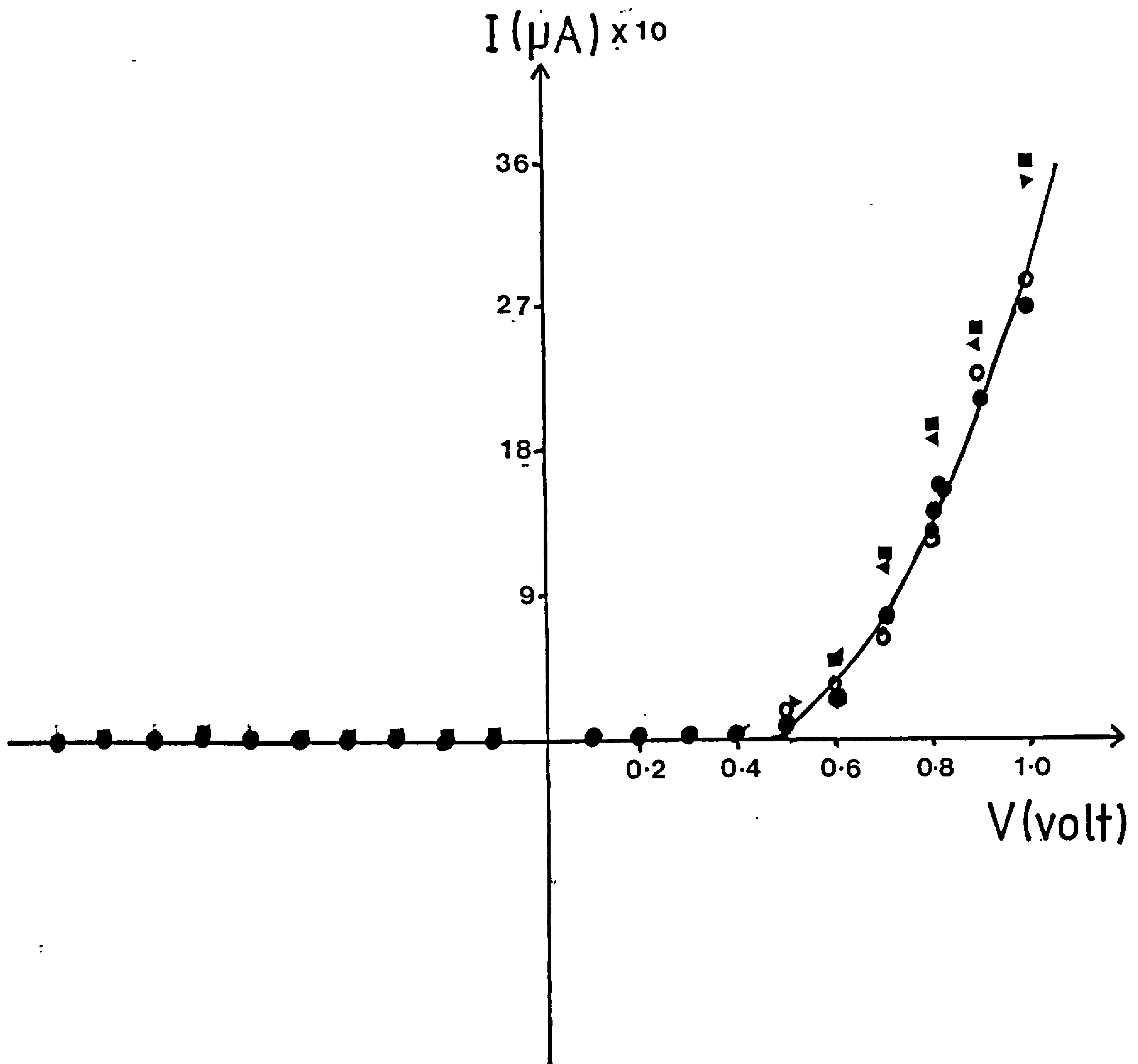

– Fig.(5.63) The dark I/V characteristics for a set of Cu_xS - CdS cells (dipping time 8 seconds) after annealing in vacuum for 1/2 hour at 200°C. The cells were exposed to air at room temperature for 306 days before annealing.

conductance of the junction without any annealing treatment, makes measurement of capacitance very difficult on many samples before annealing. However, using samples from the run of figure 5.62 which, had a slightly higher junction resistance prior to annealing (as indicated above), it proved possible to make capacitance measurements for a full set of cells (for samples dipped for 2,4,6 and 8 seconds). The variation of these capacitance values as a function of time in air can be seen in figures 5.64 where the results for dipping times of 2,4,6 and 8 seconds are represented by the curves A,B,C and D respectively. Clearly, the initial capacitance was increased for increased dipping times, as expected, due to the increase in junction area. Also, it can be seen that for the first 20 days in air, the capacitance for samples with dipping times of 4,6 and 8 seconds increased, but for longer air exposure times, a fall was observed. Each of the curves in figure 5.64 are for data obtained using a single area on each sample. As the contact covered only a small part of each area, it was assumed that the contact would not prevent the air interacting with the cell. However, in order to avoid this possibility, a new contact was applied to a fully exposed area after various periods of time and the results (shown in figure 5.65) indicate a similar behaviour. The reduction in capacitance with long exposure times in air, seen in figures 5.64 and 5.65, can be attributed to interfacial diffusion of copper causing a wider depletion layer, while the initial increase in capacitance during air exposure could be attributed to an increase in junction area of the cells, consistent with the increase in junction conductance, as previously discussed. However, it is possible that the sheet

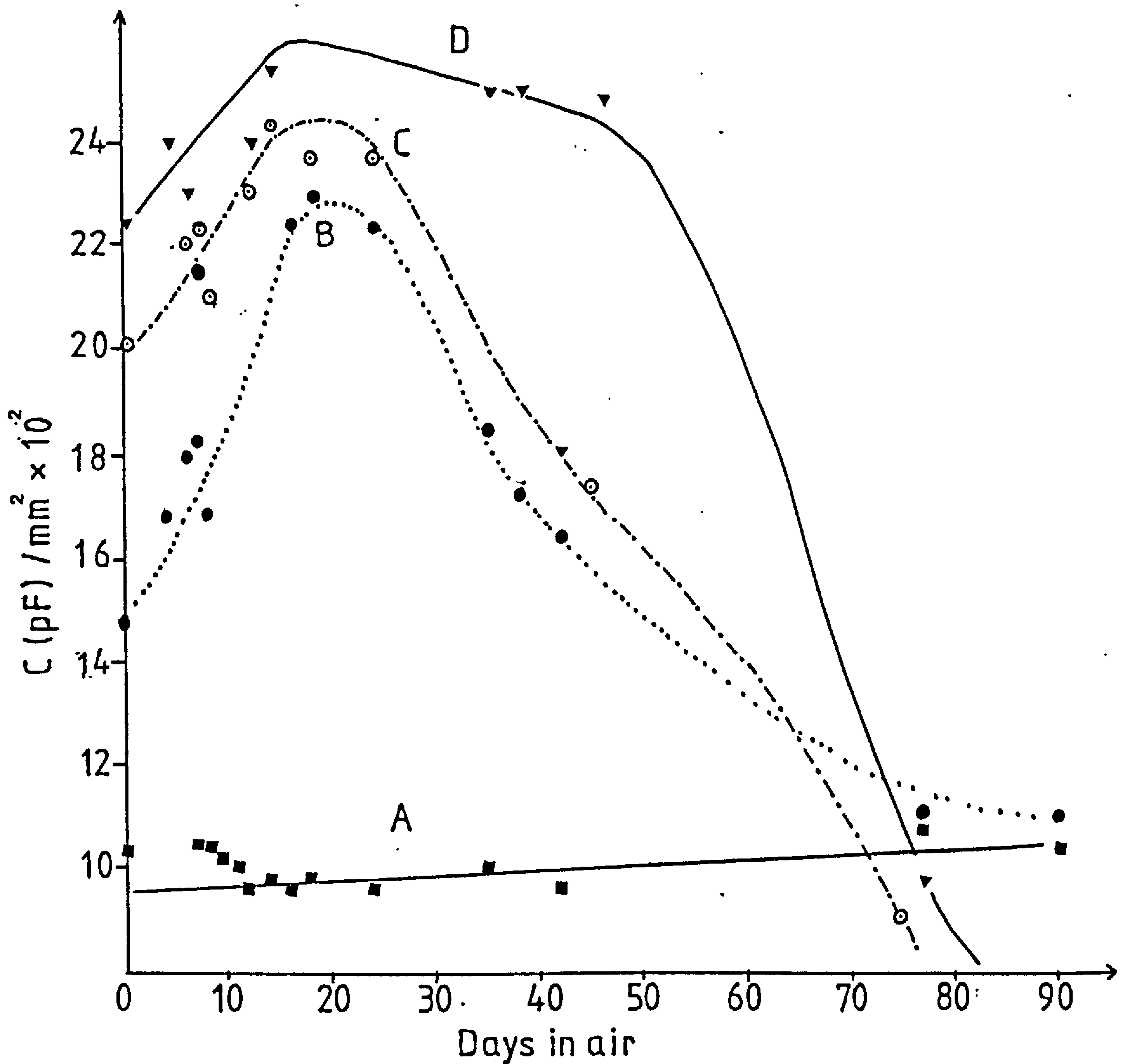

Fig.(5.64) The variation of junction capacitance for as-formed Cu_xS - CdS cells as a function of time of exposure to air. Using different dipping time, 2 seconds (curve A), 4 seconds (curve B), 6 seconds (curve C) and 8 seconds (curve D). (The evaporated contact did not cover all area).

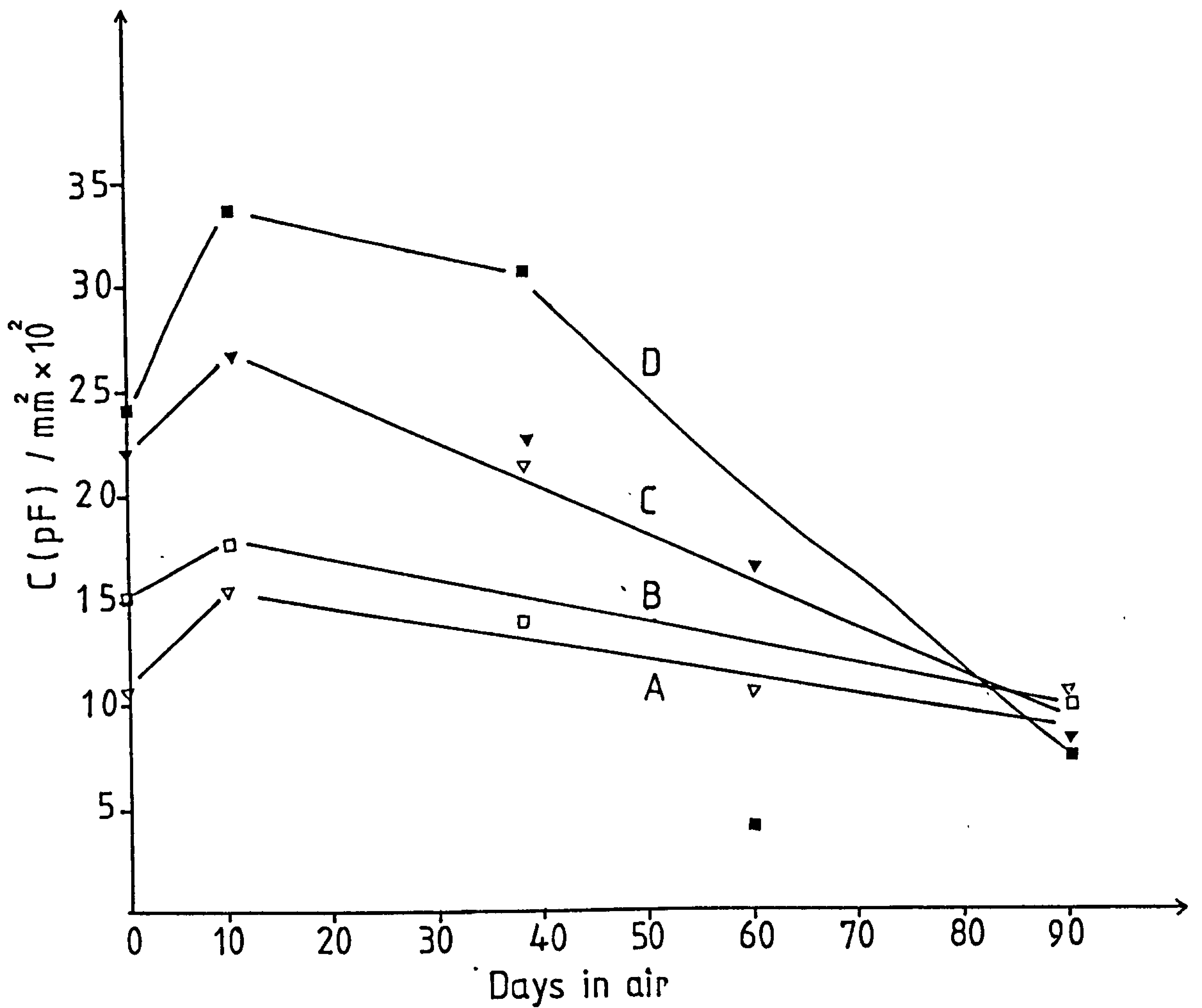

Fig.(5.65) The variation of junction capacitance for as-formed Cu_xS - CdS junction for different dipping times; 2 seconds (curve A), 4 seconds (curve B), 6 seconds (curve C) and 8 seconds (curve D). (New contact was applied to a fully exposed area after each period of time).

resistance of the Cu_xS layer could have an affect on the measured capacitance in figures 5.64 and 5.65. The Cu_xS-CdS diode can be represented as in figure 5.66 (a) when the evaporated gold contact covers the whole area of the Cu_xS layer, but when the contact covers only a small part of the surface, the representation in figure 5.66 (b) is more appropriate. In this figure R_C and R_J represent the sheet resistance of Cu_xS layer and the junction resistance of Cu_xS-CdS cell respectively. The loss of copper from the Cu_xS layer due to diffusion into the CdS film and oxidation at the surface of Cu_xS layer exposed to air, reduces the sheet resistance of the Cu_xS layer and this would have the effect of increasing the measured capacitance of a Cu_xS-CdS cell represented by figure 5.66 (b).

In order to examine this possibility, an attempt was made to measure the time variation of the sheet resistance under the same conditions as for the results shown in figure 5.64. A similar sample from the same batch as used for these results was provided with grid contacts as described in section 4.4.1. However, as expected, the sheet resistance measurements for these unannealed samples proved to be unreliable, as shown in figure 5.67. It can be seen that in every case (for dipping times of 2,4,6 and 8 seconds) the apparent sheet resistance values were very low in comparison with the results presented in section 5.2.3. For the results in section 5.2.3, the samples had been annealed so that the well formed junction barrier effectively isolated the Cu_xS layer from the underyling more conductive CdS layer. However, for the as prepared Cu_xS-CdS samples discussed here, no effective isolation was provided by the very narrow junction barrier so that the current flowing between the contacts on the Cu_xS layer was mostly passing through the junction, into the

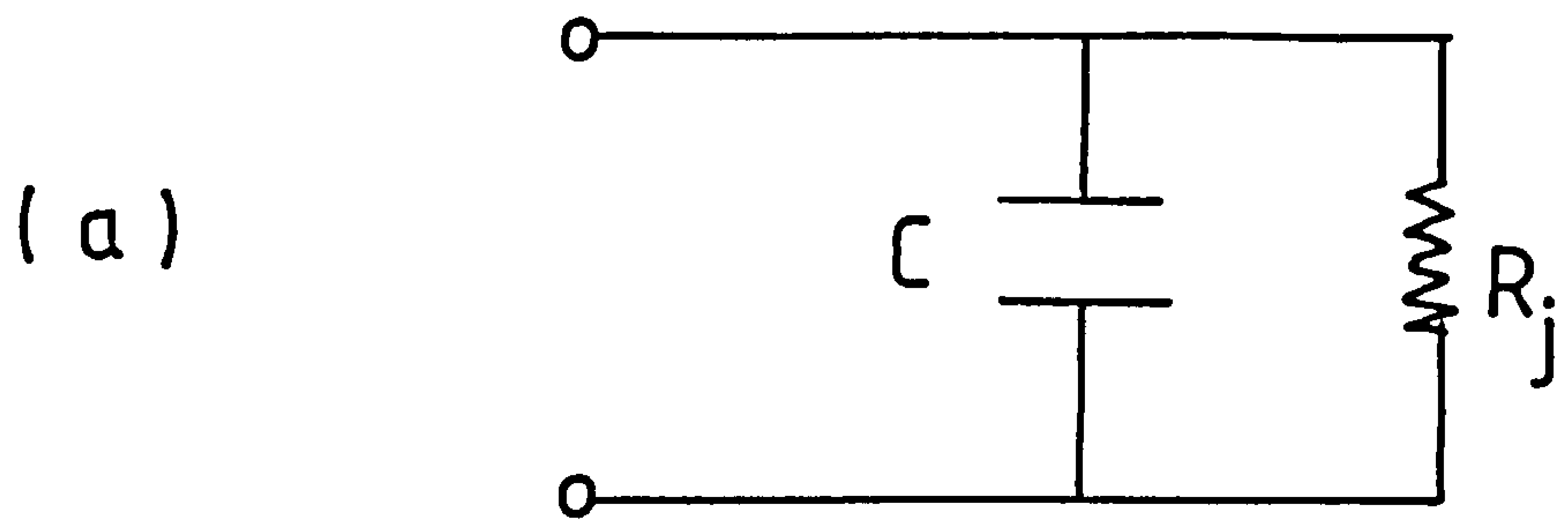

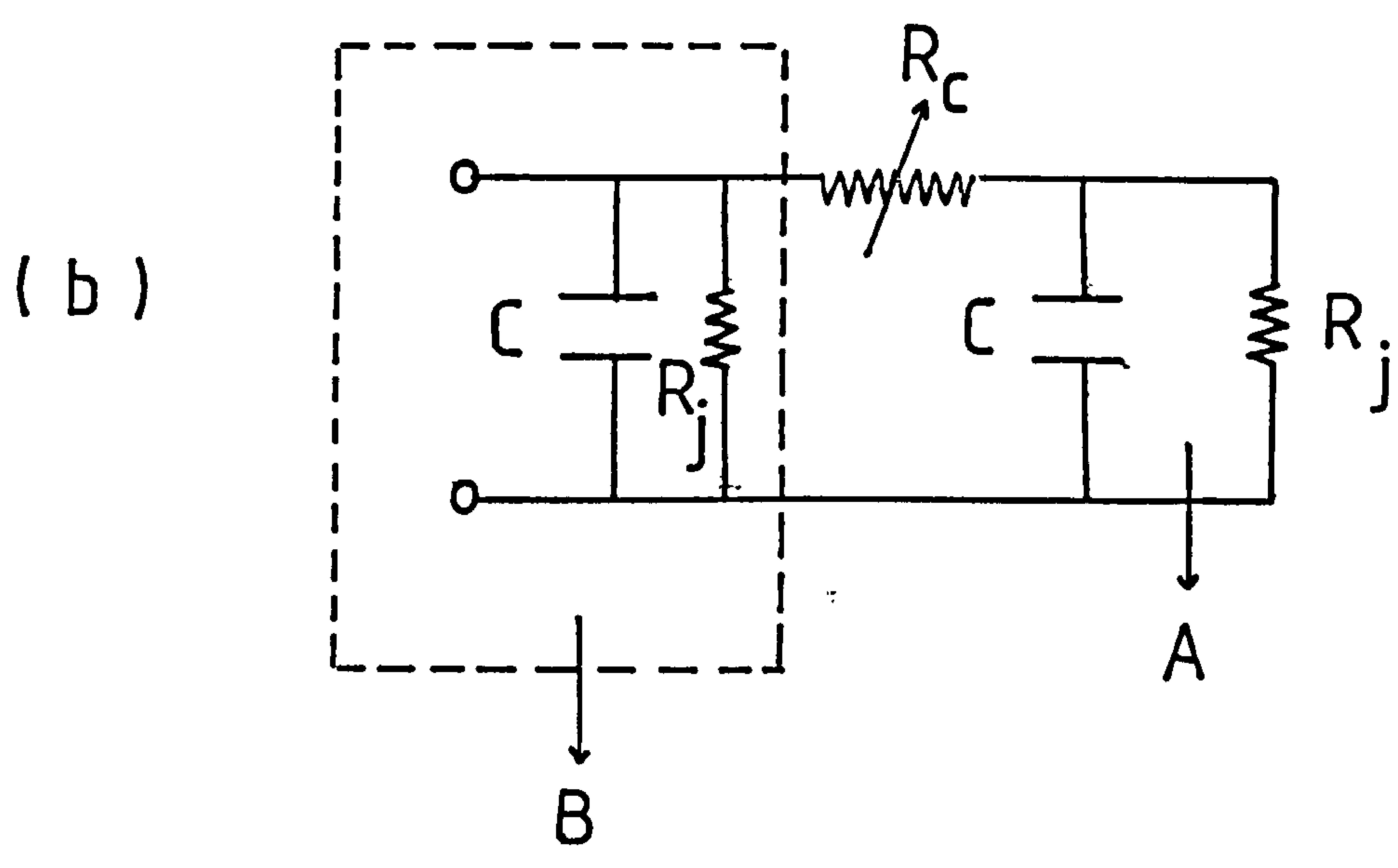

Fig.(5.66) (a) Circuit represents the Cu_xS - CdS diode.
(b) Circuit represents the Cu_xS - CdS diode when the contact covers only a small part of the surface; part (A) represents junction region surrounding contact and part (B) represents junction below contact..

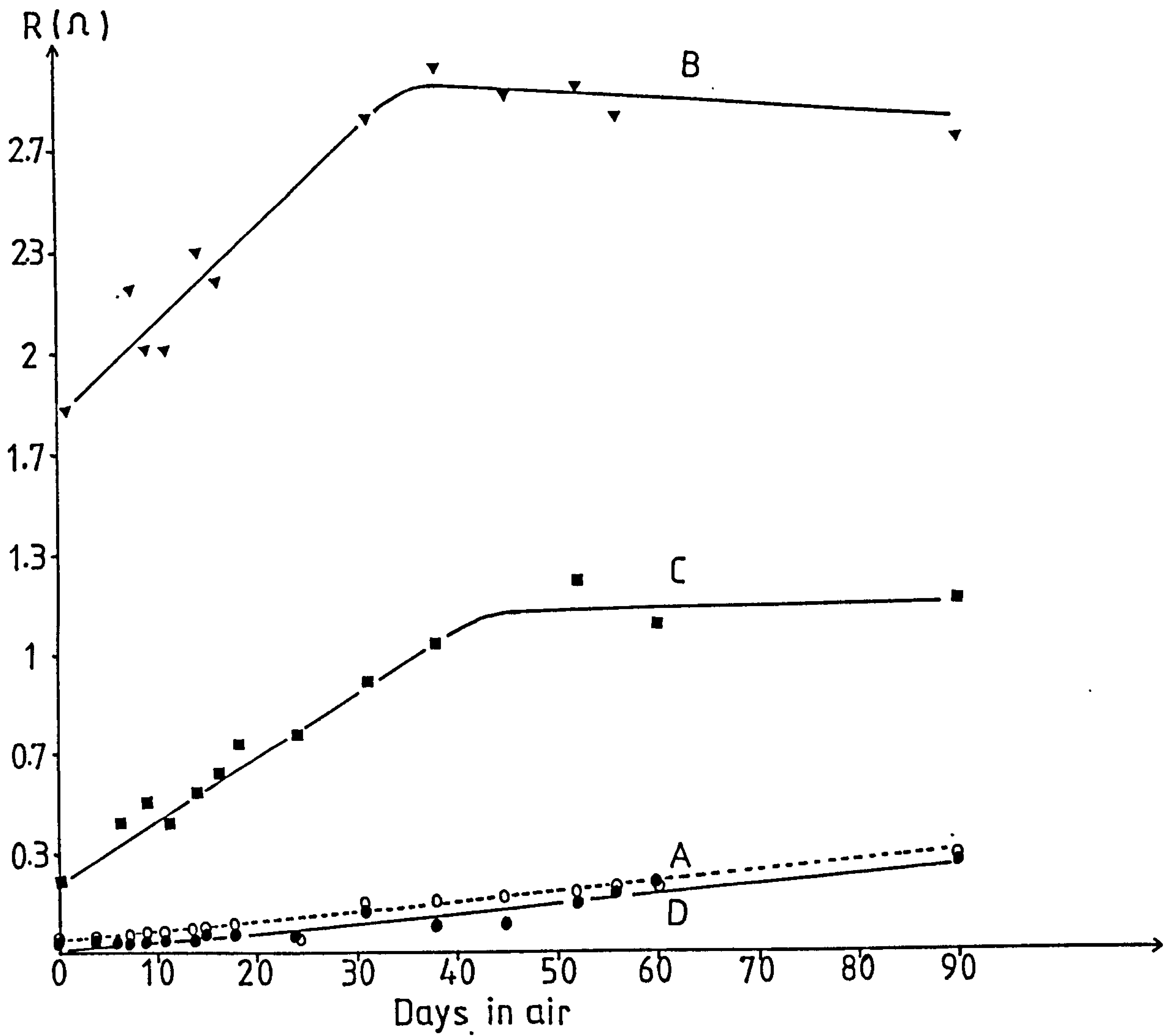

Fig.(5.67) The sheet resistance of Cu_xS layer as a function of time in air for different as-formed Cu_xS - CdS cells. Using different dipping times of 2 seconds (curve A), 4 seconds (curve B), 6 seconds (curve C) and 8 seconds (curve D).

underlying CdS layer and through to the back contact thereby short circuiting the Cu_xS layer. Thus the resistance values given in figure 5.67 were controlled by the junction and therefore show a slow increase with time as a result of copper diffusion and the associated change in junction resistance as indicated by the I/V characteristics for these samples in figure 5.62. No further sheet resistance measurements on unannealed cells were made. However, the effect of the Cu_xS layer sheet resistance on measurements of the junction capacitance is demonstrated by the results shown in figure 5.68. To obtain these results, two similar cells were given a post-fabrication annealing treatment in vacuum for 1/2 hour before gold contact were made.

For sample A the gold contact area was smaller than the cell area and it can be seen that the measured capacitance increases with time in air, eventually reaching a stable value after 60 days. For this pre-annealed cell, the structure of the junction would be expected to be relatively unaffected by diffusion processes for this period of time at room temperature so that the change in measured capacitance must be attributed to reduction in sheet resistance of the Cu_xS layer in accordance with the model for the cell in figure 5.66 (b). On the other hand, for sample B which had a contact covering all the area of the Cu_xS layer, the capacitance was found to be constant over the period of measurement which extended to 180 days in air.

In order to compare the effects of the slow diffusion processes at room temperature, with the more rapid effects which occur with annealing treatment in air, a further sample from the same batch of CdS layers used for the results in figure 5.58 was prepared in a

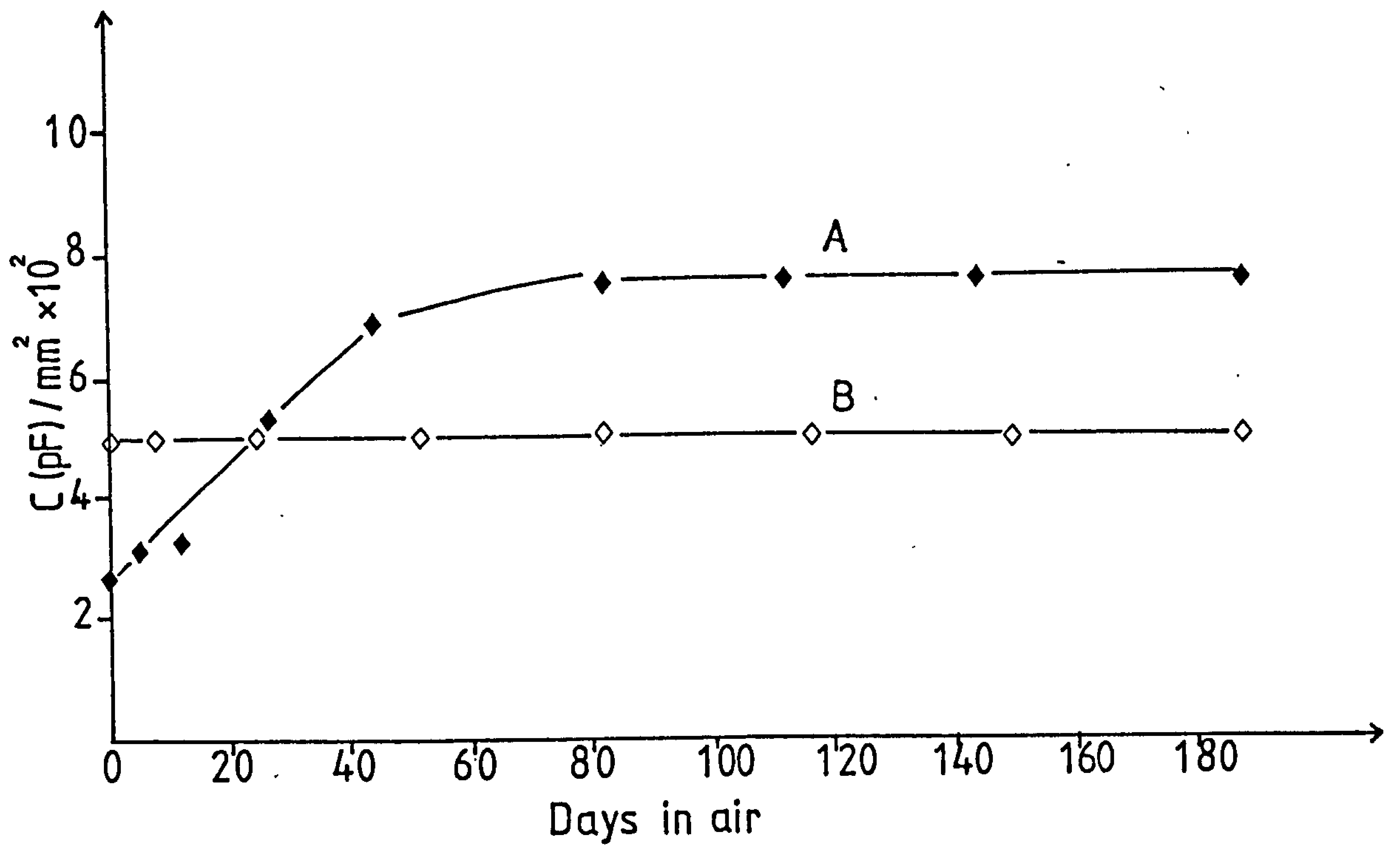

Fig. (5.68) The variation of junction capacitance for vacuum annealed (1/2 hour at 200°C) Cu_xS - CdS cell as a function of time in air using different contacts. A - the gold contact area was smaller than the cell area. B - the contact area fully covered the cell area.

similar fashion with 5 small area cells formed on a 1 cm^2 sample. A dipping time of 2 seconds was used and the dark I/V characteristics were measured before and after successive annealing cycles in air for different times as shown in figure 5.69. Prior to annealing, the I/V relationship was a straight line as indicated by the line A, similar to that for the initial curve for the similar sample in figure 5.58. After annealing in air for successive periods of 10,20,30 and 60 minutes a fresh top contact was evaporated onto one of the cell areas which had been exposed to air during the annealing process. Curves B, C, D and E show the resulting data after each of these stages of annealing respectively. These results show that, in contrast to the initial reduction in junction resistance for cells exposed to air at room temperature, the junction resistance of the annealed cells tends to gradually higher values, with improved rectification. It appears that the dominant process here is the diffusion of copper across the Cu_xS-CdS interface to broaden the depletion layer on the CdS side of the junction, rather than grain boundary diffusion. This is supported by measurements of the capacitance (listed in table 5.19) which shows a steady reduction in capacitance with increasing annealing time.

Table 5.19: Capacitance measurements for Cu_xS-CdS cells at zero voltage as a function of annealing time in air.

Annealing time	0	10	20	30	60
Cap. (PF/mm^2)	Cell 1 2000	Cell 2 664	Cell 3 444	Cell 4 319	Cell 5 -
		Cell 1 875	Cell 1 675	Cell 1 374	Cell 1 192

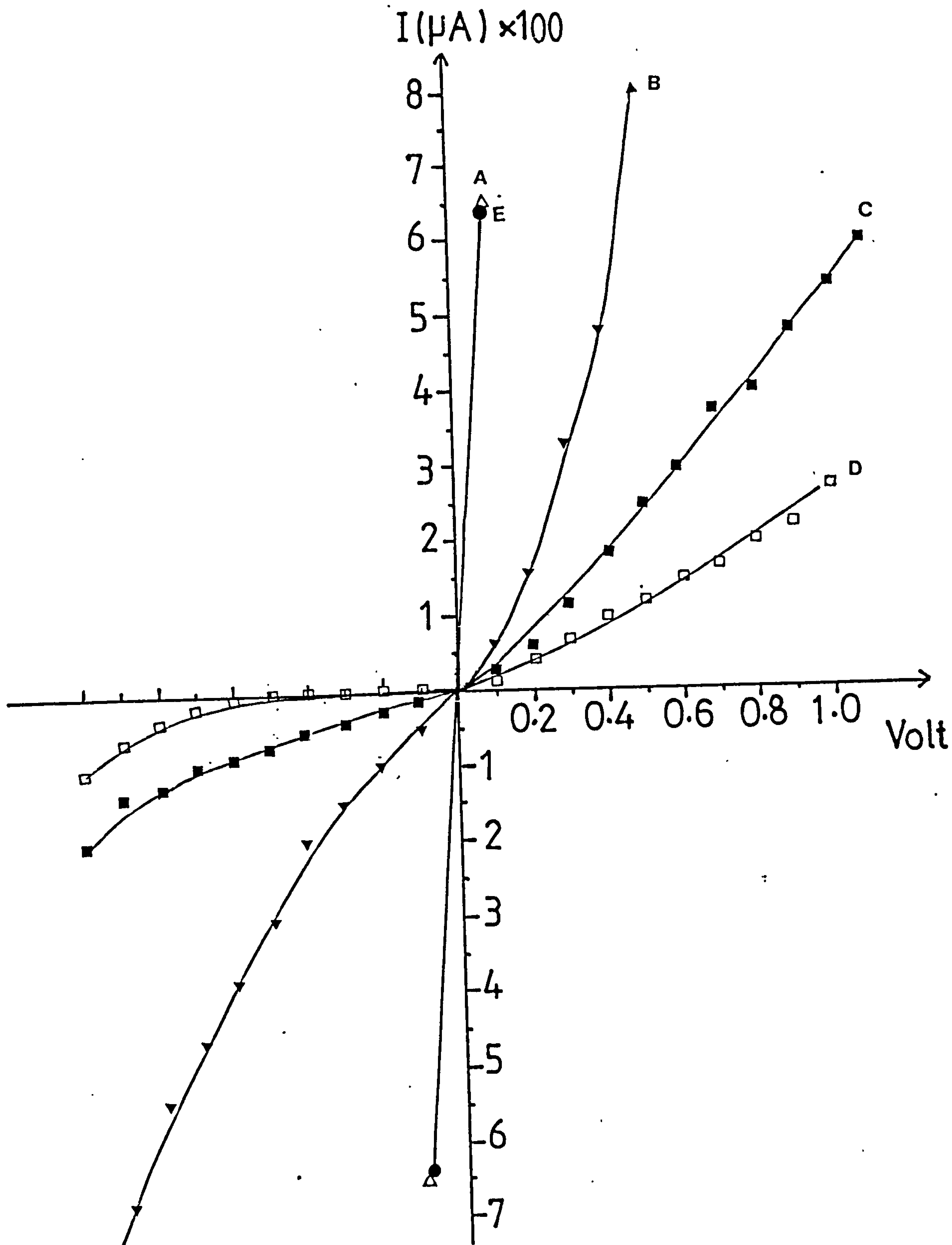

Fig.(5.69) The dark I/V characteristics of a Cu_xS -CdS cell before (curve A) and after annealing in air for 10 minutes (curve B), 20 minutes (curve C), 30 minutes (curve D) and 60 minutes (curve E). (The evaporated contact did not cover the full area of the cell).

It is of course possible that this process was accompanied by some grain boundary diffusion and this could explain the sudden return to low resistance ohmic behaviour after annealing for 60 minutes (curve E in figure 5.69). As indicated by the results of previously reported experiments (section 5.3.3), diffusion particularly into grain boundaries appears to be inhibited in the absence of air. This is supported by the results shown in figure 5.70 which shows the changing I/V characteristics for the area which was covered by a gold contact prior to any annealing. This shows more rapid progress towards improved rectifying behaviour as would be due to diffusion of copper into the grain and grain boundary regions of the CdS with grain boundary diffusion providing a less significant contribution. Thus, it seems that the relationship between bulk diffusion and grain boundary diffusion for these devices is dependent on temperature as well as on the environment.

5.4.3 Processes influencing the Cu_xS layer

As is clear from the discussion in the previous section, it is not entirely possible to separate effects occurring at the interface from those occurring in the Cu_xS layer. Processes such as diffusion clearly have an influence on both elements of the cell. However, some principles specifically related to each element have been studied in order to obtain information about the underlying physical processes involved. Changes in the properties of the Cu_xS layer have been studied using a variety of different techniques including electrochemical analysis, sheet resistance, luminescence and Rutherford backscattering and the results obtained will be described under these different headings.

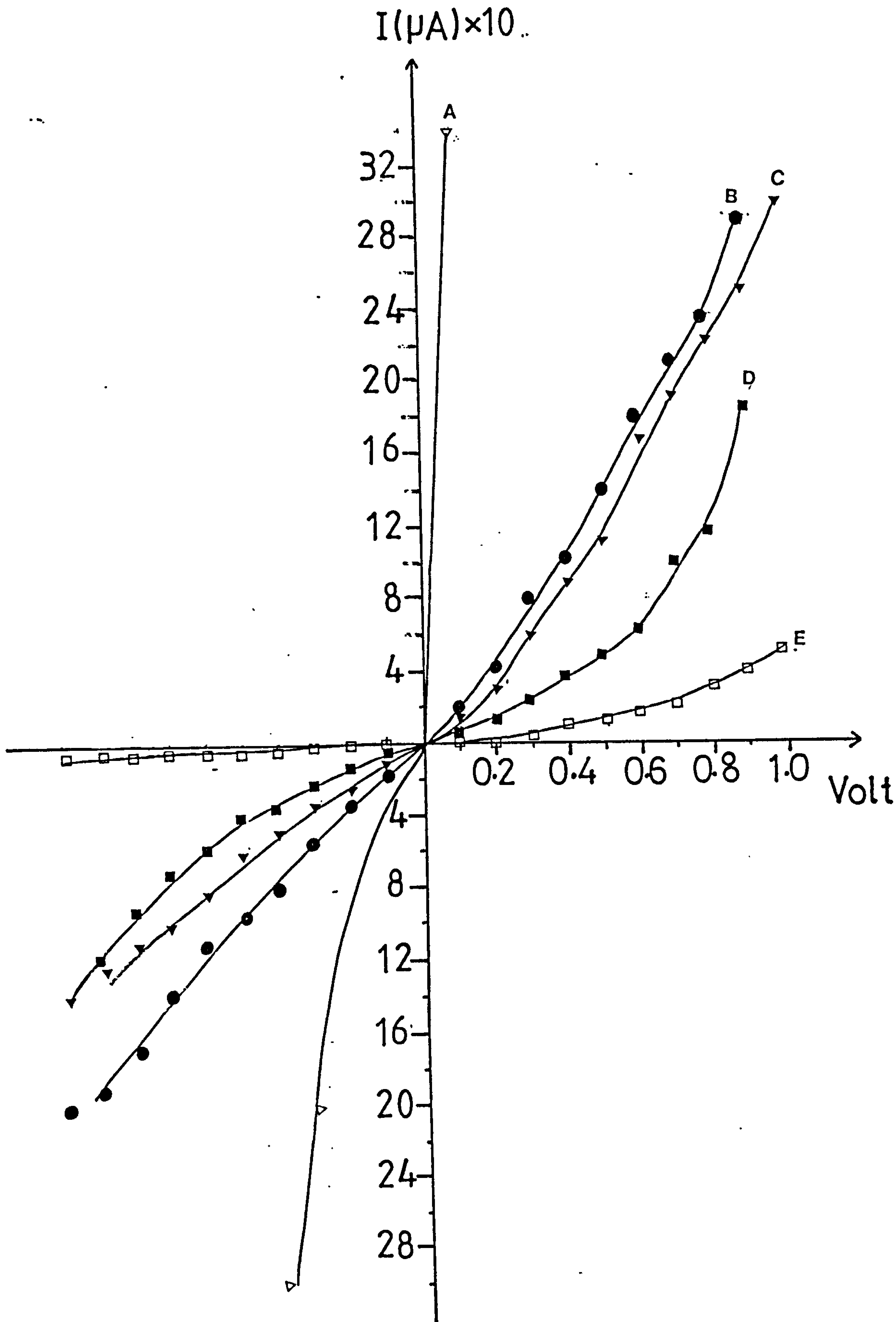

Fig.(5.70) The dark I/V characteristics of a Cu_xS -CdS cell before (curve A) and after annealing in air for 10 minutes (curve B), 20 minutes (curve C), 30 minutes (curve D) and 60 minutes (curve E). (Contact was covering the full area of Cu_xS - CdS cell prior to any annealing).

(i) Electrochemical analysis

As has been previously noted (section 3.3.1) the properties of Cu_xS are particulary sensitive to changes in composition and in front wall cells with a very thin Cu_xS layer, a reduction in the stoichiometry factor x, during operation, contributes significantly to the overall reduction in conversion efficiency. As mentioned previously, such a reduction would result partly from diffusion of copper across the Cu_xS-CdS interface into the CdS layer and partly to oxidation at the free surface if the cell is exposed to the air. As would be expected, the rate of degradation of the Cu_xS layer is dependent on its thickness, but is is also found to be dependent on the post-fabrication annealing process. An example of this effect can be seen in figures 5.71 and 5.72 which show the variation in x and the oxide growth as a function of time of exposure to air, after annealing similar cells in hydrogen for two different periods (1/2 hour and 3 hours). For this experiment, it was necessary to fabricate two sets of cells. These were both fabricated from the same batch of CdS films and dipped together in a standard hot CuCl bath at 95°C for 6 seconds. After annealing in hydrogen, the stoichiometry of the Cu_xS layer for one cell from each set was measured using the electrochemical reduction technique and the rest of the samples were left in air for different lengths of time before further measurements were made. In figure 5.71 the curves A and B represent the two different sets of cells annealed for 3 hours and 1/2 hour respectively. It can be seen that the cells annealed for 1/2 hour in H_2 degraded more rapidly than those annealed for 3 hours. However, in figure 5.72 it appears that the rate of increase in the oxide thickness formed on the Cu_xS layers was faster for the cells annealed for 3 hours than for those annealed

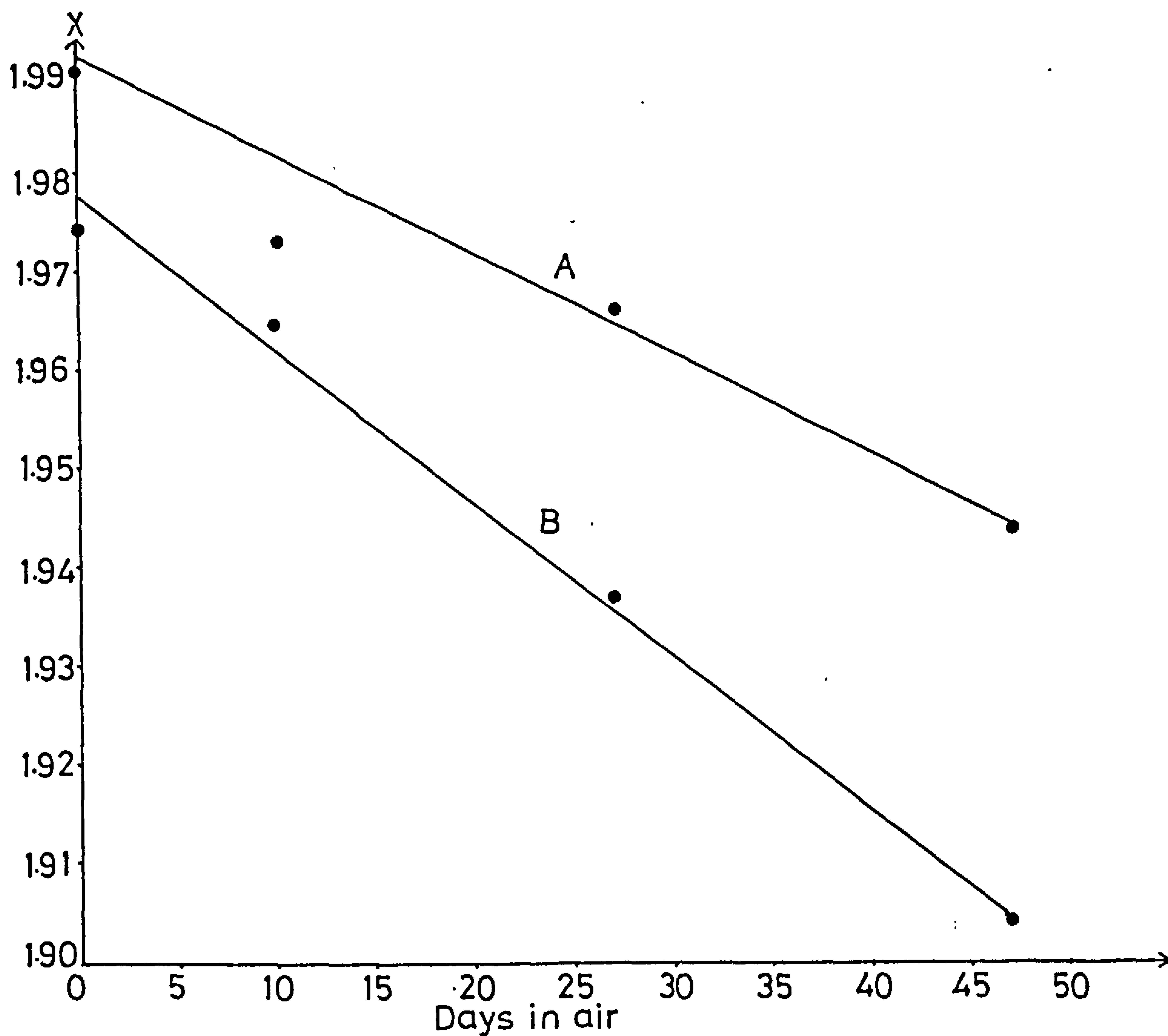

Fig.(5.71) The variation of the stoichiometry of Cu_xS layer as a function of time of exposure to air. The Cu_xS-CdS cells were annealed in hydrogen for 3 hours (curve A) and 1/2 hour (curve B) before ageing in air.

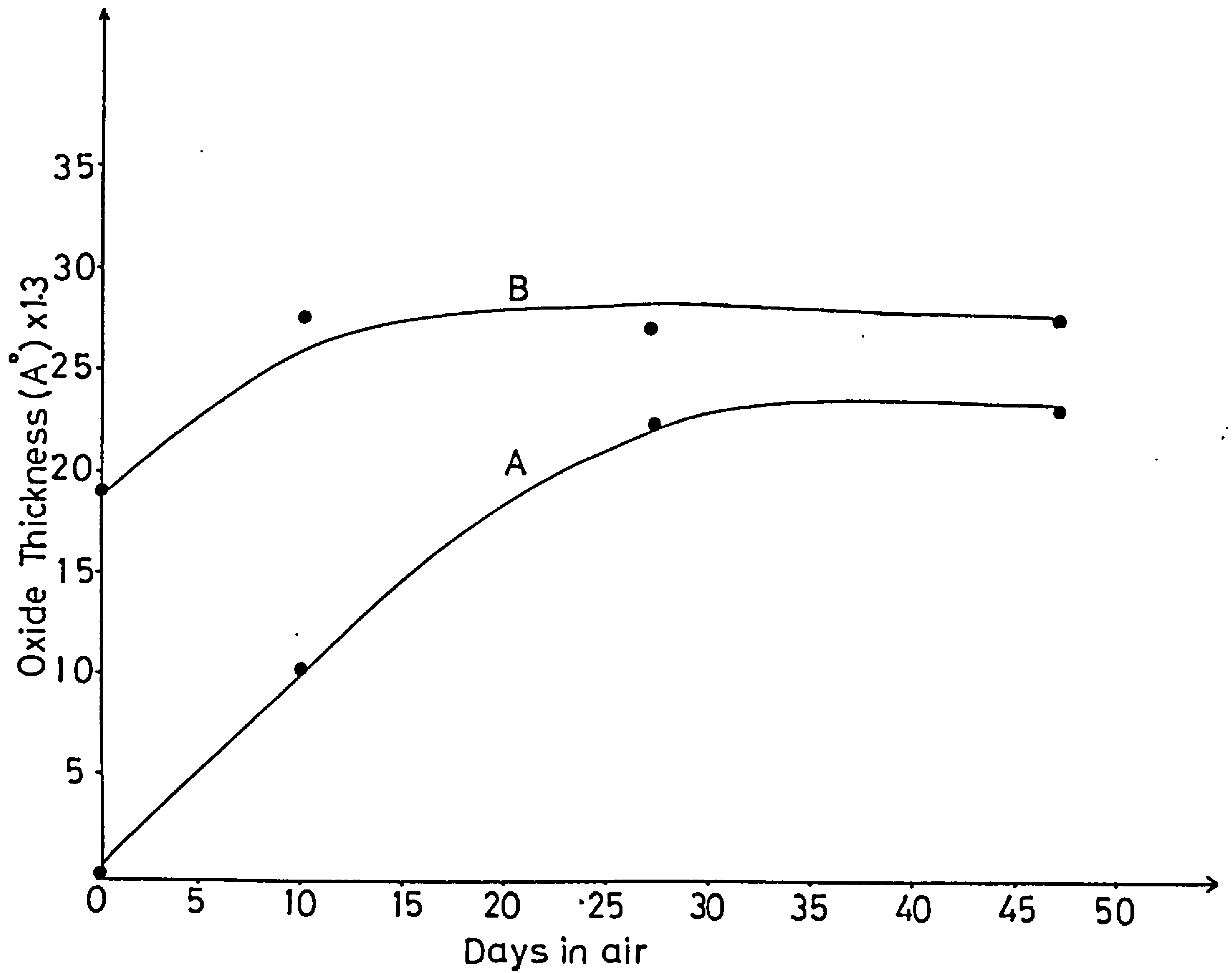

Fig.(5.72) The variation of oxide thickness at the surface of Cu_xS layer as a function of time of exposure to air. The Cu_xS-CdS cells were annealed in hydrogen for 3 hours (curve A) and 1/2 hour (curve B) at 200°C.

for 1/2 hour. This apparent inconsistency can be explained in terms of the effect of the hydrogen annealing on the cells. It is clear that a longer annealing time in H_2, produces a higher stoichiometry of Cu_xS layer, as seen from the initial points in figure 5.71. This is assumed to be due to H_2S-formation causing a relative enhancement in the Cu concentration. Free Cu formed by sulphur extraction diffuses into the underlying Cu-deficient Cu_xS-CdS. As the Cu-vacancies become filled up, a layer of elementary Cu would be expected to develop at the surface and it has been suggested that this protects the underlying Cu_xS from further reaction with the hydrogen making this process in some way self-stabilizing (59).

The existence of a superficial layer of copper at the surface of the Cu_xS layer immediately after annealing in hydrogen would mean that a thin layer of copper oxide could be formed when the cell was exposed to the air, without the need for any diffusion. This could explain the initial rapid rise in thickness of the oxide layer (from zero for the cell annealed for 3 hours) seen in figure 5.72. In addition, the results shown in this figure appear to indicate a saturation in oxide growth, which might be associated with the oxidation of all the free copper at the surface of the copper sulphide layer. The saturation observed here suggests that copper oxide formation has a protective effect once a certain thickness is reached and this will be discussed later (section 5.4.4) but it should be noted that saturation is not always observed and, when it does occur, it is not necessarily maintained for long periods. This can be seen from the results in figure 5.73. This shows the results obtained using cells similar to those used in figures 5.71 and 5.72 but the CdS films were from a

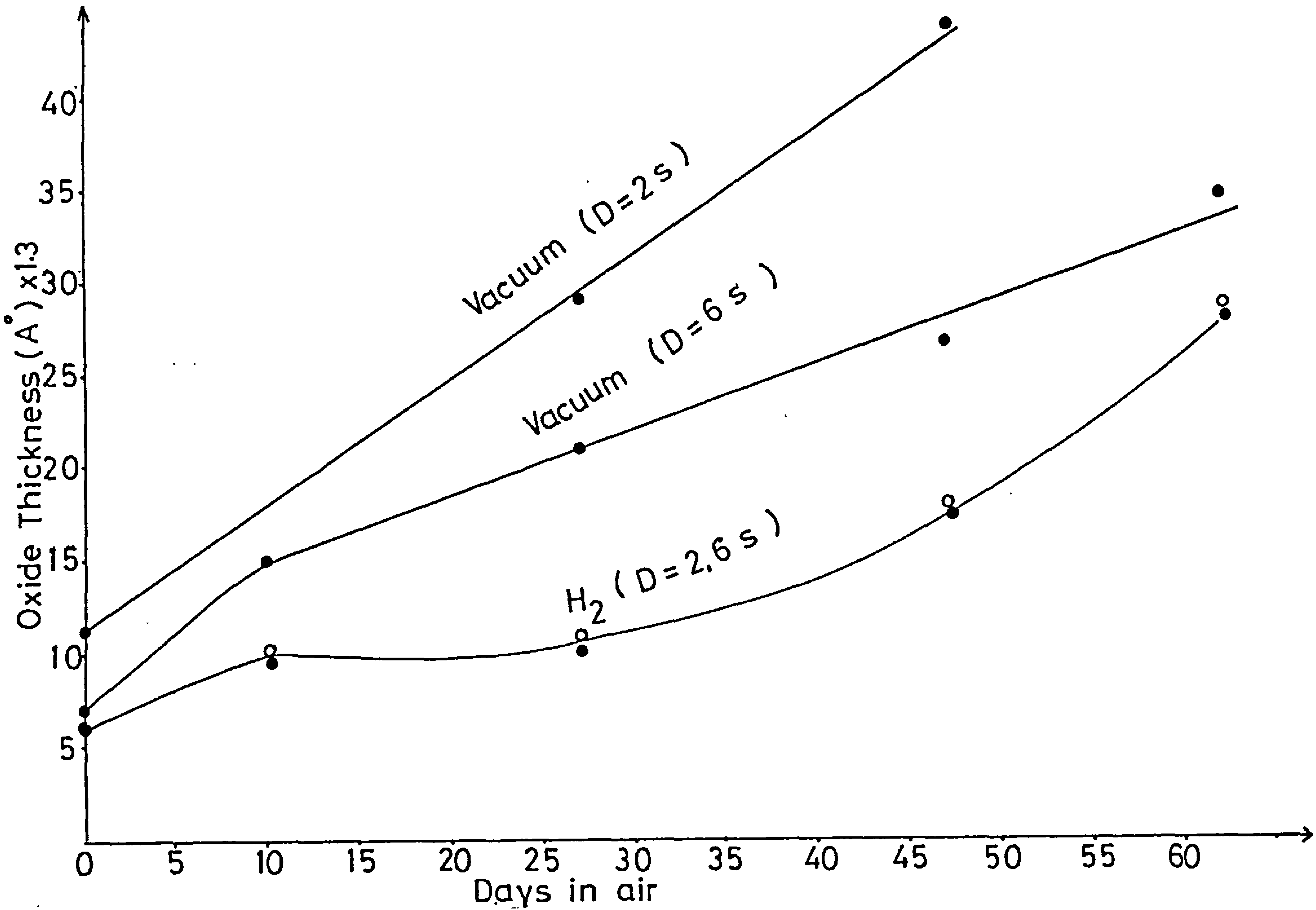

Fig.(5.73) The variation of oxide thickness at the surface of Cu_xS as a function of time of exposure to air for cells made using different annealing treatments (vacuum, H_2) and different dipping times (2,6 sec.).

different batch and two different dipping times were used (2 and 6 seconds) in order to examine the effects of different Cu_xS layer thickness. These samples were then annealed in either hydrogen or vacuum at 200°C for 1/2 hour. The results in figure 5.73 show that for the vacuum annealed cells there is no sign of saturation in the copper oxide thickness as a function of time exposed to air and the oxide growth rate appears to be faster for the thinner Cu_xS layer (dipping time, 2 seconds) than for the thicker layer (dipping time 6 seconds). However, a partial saturation in oxide thickness does appear to occur after ~ 10 days in air for the cells annealed in H_2, although there is a return to faster growth after ~ 30 days. It should also be noted that the oxide thicknesses for the H_2 annealed cells are very similar (independent of Cu_xS layer thickness) suggesting that the oxide growth is dependent on surface copper rather than on copper diffusing from the underlying layer.

(ii) Sheet resistance measurements

As the electrochemical reduction technique is destructive, it is not ideal for the type of observation required here in which repeated measurements over a long period of time are necessary. However, as discussed in section 3.3.2, the composition of the Cu_xS layer directly controls the electrical conductivity so that non-destructive measurements of the sheet resistivity can more conveniently be used to monitor changes in composition as a function of time. Numerous measurements of this kind have been recorded during the course of this investigation and figure 5.74 shows a typical set of results for Cu_xS layers of different thickness produced using CdS films from the same batch dipped for 2,4,6 and 8 seconds. These samples were annealed for 1/2 hour in vacuum in order to form a good rectifying Cu_xS-CdS

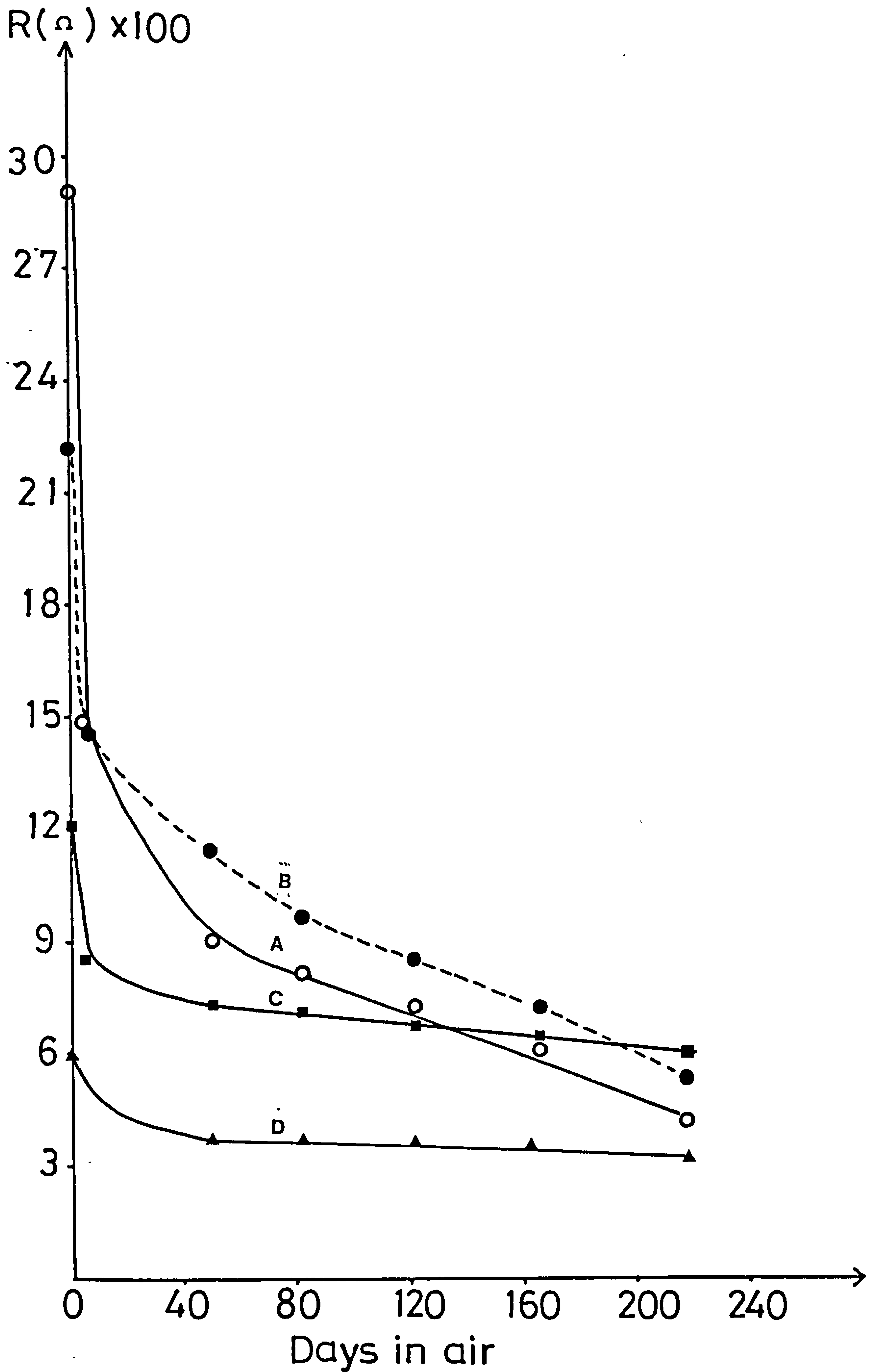

Fig.(5.74) The sheet resistance of Cu_xS layer as a function of time of exposure to air for cells made using different dipping times; 2 seconds (curve A), 4 seconds (curve B), 6 seconds (curve C) and 8 seconds (curve D). The Cu_xS-CdS cells were annealed in vacuum for 1/2 hour before ageing in air.

junction. As might be expected, the thinner layers of Cu_xS are seen to have higher resistances than the thicker Cu_xS layers, but all layers have sheet resistance values which reduce with increasing time in air in accordance with the associated reduction in x as observed in figure 5.71. However, the largest change in resistance is for the thinnest layer (dipping time 2 seconds) and the thinner layers decrease faster than for the thicker layers. In fact, it can be seen that the faster reduction in the sheet resistance of the thinner layers continues until these resistance values are smaller than those for the thicker layers (dipping times 6 and 3 seconds). It is well known that after exposure to air, leading to reduced sheet resistivity (as observed in figure 5.74) the initial stoichiometry of the Cu_xS layer can be restored by annealing in hydrogen. However, such an annealing process can also affect the rate of change in the stoichiometry of the layer on further exposure to air. An example showing this effect of annealing in hydrogen atmosphere is presented in figure 5.75 which gives results for two different cells formed using CdS films from different deposition batches so that, although the same etching and dipping times were employed, the resultant Cu_xS layers were of different thickness (0.35 μm and 0.47 μm) and slightly different composition (x = 1.98 and 1.97 respectively). These cells were given an initial short annealing treatment in vacuum (for 1/2 hour) in order to produce good rectifying Cu_xS-CdS junctions so that satisfactory sheet resistance measurements could be made on the Cu_xS layer. As expected the thinner Cu_xS layer with the higher x value had the higher sheet resistance and, like the results in figure 5.74, the resistances for both layers were seen to be reduced as a function of time in air,

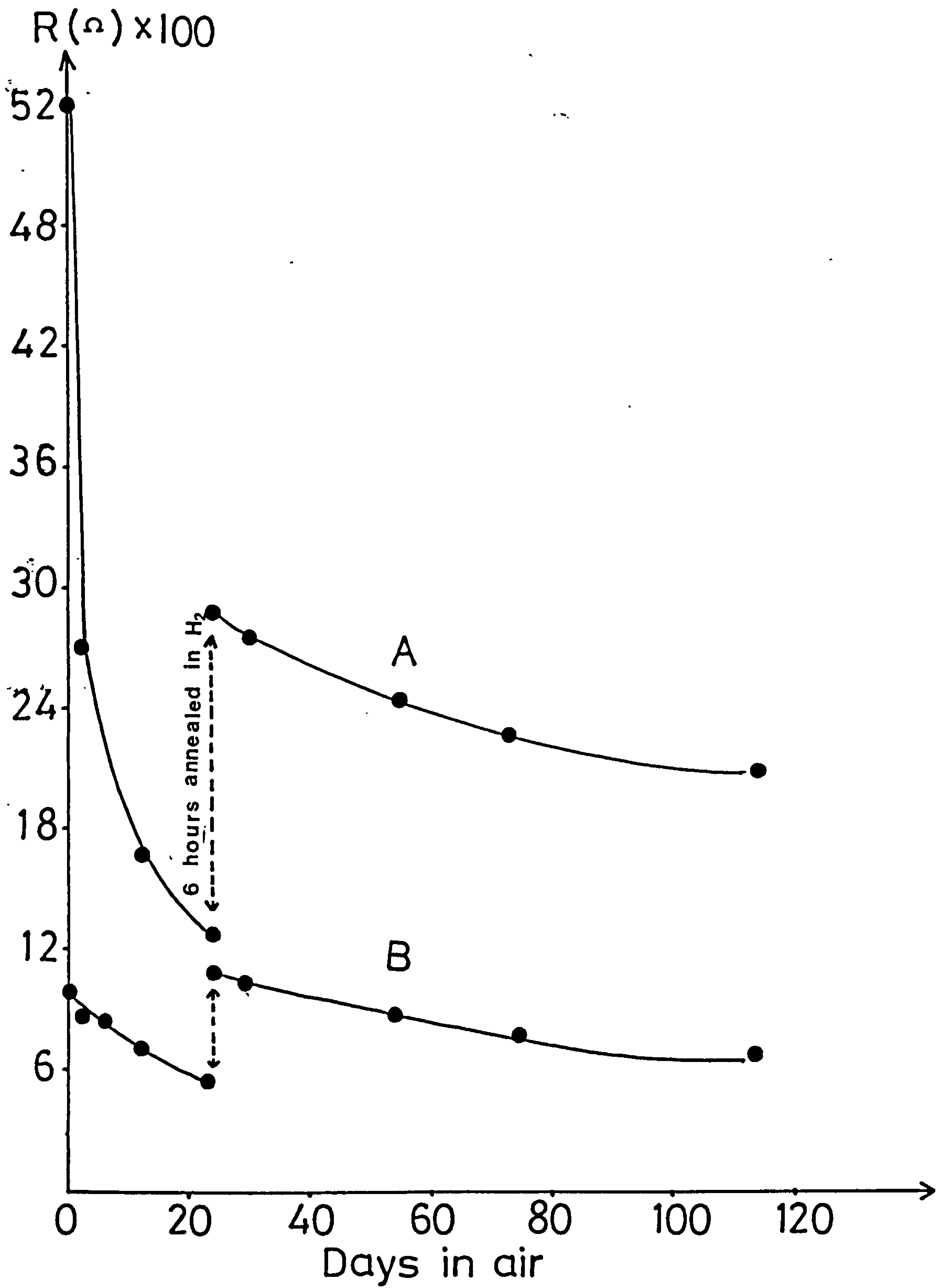

Fig.(5.75) The Cu_xS layer sheet resistance as a function of time of exposure to air for layer thicknesses of 0.35 μm (curve A) and 0.47 μm (curve B). The Cu_xS/CdS cells were given an initial short annealing in vacuum (for 1/2 hour).

with the thinner layer resistance falling faster than the thicker Cu_2S layer. After 24 days exposure to air, both samples were annealed in hydrogen for 6 hours. Figure 5.75 shows that the sheet resistance values for both Cu_xS layers were increased as would be expected, due to an increase in the x value but, in addition, the figure shows clearly that the subsequent reduction in resistance with further exposure to air is not so rapid as in the initial period of exposure. This could be explained in terms of excess copper produced by annealing in H_2 having a stabilizing effect on the Cu_xS (as discussed in the previous section).

Of course, the changes in the x value for the Cu_xS film, seen in figure 5.75 as changes in sheet resistance, alter the optical absorption properties of the layer which has a direct effect on the efficiency of the cell. The resultant effect on the cell performance is seen very clearly in figure 5.76 which shows the short circuit current as a function of time in air after an initial annealing treatment in H_2 for 6 hours at 200^oC. After 103 days in air at room temperature (curve A) the cell was annealed again in hydrogen for 6 hours to restore the degraded short-circuit current to a value close to its initial level. The cell was left again in air at room temperature for 149 days (curve B). Finally the cell was annealed again in hydrogen 5 hours before further exposure to air at room temperature (curve C). It is clear from figure 5.76 that the degradation of the short-circuit current in air at room temperature became less rapid after each annealing treatment as shown by curves A, B and C. As stated above, an improved stability could be associated with excess copper produced by annealing in hydrogen, but this would not explain the further improvement resulting from sucessive

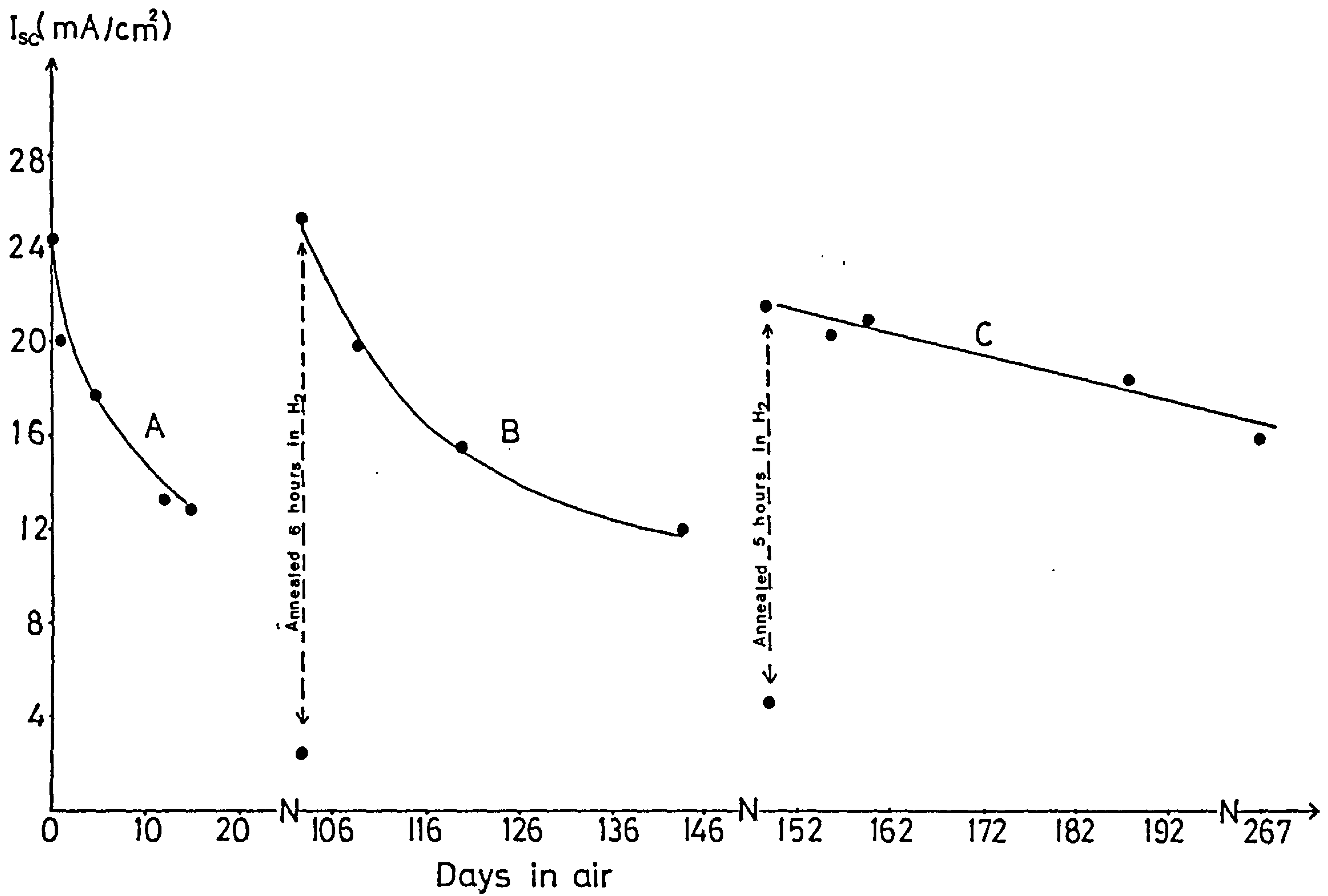

Fig.(5.76) The variation of the short circuit current as a function of time of exposure to air. (Cu_xS/CdS cell was given an initial 6 hours annealing treatment in H_2).

annealing and degradation periods. However, another possible process contributing to the improved stability of the Cu_xS layer could involve the underlying CdS layer. As discussed in Chapter 3, during exposure of Cu_xS-CdS cells to air, Cd compounds ($CdSO_4$, CdO) can be formed at the surface of the Cu_xS layer as a result of diffusion of Cd from the CdS film. Annealing in hydrogen would have the effect of releasing cadmium to dope the Cu_xS layer. Cd doping has been reported to compensate copper deficient Cu_xS and shift its properties back to those of high stoichiometry material (245). Cd doping is also reported to have a stabilizing effect on Cu_xS layers (246,167).

In order to eliminate diffusion effects associated with the underlying CdS layer, an experiment was performed on Cu_xS layers which had been evaporated onto glass substrates. The thickness of these layers was 0.2 μm. The sheet resistances for two similarly evaporated layers as a function of air exposure time are shown in figure 5.77. For these layers, on glass substrates, it was possible to make sheet resistance measurements immediately after preparation, and it can be seen that both sets of results (for samples A and B) initially reduce at the same rate. After 14 days in air sample A was left in air while sample B was annealed in H_2 for 17 hours before continuing exposure to air. The sheet resistance for sample B was significantly increased by the annealing process but, within one day, there was a substantial reduction and the subsequent rate of fall was similar to that before annealing, while the sheet resistance of the unannealed layer (sample A) slowly continued to reduce. After a further 28 days in air both samples A and B were annealed in H_2 at 200°C for 7 hours and, once again there was an increase in sheet resistance for both samples. As

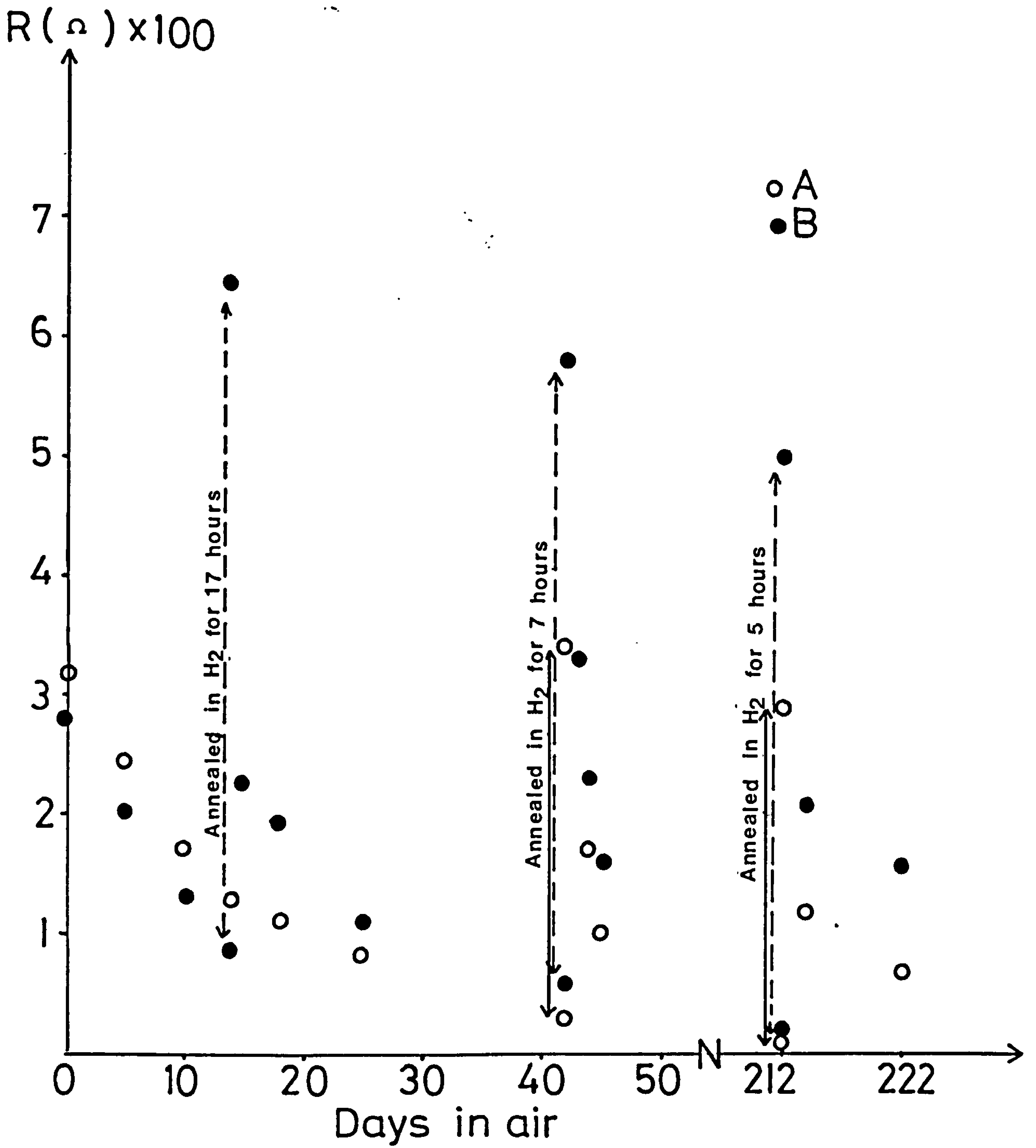

Fig.(5.77) The variation of the sheet resistance of the Cu_xS layer (deposited on glass substrate) as a function of time of exposure to air.

before, this was followed by a sharp reduction in the sheet resistance after 1 day in air with subsequent reduction at a slower rate similar to that before annealing. The same behaviour was observed after further annealing cycles following additional periods of exposure to air. For these Cu_xS films, the reduction in sheet resistance can be explained only by the formation of copper oxide and it appears that the production of excess copper on the surface of Cu_xS by hydrogen annealing has no influence on the stability of Cu_xS layer. This supports the suggestion above that it is the diffusion of cadmium from the underlying CdS which plays the dominant role in stabilizing the Cu_xS-CdS devices. However, it should be noted that the polycrystalline film of evaporated Cu_xS would be expected to have a different structure to that produced topotaxially on CdS in the chemical exchange process. Thus, it is possible that the evaporated layers would not behave similarly to the chemically formed films in terms of their stability under exposure to air.

(iii) Luminescence

An example of changes in the cathodoluminescence characteristics for Cu_xS-CdS cells following exposure to air for different periods of time, can be seen in figure 5.78, where curve A shows the emission spectrum for a Cu_xS-CdS cell immediately after annealing in hydrogen at 200°C for 1 hour. Curve B is the spectrum for the same sample after it had been in the air for 26 days at room temperature and curve C was the corresponding result for this same sample after it had been in air for 56 days. (The emission seen in curve C was unchanged when checked after 70 days in air.) The sample used for the result in figure 5.78 was fabricated from a CdS layer which was etched for 6 seconds and dipped in CuCl solution for 2 seconds. Using the ECA

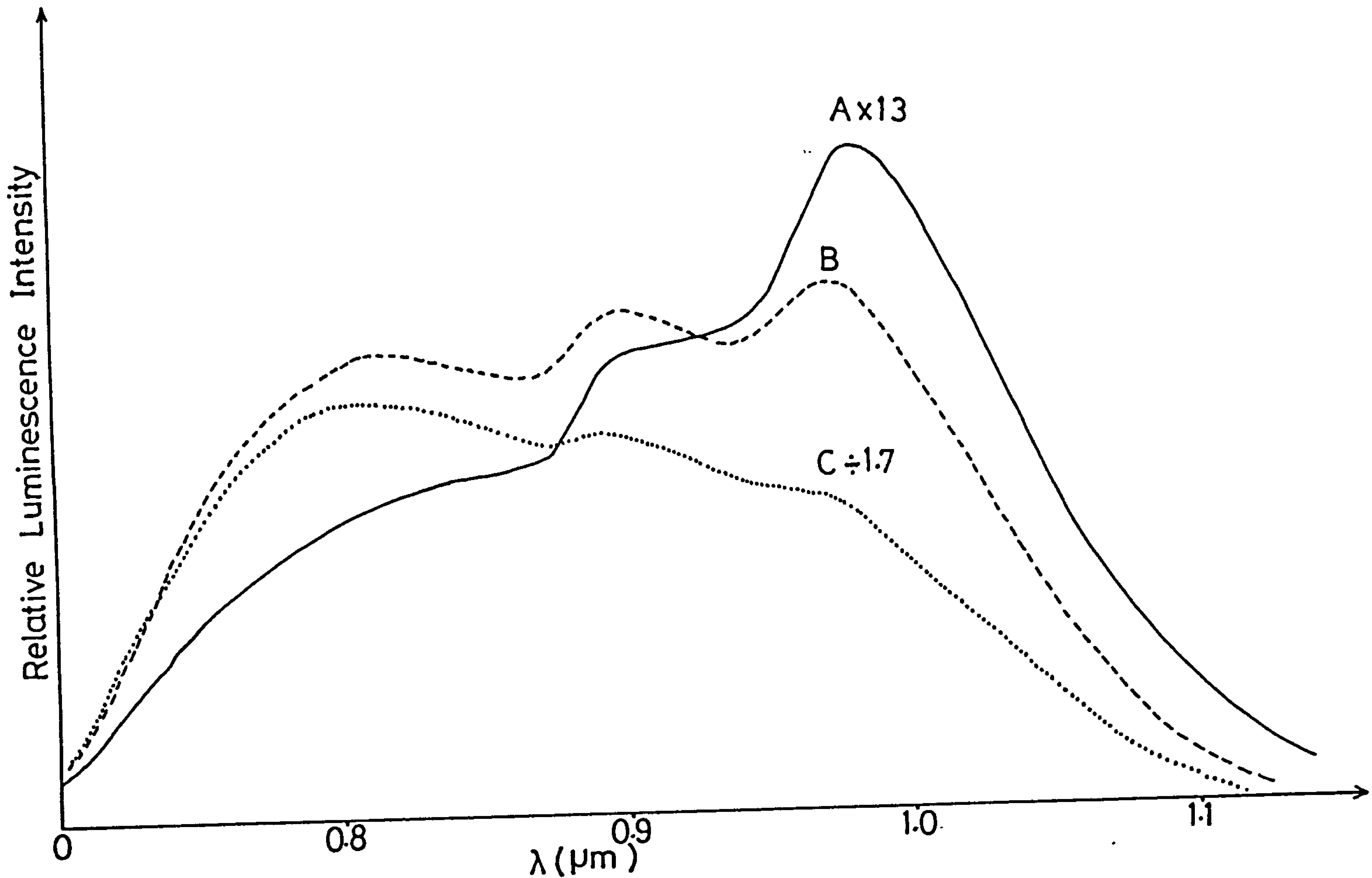

Fig.(5.78) The CL spectra for a Cu_xS/CdS cell as a function of time of exposure to air. Curve A shows the emission spectrum for the cell immediately after annealing in H_2 at 200°C for 1 hour. Curve B is the spectrum for the same sample after it had been in air for 26 days at room temperature and curve C was the corresponding spectrum for this sample after it had been in air for 56 days.

technique on similarly formed cells showed that the thickness and the stoichiometry of the Cu_xS layer after annealing in hydrogen were 0.62μm and x = 1.994 respectively. The relatively large thickness (0.62μm) of Cu_xS produced in the short dip time of 2 seconds is assumed to be due to significant grain boundary penetration which would have been encouraged by the longer than usual etch time (6 S).

It can be seen that the spectra in figure 5.78 display the usual peaks at ~ 0.8 μm and ~ 1.0 μm attributed to copper centres in the CdS layer, with the 1.0 μm peak initially the dominant feature as previously noted for samples with substantial grain boundary Cu_xS growth (section 5.2.4). The spectrum also shows the characteristic step at ~0.9 μm attributed to the copper sulphide layer absorption edge. This step is seen to be particularly steep for curve A, immediately after annealing in hydrogen. This supports the previous data indicating that the process of annealing in H_2 atmosphere increases the stoichiometry factor x for the Cu_xS layer, and correspondingly increases the optical absorption efficiency in the shorter wavelength regions of this spectrum (167).

The effect of exposing the cell to the air is seen to be a reduction in the emission across the whole spectrum with the reduction increasing with longer time in air. However, it is clear that the reduction in the emission is not uniform and is more noticeable at the longer wavelengths than at the shorter wavelengths. This can be explained in terms of the lower copper content of the Cu_xS layers after air exposure due to diffusion of copper into the CdS layer and to the growth of an oxide layer on the surface as discussed earlier. The reduced x-factor for the Cu_xS film leads to a reduction in

absorption coefficient over the shorter wavelength region of the spectrum and this accounts for the step at ~ 0.9 μm becoming less clear for curves B and C relative to curve A. This process has the effect of enhancing the 0.8 μm peak relative to the 1.0 μm peak. A further reduction of the 1.0 μm peak relative to the 0.8 μm peak might occur as a result of absorption of long wavelength photons by free carriers in the Cu_xS which increase in concentration as the x value diminishes.

The reduction in the emission at 1.0 μm relative to that at 0.8 μm (from the data of figure 5.78) is plotted in figure 5.79 as a function of air exposure time (curve i). Similar experiments were carried out with similar samples which had been annealed in vacuum or in air for 1 hour at 200°C instead of in hydrogen. Figure 5.79 (curve ii) shows that the sample which had been annealed in vacuum produced results quite similar to those for hydrogen, but the sample annealed in air (curve iii) showed the opposite behaviour with the emission ratio increasing with time. This was an unexpected result and it would have been interesting to have extended the investigation using different types of samples, if time had allowed. It is clear from the results of several other experiments reported above that annealing in air has a significantly different effect on the structure of the cell than annealing in hydrogen or vacuum. Annealing in air for 1 hour would be expected to seriously degrade the Cu_xS layer as a result of significant loss of copper due to diffusion and oxidation but it has been suggested that the reduction in copper is accompanied by Cd diffusing to the surface during annealing in air and direct evidence of this is presented in the next section. As the most rapid movement of Cd between the CdS layer and the Cu_xS layer surface would

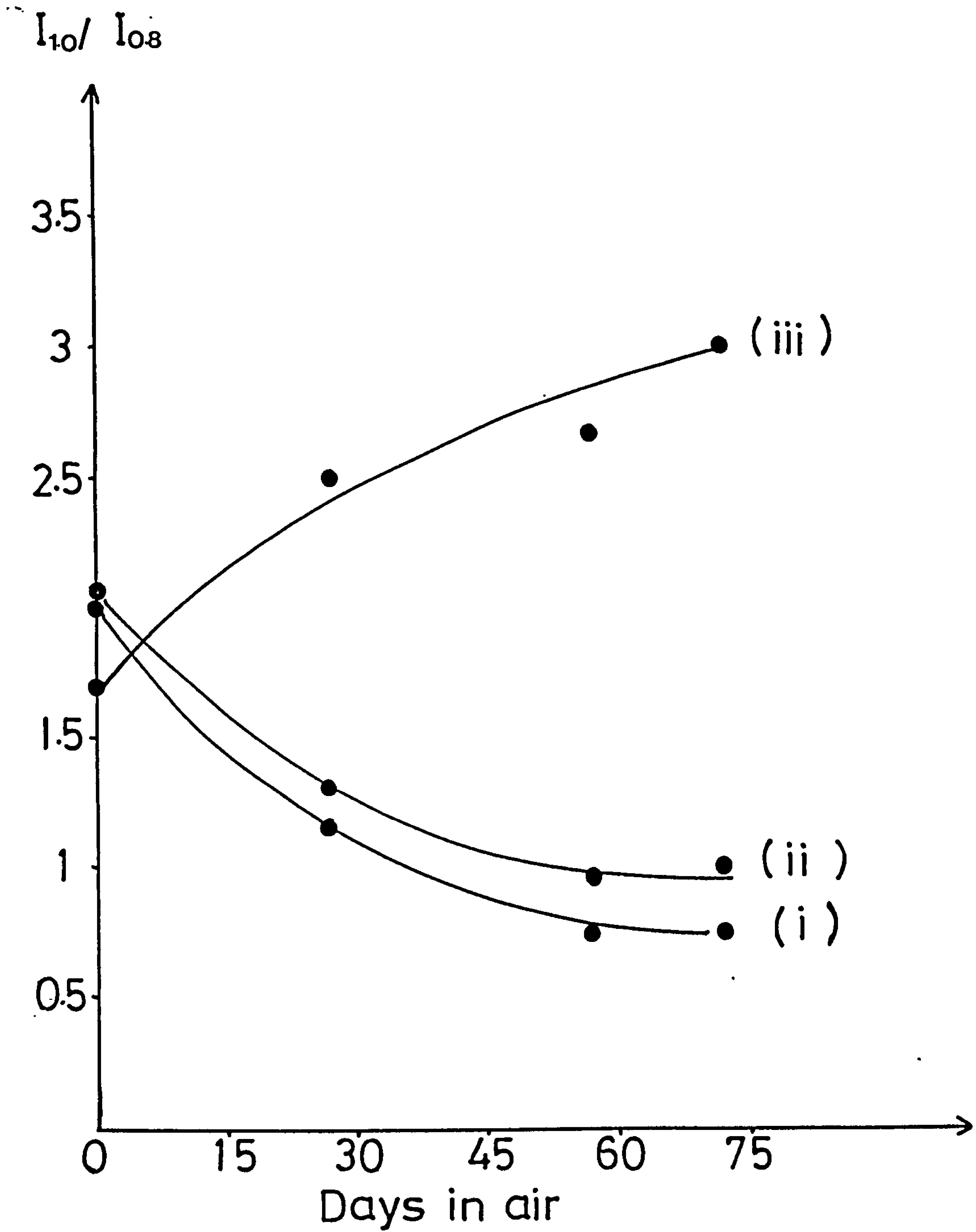

Fig.(5.79) The variation of the relative intensity of the 1.0 μm peak to the 0.8μm peak against the time of exposure to air for cells annealed in H_2 (curve i), vacuum (curve ii) and air (curve iii) for 1 hour at 200°C.

be along the grain boundaries, termination of the annealing process would leave free Cd atoms distributed along these grain boundaries. Movement to the surface would be expected to continue during exposure to air at room temperature but if some of this excess Cd in the grain boundaries diffuses into the surrounding Cu_xS grain boundary protrusions, the properties of these regions of the Cu_xS film would be shifted towards those for Cu_2S as discussed above (section 5.4.3 (ii)). This could explain the increase in the $I_{1.0}/I_{0.8}$ emission ratio which is consistent with an increase in x value for the Cu_xS layers. It should also be noted that for these samples a significant fraction of the Cu_xS layer was assumed to be in the grain boundary region.

(iv) Rutherford Backscattering

In the previous sections, reference was made to the possibility that the properties of the Cu_xS layer might be influenced significantly by the presence of Cd as a result of diffusion from the underlying CdS layer. In fact, evidence for the presence of Cd at the Cu_xS surface has previously been provided by Florio (178) and by Bryant and coworkers (166) using a chemical method and AES with ion etching respectively. As both these techniques are destructive, they are not very convenient techniques for observing changes in composition of a sample as a fraction of time whereas Rutherford backscattering (RBS) is a non-destructive method. As RBS is also a surface sensitive technique it seemed that it might be especially useful in detecting any build-up of Cd at the Cu_xS surface as a result of exposure to air. In addition, it was expected that the detection of Cd would be aided by the greater mass of Cd in comparison with Cu

and S, as can be seen by reference to equation (4.7.1) in chapter 4 which gives the energy of the backscattered protons relative to the incident energy as a function of the mass of the target atoms. According to this relationship, the maximum energy of 400 keV protons scattered through an angle of 180° is 385 keV for target atoms of Cd and 376 and 352 keV for Cu and S respectively. Thus, it was expected that scattering due to surface Cd would yield the highest energy protons in the RBS spectrum and, therefore, that these would be clearly detected.

In order to check that Cd could really be observed by means of RBS, using the kind of polycrystalline layers under investigation in this project, trial measurements were made using a CdS film without a Cu_xS layer and also a CdS film onto which additional Cd had been deposited in order to ensure a good concentration of Cd atoms at the surface of the film.

The results of these test measurements are shown in figure 5.80. It is clear that the high energy edge of the spectrum for the CdS layer above (curve i) occurs at the same energy as the corresponding edge for the sample with a layer of Cd over its surface (curve ii). Thus, this edge can be attributed to scattering from Cd and this result was used to calibrate the energy axis for subsequent work.

In order to demonstrate how quantitative information can be obtained from RBS spectra, the result shown in curve (ii) of figure 5.80 has been used to find the thickness of the surface Cd layer. This was done by measuring the width ΔE of the enhanced signal due to the surface Cd layer, where the range ΔE corresponds to the difference in energy between protons scattered from the upper and lower surfaces of the evaporated Cd film. The value of ΔE depends

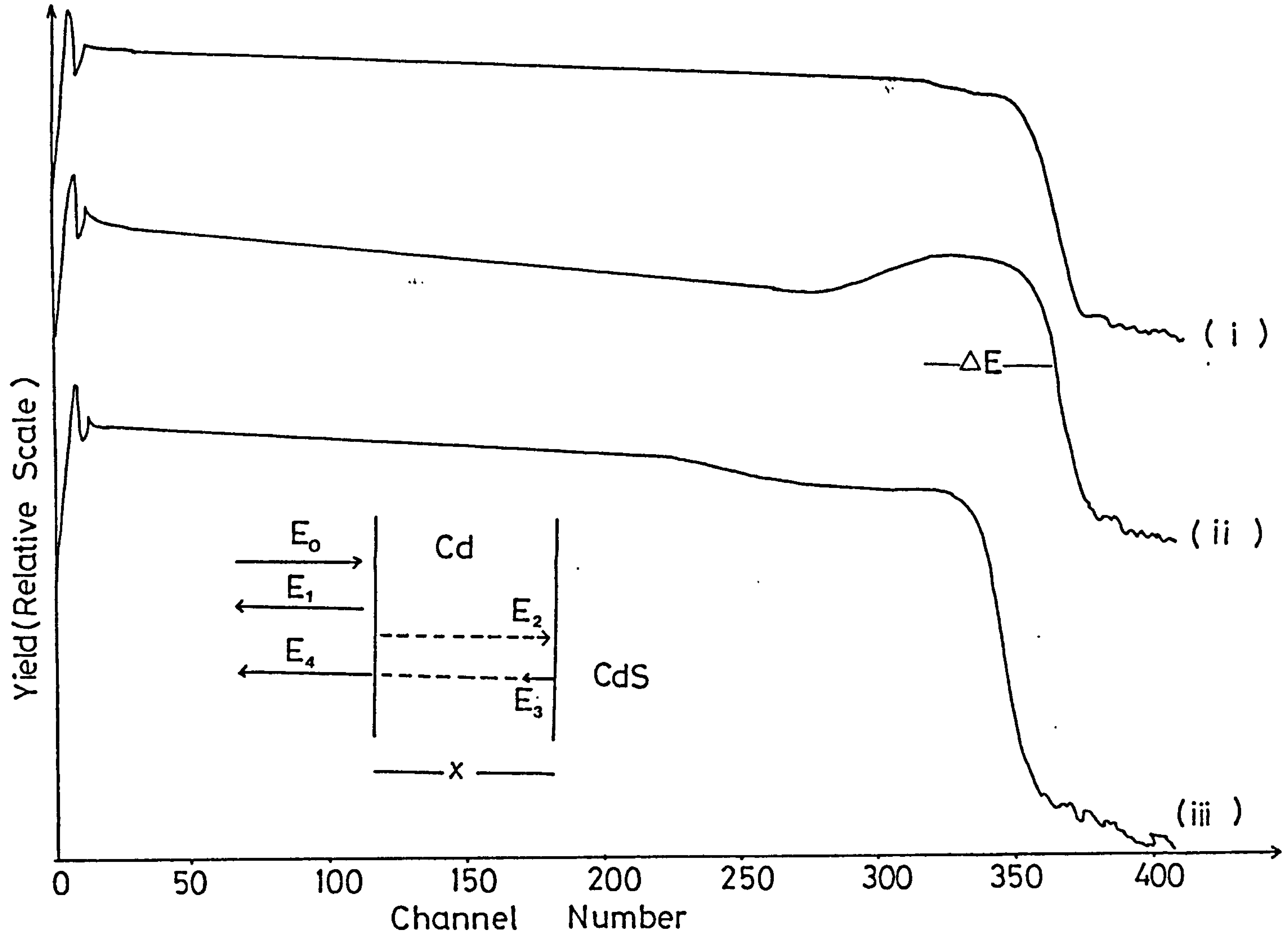

Fig.(5.80) Rutherford backscattering (RBS) spectra for a CdS layer (curve i), a CdS layer with a thin layer of Cd deposited on its surface (curve ii) and a CdS layer with a thin layer of copper deposited on its surface (curve iii). The insert figure shows the incident and backscattered proton energies for the Cd/CdS surface.

upon the scattering process and on the stopping power S, defined as the energy loss per unit path length for protons moving through the material (S depends on the density and composition of the material as well as on the proton energy). Assuming a scattering angle of 180° as used in this experiment and referring to the insert diagram in figure 5.80, it can be shown that the thickness x of the Cd layer is

$$x = \frac{K_{Cd} E_o - E_4}{S_{Cd}^{E_3} + K_{Cd} S_{Cd}^{E_o}} \qquad (5.3.1)$$

where K_{Cd} is the scattering factor for Cd as defined by equation 4.7.1 and S^{E_3} and S^{E_o} are the Cd stopping powers for protons at energy E_3 and E_o respectively (see insert in figure 5.80). For the small Cd thickness involved here, $S_{Cd}^{E_3}$ can be approximated to $S_{Cd}^{E_1}$ and using corresponding values for S obtained from tabulated data (247) the resultant thickness of the evaporated layer of Cd was estimated to be ~0.2 μm. The third RBS spectrum shown in figure 5.80 is for another (similar) CdS with an evaporated surface layer of copper (curve iii). In this spectrum, it is clear that there is a shift of the Cd edge to lower energy due to the protons losing energy in passing through the Cu layer before and after being scattered by the underlying Cd atoms in the CdS film. (Due to the smaller mass of Cu, protons scattered by the surface copper atoms will have significantly smaller energy than those scattered by Cd atoms). From the observed shift in the high energy cut-off energy, and using a similar procedure to that above, the thickness of the evaporated layer of Cu was found to be ~ 0.03μ m.

Following these preliminary studies, measurements were made on

Cu_xS/CdS cells immediately after fabrication and these measurements were repeated on the above samples after exposure to air for different lengths of time. Curve (i) in figure 5.81 shows the results for a sample immediately after fabrication. As expected, the main edge of this spectrum (attributed to Cd in the CdS film) occurs at an energy less than 385 keV due to the CdS being covered by Cu_xS (similar to curve (iii) in figure 5.80 for the CdS film with a Cu overlayer). Making use of the same procedure as above, (and assuming that x = 2 in calculating the effective stopping power for the Cu_xS layer from the tabulated data for Cu and S (247)) the thickness of the Cu_xS was estimated to be ~ 0.06 μm. Of course, this value for the Cu_xS thickness is rather small in comparison with the mean effective thickness values obtained using ECA. This confirms the importance of the grain boundary contribution to the average thickness as indicated by the results obtained by SEM (section 5.2.1). A further feature which should be noted in figure 5.81 (curve i) is that there is a definite tail from the main edge in the spectrum, extending to higher energies up to 385 keV. It is possible that the tail is partly due to non-uniformity in the thickness of the Cu_xS layer. Also, it is possible that the tail is due to Cd distributed thoughout the Cu_xS layer, as would be expected to result from the chemical exchange process. It seems probable that Cd distribution is the dominant reason for the tail as it is this feature which changes with different treatments, particularly exposure to air. This is illustrated by the curve (ii) in figure 5.81 which shows the result for a sample similar to that in curve (i), which had been heated in air for 1/2 hour at 200°C. The high energy tail is seen to be replaced by a more clearly defined shoulder with threshold at 385 keV as would be provided by a

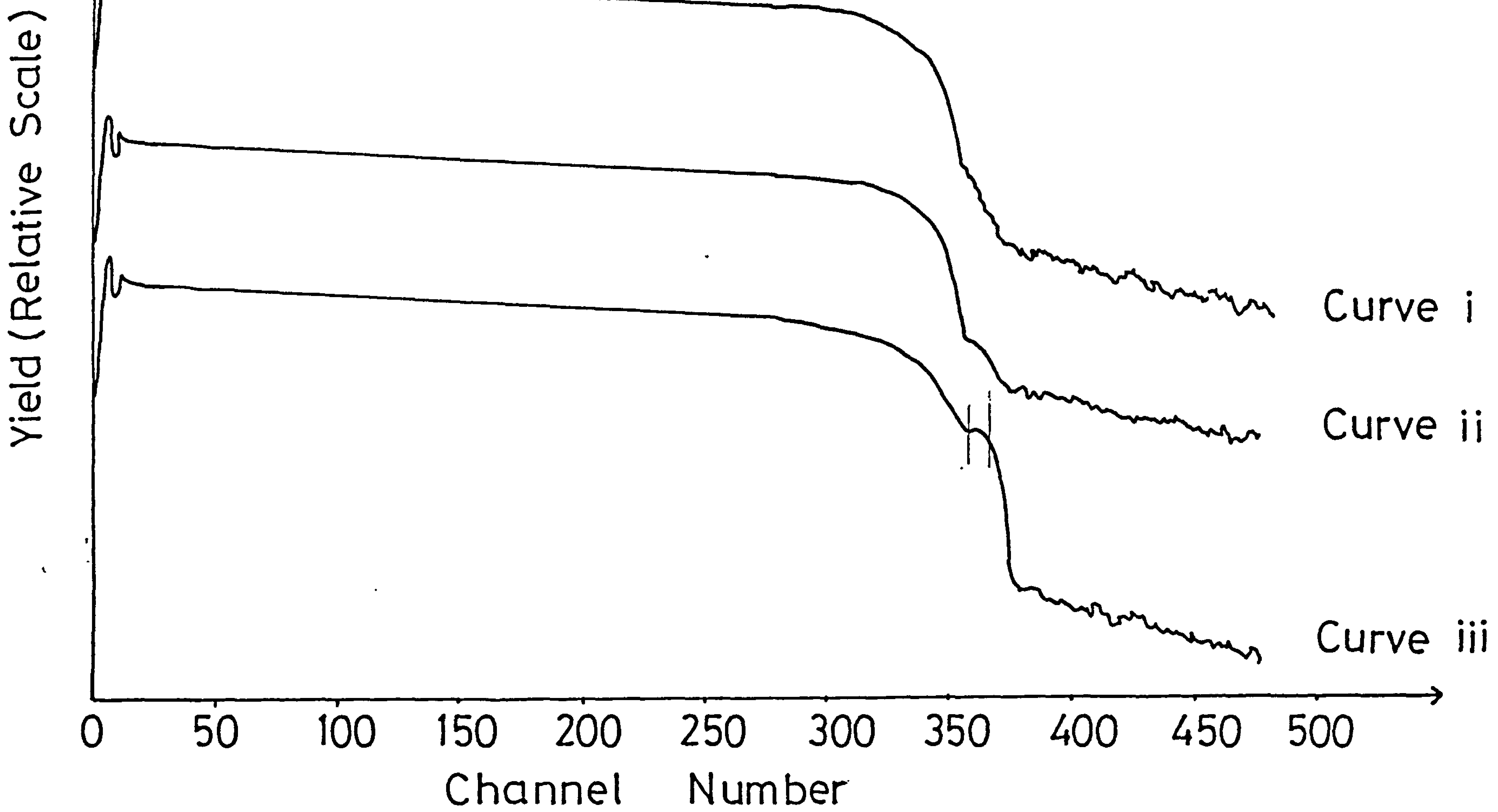

Fig.(5.81) The RBS spectra for an as-prepared Cu_xS/CdS cell (curve i), a similar cell after annealing in air at 200°C for 1/2 hour (curve ii) and an unannealed cell after ageing in air at room temperature for 1 year (curve iii).

thin layer of surface Cd. The result for an unnanealed sample which had been left in air for 1 year is also shown in figure 5.81 (curve iii). This spectrum shows an even larger high energy peak (again with a limit at 385 keV) indicating a more significant concentration of cadmium at the surface. For the case of ideal, plane, parallel structures, it can be shown that a layer of cadmium of thickness 0.033 μm would produce a RBS signal of width ~ 10 keV which would be clearly separated from the Cd signal arising from the underlying CdS layer. In practice, there would be some broadening of the signal and when cadmium is also distributed through the Cu_xS layer, the surface peak would not be clearly resolved, as in the case in figure 5.81. Taking account of the non-ideality of the layers involved in the polycrystalline samples studied here, it is probable that the peak in curve (iii) in figure 5.81 is due to a cadmium layer with a thickness less than ~ .033 μm. However, there is no doubt that this RBS data demonstrates very clearly the existence of Cd at the surface of degraded Cu_xS/CdS cells and therefore supports the evidence provided by the previously mentioned destructive techniques.

5.4.4 Stabilization of cell structure and characteristics

As previously mentioned in chapter 3 (section 3.4.3), the deposition of a thin layer of Cu (50-100 Å) on the Cu_xS surface and heating to a temperature of ~180°C in air can lead to much improved stability according to Bogus and Mattes (186). It is believed that this process leads to the formation of a copper oxide layer on the top of the Cu_xS/CdS cell which acts as a protective layer for the Cu_xS film against degradation. In addition, it is thought that the oxide layer at the surface of the absorber layer acts as a minority carrier

reflector and, thereby, reduces the surface recombination velocity. In view of the results described in the previous sections concerning the different degradation processes which occur during cell operation, measurements were carried out in order to determine which of these degradation processes was most strongly influenced by this stabilization procedure. Measurements were made of the sheet resistivity in order to monitor the stoichiometry variations in the Cu_xS layer, and the junction capacitance was studied in order to detect any diffusion at the Cu_xS-CdS interface. For the capacitance measurements, the CdS layers were first divided into arrays of small area segments using varnish as described in section 5.3.3. These CdS films were etched for 3 seconds and dipped into hot CuCl for 2 seconds. A thin layer of copper (~ 100 Å thick) was evaporated onto the newly formed Cu_xS surfaces. The cells were subsequently annealed in air at 180°C for 90 minutes. For one set of experiments, a gold contact was evaporated to cover one cell element through a mask having an aperture area larger than the cell element area. The junction capacitance for this cell element was then monitored as a function of time during which the sample was exposed to air at room temperature. In addition, at intervals of 30-40 days, a new gold contact was evaporated onto another of the exposed elements on the same sample, and the capacitance of this newly contacted element was recorded. Both sets of results are shown in figure 5.82. The full line gives the results obtained on the original contacted area and the circles indicate the results for each of the 7 elements on the sample. As might have been expected, the results for the first contact show no change over a period of over a year. For this element the gold contact which had been covering the cell throughout the whole period

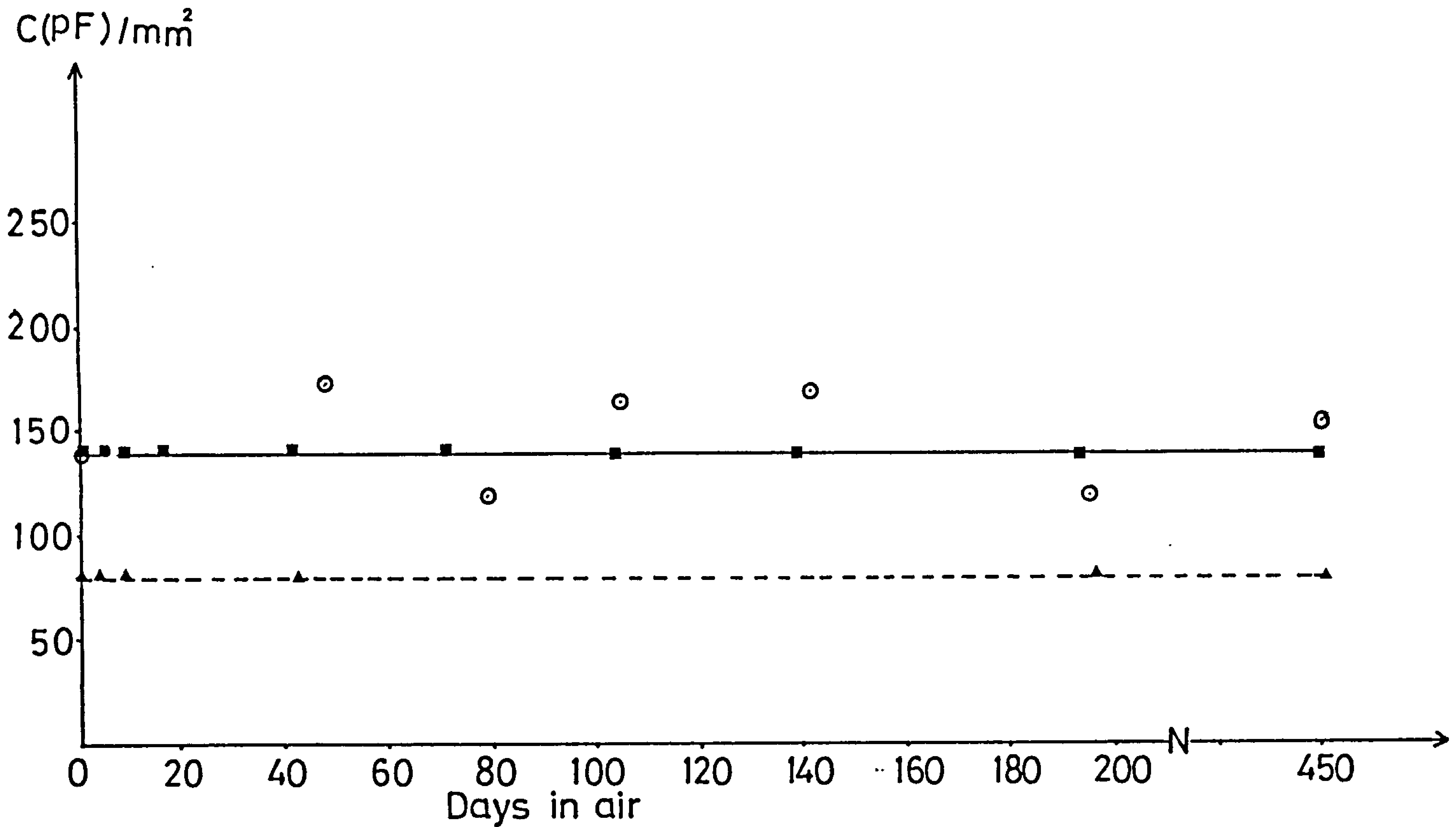

Fig.(5.82) The variation of junction capacitance for Cu_xS-CdS cell (with 100Å copper overlayer annealed in air for 90 minutes) as a function of time of exposure to air. Full line is the capacitance for a single element observed throughout the period (contact area larger than cell element). The circles are the corresponding data for 7 different elements. Dotted line is the capacitance for a single contact (contact area smaller than the cell area).

was expected to act as a protective layer as seen in section 5.4.2). On the other hand the results for the different segments which were exposed to air for different times before being covered with the gold contact also show stability although there is considerable scatter in the data which can be attributed to errors in the measurement of the areas of the different elements.

In an attempt to keep a cell element exposed to the atmosphere while making capacitance measurements without the need of using different elements with different areas, another experiment was performed using a gold contact with area smaller than the cell element area. The capacitance measurements for this experiment are also shown in figure 5.82, indicated by the dotted line. It is clear that these measurements confirm that the junction capacitance for these cells was stable for up to 450 days. As this implies that the junction area and the space charge width both remain effectively constant, it seems that the copper oxide layer on the top of Cu_xS layer controls the diffusion of copper into CdS layer at both the grain surface and within the grain boundaries. The results in figure 5.82 for the cell with the small area gold contact (dotted line) also suggest that the Cu_xS layer resistivity must remain unchanged otherwise changes in effective capacitance would result from changes in the equivalent circuit as discussed in section 5.4.2. However, sheet resistance measurements were carried out independently. For this purpose a 4-line gold grid structure was evaporated onto a copper-coated cell and the sample was annealed in air for 90 minutes as described previously. Sheet resistance measurements were made in the usual way and the measurements were repeated at regular intervals while the cell was

exposed to air. The results are presented in figure 5.83 showing that the sheet resistance was constant for up to 450 days. This indicated that the stoichiometry of the Cu_xS layer remained effectively constant for this period of time.

From these results it was concluded that the structure of the cells was maintained stable by the presence of the surface copper oxide layer. Thus it was of interest to obtain some direct evidence for this structural stability. As the RBS technique had been found to be of value in monitoring structural changes, it was decided that this should be used again to investigate the effect of the copper overlayer. Using a cell fabricated as described above with a copper oxide layer formed by heat treatment in air at 180°C for 90 minutes, the RBS spectrum shown in figure 5.84 was obtained. It can be seen that this spectrum is very similar to that in figure 5.81 for the as-formed cell prior to any heat-treatment. Both show a well defined edge which has been attributed to scattering from Cd in the CdS layer, and both show a weak tail extending to the same high energy threshold associated with Cd remaining in the Cu_xS layer at the end of the chemical exchange process. While curve (ii) in figure 5.81 for the uncoated sample which had been heat treated in air shows a substantial increase in the tail signal (due to Cd out-diffusion), the spectrum in figure 5.84 for the heat treated copper-coated sample shows no suggestion of an increased surface concentration of Cd. This is consistent with the results obtained by Bryant et al (166), using the AES profiling technique, which showed that an abrupt Cu_xS-CdS interface was maintained when a copper overlayer was present during heat treatment in air. Thus, there is substantial evidence to indicate that the structure and characteristics of Cu_xS-CdS cells can

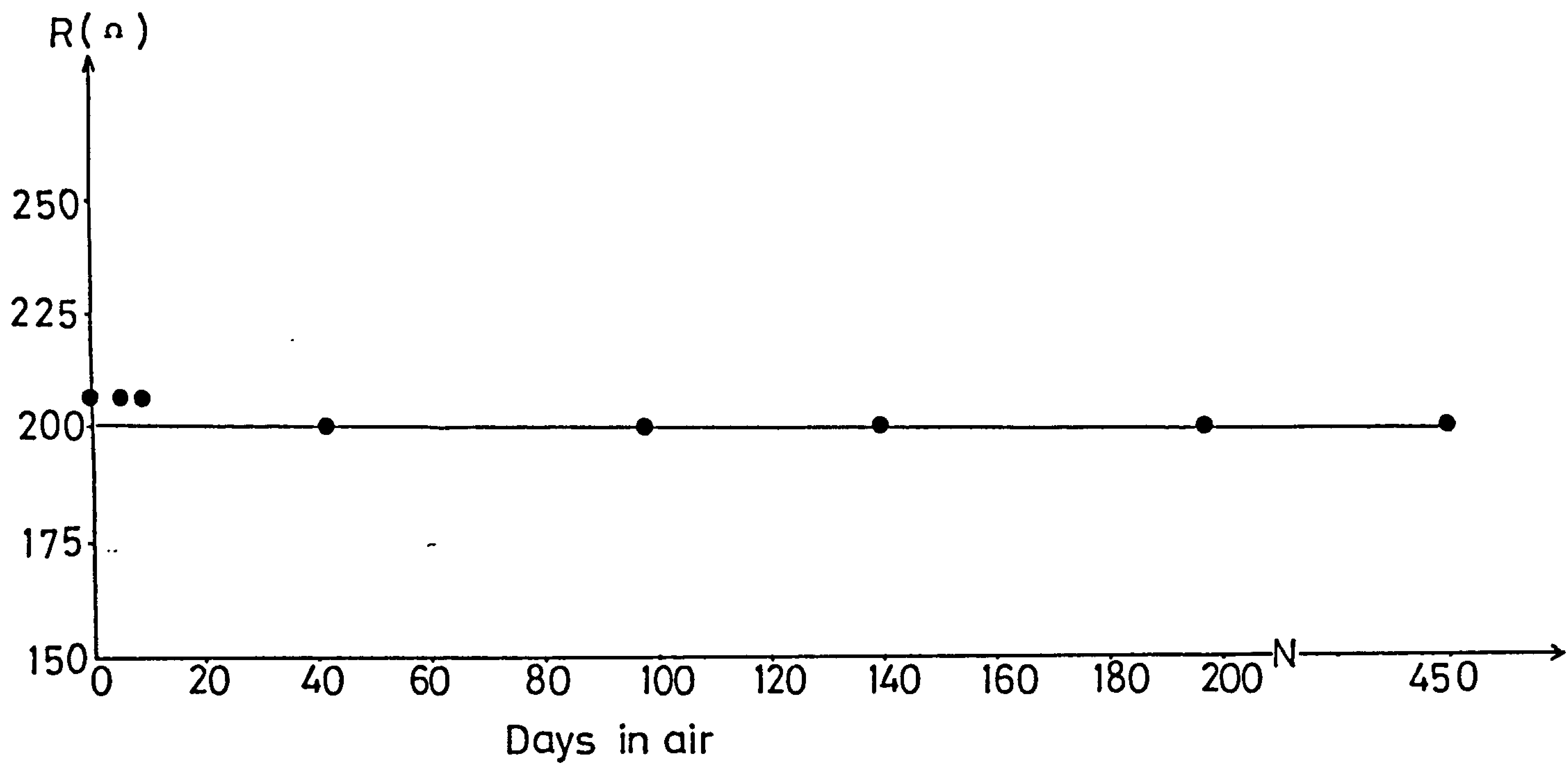

Fig.(5.83) The sheet resistance of the Cu_xS layer for a Cu_xS-CdS cell, with 100Å thick copper overlayer (annealed in air for 90 minutes) as a function of time of subsequent exposure to air at room temperature.

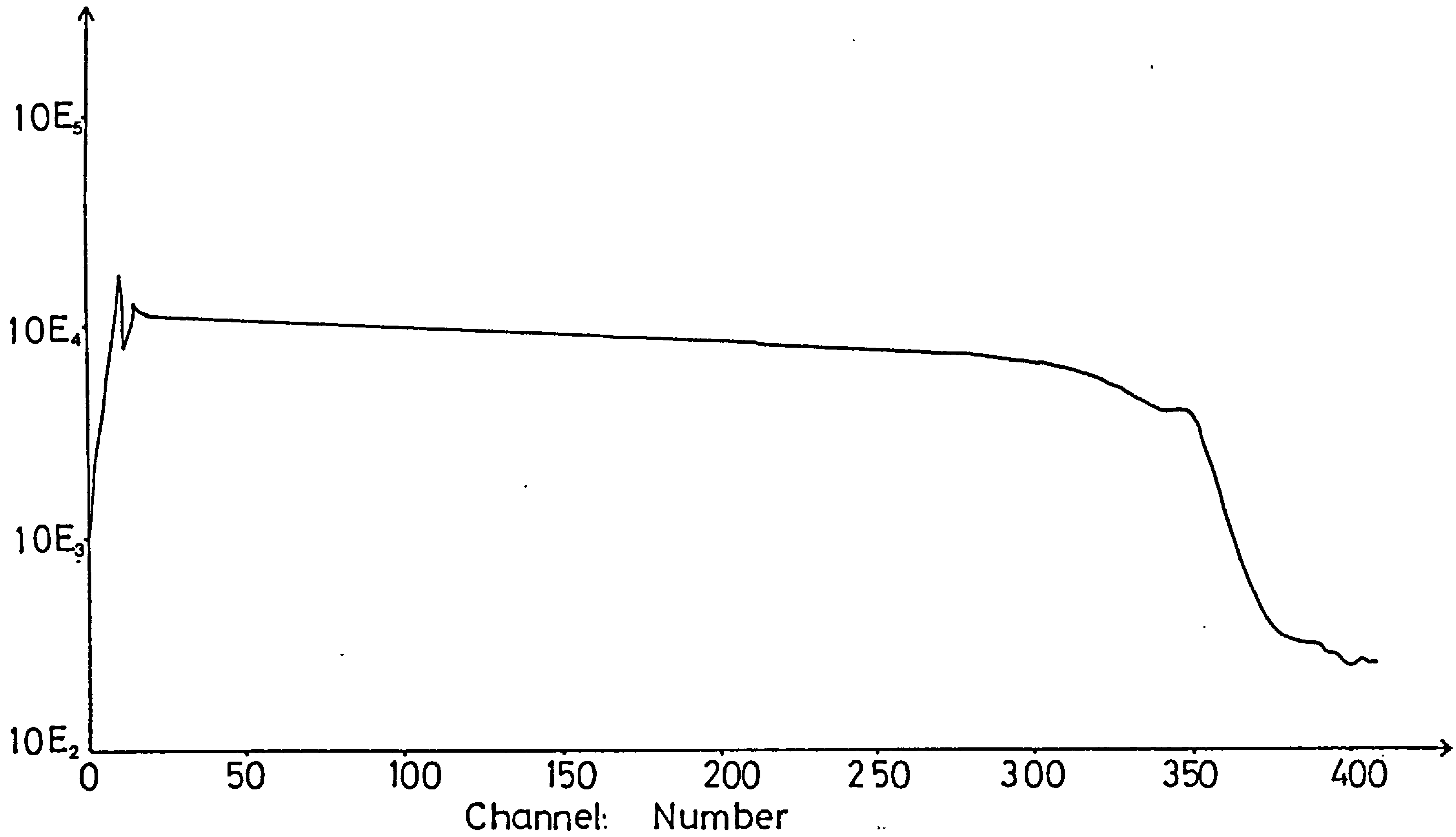

Fig.(5.84) The Rutherford backscattering spectrum for a cell with copper oxide layer formed by heat treatment in air at 180°C for 90 minutes.

be stabilized by the formation of a copper oxide layer over the surface. Using thermodynamic conclulations concerning the chemical reactions which might occur between the various elements at the cell surface, Partain and Coworkers (183) have shown that the required oxide is CuO. The same reasoning reveals that formation of $CdSO_4$ is strongly favoured in unprotected cells and this is clearly consistent with the experimental observations of Cd on the surface of degraded cells. A practical demonstration of the benefits of the copper-oxide protection treatment has been provided by Pfisterer et al (187) and Hewig (59) who used copper oxide coated cells together with encapsulation between two sheets of glass for the construction of panels which showed no significant degradation over a period of 3 years during roof-top stability tests.

CHAPTER SIX

SUMMARY AND CONCLUSIONS

As stated in chapter 1, the initial purpose of the project described in this thesis was to obtain information about the efficiency degradation processes in Cu_xS/CdS cells and to consider methods for stabilising the properties of these devices. However, in the course of the project, which has involved the fabrication of a very large number of devices, it was necessary to give attention to the problems concerning reproducibility of device characteristics. As the subject being investigated required comparisons to be made between cells treated in different ways, it was necessary to ensure that these cells were initially very similar. There is no doubt that the operational characteristics of a Cu_xS/CdS thin film solar cell depend critically on the properties of each of its component parts and it is therefore essential to exercise careful control over every stage of the cell fabrication procedure.

Thus, the first part of this study was devoted to considering how various fabrication procedures influence the final properties of a cell and in the course of this work, some interesting and unexpected results were obtained. In subsequent studies on the stability of the cells, it was found useful to employ a wide variety of different characterisation techniques in order to separate the effects of different degradation processes. In the following sections, the main results are summarised in the order in which they were presented in chapter 5.

6.1 The CdS Base Layer

The first step towards the construction of a durable and efficient Cu_xS/CdS device is the fabrication of a defect-free CdS layer with a well ordered grain structure. For evaporated CdS layers, it has been clearly shown that this depends on a large number of different factors including the nature and preparation of the metal substrate and the purity and structure of the CdS source as well as the vapour deposition parameters. A copper sheet with a coating of zinc was found to provide good adhesion and to form a suitably low resistance ohmic contact to the CdS layer provided that the zinc coating was free of pinholes, otherwise the CdS layer was found to be covered with black dots due to interaction between the vapour and the underlying copper substrate. A zinc thickness of Ø.2 - Ø.3 μm was found to be satisfactory. Using substrates with a relatively smooth surface, it was possible to deposit CdS layers with a well ordered grain structure, provided a suitable substrate temperature and CdS evaporation rate were chosen.

It is not possible to specify what deposition parameters should be used to obtain good CdS layers. This depends on the CdS source used. In this project, high purity CdS was obtained from several different suppliers but these varied significantly in deviation from stoichiometric composition and particle size. It was found that the use of a high evaporation rate with a fine powder usually leads to some powder fragments becoming embedded in the vapour deposited layer, causing gross defects in the polycrystalline structure. Rapid and preferential HCl attack at the boundaries of these defects during texturing of the CdS surface leads to pinholes in the film and penetration of the Cu_xS through the CdS along such defects can create

shunting effects and promote electrical decomposition of the Cu_xS which further degrades the performance of the device. Using larger particle powders or slower evaporation rates, defect-free CdS layers could be deposited, with the required carrier concentration around ~10^{18} cm^{-3} and grain size $\gtrsim$ 2 μm width. It should be noted that even when using different batches of CdS powder from the same supplier, it was found (section 5.1.2) that these do not usually give similar results so that it is necessary to carry out a series of tests with every new batch of material and to adjust the deposition conditions to achieve the required properties. An indication of the quality of the layers was found to be provided by luminescence studies. Layers showing weak edge emission produced poor cells.

6.2 The Cu_xS absorber layer

The conventional chemical exchange process was used during this project to form the Cu_xS layer as described in section 4.1.3. The growth of Cu_xS on polycrystalline CdS is strongly affected by the surface topography of the CdS film, by the pH and temperature of the CuCl solution and by the relative concentrations of Cu^+ and Cu^{++} ions in the solution. It is well known that the formation of Cu_xS at the front surface of the cell is a diffusion limited process so that the time dependence follows a parabolic law, while a more rapid growth process occurs in the grain boundaries giving rise to deep protrusions of Cu_xS into the CdS film as discussed in section 5.2.1. Evidence for the extensive growth of Cu_xS in the CdS grain boundaries has come indirectly from the increase of the junction capacitance with increasing dipping time as shown in table 5.4. These results were supported by the more direct evidence from SEM micrographs showing the

surface topography of a CdS layer from which the Cu_xS had been leached in KCN after dipping (figure 5.3). Previous theories for the observed increase in Cu_xS layer thickness with time have used unsatisfactory models for the grain boundary diffusion process but by making use of the theory of Whipple (217) and Le Claire (41) for grain boundary diffusion, a new model has been developed to account for the measured growth in the average thickness of the Cu_xS layer (equation 5.2.1). This relation was found to fit data obtained during this investigation as well as that obtained by other workers (147). An interesting feature of this analysis was the fact that the best fit to the experimental data was obtained by assuming a short delay between immersing the CdS film in the CuCl solution and the start of Cu_xS growth in the grain boundaries. This delay time appeared to be dependent on the acidity of the CuCl solution and also on the previous treatment of the CdS layer.

Annealing the pre-etched CdS in air was seen to increase the rate of formation of Cu_xS to a remarkable extent leading to a mean thickness of nearly 3 μm in just 2 seconds. Most of this mean thickness was contributed by Cu_xS lying in the grain boundaries and was consistent with the delay time for formation of Cu_xS in the grain boundary regions being very short. CdS layers annealed in vacuum or hydrogen showed only slight increases in thickness of the Cu_xS layer as compared with unannealed CdS layers. In addition to the thickness and structure of the Cu_xS layer, its composition is of great importance. This is influenced by the dipping conditions; for example, the stoichiometry factor x was found to be increased by increasing the dipping time of the CdS layer into the CuCl bath. The stoichiometry is also very sensitive to post-formation treatments such

as the annealing treatments which are required to form devices with good photovoltaic behaviour. Annealing the cells in vacuum was found to lead to an increase in the x factor which seemed to saturate after a short time. Annealing in air was found to have two different effects depending on the initial stoichiometry of the Cu_xS layer. For the lower initial values of the stoichiometry factor (x ~1.96) x was found to increase for short annealing times in air and then to decrease for longer times. On the other hand, for initial values of $x \geqslant 1.98$ there was only a decrease which was attributed to the formation of an oxide layer at the surface of Cu_xS layer. Annealing in hydrogen was found to have the opposite effect to air annealing, leading to a steady increase in the x factor for the Cu_xS layer with increasing annealing time. In addition, hydrogen annealing was found to make the Cu_xS layer thinner, while air annealing increased the thickness. This was seen very clearly by the data in table 5.6 for cells annealed first in air and subsequently in hydrogen. Although ECA measurements were used to obtain these results, small variations in thickness at the upper surface of the Cu_xS layer could not always be detected by ECA because the corresponding reduction in the average thickness of a Cu_xS layer (including the grain boundary regions) was in the range of error of the ECA measurements. However, it was found that information concerning such variations in the Cu_xS thickness could be obtained by studying the cathodoluminescence (CL) emission from these devices, as discussed in section 5.2.4. Being a non-destructive technique, CL was found to have additional advantages over ECA for monitoring slow changes in the properties of the Cu_xS layers. It must be emphasised that the CL emission under consideration was

produced within the CdS layer although by examining specially formed, very thick Cu_xS layers it was found possible to excite a characteristic Cu_2S emission peak together with another band attributed to Cd in the Cu_2S layer. For normal cells with thin Cu_xS layers, information about the Cu_xS layer was obtained from the effect of this layer on the CdS emission during its transmission through the Cu_xS layer. By comparing the emission from CdS layers with and without an overlayer of Cu_xS, it was possible to account for the observed CL spectrum from the Cu_xS/CdS cells by making use of data for the spectral dependence of the optical absorption coefficient for the Cu_xS layer. The optical transmission for this layer was found to be very dependent on the thickness and stoichiometry of the layer and the observed emission was therefore very sensitive to variations at the upper surface (thinnest) regions of the Cu_xS layer in contrast to the results obtained using ECA which are dominated by the Cu_xS in the deep, grain boundary regions.

6.3 Characteristics of Cu_xS-CdS cells

Following the fabrication of good quality CdS films and Cu_xS layers, the I/V characteristics of the completed devices were found to be very dependent on the structure of the top contact. The best results were obtained using gold grids having 20 lines/cm. As discussed in section 5.3.1, this achieved the desired reduction in the series resistance, with associated improvements in the fill factor and conversion efficiency of the cell. As mentioned earlier, there is also a need for a post-fabrication annealing process to optimise both the Cu_xS/CdS junction characteristics and the properties of the Cu_xS absorber layer (particularly the optical absorption spectral response). The interfacial diffusion of copper into the CdS layer

during post-fabrication annealing was studied through its effect on the junction capacitance (as discussed in section 5.3.3). Using the results from C-V measurements on cells annealed for different lengths of time in air or hydrogen, it was concluded that the diffusion coefficient of copper into the CdS layer was higher when annealing in air than it was during annealing in hydrogen. The diffusion coefficients were estimated to be 2.10^{-13} cm^2 s^{-1} and $3.7.10^{-14}$ cm^2 s^{-1} respectively. These values are of similar magnitude to a previous report (38) for single crystals annealed in vacuum but these estimates are subject to considerable uncertainty due to changes in the effective areas of the junctions as a result of diffusion related changes in the structure of the junction particularly in the grain boundary regions.

In addition to causing diffusion of Cu into the CdS film, as required to broaden the space charge width on this side of the junction, annealing in hydrogen has the added benefit of removing surface oxides and increasing the x value for the Cu_xS layer. However, when the initial x value is significantly less than 2, rather long annealing times are required for the optimum value to be reached. As shown in a previous study (213), one way of increasing the initial x value is to implant Cu into the CdS film surface before forming the Cu_xS layer. The results obtained during the present project confirmed that x can be increased by Cu ion implantation but, in contrast to the previous report (213), it was found that this effect can be accompanied by an increase (rather than a reduction) in the Cu_xS film thickness leading to a lower open-circuit voltage and short circuit current for the completed cell. As a result of further investigations

it was concluded that the effect of ion implantation on the Cu_xS growth process was dependent upon the structure of the CdS films and also on the energy and dose of the implanted ions. It was of particular interest to find that for cells formed on CdS films with poor crystal structure (normally yielding poor cells with efficiency ~ 1%) the effect of ion implantation was to improve the cell performance considerably to give an efficiency of over 4%. This was considered to be due mainly to a reduction in the growth of Cu_xS in the grain boundaries and was probably related more to structural changes brought about by implantation than to the nature of the implanted ions. In fact, when zinc was implanted into the CdS layers instead of Cu similar results were obtained.

6.4 Stability of Cu_xS-CdS cells

It is well known that the photovoltaic conversion efficiency of Cu_xS/CdS cells exposed to air becomes degraded due to structural and chemical changes within the cell. The main degradation processes considered during this study were the diffusion of copper from the Cu_xS layer into the CdS and oxidation processes at the Cu_xS surface. Both these effects reduce the x-value of the Cu_xS layer causing a lowering of its sheet resistance and optical absorption efficiency with a consequent reduction in the photovoltaic performance. A number of different techniques were employed to help to distinguish between the different processes giving rise to these effects. Copper diffusion from the Cu_xS layer into the CdS was detected from changes in the junction capacitance and conductance as a function of the applied voltage. For unannealed Cu_xS/CdS cells, changes in the junction properties at room temperature appeared to be dominated by the diffusion of copper along the grain boundaries causing the

junction area of the cells to be increased and the junction resistance to be reduced. Only after long periods of time in air did diffusion into the grains appear to become important. However, the relative importance of diffusion into the grains was clearly increased at elevated temperatures (during annealing). For annealed cells the effects of interfacial diffusion were reduced and the main degradation mechanism at room temperature was then due to oxidation at the surface of the Cu_xS layer. The effects of this were studied by a variety of techniques including ECA, sheet resistance measurements, luminescence and RBS.

Using ECA measurements it was shown that exposure to air leads to a rapid reduction in the x-value for the Cu_xS layer due to oxide formation and that this process can be reversed by annealing in hydrogen. This was confirmed by measurements of the Cu_xS layer sheet resistance and also by monitoring the short circuit current of completed cells. Changes in the luminescence spectra for cells exposed to air after annealing in hydrogen were also consistent with a reduction in the x-value for the Cu_xS layer. A similar behaviour was observed for cells annealed in vacuum, but it was interesting to find that the changes in the luminescence spectra for cells annealed in air were significantly different. This was thought to be associated with an increase in the concentration of Cd in the Cu_xS layer after annealing the cells in air. Direct evidence for the presence of Cd at the surface of degraded cells (and cells annealed in air) has been provided during this study by the use of RBS, confirming previous results by other workers using different techniques (166, 178). It seems possible that Cd in the Cu_xS layer can contribute to improved

stability. It has previously been mentioned that cells with degraded efficiency due to exposure to air can be restored to their previous performance by annealing in hydrogen. However, from sheet resistance measurements and short circuit current measurements it was noted that repeated degradation and restoration cycles caused a gradual reduction in the rate of the subsequent degradation process. However, in a corresponding experiment with free-standing evaporated layers of Cu_xS, no gradual slowing of the degradation process was observed, suggesting that the presence of the CdS layer in the Cu_xS-CdS cells was important in the mechanism for this effect. In view of the above evidence for Cd diffusion into the Cu_xS layer, it seems that this must have a role in the improved stability as suggested by others (167, 246).

A more controlled procedure for improving the stability of the Cu_xS-CdS cells is that suggested by Bogus and Mattes (186) involving the deposition of a thin layer of Cu (~ 100 Å thick) and annealing in air to produce a layer of copper oxide over the surface of the Cu_xS layer. During this project, the above procedure was found to be very successful. By monitoring the junction capacitance and Cu_xS layer sheet resistance for cells exposed to air for 15 months, no evidence was found for interfacial diffusion processes or any variations in the composition of the Cu_xS layer. Furthermore, RBS measurements indicated a stable Cu_xS-CdS junction with no evidence of Cd out-diffusion during the air annealing process.

6.5 Concluding remarks

It is clear from the results summarised above that, although the main aim of this investigation was concerned with degradation processes in Cu_xS-CdS cells, many points of interest arose from the

initial studies concerning the need to fabricate cells with reproducible characteristics. As many different factors influence the cell characteristics, great care needs to be taken at every stage of the fabrication process in order to ensure reproducible behaviour. Of course this problem is made more difficult by the complex geometry of these cells which are based on polycrystalline CdS films and, in investigating these complex structures, the use of a variety of different characterisation techniques was found to be essential. For the long term stability studies, non-destructive methods for analysing the Cu_xS layer (e.g. sheet resistance, luminescence, RBS) were particularly useful. The luminescence and RBS methods had the added advantage of being very sensitive to changes at the front surface of the Cu_xS layer, in contrast to the ECA technique which gave average results for the layer which could be dominated by material in the grain boundary regions.

The deep grain boundary protrusions of Cu_xS, which result from the chemical exchange process for forming these layers, have been the subject of many studies in the past, but it seems that this subject could usefully be given more attention in the light of the theoretical analysis (in section 5.2.2) which suggests that the final structure of the Cu_xS layer depends on the length of the delay time t_o before significant grain boundary growth begins. The results presented here indicate that the time t_o is dependent on the acidity of the CuCl solution and also on the previous treatment given to the CdS layer. This could be checked in future studies by analysing the Cu_xS layer growth kinetics for CdS layers given different treatments, such as annealing in different atmospheres. It would be particularly

interesting to investigate further the observed reduction in grain boundary penetration, and the associated improvements in efficiency, of cells formed on poorly structured CdS layers which had been implanted with Cu or Zn ions. Such studies could lead to new procedures for optimising the cell properties, although, in the case of cells formed on poor quality CdS layers, it would be necessary to consider the long term stability of these devices in comparison with cells formed on well structured CdS layers.

In spite of the many previous studies of Cu_xS-CdS cells and related devices, it seems that there is still much to be learned. The work reported here has revealed some new points of interest and it is hoped that these might contribute to future improvements in the efficiency, stability and production costs of these devices.

References

1. E. Becquerel, Acad. Sci. Compt. Rend. (Paris) vol. 9 (1839) p561.
2. W.G. Adams and R.E. Day. Prac. Roy. Soc. (London), vol. A25, (1877) p113.
3. W. Schottky, Physik, Zs, vol. 31 (1930) p913.
4. D.M. Chapin,C.S. Fuller, and G.L. Pearson, J. Appl. Phys. 25 (1954) p676.
5. R. Remoel, G. Shushrar, E. Bernan, J. Caldwell and J. Arnett. 6th E.C. Photovoltaic Solar Energy Conference (1985) p519.
6. J.C.C. Fari, B.Y. Tsaur and B.J. Palm. Proc. Soc. Photo-opt. Inst. Eng. 407 (1983) p73.
7. E.D. Jackson, Trans. Conf. on the use of solar energy, Tucson, 1955, vol. 5, University of Arizona Press, Tucson, AZ, 1958, 122-126.
8. J.C.C. Fan, B.Y. Tsaur and B.J. Palm, 16th IEEE Photo. Special Conf. (1982) p692.
9. R.P. Gale, G.W. Turner, J.C.C. Fan, R.C. Chapman and J.V. Pantano, Proc. of the 17th IEEE Photovoltaic Special. Conf. May 1-4, (1984) Kissimmee, Fla, p721.
10. D.E. Carlson, 8th E.C. Photovoltaic Solar Energy Conf. proceedings of the international conference, held at Florence, Italy, 9-13 May (1983) p635.
11. S.S. Chu, T.L. Chu, F.S. Zhang, W.J. Chen and Q.H. Wang, Proc. 16th IEEE Photo. Special Conf. (1982) p1149.
12. W.H. Bloss and H.W. Schock, 8th E.C. Photovoltaic Solar Energy Conference, held at Florence, Italy, 9-13 May (1988) p1575

13. R.A. Mickelsen, Proc. polycrystalline thin film program meeting, Lakewood (1987), SERI, C-P-211-3171, p61.

14. J.A. Bragagnolo, A.M. Barnett, J.E. Phillips, R.B. Hall, A. Rothwarf and J.D. Meakin, IEEE Trans. Electron Devices, ED-27 (1980) p645.

15. R.B. Hall, R.W. Birkmire, J.E. Phillips and J.D. Meakin, Proc. 15th IEEE Photo. Special Conf. held at Kissimmee, Florida, USA, 12-15 May (1981) p777 or in Appl. Phys. Lett. 38 (1981) 925.

16. S. Ikegami, Technical Digest, 3rd Int. PVSEC, Tokyo, 1987, Jap. Conversion Service, p677.

17. L.L. Kazmerski, Univ. of Mine, Orono, Second Quarter report to NSF-RANN and ERDA, NSF/AER 75-19576/OR/77/2 (1977) p13.

18. J.L.S. Lay, S. Wangner, M. Bettini, K.J. Bachman and E. Buehler, IEEE Trans. Electron Devices, ED-24 (1977) p483.

19. M. Bhshan, Appl. Phy. Lett. 40, (1982) p542.

20. H. Von Compe, G.H. Hewing, W. Hoffmann, H. Huschka, B. Schurich, and J. Worner, 6th E.C. Photo. Solar Energy Conference, proceedings of the international conference, held in London (UK) 15-19 April (1985) p778.

21. W.H. Bloss and H.W. Shock, 8th E.C. Photovoltaic Solar Energy Conference, proceedings of international conference, held at Florence, Italy, 9-13 May (1988) p1571.

22. M. Prince, J. Appl. Phys., 26, (1955) p534.

23. J.J. Loferski, J. Appl. Phys., 27, (1956) p777.

24. C. Wagner, Phys. Z.32 (1931) p641.

25. H.C. Cord, E.H. Rhoderick: J. Phys. D, 4 (1971) 1589.

26. E.H. Rhoderick: Inst. Phys. Conf. Ser. no. 22 (1974) 3.

27. B.O. Seraphin, Solar Energy Conversion (Solid State Physics Aspects), Vol (31), 1978.

28. S.M. Sze, Semiconductor devices, Physics and Tech. Wiley, (1985) p296.

29. R. Hill, Active and Passive Thin Film Devices, Ed. T.J. Coutts, Academic Press, London, p487.

30. H.B. Panish and H.C. Casey, Heterojunctions Lasers, Academic Press, New York (1978).

31. S.J. Fonash, Photovoltaic Devices, C.R.C. Critical Review in Solid State and Materials Science (1980).

32. A.L. Fahrenbruch and R.B. Bube, Fundamentals of solar cells. Academic Press, Inc. (1983).

33. R.J. Anderson, Solid State Electron, 5 (1962) p341.

34. A. Rothwarf, Solar Cells 2 (1980) p115.

35. W. Palz et al. in Rec. 10th IEEE Photovoltaic Spec. Conf. (1973) p69.

36. L.R. Shiozawa, G.A. Sullivan and F. Augustine, Proceedings of the 7th IEEE photovoltaic Spec. Conf. (1968) p39.

37. R.B. Hall and V.P. Singh, J. Appl. Phys. 50 (1979) p6406.

38. G.A. Sullivan, Phys. Rev. Vol. 184, No. 3 (1969) p796.

39. B. Tuck, Introduction to diffusion in Semiconductors Chapter (1), (1974).

40. H.S. Levine and C.J. MacCallum, J. Appl. Phys. 31 (1960) p595.

41. A.D. Le Claire, British J. Phys. D: 14 (1963) p351.

42. A.C. Rastogi and S. Salkalachen, Solar Cells, 9 (1983) p185.

43. G. Nadjakov, R. Andreitchine, and M. Borissov, IZV. Bulg. Akad. Nowk, 4, (1954) p10.

44. A.E. Carlson: Research on semiconductor films WADC Tech. Rep. 56-62 Clevite Group (1956).

45. D.C. Reynolds, G. Leies, L.L. Antes, R.E. Marburger, Phys. Rev. 96 (1954) p533. Also D.C. Reynolds and S.J. Czyzak, Phys. Rev. 96, (1954) p1705.

46. R. Williams, R.H. Bube, J. Appl. Phys. 31, (1960) p968.

47. D.A. Cusano, Solid-State Electron 6 (1963) p217.

48. P.N. Keating, J. Phys. Chem. Solids, 24 (1963) p1101.

49. H. Moss, Proc. National Aeronautical Electronics Conference, (1960) p47.

50. A.E. Middleton, D.A. Gorski and F.A. Shirland, Progress in Astronautics and Rocketz, 3, (1961) p275.

51. E.R. Hill and B.G. Kermidas, IEEE Trans. Electron Devices ED-14 (1967) p22.

52. B. Selle, W. Ludwing, and R. Mach, Phys. Status Solidi, 24, (1967) pK145.

53. A.E. Potter and R.L. Schalla, NASA Tech. Note, NASATND-3849 Washington DC (1967).

54. F.A. Shirland, Adva. Energy Con. 6 (1966) p201.

55. F.A. Shirland, and J.R. Hietanen, Proc. 19th Annu. Power Sources Conf. (1965) p177.

56. F.A. Shirland, J.R. Hietanen and W.K. Bower, Quart. Progr. Rep. and Final Rep. Contract NAS3-3502 Clevite Corp. (1966).

57. W.H. Bloss and F. Pfisterer, 5th EC Photov. Solar Energy Conf. (1983) p728.

58. G.H. Hewing, W. Hoffmann, H. Huschka, B. Schurich, J. Wärner, Nukem Gmbh, Hanau, Federal republic of Germany. 5th EC Photovoltaic Solar Energy Conf. (1983) p460.

59. G.H. Hewing, F. Pfisterer, H.W. Schock, W. Arndt, and W.H. Bloss, 16th IEEE Photon. Special. Conf. (1982) p713.

60. W.H. Bloss and G.H. Hewing 14th, IEEE Photon. Spec. Conf. (1980) p287.

61. H. Von Compe, G.H. Hewing, W. Hoffmann and H. Huschka and J. Wörner, 6th E.C. Photov. Solar Energy Conf. (1985) p821.

62. R. Hill and J.D. Meakin, Current topics in Photovoltaics, Academic Press, Chapter (5) (1985) p223.

63. M. Bujatti, J. Phys. D. (2), 1 (1968) p983.

64. M. Bujatti, Phys. Lett. A24 (1967) p36.

65. L.S. Palatnik, M.N. Naboka, and V.E. Marincheva, I_{2v}. Akad. Nauk SSSR Neorg. Mater. 6 (1970) p1526. Inorg. Mater (USSR) 6, (1971) p1344.

66. L.L. Kazmerski, F.R. White and G.K. Morgan, Appl. Phys. Lett. 29 (1976) p268.

67. B. Tell and P.M. Bridenbaugh, J. Appl. Phys. 48 (1977) p2477.

68. S. Wagner, J.L. Shay, K.J. Bachmann and E. Buehler, Appl. Phys. Lett. 26 (1975) p229.

69. M. Bettini, K.J. Bachmann and J.L. Shoy, J. Appl. Phys. 49, (1978) p865.

70. A.L. Fahrenbruch, V. Vaslichenko, P. Buch, K. Mitchell and R. H. Bube. Appl. Phys. Lett. 25 (1974) p605.

71. K. Yamaguchi, N. Nakayama, H. Matsumoto and S. Ikegami, Jap. J. Appl. Phys. 16 (1977) p1203.

72. J.L. Chu: Conf. Rec. 19th IEEE Photov. Spec. Conf., New Orleans (1987) p1466.

73. V.M. Yefremenkova, I.V. Egorova, V.E. Yurasova, IZV Akad. Nauk. SSS, Ser. Fiz. 32 (1968) p1242.

74. D.B. Fraser, H. Melchior: J. Appl. Phys. 43 (1972) p3120.

75. K.R. Albrand, E.W. Justi, W. Mohle, G.H.A. Schneider, D. Vllrich: Cooperation mediterraneenne energie solaire, Bull. 13-5 (1967).

76. J.F. Jordan: Proc. Int. Conf. Solar electricity (CNES), Toulouse (1976) p57.

77. R.R. Chamberline, J.S. Skarman, J. Electrochem. Soc. 113 (1966) p86.

78. R.R. Chamberline, J.S. Skarman, Solid-State Electron, 9 (1966) p819.

79. N. Nakayama, Jap. J. Appl. Phys. 8 (1969) p450.

80. T.J. Cumberbath, N.M. Pearsal and R. Hill, 5th EC photovoltaic Solar Energy Conf. Proceedings of international conference held at Kavouri (Athens), Greece (1983).

81. G.J. Russell, P.C. Pande, A.E. Thomas and J. Woods, 5th EC Photovoltaic Solar Energy Conference. Proceedings of international conference held at Kavouri (Athens) Greece (1983) p855.

82. B. Ray: II-VI Compounds, Monographs in the science of the solid state, vol. 2 (Pergamon Oxford 1969).

83. W.H. Bloss and H.W. Shock, Energy Conversion, Ed. F. Cardon et al, Plenum Press, New York, (1981) p117.

84. J.I.B. Wilson and J. Woods, J. Phys. Chem. Solids 34, (1973) p171.

85. K.V. Shalimova, A.F. Andrushko, V.A. Dmitriev and L.P. Pavlov, Kristallografiya, 8, (1963) p774, Sov. Phys. Crystallogr. 8, (1964) p618.

86. R.B. Hall, Int. Workshop on CdS cells (1975) p234.

87. F.V. Shallcross, Tran. AIME, 236 (1966) p309.

88. F.A. Shirland, Solar cell, 1 (1979/80) p183.

89. K.W. Boer, C.E. Birchenall, I. Greenfield, H.C. Hadley, T.L. Lu, L. Partain, J.E. Phillips, J. Schultz and W.F. Tsen, Proc. 10th IEEE Photo. Special. Conf. New York (1973) p78.

90. L.F. Donaghey, J.A. Duisman, T.M. Peter and P.R. Ryason, 14th IEEE Photo. Special. Conf. (1980) p728.

91. F.A. Shirland, J. Appl. Phys. 50, (1979) p4714.

92. K.A. Norian and J.W. Edington, Proc. 14th IEEE Photo. Special. Conf. Jan 7-10, California, USA, (1980) p701.

93. L. Fraas, J. of Crystal Growth 39 (1977) p92.

94. C. William and R.H. Bube, J. Appl. Phys. 45, (1974) p648.

95. N.F. Foster, Proc. IEEE 53, (1965) p1400.

96. F.J. Bryant, A. Hariri, C.G. Scott, J. of Materials Science, 22 (1987) p3745.

97. R. Banerjee, S. Roy and A.K. Barua, J. Appl. Phys. (1980) p1839.

98. L.D. Massie, Space-Aeronatics, (1964) p60.

99. A.G. Stanley, Appl. Solid State Science, 5, (1975) p251.

100. F.V. Shallcross, Tran. Met. Soc. AIME 236, (1966) p309.

101. D.A. Goçski, U.S. Patent, 3 (1965) p186.

102. H. Berger, J. Aniche, and G. Vskaya, Phys. Status Solidi, 33, (1969) p417.

103. F.I. Verguna, Soviet Phys. Grystallogr. 11 (1967) p420.

104. F.A. Shirland, F. Augustine and W.K. Bower, 2nd Quart. Rep. contract NAS3-6461, NASA-CR-54413 Clevite Corp. (1965).

105. F.A. Shirland, J.R. Hietanen, F. Augustine and W.K. Bower, 3rd Quart. Rep. Contract NAS3-6461 Clevite Corp. (1965).

106. H.E. Nasteline, J.R. Hietanen and F.A. Shirland, Final Rep. AF33 (615) 3253. Clevite Corp. (167).

107. J.P. David, S. Martinuzzi, F. Cabane, Brouty, J.P. Sorbier, J.M. Mathieu, J.M. Roman and J.F. Bretzner, Proc. Int. Colloq. Solar Cells (1971) p81.

108. M. Savelli and J. Bougnot, Solar energy conversion solid-state physics aspects (1979) p228.

109. W.R. Cook, Jr., L. Shiozowa, and F. Augustine, J. Appl. Phys. 41, (1970) p3058.

110. H.S. Mathieu, PhD Dissertation, Dortmund, Germany (1971).

111. J. Vedel, E. Castel: Int. Conf. Photon. Power and its application in space and on earth (CNES, Paris 1973) p199.

112. J.J. Loferski, J. Schewchun, E.A. de Meo, R. Armote, E.E. Crisman, R. Beaulieu, H.L. Hwang, C.C. Wu, Photon. Conf. Rec. 12th (IEEE New York) (1976) p496.

113. B.J. Mulder, Phys. Status Solidi a 13, (1972) p79.

114. H. Rau, J. Phys. Chem. Solids, 28 (1967) p903.

115. T.S. Te Velde, Energy Conversion, 14 (1974) p111.

116. G.B. Abdullav, Z.A. Aligorova, E.H. Zamonova, G.A. Asadov, Phys. Stat. Soli, 26, (1968) p65.

117. F. Guastavino, H. Luguet, J. Bangnot, C.R. Acad. Scie, 26, B, (1969) p831.

118. W. Palz, J. Besson, T. Ngyen, J. Vedel, Photon. Spec. Conf. Rec. 9th IEEE (1972) p91.

119. L.C. Burton and H.M. Windawi, J. Appl. Phys. 47, (1976) p4621.

120. B.J. Mulder, Phys. Stat. Soli. (a) 13 (1972) p569.

121. W.D. Gill and R.H. Bube, J Appl. Phys. 41 (1970) p1694.

122. L.R.S. Liozawa, 8th Quart. Progr. Rep. Contract AF33 (615)-5224. Clevite Corp. 1968.

123. B.J. Mulder, Proc. Int. Colloq. Solar Cells, (1971) p131.

124. J.J. Oakes, I.G. Greenfield, L.D. Partain: J. Appl. Phys. 48 (1977) p2548.

125. J. Dieleman, Int. Workshop CdS Solar Cells and other abrupt heterojunction. Univ. of Delaware, Newark, (1975) p92.

126. L. Eiesenmann: Ann. Phys (Leipzig) 10 (1952) p129.

127. G.P. Sorokin, Yu, M. Papshiev, P.T. Oush: Sov. Phys. Solid State 7 (1966) p1810.

128. R. Marshall, S.S. Mitra, J. Appl. Phys. 36 (1965) p3882.

129. F. Guastavino, PhD Dissertation, Montpellier, France (1974).

130. L.R. Shiozawa, G.A. Sullivan, F. Augustine: Contract No. AF33 (615) 5224, Clevite Corp. Cleveland, Ohio (1967).

131. N. Nakayama, J. Phys. Soc. Japn. 25 (1968) p290.

132. M. Ramoin, J.P. Sorbier, J.F. Bretzner, S. Martinuzzi: C.R. Acad. Sci. Ser. B268 (1969) p1097.

133. E. Eser, and J.A. Cambridge, Solar Cells 5 (1982), p343.

134. J.J. Loferski, J. Schewchun, E.A. de Meo, R. Arnote, E.E. Crisman, R. Beaulieu, H.L. Hwang, C.C. Wu, Photon Sepecl. Conf. 12th (IEEE New York) (1976) p496.

135. J. Schewchun, J.J. Loferski, A. Wold, R. Arnote, E.A. Demeo, R. Beaulieu, C.C. Wu, H.L. Hwang, Photon. Spec. Conf. 11th (IEEE New York 1975) p482.

136. A. Rothwarf and H. Windawi, IEEE Trans. Electron Devices, ED-28 (1981) p64.

137. L. Clark, R. Gale, K. Moore, R.S. Mytton, R.S. Pinder: Int. Colloq. Solar Cells 1970 (CNES, Toulouse 1971) p241.

138. R.A. Mickelsen, D.D. Abbott, Final Rep. Contract NAS 3-13232, NASA-CR-120812 (Boeing Co, Seattle Washington 1971).

139. T.S. teVelde and J. Dieleman, Philips Res. Rep., 28 (1973) p573.

140. A. Vervaet, M. Burgelman and D. Van Wassenhove, Thin Solid Films, 151. (1987) p133.

141. P.A. Crossley, G.T. Noel, M. Wolf, Final Rep. Contract NASW 1427, RCA Astro Electron Div. Hightstour New Jersey (1968).

142. R.R. Chamberlin, J.S. Skarman, J. Electrochem, Soc. 113. (1966) p86.

143. L.R. Shiozawa, F. Augustine, G.A. Sullivan, J.M. Smith and W.R. Cook, 1969 Aerospace Research Laboratories Report ARL 69-0155 contract AF 33 (615)-5224.

144. K.W. Boer and J.D. Meakin (Eds) 1975 Proc. Int. Workshop on CdS solar cells and other abrupt Heterojunctions University of Delaware NSF RANN AER75-15858.

145. H.W. Schock, G. Bilger, W.H. Bloss, G.H. Hewing and F. Pfisterer, Vacuum 27, (1977) p281.

146. V.G. Bhide, A.C. Rastogi, S. Salkalachen and S Jatar. Proc. Nat. Solar Energy Convention, Bombay, (1979) p343.

147. S. Salkalachen, S. Jatar, A.C. Rastogi and V.G. Bhide, Solar Cells, 3 (1981) p341.

148. R. Hill and I.A.S. Edwards, Vacuum, 27, (1977) p277.

149. M.K. Mukherjee, F.Pfisterer, C.H. Hewing, H.W. Shock and W.H. Bloss, J. Appl. Phys. 48, (1977) p1538.

150. A.N. Casperd and R. Hill, Proc. 1st Commission of European Communities Conference on Photovoltaic Solar Energy, Luxembourg, Sept. 27-30 (1977) p1131.

151. S. Martinuzzi, Solar Cells, 5, (1982), p243.

152. G.H. Hewing and W.H. Bloss, Proc. 12th IEEE Photon. Special. Conf. (IEEE, New York 1976) p483.

153. J. Vedel, Thin Solid Films 111 (1984) p121.

154. A.E. Van Aerschodt, J.J. Capart, K.H. David, F. Abbricotti, K.H. Heffels, J.J. Loferski and K.K. Reinhartz, IEEE Trans. Electron Devices, ED-18, (1971) p471.

155. H.G. Grimmeiss and R. Memming, J. Appl. Phys. 33 (1962) p2217.

156. A. Potter and J. Schalla, 6th IEEE Photovoltaic Specialists Conf. (1967) p267.

157. M. Balkanski, and B. Chone, Rev. Phys. Appl. 1 (1966) p179.

158. W.D. Gill and R.H. Bube, J. Appl. Phys. 41, (1970) p3731.

159. P.F. Lindquist and R.H. Bube, J. Appl. Phys. 43, (1972) p2839.

160. G.H. Hewing, F. Pfisterer, W.H. Bloss, Proc. Int. Conf. on Photovoltaic Power Generation, (1974) p255.

161. T.S. Te Velde, Solid-State Electron 16 (1973) p1305.

162. S. Deb, H. Saha, Photovoltaic Solar Energy Conf. (Reidel Dordrecht, Holland 1977) p570.

163. A.R. Riben and D.L. Fencht, Int. J. Electron, 20, (1966) p583.

164. M.M. Syed and L.D. Partain, Electron. Lett. 10 (1974) p163.

165. E. Konstantinova and S. Kanev, J. Appl. Phys 42 (1971) p5851.

166. F.J. Bryant, A.K. Hariri, and C.G. Scott, J. Phys. D. 16 (1983) p2341.

167. L.D. Partain, P.S. Mcleod, J.A. Duisman, T.M. Peterson, D.E. Sawyer and C.S. Dean, J. Appl. Phys. 54, (1983) p6708.

168. H.W. Brandhorst, and D.T. Bernatowicz. Proc. Int. Colloq. Solar Cells, 1970 (1971) p215.

169. T. Tevelde, 8th IEEE Photovoltaic Special. Conf. (1970) p372.

170. S. Martinizzi, F. Cabane, Bronty and J.F. Bretznes. 9th IEEE Photovoltaic Special. Conf. (1973) p111.

171. R.J. Mytton, L. Clark, R.W. Gale and K. Moore. 9th IEEE Photon. Special. Conf. (1973) p133.

172. H.J. Mathieu, K.K. Reinhartz and H. Rickert, 10th IEEE Photon Special. Conf. (1973) p93.

173. IEC Final report XE-9-F309-1 Feb 1983.

174. R.B. Hall and J.D. Meakin. Thin Solid Films 63 (1979) p203.

175. F.J. Bryant, A.K. Hariri, S. Salkalachen and C.G. Scott, J. Phys. D 16, (1983) p1755.

176. J.D. Meakin and J.E. Phillips, in NBS/DOE Workshop, stability of (Thin Film) Solar Cells and Materials, ed. by D.E. Sawyer and H.A. Schafft (National Bureau of Standards Special Publication 400-58, Washington, DC, 1979) p17.

177. G.T. Noel, G.B. Gaines and N.A. Richard, 16th IEEE Photon Special Conf. (1982) p723.

178. J.V. Florio, K.J. Matysik and F.G. Ramos, 15th IEEE Photon. Special. Conf. (1981) p793.

179. P.N. Uppal and L.C. Burton, J. Vac. Sci. Technol. A1, (1983) p479.

180. P.N. Uppal, D.W. Dwight and L.C. Burton, J. Electrochem. Soc. 130 (1983) p1136.

181. E. Castal, and J. Vedel, Analysis, 3 (1975) p487.

182. B. Baron, A.W. Catalano and E.A. Fagen, 13th IEEE Photon. Special. Conf. (1978) p406.

183. L.D. Partain, R.A. Schneider, L.F. Donaglz and P.S. Mcleod, J. Appl. Phys. 57 (11) (1985) p5056.

184. V.G. Bhide, S. Salkalachen, A.C. Rastogi, C.N.R. Rao and M.S. Hegde, J. Phys. D. 14 (1981) p1647.

185. J.C.W. Folmer and F.Jellinck, J. Less Common Metals 76, (1980) p153.

186. K. Bogus and S. Mattes, 9th IEEE Photon. Special Conf. (1972) p106.

187. F. Pfisterer, H.W. Schock and J. Worner, 3rd EC Photon. Solar-Energy Conf Proceedings, Cannes, France, (1980) p762.

188. P.K. Roy, U.S. Patent No. 4, 260, 428, April 7, 1981.

189. S.F. Dizio, Workshop on stability of thin-film solar cells based on Cds, Newark, Delaware, February 1981 (Oral presentation).

190. G.H. Hewing, F. Pfisterer, H.W. Schock, W. Arnot, and W.H. Bloss, 16th IEEE Photon. Special. Conf. (1982) P713.

191. L.F. Donaghey, U.S. Patent No. 4,366,336 December 28, 1982.

192. T. Sands, J. Washburn and R. Gronsky, Sol. Energy Mater. 10 (1984) p349.

193. T.D. Sands, PhD Thesis, Dept. of Materials Science and Mineral Engineering, US, California, Berkeley (1984).

194. F.A. Shirland and I. Rai-Choudhury, Rep. Prog. Phys Vol 41, (1978) p1839.

195. R.W. Glew, PhD thesis, University of Hull (1975).

196. J.J. Thomson, Phil. Mag. 4 (1897) p293.

197. L. de Broglie, Phil. Mag. 47 (1924) p446.

198. H. Bush, Ann. Physik 81 (1926) p74.

199. D.G. Thomas and J.J. Hopfield, Phys. Rev. 128 (1962) p2135.

200. C.H. Henry, K. Nassau and J.W. Shiever, Phys. Rev. B, 4 (1971) p2453.

201. J.J. Hopfield, J. Phys. Chem. Solids 10 (1959) p110.

202. P. Groede and E. Coutschke, Phys. Stat. Sol. 17 (1966) p911.

203. N. Susa, H. Watanabe and M. Wada, Jpn. J. Appl. Phys. 15 (1976) p2365.

204. B.A. Kulp, Phys. Rev. 125 (1962) p1865.

205. Y. Shiraki, T. Shimada and K.F. Komatsubara, J. Appl. Phys, 45 (1974) p3554.

206. G.A. Somorjai and D.W. Jepsen, J. Chem. Phys. 41 (1964) p1394.

207. R.B. Hall, R.W. Birkmire, E. Eser, T.L. Hench and J.D. Meakin, 14th IEEE Photov. Special. Conf. (1980) p706.

208. J. Humenberger, G. Linvert and K. Lischka, Thin Solid Films, 121 (1984) p75.

209. J. Humenberger, H. Sitter, W. Huber, N.C. Sharma and A. Lopez-Otero, Thin Solid Films, 90 (1982) p101.

210. D.I. Dimova, M.S. Lakova, M.G. Kalitsova and D.G. Ivanova, Bulg. J. Phys. 6 (1979) p544.

211. K.W. Boer, 12th IEEE Photov. Special. Conf. (1976) p475.

212. L.C. Burton, T. Hench, G. Storti and G. Haacke, J. Electrochem. Soc., (1976) p1742.

213. F.J. Bryant, A.K. Hariri and C.G. Scott, Phys. Stat. Sol. (a) 93, (1985) p779.

214. A. Rothwarf, Proc. 12th IEEE Photovoltaic Specialist Conference. (1976) p488.

215. T. Singer and P.A. Faeth, Appl. Phys. Lett., 11, (1967) p130.

216. R.W. Buckley and J. Woods, J. Phys. D., 7, (1974) p663.

217. R.T.P. Whipple, Phil. Mag., 45 (1954) p1225.

218. R.H. Bube, J. Appl. Phys. 37 (1966) p21.

219. P. Mark, J. Phys. Chem. Solids, 26 (1965) p959.

220. E.H. Weber, Phys. Stat. Sol. 28 (1968) p649.

221. J.P. Lergre and S. Martinuzzi, Phys. Stat. Sol. (a) 1 (1970) p689.

222. F.B. Micheletti and P. Mark, J. Appl. Phys. 39 (1968) p5274.

223. D.M. Hughes and G. Carter, Phys. Stat. Sol. 25 (1968) p449.

224. S. Achour and G.H. Talat, Thin Solid Films 144 (1986) p1.

225. S. Kolhe, S.K. Kulkarni, A.S. Nigavikar and S.K. Sharma, Sol. Energy Mater, 10 (1984) p47.

226. B.A. Kulp and R.H. Kelley, J. Appl. Phys. 31 (1960) p1057.

227. E. Grillot and P.G. Guintinc: Compt. rond 236 (1953) p802.

228. B.J. Fiedman and J.A. Duisman, Appl. Phys. Lett. 37, (1980) p1092.

229. B.A. Kulp, J. Appl. Phys. 32, (1961) p1966.

230. F.J. Bryant and A.F.J. Cox, British J. Appl. Phys. 16, (1965) p1065.

231. A.C. Rastogi and S. Salkalachen, 16th IEEE Photovoltaic Specialists Conference (1982) p877.

232. H.L. Huang, J.J. Loferski, E.A. Demeo, and R. Beaulieu, J. Of Crystal Growth, 59 (1982) p425.

233. F. Guastavino, S. Duchemin, B. Rezing, B. Girault, and M. Savelli, 13th IEEE Photovoltaic Special. Conf. (1978) p303.

234. J.J. Loferski, J. Shewchun, S.D. Mittleman, E.A. Demeo, R. Arnott, H.L. Hwang and R. Beaulieu, Solar Energy Materials 1 (1979) p157.

235. A.N. Casperd and R. Hill, Solar Cells, 1 (1979) p347.

236. M.J. Robertston and J. Woods, Proc. 2nd EC Conference on Photovoltaic Solar Energy, Berline (1979) p909.

237. B.G. Caswell, G.J. Russell and J. Woods, J. Phys. D.8, (1975) p1889.

238. N.C. Wyeth and A. Rothwarf, J. Vac. Sci. Tech. 16 (1979) p1402.

239. J. Lindnayer and A.G. Revesz. Sol. St. Electr. 14 (1971) p647.

240. G.H. Hewing et al. Proc. 11th IEEE Photovoltaic Conference (1975) p441.

241. F.J. Bryant, A.K. Hariri, S. Salkalachen and C.G. Scott. Thin Solid Films, 105 (1983) p343.

242. R.L. Clarke, J. Appl. Phys. 30 (1959) p957.

243. R.K. Purohit, B.L. Sharma and A.K. Sreedhar, J. Appl. Phys. 40 (1969) p4677.

244. G. Dearnaley, J.H. Freeman, R.S. Nelson and J. Stephen. Ion implantation, North-Holland Publishing Company, Amsterdam - London 1973.

245. J. Bougnot, F. Guastavino, G.M. Moussalli, and M. Savelli, Int. Workshop, Cadmium Sulfied Solar Cells and Other Abrupt Hetero-junctions, Newark, Delaware (1975) p337.

246. J.E. Chigoya and J.W. Edington, Phys. Stat. Solidi. A72 (1982) p304.

247. J.F. Ziegler and H.H. Anderson, Hydrogen Stopping Powers and Range in all Elements (Pergamon Press, N.Y., 1978).